Synthesis, Characterization, and 3D Printing of Conductive Polyhydroxybutyrate-Graphenic Nanomaterial Composites

by

Dan Li

A thesis submitted in partial fulfilment of the requirements for the degree of

Doctor of Philosophy

in

Materials Engineering

Department of Chemical and Materials Engineering

University of Alberta

Abstract

Advances in materials development are leading to the emergence of new classes of printable and inexpensive electronic devices, including sensors for healthcare monitoring. Most traditional sensors are built on rigid substrates, which restricts the use of these sensors. Research is driven by developing functional materials including conductors and composites that can respond to changes in their surroundings, and device fabrication techniques for patterning these materials on the micro scale. Among printable conductors, carbon nanomaterials including graphene, reduced graphene oxide (rGO), carbon nanotubes (CNTs) are highly conductive materials that can be printed from solution. However, these materials are comprised of rigid particles and tend to form brittle layers when printed without binders or additives, and their electrical properties are highly sensitive to moisture. A promising alternative is to incorporate carbon materials into polymer nanocomposites- consisting of conductive nanofiller embedded with an insulating, hydrophobic polymer matrix. The polymer matrix not only acts as a binder, but also provides mechanical support for the graphenic materials, allowing a variety of patterns and structures to be formed and maintained, while also protecting the conductive particles from moisture. Biopolymers, which are polymers that are derived from biological sources, can be introduced to this system as a more sustainable alternative to conventional polymers. In this thesis, conductive polymer composites comprised of the biopolymer polyhydroxybutyrate (PHB) and graphenic materials (i.e. rGO and CNTs) were formed through both solution processing and thermal mixing, with the aim of integrating these materials in conductive printable inks for flexible healthcare monitoring devices.

A simple, solvent casting process was used to prepare the PHB/rGO composites using acetic acid as a food-safe solvent, and the effects of different reducing agents (sodium borohydride, hydrazine,

and ascorbic acid (L-A.A)) have been systematically investigated. The L-A.A reduced rGO composites were found to be the most conductive composites, due to good dispersion, large particle size, and high intrinsic conductivity. The solvent method is compatible with many printing techniques such as direct ink writing and screen printing.

The conductivity of PHB/rGO composites was tuned by varying the nanofiller concentration. The composites showed temperature-dependent resistivity, and in terms of sensing were found to have good selectivity to temperature with respect to both pressure and moisture. Flexible thin temperature sensors were developed by first printing silver electrodes and then depositing responsive composites on top of these electrodes. Stretchable sensors were fabricated through direct ink writing (customized 3D printing) of polydimethylsiloxane (PDMS) substrates on top of which a conductive composite ink was printed in a meandering pattern. Devices exhibited good sensitivity and stability, and thermal mapping was demonstrated using up to 12 × 12 array of sensing elements.

Conductive PHB composites were made by an industrially-relevant thermal mixing process. Multi-walled carbon nanotubes (MWCNTs) were melt mixed in concentrations from 0.25 to 5 wt% using two types of polyhydroxybutyrate: one supplied by BRS (with some silicon impurities) and Biomer (PHB with plasticizers and nucleating agents), with a molecular weights of 190 kDa and 560 kDa, respectively. The extruded filaments were deposited in a layer by layer structure using a desktop 3D printer using a technique called ‘Fused Deposition Modeling’ (FDM), and the mechanical and electrical properties of printed designs were compared with hot compressed samples. 3D printed scaffolds with well-defined pore structure, tunable porosity, and high compressive modulus demonstrated that the composite materials have the potential for use in bone regeneration applications. The printed models showed geometrical and dimensional features close to the drawn

model, reflecting the good printability of PHB composite materials. Overall, this work presents opportunities for the development of biopolymers that can be functionalized into printable composite inks in 2D and 3D printing for a variety of applications.

Preface

Parts of this work has been previously published in the literature.

Chapter 3 uses contents published in - Dan, L., Pope, M.A. and Elias, A.L., 2018. Solution-processed conductive biocomposites based on polyhydroxybutyrate and reduced graphene oxide. The *Journal of Physical Chemistry* C, *122*(30), pp.17490-17500. Reproduced with permission from Dan, L., Pope, M. A., & Elias, A. L. (2018). Solution-processed conductive biocomposites based on polyhydroxybutyrate and reduced graphene oxide. *The Journal of Physical Chemistry C*, *122*(30), 17490-17500. Copyright 2018 American Chemical Society. L.D performed all experiments and wrote the manuscript. M.A.P.'s group prepared graphite oxide slurries, and M.A.P. helped to interpret data and prepare the manuscript. A.L.E. supervised the work, and contributed to designing the research and to writing the manuscript.

Chapter 4 contains materials published in - Dan, L., & Elias, A. L. 2020. Flexible and Stretchable Temperature Sensors Fabricated Using Solution-Processable Conductive Polymer Composites. *Advanced Healthcare Materials*, *9*(16), 2000380. L.D designed and performed all the experiments and wrote the manuscript, A.L.E supervised the works and contributed to designing the research and to writing the manuscripts.

Chapter 5 has contents published in - Dan, L., Cheng, Q.L., Narain, R., Krause, B., Pötschke, P., and Elias, A., 2021. 3D printed and biocompatible conductive composites comprised of polyhydroxybutyrate and multi-walled carbon nanotubes. *ACS Industrial & Engineering Chemistry Research, 0c04753*. Reproduced with permission from Dan, L., Cheng, Q., Narain, R., Krause, B., Pötschke, P., & Elias, A. Three-Dimensional Printed and Biocompatible Conductive Composites Comprised of Polyhydroxybutyrate and Multiwalled Carbon Nanotubes. *Industrial &*

Engineering Chemistry Research. Copyright 2021 American Chemical Society. As the primary author in this chapter, L. Dan performed the experiments and wrote the manuscript. Qiuli Cheng was involved in the cell cultures and cell proliferation imaging. Dr. Beate Krause and Dr. Petra Pötschke at the Leibniz Institute of Polymer Research Dresden (IPF) provided MWCNTs nanofillers and assisted to design experiments on thermal mixing, compression molding samples and strands, and morphology characterization and interpret the results. These experiments were performed at IPF during a research visit of Dr. A. Elias. Dr. Ravin Narain instructed me on using 3D printer, and Dr. A. Elias. conceived the project, supervised the work and contributed to designing the research and to writing the manuscript.

Dedication

This thesis is dedicated to my parents, who have always encouraged me from every aspect.

Acknowledgements

I had the great privilege to work with wonderful academics, great supervisor and colleagues throughout my five years study. This research work was a collaborative effort that for sure I could have not been able to finish by myself.

First, I would like to express my sincere appreciation to my supervisor Dr. Anastasia Elias for her mentorship and guidance. I admire the attentive altitude, leadership, and creativity that she put into my projects, as well as the care for my life besides research. I was super lucky to have you being my supervisor, which I could not have asked more. I am immensely grateful for giving me the opportunity to my graduate study while helping me grow at the professional level. Dr. Elias, thank you for telling me that should feel confident of myself and my work, and teaching me to be more efficient and critical thinking.

I was so fortunate to get to know other great professors at the University of Alberta in different ways. Some examples include, inspired by courses and seminars given by professors, had meaningful discussion or received wonderful research suggestions, trained and generously helped by them and their students. I especially want to thank Dr. Hyun Joong Chung and Dr. Ravin Narain for allowing me use the instruments in their labs. Besides, I would like to thank the previous and present members of Elias Lab for their assistance, ideas and help. Special thanks to Dr. Anbukarasu Preetam for advise on research and guidance in my first year, Dr. Adrian Lopera Valle for guidance and taking care of the lab. Dr. Diana Martinez Tobon for providing me enzymes and buffer solutions, and Anuja Tripathi for being an excellent and close friend to me and willing to share and listen to my ideas. I also like to thank my summer students over the five years who have helped me with experiments and paper editing. A number of characterizations in my PhD work would not have been possible without the expertise of many intelligent people throughout the campus. Thank

you very much, Nancy Zhang, Peng Li, Shiau-yin Wu and Shihong Xu (Nanofab), Mike Xia (NINT), Xuejun Sun and Pricilla Gao (Cross Cancer Institute), for helping and advising me fabricate and characterize many of my samples. Thank you for offering such a useful community of researchers at the university.

Finally, I would like to thank my family members that have provided me with immense support when I was down. To my mother Zhaoxia Zhang, father Weizheng Li, uncle Weidong Li and more recently my boyfriend Chenxi Wang. You have been alongside me each step of my way and I must express my appreciation. Thank you for providing me with continuous support and encouragement through years of study. This work might not have been down without each one of you. To the memories of my grandfather Tingxi Li (1936-2020) who always cheered me up and was being proud of me.

Table of Contents

List of Tables

List of Figures

Chapter 1. Introduction

1.1 Responsive Biopolymer Composites for Healthcare Monitoring

Flexible electronics are under development towards enriching our daily lives, for example in the form of wearable devices to monitor healthcare signals. Flexible electronics could fulfil a growing interest in long-term and continuing monitoring of blood pressure, pulse, and body temperature.[2] For example, Jeong In Han and co-workers demonstrated temperature sensors fabricated by depositing thin films of Ni-Cr composites on flexible polymer substrates. [3] John Rogers and co-workers reported arrays of electrical devices both for sensing prosthetic stimuli and for electrical muscle activation, fabricated using typical lithography technique.[4] However, many of the materials used in conventional planar electronics are unsuitable for flexible electronics because of their rigid and brittle nature. Furthermore, significant barriers remain in the large-scale and inexpensive fabrication of devices based on these materials. Most microfabrication involves expensive lithography technique that must be performed in a cleanroom. In terms of sensing materials, good selectivity to desired stimuli such as temperature, moist, pressure, bending, etc. is also required for healthcare monitoring. Biocompatibility is another factor that needs to be taken into account when the sensor is in contact with the human body.

Conventional sensors have been built with the use of transistors constructed on semiconductor wafers, and are well developed. Silicon wafers are perfectly planar but brittle, rigid and not biocompatible, thus making them poor substrates for use in biosensing. A flexible substrate is needed to overcome this mismatch in mechanics. One approach to achieve this involves building devices on flexible substrates, which are conformable and can facilitate better attachment to a curved surface than rigid ones. Thin polymer sheets or films are therefore generally used as

substrates, including polyimide, elastomers, polyethylene terephthalate (PET), fabrics. For example, Rogers and coworkers designed platinum (Pt) on the surface of Kapton^{TN} (polyimide) tape for use of flexible temperature sensor with high accuracy; though Pt is quite expensive and difficult to process.[5] It often involves patterning metals using the standard microfabrication techniques such as sputtering and lithography.

Recently, electrically conductive polymer composites (CPCs) have been implemented as printable conductors. In these composites systems, conducting nanoparticles (e.g. carbon-based materials or metal particles) impart electrical conductivity to the composite, while the polymer matrix (which is typically insulating) provides mechanical stability.[6–8] At a given temperature, the resistance of composite is usually highly dependent on the concentration of conductive nanofillers. At low concentration the composite may be non-conductive, however when the loading of nanomaterials is increased beyond a certain electrical percolation threshold the resistance may drop abruptly. The particular filler content is called the electrical percolation threshold. A conductive filler is an important part of a CPC. In terms of conductive materials, graphenic materials are popular because they are widely available, light weight, inexpensive, and have excellent conducting properties. One advantageous property of CPCs is that they may be compatible with printing techniques including drop casting, direct ink writing (DIW), fused deposition modelling, and screen printing, and may therefore be patterned without the use of photolithography.

Through proper selection of the conductive filler and/or the polymer matrix, responsive CPCs may be engineered. Responsive CPCs undergo a change in electrical conductivity upon small variation of environmental conditions such as temperature, humidity, and light. In the responsive CPCs, either the polymer matrix or the conductive filler undergoes a response that shows the change in conductivity to a selected stimulus, such as mechanical stress, vapor, and temperature.[9] Sensors

can be formed by leveraging the stimuli-responsive properties of CPCs. Compared to traditional sensors that were made of metal and semiconductors, the responsive CPCs-based sensors present more advantages, such as ease processing (better printing ability), corrosion resistance, and tunable sensing performance. Graphenic materials are responsive to many external stimuli including light, heat, and humidity. Graphenic materials can be blended in polymers to engineer responsive materials that may respond to some typical stimuli. Graphenic/polymer composites can be solvent processed, generating good printing property for fabricating inexpensive and printable sensor. However, a few challenges exist for the graphenic based ink printing, for instance, cracks are easily formed during printing graphene owing to its brittle nature. Plasticizers and binders are widely used in graphene inks to control the rheological behaviour of ink and stability of the printed layers, and these inevitably reduce the conductivity of ink itself. It is also challenging to form composites that have maximum conductivity with minimum loading of nanofillers. A good dispersion of nanofiller inside the polymer matrix and high intrinsic conductivity of fillers are critical to address the above problems. Among the varying processing methods, solvent processing and thermal mixing turn out to be versatile methods not only in forming highly conductive composites but are also compatible with many printing methods.

A variety of matrix materials may be utilized in CPCs, including biopolymers. Biopolymers produced from renewable resources have attracted immense interest in research and industrial field. To reduce the impact on the environment and to reduce safety concerns around sensors that are in contact with humans, investigations on biopolymers (e.g. polyhydroxybutyrate, gelatin, cellulose, silk) have become more popular in recent years. Polyhydroxybutyrate (PHB), derived from micro-organisms in a fermentation process, has a number of attractive features. PHB is biocompatible, and is stable in vivo. It can be biodegraded by micro-organisms in the environment

for the use of sensors that can be eventually biodegraded. Therefore, PHB could be potentially used in vivo applications that requires high stiffness, such as bone regeneration applications (e.g. scaffolds). In addition, it may find application in sensors formed using CPCs as the sensing element intended for use in biomedical applications.

1.2 Objective and Approach

The main goal of the work described in this thesis is to investigate and develop highly conductive polyhydroxybutyrate (PHB)/graphenic materials based composites that can used in low-cost, flexible sensors for healthcare monitoring. In these systems, the temperature-dependent properties of the graphenic materials will be leveraged to engineer materials that undergo a change in conductivity as a function of temperature. The selectivity to the stimuli and sensitivity of these composites will be explored. In the final part of this work, these materials will also be investigated for use as cell scaffolds.

This work specifically focuses on how to formulate PHB/graphenic material composites that have high conductivity at minimal loading of graphenic nanomaterials while maintaining some mechanical flexibility. In these systems the graphenic nanomaterials will provide temperature dependent conductivity, while the PHB matrix will offer the mechanical flexibility, and prevent the graphenic materials respond to moisture as fillers were embedded into the PHB that is a hydrophobic material. This temperature-responsive property was utilized to make a sensor that has high selectivity and sensitivity of temperature in the ambient environment. Emphasis is placed on using the temperature dependent resistivity property of rGO to develop a flexible and stretchable temperature sensor that can be potentially used for human temperature monitoring. The temperature responsive mechanism, physical, electrical and mechanical properties of composites

are systematically investigated, and methods to print these materials are developed. Proof of concept printed devices are used to monitor temperature on the surface of skin. To further expand the use of PHB and minimize the employment of organic solvents, thermal mixing (solvent free) is investigated to form PHB/multi walled carbon nanotubes (MWCNTs) composites. From these composites, 3D printing filaments are formed and utilized in FDM printing, where the mechanical, thermal, electrical properties of printed 3D designs are characterized.

1.3 Organization of Thesis

Chapter 2 presents a broad overview of the literature about biopolymers including polyhydroxybutyrate (PHB) and provides the background to synthesis and characterize conductive biopolymer composites with a focus on responsive CPCs. Graphenic family materials, including graphene, reduced graphene oxide (rGO), carbon nanotubes (CNTs) are also introduced in chapter 2, with a focus on the advantages of using them as nanofillers. Different printing techniques such as solvent casting, inkjet printing, screen printing, direct ink writing, and fused deposition modeling will be introduced, and the basic formulation of the inks/solid filaments used in these processes will be discussed.

Chapter 3 compares three different reducing agents (e.g. N_2H_4, $NaBH_4$, L-A.A) for the reduction of graphene oxide (rGO) to form conductive rGO/PHB composites in solution. The effects of the three reducing agents are systematically investigated by comparing their reduction efficiency, the residual functional groups presented on the graphene oxide (GO), and the properties of the resulting composites of all the composites. The mechanical properties of the composites are characterized; and a strain sensor is demonstrated using these composites.

Chapter 4 presents the design, fabrication, and characterization of simple and low-cost temperature sensors using conductive rGO/PHB composites patterned on both flexible and stretchable substrates through both drop coating and direct ink writing (DIW). These composites are formed using a high melting point biopolymer polyhydroxybutyrate (PHB) as the matrix and the graphenic nanomaterial reduced graphene oxide (rGO) as the nanofiller (from 3 to 12 wt%), resulting in a material that exhibits a temperature-dependent resistivity.

Chapter 5 explores 3D printing of unconventional polymer composites comprised of multi-walled carbon nanotubes (MWCNTs) and biopolymer polyhydroxybutyrate (PHB) on a commercially available fused deposition modeling (FDM) 3D printer, to print electrically conductive designs. The MWCNTs were melted mixed in amounts from 0.25 to 5 wt% in PHB from two different suppliers with slightly different physical properties. The incorporation of PHB and MWCNT can be printed out into neat scaffolds structure with organized pore size, tunable porosity, and low cytotoxicity.

Chapter 6 provides a summary of the contributions, impacts and conclusions made in this thesis. The future direction and suggestions of the conductive 2D materials/biopolymer composites for inexpensive sensors are briefly discussed.

1.4 References

(1) Anbukarasu, P., Sauvageau, D., & Elias, A. Tuning the properties of polyhydroxybutyrate films using acetic acid via solvent casting. *Scientific reports*, **2015**, *5*, 17884.

(2) Jayathilaka, Wanasinghe Arachchige Dumith Madushanka, et al. Significance of nanomaterials in wearables: a review on wearable actuators and sensors. *Advanced Materials* 31.7 **2019**, 1805921.

(3) Eom, T. H.; Han, J. I. The Effect of the Nickel and Chromium Concentration Ratio on the Temperature Coefficient of the Resistance of a Ni–Cr Thin Film-Based Temperature Sensor. *Sens. Actuators Phys.* **2017**, *260*, 198–205. https://doi.org/10.1016/j.sna.2017.04.024.

(4) Xu, Baoxing, et al. An epidermal stimulation and sensing platform for sensorimotor prosthetic control, management of lower back exertion, and electrical muscle activation. *Advanced Materials* 28.22, **2016**, 4462-4471.

(5) Kim, Dae-Hyeong, et al. Materials for multifunctional balloon catheters with capabilities in cardiac electrophysiological mapping and ablation therapy. *Nature materials* 10.4, **2011**, 316-323.

(6) Yang, Weixing, et al. Ultrathin flexible reduced graphene oxide/cellulose nanofiber composite films with strongly anisotropic thermal conductivity and efficient electromagnetic interference shielding. *Journal of Materials Chemistry C* 5.15, **2017**, 3748-3756.

(7) Wan, Yan-Jun, et al. Improved dispersion and interface in the graphene/epoxy composites via a facile surfactant-assisted process. *Composites science and technology* 82, **2013**, 60-68.

(8) Yun, Sungryul, and Jaehwan Kim. Mechanical, electrical, piezoelectric and electro-active behavior of aligned multi-walled carbon nanotube/cellulose composites. *Carbon* 49.2, **2011**, 518-527.

(9) Chen, Jianwen, et al. "Advances in Responsively Conductive Polymer Composites and Sensing Applications." *Polymer Reviews*, **2020**, 1-37.

2. Background and Review of the Literature

There is a rising demand for inexpensive and printable sensors that can be used in short term applications and then discarded, including in healthcare monitoring. Printable materials with a variety of characteristics, including high conductivity and tunable Young's modulus, are required. Therefore, conductors such as metals and conductive polymers are often used as printable sensing materials. Conductive polymer composites (CPCs) are being explored as viable materials for making inexpensive sensors as a variety of polymers and fillers are available. CPCs are often composed of conductive micro- or nano-particles ("fillers") that are blended into a polymer matrix, wherein the matrix mainly offer mechanical support/flexibility and the filler provides electrically conductive pathways through the otherwise insulating material.

In this chapter, CPCs for flexible sensors used in healthcare monitoring are discussed along with a brief introduction to biopolymers and nano-fillers, with the focus on polyhydroxybutyrate (PHB) matrices and graphenic fillers. An overview of tuning the mechanical and electrical properties of PHB/graphenic CPCs is given, as PHB is intrinsically brittle and not electrically conductive, along with fabrication methods using different processing methods such as solvent processing and thermal mixing. This includes several printing approaches: drop casting, inkjet printing, direct ink writing and filament-based fused deposition modelling. Additionally, detailed descriptions and comparisons relevant to the current state-of-the-art printable CPCs and predicted future trends are provided in this chapter.

2.1 Current State of the Art of Flexible Electronics

Flexible electronics made with carbon-based, metallic and organic components could enable technologies such as low-cost sensors used in healthcare monitoring. Most traditional electronic

components are rigid and have limited stretchability, flexibility, and portability. In contrast, flexible electronic components, normally built on flexible plastic or elastomeric substrates, can far better withstand repeatedly induced strains and pressures with negligible effect on electronic function.

The idea of flexible electronics started in the middle of the Cold War and has existed over 60 years. During this time in history, space technologies were being heavily researched and rapidly developed and the idea to make solar cells thinner and flexible to reduce weight and save space in spacecrafts was proposed. These flexible solar cells, very first flexible electronic devices, were fabricated on plastic substrates with a thin, single-crystal silicon layer around 100 μm thick. Later on Brody and his colleagues developed the first flexible thin film transistors (TFTs) on different flexible substrates, although the crystalline silicon or tellurium used for deposition are not intrinsically flexible materials.[12]

Flexible sensors for biomonitoring purposes should be soft, biocompatible, lightweight, and naturally conformal to the surface of the skin, evoking minimal user awareness. To achieve this goal, it is critical to overcome the rigid, brittle, and largely planar structures of silicon semi-conductors used in traditional electronics. In addition to replacing the stiff substrate with a flexible polymer one, there is great interest in replacing typical cleanroom fabrication methods used to pattern the conductors, insulators, and other components of these electronic devices with printable materials. In the literature, flexible sensors for monitoring healthcare signals have been made using tuned composite materials (e.g. CPCs) patterned using traditional methods on compliant substrates, although much room for improvement remains.

2.2 Conductive Polymer Composites

Conductive composites used in flexible electronics are typically comprised of conductive filler particles dispersed in a polymer matrix. Polymers are highly deformable relative to metals, offering the mechanical flexibility for the CPCs (since most fillers are small particles of materials that are rigid in bulk form), but polymers are typically electrically insulating, requiring the addition of electrically conductive filler particles. The blending of these two different materials results in CPCs useful for sensing purposes, wherein either the matrix or conductive particle undergoes a measurable change in some properties in response to a desired stimulus. Compared to a pure metallic conductor, CPCs are advantageous in ease of printing patterns, oxidation resistance, and are tunable (able to exhibit a broad range of electrical conductivities). The minimum loading of nanofiller required to form a continuous network inside the polymer matrix is called electrical percolation threshold, at which point the composite can be considered conductive.[13] Many CPCs show electrical behaviour that can be described and predicted by percolation theory, illustrated below in Figure 2.1.

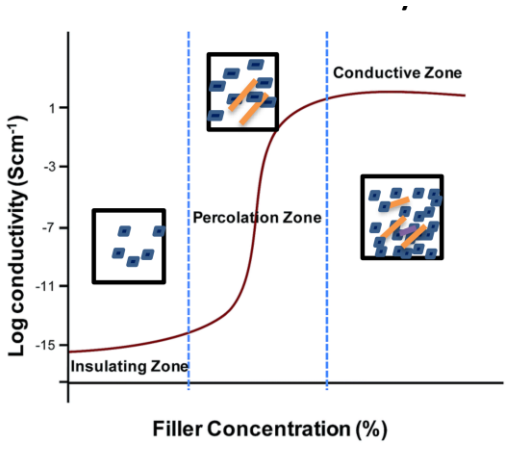

Figure 2.1 Percolation theory illustration

When the concentration of nanofiller is low (well below the electrical percolation threshold) a CPC film will be highly resistive. Near or slightly above the electrical percolation threshold (where a continuous conductive network has formed), the resistivity of CPC film substantially decreases several orders of magnitude. Well above the threshold, the electrical conductivity continues gradually increasing with the increasing number of internal conductive pathways. However, continuing to add more filler results in undesirable effects such as particle agglomeration, impaired mechanical properties, and increased cost. Obtaining a low electrical percolation threshold is essential and this can be strategically achieved by large particle geometry and a uniform dispersion of filler particles that have intrinsic high electrical conductivity.

The electrical and mechanical properties of the resulting CPC material depend on numerous factors, including: the properties of the conducting filler; the proportion of filler added to the polymer matrix; the dispersion and the orientation of the conducting filler; and the adhesion between the matrix and filler. Some of the resulting characteristics depend not only on the properties of the conducting particles and the polymer matrix but on the manners in which they are processed.

CPCs have been demonstrated with a variety of fillers (e.g. cellulose, metallic materials, and graphenic materials).[14–16] Graphenic materials, for example, can be easily processed and are good candidates for nanofiller materials, especially reduced graphene oxide (rGO). The first rGO/polymer composites were prepared by Stankovich et al. using solvent mixing in the presence of dimethylformamide (DMF).[17] These rGO/polystyrene composites had an electrical percolation threshold of 0.1 vol% and conductivity of 1 S m^{-1} at 2.5 wt% loading, and around 10 S m^{-1} at ultimate conductivity. Similar "ultimate" conductivity values have been reported in polyurethane (around 1 wt%), poly(vinylidene fluoride) (around 4 wt%), gelatin (around 5 wt%).[18,19] However,

to further increase the conductivity of CPCs and enhance the ease of processing, further research is required. The randomly distributed CNTs blended in the polymer matrix can form multiple electrical pathways to allow the current flow; however, the mechanical properties of CPCs are not always as desired. For example, the addition of conductive nanofillers results in increased stiffness (increased Young's modulus) along with increased conductivity. This means the opposing forces of increasing modulus and conductivity for a given CPC can be tuned by varying the concentration of nanofillers. One such filler material is graphene and research efforts around this material have resulted in a family of graphene-based materials being used as fillers in CPCs.

2.3 The Graphenic Material Family

Graphene occurs naturally in graphite, a naturally soft rock with a laminar structure that is comprised of flat layers of carbon atoms bound together in a single atomic planes, known as graphene. The 2D structure of graphene results in high conductivity and can be further processed to create the family of graphenic materials described in this chapter. The laminar 2D structure results high conductivity to the graphite-like carbon materials. Graphenic materials include: graphite, graphene, graphene oxide (GO), reduced graphene oxide (rGO), carbon black (CB), and carbon nanotubes (CNTs). The atom structures of the carbon family of nanomaterials are shown below in Figure 2.2.

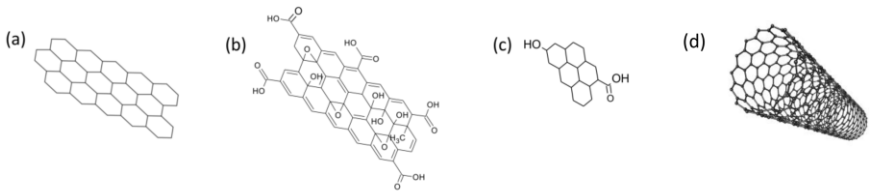

Figure 2.2 Structure of graphene (a), graphene oxide (GO) (b), and reduced graphene oxide (rGO) (c), carbon nanotubes (CNTs) (d).[20]

Pristine graphene is a 2D honeycomb lattice of carbon atoms, as shown in Figure 2.2 (a). Graphene oxide (GO) is an oxidized form of graphene and has a 3D structure with different oxygen-containing functional groups, shown in Figure 2.2 (b). Reduced graphene oxide (rGO) is a two-dimensional material containing carboxyl and hydroxyl functional groups derived from GO's three-dimensional structure, shown in Figure 2.2 (c). rGO has similar electrical, thermal, and mechanical properties as graphene but is less expensive. Carbon nanotubes (CNTs) are rolled up graphene with extraordinary electrical properties, listed in (d). [20] Particles of these graphenic materials are used in CPCs as conductive fillers owing to their good electronic and mechanical properties, chemical stability, and inexpensive processing.

These particular properties aroused widespread interests in fabricating conductive polymer composites. Production of graphene oxide (GO) was firstly reported by Brodie in 1859.[21] A standard solvent-based oxidation method was then developed by Staudenmaier, Hummers and Offeman using a mixture of potassium permanganate ($KMnO_4$) and concentrated sulfuric acid (H_2SO_4).[21,22] Subsequently, several strategies were carried out to reduce GO to restore the properties of conductivity. Reduction methods now include solvent routes in alkaline or acidic environments and thermal routes using ultra-high temperature or lasers and have been extensively reported.[23–26] The first graphite flakes consisting of a few layers were first observed in 1948 and the term of graphene was coined to describe a single layer of graphite. It was not until 2004 that graphene was experimentally observed by Novoselov's group using the exfoliation method to remove single sheets of graphene from graphite with adhesive tape. This exfoliation method is commonly called the "scotch-tape" method.[27] Since 2004, materials that share a similar laminar structure with graphene have been investigated, widely referred to as 'graphenic materials' to distinguish them from graphene, typical examples include graphene oxide (GO) and reduced

graphene oxide (rGO). [28,29] GO, a compound of carbon, oxygen, and hydrogen in variable ratios, is obtained by graphite oxidation using strong chemicals. The extra oxygen related groups show a 3D atomic spacing, and result in a highly resistive property. rGO, synthesized via chemical or thermal reduction of exfoliated GO has similar excellent electrical and mechanical properties as pristine graphene, but the price is much lower. rGO contains some defects and a small number of residual oxygen and other heteroatoms, as well as some structural defects, and may consist of a structure of several layers. Despite rGO's less-than-perfect geometric nature (as compared to pristine graphene) in terms of purity and arrangement, it is still an attractive material that can be synthesized sufficiently in quality with many different reduction methods. Gradually, researchers have become more focused on how to produce reduced graphene oxide (rGO) that has a neat laminar structure and fewer layers. rGO, depending on the specific material's quality, is suitable for use in many fields such as composite materials, conductive inks, and responsive materials.

Among the methods that can be used for the preparation of rGO, solvent reduction is a versatile method. Many studies have focused on optimizing reducing agents and processes, as well as investigating the properties of the resulting rGO. Sodium borohydride ($NaBH_4$) is a widely used reducing agent, which can trigger a hydride transfer reaction and effectively remove the oxygen functional groups from GO.[30] $NaBH_4$ is viewed as a mild reducing agent and is relatively safe to handle. However, it generally results in a low reduction efficiency, where a low ratio of C:O atoms in the final product is expected. Hydrazine (N_2H_4) is another popular used reducing agent for GO that tends to result in a high reduction efficiency (high C:O atom ratio).[31] Hydrazine itself is highly toxic to humans and the environment, and is not compatible with most organic solvents. Ascorbic acid (L-A.A), commonly known as vitamin C, is considered a natural, "green" (less hazardous chemical compared to other reducing agents that generates toxicity to human health and the

environment) reducing agent with good reduction efficiency.[24] Another advantage of L-A.A as a reducing agent is that it can also be used as a stabilizer in rGO dispersions, so it does not need to be removed after the GO reduction.

Carbon nanotubes (CNTs), typically 0.4-40 nm in diameter, are two-dimensional graphene sheets rolled-up into a tube, with high length-to-diameter aspect ratios (up to 1000:1), high electrical conductivity (10^7 to 10^8 S/m), and high mechanical strength (Young's modulus of 1 TPa and yield stress of 100 GPa).[32,33] CNTs have two main structures: single-walled CNTs (SWCNTs) and multi-walled CNTs (MWCNTs), where MWCNTs are formed by several concentric SWCNTs connected by Van der Waals forces. Single-walled CNTs were first produced by Iijima in 1991, and have cylindrical structure composed of hexagonal carbon atoms by sp^2 (planar) bonds.[34] In addition to the two different CNTs structures, there are three different types of CNTs: armchair, zigzag, chiral carbon nanotubes. Different atomic orientations result in different behaviours of CNTs such that they can behave like metals, insulators, or semiconductors. Reinforced polymeric nanocomposites containing CNTs have been a hot topic since the first reported research of CNT/epoxy composites in 1994.[35] CNTs have also been functionalized prior to blending into the polymer matrix to engineer functional materials. In a CNT/polymer composite the proportional loading of CNT filler is usually limited to below 10 % due to the significant increase of viscosity, leading to poor processability and cracks within the resulting composite materials.

2.4 Flexible Electronic Substrates

A flexible electronic device needs to maintain its performance under mechanical deformation such as bending, compression, and twisting. A certain range of Young's moduli are acceptable for flexible substrates, while for stretchable electronic devices, intrinsically stretchable substrates with

low modulus are required (e.g. elastomers). Polymeric substrates are gaining popularity in flexible electronics and sensors and are being selected not only for the mechanical properties, but also for their thermal properties. Some metal inks, such as ones comprised of silver nanoparticles, need to be sintered to improve the conductivity, thus substrates should withstand the high temperatures required for this process. Substrates, especially plastic substrates, will soften or melt if the temperature exceeds the glass transition temperature. Thermal expansion also needs to be considered. If the thermal expansion coefficient of the substrate and the responsive layers do not match, internal stresses will be introduced to the device that will likely cause device failure.

Polymer substrates like polyesters, polylactic acid (PLA), and polyimide (PI) are flexible, light-weight, and inexpensive - meeting many of the above described requirements. The most popular polymer substrates are polyethylene terephthalate (PET), polyethylene naphthalate (PEN) and PI. PET and PEN are semi-crystalline polymers and PI is amorphous. PET is transparent in color, has a Young's modulus around 2.9 GPa, and resists most chemicals, however, the Tg is relatively low (150-200 ^{o}C). PI, which is orange/yellow in color, provides excellent thermal stability up to ~350 ^{o}C, has reasonable mechanical strength, and good chemical resistance.

2.4.1 Biopolymers

Fossil fuel-based polymers brought serious environmental problems in this century. According to recent data reported by Plastics Europe, world-wide plastic production reached almost 322 metric tons in the year 2015, with an annual growth rate of 8.4 %. A study reports that almost 5.25 trillion kgs of plastic waste are currently floating in the marine environment. It is predicted that the oceans will contain more plastic waste than marine life by 2050 if this trend continues.[36–38]

All this plastic waste poses serious problems regarding global and local ecosystems. As a result, there is a growing demand for the discovery and development of a new class of polymers (biopolymers) that are not only safe and inexpensive to use but can be biodegraded in specific environmental conditions. Biopolymers have two general definitions: (1) a polymer that is produced from biological resources, including microorganisms such as bacteria or from renewable resources such as plants; (2) a polymer that is biodegradable. Biopolymers derived from natural resources (bioderived) came into the market as "green" materials, more sustainable and causing minimal harm to the existing ecosystem. 80 % of all commercially available polymeric materials are derived from fossil fuels, so the need of biopolymers has grown significantly in recent years as fossil fuel resources diminish. Biopolymers are expected to be used as alternatives to current fossil fuel-based polymeric materials to reduce the environmental impact of these materials after disposal.[39]

Initial research on non-bioderived biopolymers focused on chemical modifications or bio-derived additives to favour the degradation behaviour .[40–42] These modifications may reduce a polymer's overall environmental stability and increase the cost. Another approach involves polymerization of monomers that are originally degradable and safe in the environment. The resulting non-bioderived (or synthetic) biopolymers were found to be susceptible to degradation under certain conditions, such as hydrolysis and catalytic attack by reactive agents present in the environment.[43,44] Using this method, many synthetic degradable polymers have been developed. Polylactic acid (PLA) and polycaprolactone (PCL) are the most popular degradable synthetic polymers, and are produced by direct polymerization.[45–48] This technique makes them suitable for fabrication processes using filaments, films, and coatings required for various biomedical devices.[49–52] However, the synthetic polymers produced by polymerization route have limitations

related to their slow degradation rate in the natural environment.[53,54] They either require high temperature for accelerating the degradation speed or need several biological agents that can actually break down the polymer chains in a natural environment.

Cellulose and starch, each produced by plants, are the most common biopolymers that are known to degrade naturally and produce no hazardous products during degradation. In addition to plants, some bacteria and fungi can accumulate polymeric materials within their cell wall under specific conditions.[55–58] Polyhydroxyalkanoates (PHAs) are produced by certain bacteria as an energy reserve under limited source conditions and in the presence of excess carbon.[59–61] PHAs are an attractive class of bioderived biopolymer because it is chemically stable, biocompatible, and degradable under conditions.[62] The degradation products of PHAs are safe for the environment and humans, as they exist in all living organisms. PHA tends to undergo mild hydrolytic degradation under acidic conditions due to its unstable ester bond in the backbone.[63,64] Many depolymerase enzymes accelerate the hydrolysis rate by attacking these weak ester bonds. Within the family of PHAs, polyhydroxybutyrate (PHB), polyhydroxyvalerate (PHV), and poly(3-hydroxybutyrate-co-3-hydroxyvalerate) (PHBV) are the most popular in current research. This is due to the ease of their production and because they share similar mechanical properties as polypropylene.

2.4.2 Polyhydroxybutyrate (PHB)

PHB is a highly-crystalline, biocompatible thermoplastic in the PHA family of aliphatic polyesters, discussed above and shown below in Figure 2.3. This hydrophobic polyester is produced by bacteria, with its most common form being poly(3-hydroxybutyrate); its monomer, R-3-hydroxybutyric acid, is nontoxic and exists naturally in the human body.[65–67]

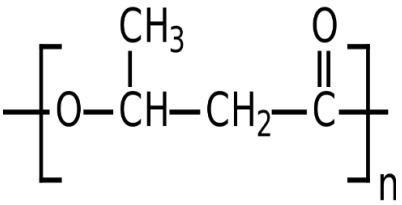

Figure 2.3 Molecular diagram of polyhydroxybutyrate (PHB).

More than 20 bacterial species such as *Basillus megaterium*, *Escherichia coli*, etc. are known to produce PHB under nutrient imbalance conditions.[68–70] During PHB monomer formation, a shell is formed around the granule to separate the polymers from the aqueous cytosol. Polymer granules then can be separated from the medium by centrifugation after fermentation. The intracellular PHB granules are formed in an amorphous state while the obtained extracellular PHB granules are in a semi-crystalline state after solvent extraction using centrifuge. PHB granules accumulated in bacterial cells are quickly broken down by depolymerase enzymes. This biopolymer has attracted intense attention because of its ease of production and biocompatibility. PHB suffers from some drawbacks such as intrinsic brittleness, poor processability, and a narrow thermal processing window. However, the properties of PHB (e.g. mechanical and electrical) can be tuned to some degree by adding specific fillers and creating composite materials as described elsewhere in this chapter.

To optimize the mechanical, electrical and thermal properties of PHB, nanoparticle fillers can be blended into PHB. Nanofillers from the carbon family are of particular interest due to their extraordinary electrical and thermal properties and low cost. It has been reported that adding graphenic materials to PHB not only improves the mechanical properties (e.g. Young's modulus, toughness, etc.), but also yields composites with good electrical properties.[18,71,72] Barletta et al. used thermal mixing to prepare a PHB/graphene nanoplates (GNP) nanocomposites with improved

hardness and scratch performance.[18] Manikandan et al. reported a PHB/GNP composites formed by a solvent casting method, which exhibited good barrier and mechanical properties. The composites also presented low cytotoxicity and biodegradability by soil biomes, which has the potential use in food-packaging applications.[73] However, even though GNP is a highly conductive nanofiller, neither composite showed noticeable increase in electrical conductivity. The most common solvent for dissolving PHB used in literature is chloroform, which is a toxic organic solvent, making it undesirable for processing PHB films. Acetic acid was found to be an alternative solvent for processing PHB by our group.[1] Acetic acid is a greener solvent compared to chloroform, and produces smooth, flat PHB thin films.

2.5 Responsive Conductive Polymer Composites (RCPCs)

Stimuli responsive polymers, also called smart materials, undergo a measurable property change when exposed to an appropriate external stimulus such as humidity, heat, light, or magnetic fields.[74] They differ from the conventional polymers in that they show rapid physiochemical response to the specific stimuli. To engineer a measurable change, some stimuli-responsive polymers are blend with conductive nanofillers to obtain responsive conductive polymer composites (RCPCs). RCPCs mainly show resistivity or capacitance change under an appropriate stimulus, and have been involved in making sensors for detecting temperature, humidity, pH, etc.[75,76] The response to the external stimuli through resistive changes have attracted considerable attention for use in sensors due to their high sensitivity, ease of manufacturing, light-weight, mechanical flexibility, simple mode of data collection, and easy interpretation.

The stimulus-response behavior of RCPCs has been investigated for different sensors types, including strain sensors, pressure sensors, temperature sensors to detect a specific stimulus.[77]

Although great potential can be seen in the possible uses of RCPCs for sensors, especially for biosensors used in healthcare monitoring, more investigations are needed to achieve the high-stability, -selectivity, -sensitivity, and reproducibility required. In some cases, a non-linear relationship between the electrical signals and the applied stimuli is observed. This makes it hard to conduct data interpretation, which limits the practical applications. Fast response to the certain stimuli is challenging for some RCPCs-based sensors. For example, temperature sensors that are based on the thermal expansion of the matrix polymer have been demonstrated, however it often takes several seconds to respond to the change in temperature, and some are not responsive at low temperatures, which are not good for body temperature sensing.[78] To overcome these challenges, both better design of the internal architecture of the RCPCs and better informed choices of suitable nanofillers and polymer matrices are required.

2.6 Requirements for Applications of Printed CPCs

As previously stated, CPCs are normally comprised by conductive nanofillers embedded into a polymer matrix, where polymer offers the mechanical flexibility while the conductive nanofillers are normally rigid. Numerous demonstrations and prototype devices using solution-processed CPCs have been reported over the last decades, though applications with a high level of complexity and functional integration need further investigation and development. Generally, in a typical conductive ink formulation, the dried film obtained contains randomly distributed flakes or sheets of conductive filler embedded in a polymer matrix. The film becomes conductive when these nanofillers compose enough of the inner structure to form a continuous pathway for a current to flow through.

Transparent conductive electrodes (TCEs) are largely used within applications such as touch-screens, light-emitting devices, and photovoltaics.[79–83] This type of materials need to be highly transparent and highly conductive. Current TCE materials are mostly ceramic-based, such as indium oxide, tin oxide, and zinc oxide. Indium tin oxide (ITO) is currently widely used owing to its high optical transparency (> 80 %) and low sheet resistance (around 15 Ω/□), though it is mechanically brittle.[84,85] Researchers are trying to find alternatives that can offer certain flexibility to meet the requirement of next-generation electronics. Different approaches using liquid phase exfoliated graphene have been investigated through drop or dip casting, spray coating, Langmuir-Blodgett assembly, screen printing, and inkjet printing. In 2008, Cote et al. reported Langmuir-Blodgett assembly of graphene oxide (GO) thin-films on substrates such as quartz, mica, and glass through dip-coating. Relatively high sheet resistance of 19 MΩ/□ was measured after 3 cycles of dip coating while maintaining a high 95 % transparency has been achieved in this early-stage research.[86] Other methods, as reported by Eda et al., involved a reduced graphene oxide (rGO) dispersion was directly spin-coated on to glass and plastic substrates with improved results. The film thickness could be controlled by varying the filtration volume, and the resulting sheet resistance was 43 kΩ/□ and 65 % transparent. Sheet resistance as low as 5 kΩ/□ is the best performance of solution-processed graphene films up to date and was fabricated by spray coating followed by annealing.[87] The high resistance is likely owing to the small particle size of conductive nanomaterials and the lack of percolation. Larger particle sizes (e.g. flakes) of graphenic materials are usually preferred as they have shown decreased sheet resistance from 6 kΩ/□ to 2 kΩ/□ as flake size was increased 77 %.[88] Graphene grown by chemical vapor deposition (CVD) has performed significantly better than solution-processed methods with higher transparency. For example, Bae et al. reported sheet resistance as low as 30 Ω/□ with transparency up to 90 % with

a transfer method using CVD-grown graphene films.[89] Despite this markedly improved performance, CVD-grown graphene is expensive and hard for large manufacturing. The large-scale fabrication of transparent conductive electrodes (TCEs) through printing needs a certain degree of fluidic control and patterning resolution by achieved by optimizing solution properties such as the concentration of conductive graphenic materials, low viscosity of suspension, and quick solvent evaporation rate. Custom-patterned solar cells, for example, require more control in patterning over large areas.

Opaque conductive inks are getting popular in recent years as their preparation is often simple compared to transparent conductive inks. A value of 40,000 S m^{-1} was demonstrated by Secor et al. in 2017 with an opaque composite ink using nitrocellulose and graphene nanoparticles as fillers.[90] This conductivity is several orders of magnitude higher than the transparent ink composition, but it is still three orders of magnitude lower than those of existing metal-based inks. (e.g. silver paste: 100,000 S m^{-1}). Using metallic inks brings several limitations to printing processing, even if only a small proportion of metal is introduced. Metal inks often need sintering or curing at high temperature to create a conductive network that enables the conductivity. This process requires that substrates can withstand these high temperatures, greatly limiting polymeric material choices and adding complexity to the material's processing. Another issue is the high cost of metals, though only a small proportion is required for each application. Electronic devices made using these inks might be recyclable but can typically not be degraded. By comparison, graphenic inks are highly promising for their versatile processing, low cost, and high conductivity. The lowest electrical resistance of printed graphene films is generally reported by using screen printing so that a relatively thick layer is produced. Hyun et al. reported a screen-printed graphene ink with a sheet resistance of 30 Ω/□ at 25 μm thickness.[91] Such films can be post-treated by thermal

annealing to enhance the inter-sheet connections, although this results in diminishing mechanical properties.[91,92]

2.6.1 Printed Sensors

Sensors are a major application field for printed CPC materials. Their unique electronic, mechanical, photonic properties as well as large specific surface area make them promising to respond changes in the ambient conditions. Generally, the signals from the output could be transformed into readable signals through specific transduction mechanisms such as resistivity, capacity. Proof-of-concept sensors based on 2D nanomaterials have been intensively explored and have demonstrated good performance.

Resistive sensors – which undergo a change in electrically conductivity in response to a stimulus – are typically engineered by using a network of conductive particles in a deformable polymer matrix. Resistive sensors, with their simple design and smooth read-out properties, appear to be most useful architecture for printable graphenic CPC sensors. Resistive sensors can be engineered by using a broad selection of responsive materials and a simple data interpretation mechanism (resistance change recording); therefore, resistive sensors remain much cheaper than other types of sensors (e.g., capacitive sensors). In the literature, pressure sensors have been demonstrated by using responsive fillers which include carbon nanomaterials (e.g., carbon nanotubes, reduced graphene oxide, and carbon black); these fillers are typically embedded in elastomeric matrices (e.g., polydimethysiloxane (PDMS) and Ecoflex®). In these composites, electrical current is carried through the network of conducting particles. When a pressure is applied, the distance between particles is reduced, and the current can be transported more easily, shown in Figure 2.4. For example, a MWCNT-PDMS composite blend has been printed out to measure planar

pressures.[93] In a different approach, microfabricated structures that form pressure-sensitive bridged connections can be utilized.[94]

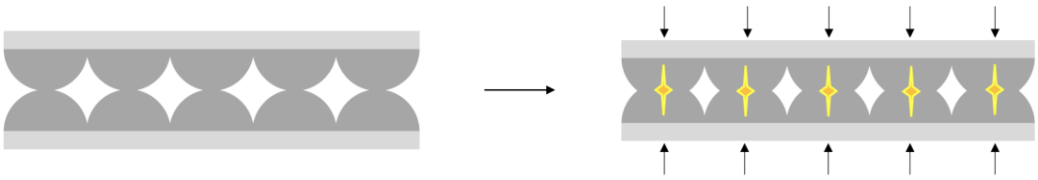

Figure 2.4 sensing mechanism of loading and unloading of PDMS pressure sensor.

The planar surface of responsive materials with no compressible elements (e.g. pores or pillars) typically has low-pressure sensitivity and long relaxation time. In addition to pressure sensing, temperature sensing has a growing interest utilized in industrial transportation and health monitoring. There is intensive ongoing research into wearable temperature sensors that are intrinsically flexible and stretchable to better monitor skin temperature to provide healthcare information. For example, graphene/PEDOT:PSS was inkjet-printed on a flexible polyurethane thin-film, and the resistance of the CPC material was monitored as a function of temperature. The material exhibited resistance changes under heating and cooling within a low-temperature range (< 40 ^{o}C) with low sensitivity (less than 0.01 /^{o}C).[95]

2.6.2 Sensitivity

Sensitivity is an important parameter determining the accuracy of measurement in a device. A sensor's sensitivity can be defined as the change in output (Δy) of the sensor per unit change divided by the parameter being measured (Δx) as shown in the following equation: [1]

$$S = \lim_{\Delta x \to 0} \left(\frac{\Delta y}{\Delta x} \right) = \frac{dy}{dx}$$

For example, for a typical strain sensor, the gauge factor refers to its sensitivity as:

$$\mathrm{GF} = \frac{\Delta R}{R} / \varepsilon$$

where $\frac{\Delta R}{R}$ is the percentage of resistance change, and the ε is the change in measured strain.

For a pressure sensor, the sensitivity is defined as:

$$\mathrm{S} = \Delta X / \Delta P$$

where ΔP represents the change in applied pressure and ΔX is the change in quantitative output to be measured: resistance, capacitance, or voltage in piezoresistive, capacitive, and piezoelectric sensors, respectively.

2.6.3 Limitation of Detection (LOD)

The detection limit refers to the smallest signal that can be detected. Knowing this parameter is important for choosing a sensor with the right useful range for its end use. For instance, physiologically relevant pressures include low-pressure changes generated due to the flow across the upper lip during inhaling and exhaling (<1 kPa), moderate pressures associated with both the pulse and with finger tapping (1-10 kPa), and relatively high pressures such as the weight of a person as measured through their feet while standing (>10 kPa). Having such pressure information is beneficial in designing different pressure sensors for each given range. For a typical temperature sensor, the lowest and highest temperatures it can measure are referred to as the LODs. For measuring body temperature, the required sensitivity range is considered within the low temperature range for temperature sensors, with an upper LOD around 50 ºC, , and a lower LOD of 0 ºC, the temperature of skin.

2.6.4 Response Time

Response time refers to how long it will take for a sensor to respond under a stimulus. The response time can be largely influenced by the viscoelastic property of the polymer.[3] For the development of real-time monitoring, short response time is required, and the sensing response time has been reduced to less than 10 ms.

2.6.5 Repeatability

Repeatability refers to the consistency of a single sensor to produce the same results despite changing working conditions, such as temperature, vibration, and time. Repeatability reflects the stability of a sensor, which is essential for a long-term use. Taking strain or pressure sensor as examples, loading and unloading tests are usually conducted to evaluate the repeatability of sensors. The cyclic test can go up to 10000 times in literature; however, it is still not large enough for industrial needs. To achieve higher repeatability, many factors have to be optimized, including a robust design, choices of materials, and manufacturing processes.

2.7 Conductive Polymer Composites (CPCs) Deposition Techniques

Either solution or melt mixing can be utilized to synthesize CPCs. Solution mixing approaches generally involve dispersing the nanofiller and mixing with a dissolved the polymer (in a suitable solvent. The resulted viscosity of suspension can be tuned so it can fit 2D printing very well for patterning CPCs in macro and micro scale. By another route, nanofiller and polymer can be thermally melted and mixed thoroughly without the use of any solvents. This technique is called melt-mixing and is considered to be more compatible with the industrial applications compared to the solvent route. Melt mixing is suitable for extruding CPC filaments used in 3D printing which,

using an appropriate 3D printer technique called fused deposition modeling (FDM) in which the CPC filaments are formed into functional 2D/3D structures to be used in sensors.

Lately, 2D/3D printing using solutions of specialized CPC inks are being used more and more for fabricating electronic devices. These printing methods include inkjet-printing, screen-printing, and extrusion-based 3D printing utilizing direct-ink writing (DIW), listed in Figure 2.7. Ink-jet printing works best for the low viscosity inks, while screen printing works better using higher viscosity inks (paste-like inks). Direct ink writing (DIW) is an extrusion based mode of 3D printing, which works for inks with a large range of viscosities. For printed electronics and sensors it is vital to ensure the printing quality (e.g. layering, deposition position on substrates) for accurate deposition of multilayer structures with no apparent mismatch. Thickness is also an important factor in process selection. Normally inkjet-printing is capable of printing thinner designs (< 2 µm) compared to screen-printing, drop-casting, and 3D-printing (< 10 µm).

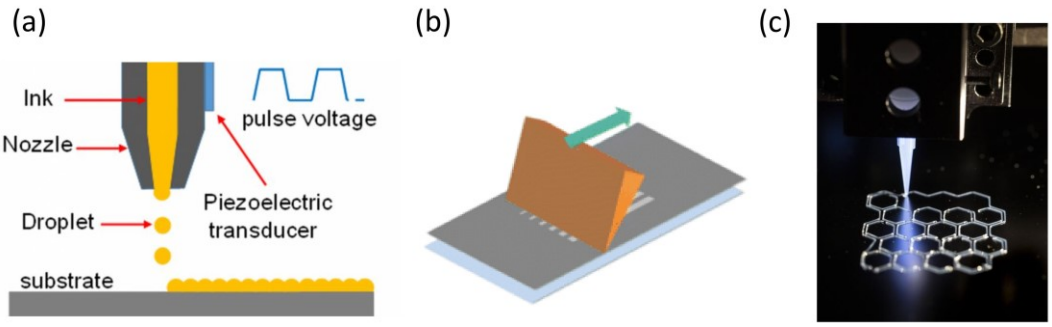

Figure 2.5 Ink-jet printing (a), screen printing (b), direct ink writing (c).

2.7.1 Drop-Casting

Drop-casting is a simple and inexpensive method for depositing nanoparticle-containing dispersions onto substrates that does not require any specific ink formations or control over

rheological parameters.[96] This approach consists of casting materials onto flexible or rigid substrates followed by solvent evaporation in forming of a thin-film. Poly(ethylene terephthalate) (PET) and PI (Kapton^{TM}) are commonly used as flexible substrates, while rigid substrates such as glass slides are frequently used as well.[97,98] Thermal annealing is often performed to remove the residual solvent or enhance the conductivity of conductive nanofillers such as silver nanoparticles, graphene oxide (GO). Overall this method is simple and easy to perform; however, it does not allow good control of homogeneity and tends to result in uneven film thickness. Though printing quality could be improved by controlling the solid/solvent volume ratio (concentration), a change in evaporation rate can lead to a "coffee ring effect" near the edges of the film.[99]

Many approaches, such as vacuum gas purging, inert gas purging, or ultrasonic-assisted shaking substrate, have been developed to improve the quality of the deposited film by slowing the solvent evaporate rate.[100] The chemical nature of the solvent and nanoparticles also influences the evaporation rate. Organic solvent such as ethanol or chloroform evaporates rapidly, while water tends to evaporate more slowly at ambient environment. Another example is that GO tends to absorb water from the environment and block the water evaporation path at the same time, resulting an extended evaporation time. Lastly, the surface properties of substrates also influence the uniformity of the deposited films. For example, rGO tends to have a good adhesion to PET substrates that contain catechol groups. The drop-casting method is widely used in the deposition of nanomaterials suspension in the areas where the resulting film quality is not strictly required, as for the case of strain sensor that are used in flexible devices, electrodes in batteries, supercapacitors, etc.

Drop-casting method of graphenic materials has been used for the sensing area of flexible, free-standing film that can be used to detect hazard gases, humidity, temperature, strain, etc.[101–103] For example, drop-casted free-standing GO films can be used to measure the humidity change in the ambient environment.[104,105] Semitransparent conductive rGO films on PET substrates can be achieved using drop-casting, but the films have high resistance of several kΩ.[106,107]

2.7.2 Fused Deposition Modelling (FDM)

A popular type of 3D printing is fused deposition method (FDM), in which plastic filaments are melt-deposited onto a desired substrate, layer-by-layer to produce planar or three-dimensional object.[108] FDM printing has primarily been used to develop customized engineering prototypes with comparable mechanical properties as hot compressed solid products. Polylactic acid (PLA) and acrylonitrile butadiene styrene (ABS) are generally used for FDM without additional functions. Recently, CPCs such as PLA blends, biopolymer composites, graphenic-polymer composites, etc. have been used for FDM to add functionalities to the printed objects.[109–111] FDM has been used to print CPCs using graphenic materials as fillers, such as rGO, GO, and CNTs, for a number of applications such as conductive flexible circuits, aerogels, scaffolds, batteries, etc.[112–114] Jakus et al. firstly reported a good demonstration of graphene heterostructure printing using graphene polymer composites for bioelectronic applications.[115] In addition, 3D printing of graphenic materials has been used in electrical applications.

FDM is not a fast process and may take days to build sizeable complex designs. To save printing time and materials, printing density can be tuned based on needs. A lower density means more holes and pores inside the design, resulting a low mechanical strength and compressive modulus

to the final product. The integration of nanomaterials and 3D printing method can enhance the paradigm of 3D printing to an efficient, heterogeneous deposition manufacturing.

2.7.3 Direct ink writing (DIW)

Due to the nature of graphenic materials (i.e. easy agglomeration), sometimes a liquid dispersion is preferred rather than the solid state, so, often a modified method is used in which liquid is deposited layer-by-layer from extruder tips instead of a melted plastic filament. This method is called direct ink writing (DIW) is a modified extrusion-based mode of 3D printing, where a syringe of the liquid is fed into the nozzle to extruded out through a tip as per the designs.[115,116] DIW requires specific viscosities of inks, although it can work for a larger range of ink viscosities compared to inkjet-printing.

Recently, biological scaffolds that were printed from biomaterials rather than traditional polymer filaments have been explored using DIW, with an emphasis on pore size and porosity control. Achieving such a level of complexity using conventional manufacturing is challenging. Other applications such as batteries, sensors and supercapacitors have also been investigated. To achieve well-defined features, the ink should retain its shape after being extruded. Unlike inkjet printing which requires low viscosity inks (2-10^2 mPa s), DIW works best with more viscous inks range of ink viscosity (2-10^6 mPa s) and inks containing nanoparticles. Highly viscous ink has better capability to hold three dimensional shapes during printing, but also has a higher risk of nozzle clogging than lower viscosity inks and also has lower the printing resolution. A good balance between ink viscosity and printed design resolution is needed for a smooth DIW. Printing parameters such as nozzle diameter, printing speed, extrusion speed can be modified for the best printing. Recently, many composite inks have been developed for DIW, including liquid metal,

graphenic polymer composites, silicone-based viscous ink, and biological materials. Graphene-based inks offer more choice of functionality, such as electrical conductivity and enhanced mechanical properties for a number of 3D printing applications.[117] One difficulty in DIW is control of the suspension and particle size. For instance, an ink that contains large particles needs a large size diameter needle, which can result in low-resolution designs. DIW of graphenic composites with high resolution is challenging because the sheet-like fillers or small agglomerations inside the ink may result in nozzle clogging.

2.8 References

(1) Brody, T. P. The Birth and Early Childhood of Active Matrix — A Personal Memoir. *J. Soc. Inf. Disp.* **1996**, *4* (3), 113–127. https://doi.org/10.1889/1.1985000.

(2) Stauffer, D.; Aharony, A. *Introduction To Percolation Theory: Second Edition*; CRC Press, **2018**.

(3) Stankovich, S.; Dikin, D. A.; Dommett, G. H. B.; Kohlhaas, K. M.; Zimney, E. J.; Stach, E. A.; Piner, R. D.; Nguyen, S. T.; Ruoff, R. S. Graphene-Based Composite Materials. *Nature* **2006**, *442* (7100), 282–286. https://doi.org/10.1038/nature04969.

(4) Barletta, M.; Trovalusci, F.; Puopolo, M.; Tagliaferri, V.; Vesco, S. Engineering and Processing of Poly(HydroxyButyrate) (PHB) Modified by Nano-Sized Graphene Nanoplatelets (GNP) and Amino-Functionalized Silica (A-FnSiO2). *J. Polym. Environ.* **2016**, *24* (1), 1–11. https://doi.org/10.1007/s10924-016-0753-z.

(5) Nguyen, D. A.; Lee, Y. R.; Raghu, A. V.; Jeong, H. M.; Shin, C. M.; Kim, B. K. Morphological and Physical Properties of a Thermoplastic Polyurethane Reinforced with Functionalized Graphene Sheet. *Polym. Int.* **2009**, *58* (4), 412–417. https://doi.org/10.1002/pi.2549.

(6) Shih, W.-P.; Tsao, L.-C.; Lee, C.-W.; Cheng, M.-Y.; Chang, C.; Yang, Y.-J.; Fan, K.-C. Flexible Temperature Sensor Array Based on a Graphite-Polydimethylsiloxane Composite. *Sensors* **2010**, *10* (4), 3597–3610. https://doi.org/10.3390/s100403597.

(7) R. Dreyer, D.; Park, S.; W. Bielawski, C.; S. Ruoff, R. The Chemistry of Graphene Oxide. *Chem. Soc. Rev.* **2010**, *39* (1), 228–240. https://doi.org/10.1039/B917103G.

(8) Brodie, B. C. XIII. On the Atomic Weight of Graphite. *Philos. Trans. R. Soc. Lond.* **1859**, *149*, 249–259. https://doi.org/10.1098/rstl.1859.0013.

(9) Basirun, W. J.; Sookhakian, M.; Baradaran, S.; Mahmoudian, M. R.; Ebadi, M. Solid-Phase Electrochemical Reduction of Graphene Oxide Films in Alkaline Solution. *Nanoscale Res. Lett.* **2013**, *8* (1), 397. https://doi.org/10.1186/1556-276X-8-397.

(10) Zhang, J.; Yang, H.; Shen, G.; Cheng, P.; Zhang, J.; Guo, S. Reduction of Graphene Oxide ViaL-Ascorbic Acid. *Chem. Commun.* **2010**, *46* (7), 1112–1114. https://doi.org/10.1039/B917705A.

(11) Cheng, Yehong, et al. "Enhanced mechanical, thermal, and electric properties of graphene aerogels via supercritical ethanol drying and high-temperature thermal reduction." *Scientific reports* 7.1 **2017**: 1-11.

(12) Trusovas, R.; Ratautas, K.; Račiukaitis, G.; Barkauskas, J.; Stankevičienė, I.; Niaura, G.; Mažeikienė, R. Reduction of Graphite Oxide to Graphene with Laser Irradiation. *Carbon* **2013**, *52*, 574–582. https://doi.org/10.1016/j.carbon.2012.10.017.

(13) Nair, R. R.; Blake, P.; Grigorenko, A. N.; Novoselov, K. S.; Booth, T. J.; Stauber, T.; Peres, N. M. R.; Geim, A. K. Fine Structure Constant Defines Visual Transparency of Graphene. *Science* **2008**, *320* (5881), 1308–1308. https://doi.org/10.1126/science.1156965.

(14) Sun, Z.; Hasan, T.; Torrisi, F.; Popa, D.; Privitera, G.; Wang, F.; Bonaccorso, F.; Basko, D. M.; Ferrari, A. C. Graphene Mode-Locked Ultrafast Laser. *ACS Nano* **2010**, *4* (2), 803–810. https://doi.org/10.1021/nn901703e.

(15) Das, A.; Pisana, S.; Chakraborty, B.; Piscanec, S.; Saha, S. K.; Waghmare, U. V.; Novoselov, K. S.; Krishnamurthy, H. R.; Geim, A. K.; Ferrari, A. C.; Sood, A. K. Monitoring Dopants by Raman Scattering in an Electrochemically Top-Gated Graphene Transistor. *Nat. Nanotechnol.* **2008**, *3* (4), 210–215. https://doi.org/10.1038/nnano.2008.67.

(16) Shin, H.-J.; Kim, K. K.; Benayad, A.; Yoon, S.-M.; Park, H. K.; Jung, I.-S.; Jin, M. H.; Jeong, H.-K.; Kim, J. M.; Choi, J.-Y.; Lee, Y. H. Efficient Reduction of Graphite Oxide by Sodium Borohydride and Its Effect on Electrical Conductance. *Adv. Funct. Mater.* **2009**, *19* (12), 1987–1992. https://doi.org/10.1002/adfm.200900167.

(17) Park, S.; An, J.; Potts, J. R.; Velamakanni, A.; Murali, S.; Ruoff, R. S. Hydrazine-Reduction of Graphite- and Graphene Oxide. *Carbon* **2011**, *49* (9), 3019–3023. https://doi.org/10.1016/j.carbon.2011.02.071.

(18) Eatemadi, A.; Daraee, H.; Karimkhanloo, H.; Kouhi, M.; Zarghami, N.; Akbarzadeh, A.; Abasi, M.; Hanifehpour, Y.; Joo, S. W. Carbon Nanotubes: Properties, Synthesis, Purification, and Medical Applications. *Nanoscale Res. Lett.* **2014**, *9* (1), 393. https://doi.org/10.1186/1556-276X-9-393.

(19) Coleman, J. N.; Khan, U.; Blau, W. J.; Gun'ko, Y. K. Small but Strong: A Review of the Mechanical Properties of Carbon Nanotube–Polymer Composites. *Carbon* **2006**, *44* (9), 1624–1652. https://doi.org/10.1016/j.carbon.2006.02.038.

(20) Wick, P.; Manser, P.; Limbach, L. K.; Dettlaff-Weglikowska, U.; Krumeich, F.; Roth, S.; Stark, W. J.; Bruinink, A. The Degree and Kind of Agglomeration Affect Carbon Nanotube Cytotoxicity. *Toxicol. Lett.* **2007**, *168* (2), 121–131. https://doi.org/10.1016/j.toxlet.2006.08.019.

(21) Ajayan, P. M.; Stephan, O.; Colliex, C.; Trauth, D. Aligned Carbon Nanotube Arrays Formed by Cutting a Polymer Resin—Nanotube Composite. *Science* **1994**, *265* (5176), 1212–1214. https://doi.org/10.1126/science.265.5176.1212.

(22) Publications : PlasticsEurope https://www.plasticseurope.org/en/resources/publications/3-plastics-facts-2016 (accessed Apr 14, 2020).

(23) Derraik, J. G. B. The Pollution of the Marine Environment by Plastic Debris: A Review. *Mar. Pollut. Bull.* **2002**, *44* (9), 842–852. https://doi.org/10.1016/S0025-326X(02)00220-5.

(24) Plastic Pollution in the World's Oceans: More than 5 Trillion Plastic Pieces Weighing over 250,000 Tons Afloat at Sea (accessed Apr 14, **2020**).

(25) Karlsson, S.; Albertsson, A. Biodegradable Polymers and Environmental Interaction. *Polym. Eng. Sci.* **1998**, *38* (8), 1251–1253. https://doi.org/10.1002/pen.10294.

(26) Kay, M. J.; McCabe, R. W.; Morton, L. H. G. Chemical and Physical Changes Occurring in Polyester Polyurethane during Biodegradation. *Int. Biodeterior. Biodegrad.* **1993**, *31* (3), 209–225. https://doi.org/10.1016/0964-8305(93)90006-N.

(27) Shah, A. A.; Hasan, F.; Hameed, A.; Ahmed, S. Biological Degradation of Plastics: A Comprehensive Review. *Biotechnol. Adv.* **2008**, *26* (3), 246–265. https://doi.org/10.1016/j.biotechadv.2007.12.005.

(28) Chiellini, E.; Corti, A.; D'Antone, S.; Solaro, R. Biodegradation of Poly (Vinyl Alcohol) Based Materials. *Prog. Polym. Sci.* **2003**, *28* (6), 963–1014. https://doi.org/10.1016/S0079-6700(02)00149-1.

(29) Liu, X.; Gao, C.; Sangwan, P.; Yu, L.; Tong, Z. Accelerating the Degradation of Polyolefins through Additives and Blending. *J. Appl. Polym. Sci.* **2014**, *131* (18). https://doi.org/10.1002/app.40750.

(30) Abd El-Rehim, H. A.; Hegazy, E.-S. A.; Ali, A. M.; Rabie, A. M. Synergistic Effect of Combining UV-Sunlight–Soil Burial Treatment on the Biodegradation Rate of LDPE/Starch Blends. *J. Photochem. Photobiol. Chem.* **2004**, *163* (3), 547–556. https://doi.org/10.1016/j.jphotochem.2004.02.003.

(31) Tawakkal, I. S. M. A.; Cran, M. J.; Miltz, J.; Bigger, S. W. A Review of Poly(Lactic Acid)-Based Materials for Antimicrobial Packaging. *J. Food Sci.* **2014**, *79* (8), R1477–R1490. https://doi.org/10.1111/1750-3841.12534.

(32) Dorgan, J. R.; Braun, B.; Wegner, J. R.; Knauss, D. M. Poly(Lactic Acids): A Brief Review. In *Degradable Polymers and Materials*; ACS Symposium Series; American Chemical Society, **2006**; Vol. 939, pp 102–125. https://doi.org/10.1021/bk-2006-0939.ch007.

(33) Ren, J. M.; McKenzie, T. G.; Fu, Q.; Wong, E. H. H.; Xu, J.; An, Z.; Shanmugam, S.; Davis, T. P.; Boyer, C.; Qiao, G. G. Star Polymers. *Chem. Rev.* **2016**, *116* (12), 6743–6836. https://doi.org/10.1021/acs.chemrev.6b00008.

(34) Labet, M.; Thielemans, W. Synthesis of Polycaprolactone: A Review. *Chem. Soc. Rev.* **2009**, *38* (12), 3484–3504. https://doi.org/10.1039/B820162P.

(35) Castro-Aguirre, E.; Iñiguez-Franco, F.; Samsudin, H.; Fang, X.; Auras, R. Poly(Lactic Acid)—Mass Production, Processing, Industrial Applications, and End of Life. *Adv. Drug Deliv. Rev.* **2016**, *107*, 333–366. https://doi.org/10.1016/j.addr.2016.03.010.

(36) Tyler, B.; Gullotti, D.; Mangraviti, A.; Utsuki, T.; Brem, H. Polylactic Acid (PLA) Controlled Delivery Carriers for Biomedical Applications. *Adv. Drug Deliv. Rev.* **2016**, *107*, 163–175. https://doi.org/10.1016/j.addr.2016.06.018.

(37) Drumright, R. E.; Gruber, P. R.; Henton, D. E. Polylactic Acid Technology. *Adv. Mater.* **2000**, *12* (23), 1841–1846. https://doi.org/10.1002/1521-4095(200012)12:23<1841::AID-ADMA1841>3.0.CO;2-E.

(38) Auras, R.; Harte, B.; Selke, S. An Overview of Polylactides as Packaging Materials. *Macromol. Biosci.* **2004**, *4* (9), 835–864. https://doi.org/10.1002/mabi.200400043.

(39) Hidalgo-Ruz, V.; Gutow, L.; Thompson, R. C.; Thiel, M. Microplastics in the Marine Environment: A Review of the Methods Used for Identification and Quantification. *Environ. Sci. Technol.* **2012**, *46* (6), 3060–3075. https://doi.org/10.1021/es2031505.

(40) Cole, M.; Lindeque, P.; Halsband, C.; Galloway, T. S. Microplastics as Contaminants in the Marine Environment: A Review. *Mar. Pollut. Bull.* **2011**, *62* (12), 2588–2597. https://doi.org/10.1016/j.marpolbul.2011.09.025.

(41) Lee, S. Y. Bacterial Polyhydroxyalkanoates. *Biotechnol. Bioeng.* **1996**, *49* (1), 1–14. https://doi.org/10.1002/(SICI)1097-0290(19960105)49:1<1::AID-BIT1>3.0.CO;2-P.

(42) Zinn, M.; Witholt, B.; Egli, T. Occurrence, Synthesis and Medical Application of Bacterial Polyhydroxyalkanoate. *Adv. Drug Deliv. Rev.* **2001**, *53* (1), 5–21. https://doi.org/10.1016/S0169-409X(01)00218-6.

(43) Khanna, S.; Srivastava, A. K. Recent Advances in Microbial Polyhydroxyalkanoates. *Process Biochem.* **2005**, *40* (2), 607–619. https://doi.org/10.1016/j.procbio.2004.01.053.

(44) Lee, S. Y. Plastic Bacteria? Progress and Prospects for Polyhydroxyalkanoate Production in Bacteria. *Trends Biotechnol.* **1996**, *14* (11), 431–438. https://doi.org/10.1016/0167-7799(96)10061-5.

(45) Vert, M. Aliphatic Polyesters: Great Degradable Polymers That Cannot Do Everything. *Biomacromolecules* **2005**, *6* (2), 538–546. https://doi.org/10.1021/bm0494702.

(46) Verlinden, R. a. J.; Hill, D. J.; Kenward, M. A.; Williams, C. D.; Radecka, I. Bacterial Synthesis of Biodegradable Polyhydroxyalkanoates. *J. Appl. Microbiol.* **2007**, *102* (6), 1437–1449. https://doi.org/10.1111/j.1365-2672.2007.03335.x.

(47) Chen, G.-Q. A Microbial Polyhydroxyalkanoates (PHA) Based Bio- and Materials Industry. *Chem. Soc. Rev.* **2009**, *38* (8), 2434–2446. https://doi.org/10.1039/B812677C.

(48) Orts, W. J.; Nobes, G. A. R.; Kawada, J.; Nguyen, S.; Yu, G.; Ravenelle, F. Poly(Hydroxyalkanoates): Biorefinery Polymers with a Whole Range of Applications. The Work of Robert H. Marchessault. *Can. J. Chem.* **2008**, *86* (6), 628–640. https://doi.org/10.1139/v08-050.

(49) Vert, M.; Li, S. M.; Spenlehauer, G.; Guerin, P. Bioresorbability and Biocompatibility of Aliphatic Polyesters. *J. Mater. Sci. Mater. Med.* **1992**, *3* (6), 432–446. https://doi.org/10.1007/BF00701240.

(50) Madison, L. L.; Huisman, G. W. Metabolic Engineering of Poly(3-Hydroxyalkanoates): From DNA to Plastic. *Microbiol. Mol. Biol. Rev.* **1999**, *63* (1), 21–53.

(51) Sreedevi, S.; Unni, K. N.; Sajith, S.; Priji, P.; Josh, M. S.; Benjamin, S. Bioplastics: Advances in Polyhydroxybutyrate Research. **2014**, 1–30. https://doi.org/10.1007/12_2014_297.

(52) Hankermeyer, C. R.; Tjeerdema, R. S. Polyhydroxybutyrate: Plastic Made and Degraded by Microorganisms. In *Reviews of Environmental Contamination and Toxicology: Continuation of Residue Reviews*; Ware, G. W., Ed.; Reviews of Environmental Contamination and Toxicology; Springer: New York, NY, **1999**; pp 1–24.

(53) Chan, R. T. H.; Russell, R. A.; Marçal, H.; Lee, T. H.; Holden, P. J.; Foster, L. J. R. BioPEGylation of Polyhydroxybutyrate Promotes Nerve Cell Health and Migration. *Biomacromolecules* **2014**, *15* (1), 339–349. https://doi.org/10.1021/bm401572a.

(54) Paganelli, F. L.; de Macedo Lemos, E. G.; Alves, L. M. C. Polyhydroxybutyrate in Rhizobium and Bradyrhizobium: Quantification and PhbC Gene Expression. *World J. Microbiol. Biotechnol.* **2011**, *27* (4), 773–778. https://doi.org/10.1007/s11274-010-0515-3.

(55) Jung, I. L.; Phyo, K. H.; Kim, K. C.; Park, H. K.; Kim, I. G. Spontaneous Liberation of Intracellular Polyhydroxybutyrate Granules in Escherichia Coli. *Res. Microbiol.* **2005**, *156* (8), 865–873. https://doi.org/10.1016/j.resmic.2005.04.004.

(56) Lenz, R. W.; Marchessault, R. H. Bacterial Polyesters: Biosynthesis, Biodegradable Plastics and Biotechnology. *Biomacromolecules* **2005**, *6* (1), 1–8. https://doi.org/10.1021/bm049700c.

(57) Anbukarasu, Preetam, Dominic Sauvageau, and Anastasia Elias. "Tuning the properties of polyhydroxybutyrate films using acetic acid via solvent casting." *Scientific reports* 5 **2015**: 17884.

(58) Miloaga, Dana Gabriela. *Nucleating effect of exfoliated graphite nanoplatelets on poly (hydroxybutyrate) and poly (lactic acid) and their nanocomposites properties*. Thesis, **2008**.

(59) Li, Z.; Ju, D.; Han, L.; Dong, L. Formation of More Efficient Thermally Conductive Pathways Due to the Synergistic Effect of Boron Nitride and Alumina in Poly(3-Hydroxylbutyrate). *Thermochim. Acta* **2017**, *652*, 9–16. https://doi.org/10.1016/j.tca.2017.03.006.

(60) Manikandan, N. A.; Pakshirajan, K.; Pugazhenthi, G. Preparation and Characterization of Environmentally Safe and Highly Biodegradable Microbial Polyhydroxybutyrate (PHB) Based Graphene Nanocomposites for Potential Food Packaging Applications. *Int. J. Biol. Macromol.* **2020**, *154*, 866–877. https://doi.org/10.1016/j.ijbiomac.2020.03.084.

(61) Withers, F.; Yang, H.; Britnell, L.; Rooney, A. P.; Lewis, E.; Felten, A.; Woods, C. R.; Sanchez Romaguera, V.; Georgiou, T.; Eckmann, A.; Kim, Y. J.; Yeates, S. G.; Haigh, S. J.; Geim, A. K.; Novoselov, K. S.; Casiraghi, C. Heterostructures Produced from

Nanosheet-Based Inks. *Nano Lett.* **2014**, *14* (7), 3987–3992. https://doi.org/10.1021/nl501355j.

(62) Valentini, L.; Cardinali, M.; Fortunati, E.; Torre, L.; Kenny, J. M. A Novel Method to Prepare Conductive Nanocrystalline Cellulose/Graphene Oxide Composite Films. *Mater. Lett.* **2013**, *105*, 4–7. https://doi.org/10.1016/j.matlet.2013.04.034.

(63) Zhao, C.; Xing, L.; Xiang, J.; Cui, L.; Jiao, J.; Sai, H.; Li, Z.; Li, F. Formation of Uniform Reduced Graphene Oxide Films on Modified PET Substrates Using Drop-Casting Method. *Particuology* **2014**, *17*, 66–73. https://doi.org/10.1016/j.partic.2014.02.005.

(64) Chen, J.; Tee, C. K.; Shtein, M.; Martin, D. C.; Anthony, J. Controlled Solution Deposition and Systematic Study of Charge-Transport Anisotropy in Single Crystal and Single-Crystal Textured TIPS Pentacene Thin Films. *Org. Electron.* **2009**, *10* (4), 696–703. https://doi.org/10.1016/j.orgel.2009.03.007.

(65) Mahmood, Javeed, et al. "Nitrogenated holey two-dimensional structures." *Nature communications* 6.1 **2015**: 1-7.

(66) Chakravarty, D.; Late, D. J. Exfoliation of Bulk Inorganic Layered Materials into Nanosheets by the Rapid Quenching Method and Their Electrochemical Performance. *Eur. J. Inorg. Chem.* **2015**, *2015* (11), 1973–1980. https://doi.org/10.1002/ejic.201500039.

(67) Sun, H.; Castillo, A. E. D. R.; Monaco, S.; Capasso, A.; Ansaldo, A.; Prato, M.; Dinh, D. A.; Pellegrini, V.; Scrosati, B.; Manna, L.; Bonaccorso, F. Binder-Free Graphene as an Advanced Anode for Lithium Batteries. *J. Mater. Chem. A* **2016**, *4* (18), 6886–6895. https://doi.org/10.1039/C5TA08553E.

(68) Krueger, M.; Berg, S.; Stone, D.; Strelcov, E.; Dikin, D. A.; Kim, J.; Cote, L. J.; Huang, J.; Kolmakov, A. Drop-Casted Self-Assembling Graphene Oxide Membranes for Scanning Electron Microscopy on Wet and Dense Gaseous Samples. *ACS Nano* **2011**, *5* (12), 10047–10054. https://doi.org/10.1021/nn204287g.

(69) Chen, C.; Yang, Q.-H.; Yang, Y.; Lv, W.; Wen, Y.; Hou, P.-X.; Wang, M.; Cheng, H.-M. Self-Assembled Free-Standing Graphite Oxide Membrane. *Adv. Mater.* **2009**, *21* (29), 3007–3011. https://doi.org/10.1002/adma.200803726.

(70) Compton, O. C.; Nguyen, S. T. Graphene Oxide, Highly Reduced Graphene Oxide, and Graphene: Versatile Building Blocks for Carbon-Based Materials. *Small* **2010**, *6* (6), 711–723. https://doi.org/10.1002/smll.200901934.

(71) Pei, S.; Zhao, J.; Du, J.; Ren, W.; Cheng, H.-M. Direct Reduction of Graphene Oxide Films into Highly Conductive and Flexible Graphene Films by Hydrohalic Acids. *Carbon* **2010**, *48* (15), 4466–4474. https://doi.org/10.1016/j.carbon.2010.08.006.

(72) Schubert, C.; Langeveld, M. C. van; Donoso, L. A. Innovations in 3D Printing: A 3D Overview from Optics to Organs. *Br. J. Ophthalmol.* **2014**, *98* (2), 159–161. https://doi.org/10.1136/bjophthalmol-2013-304446.

(73) Bitounis, D.; Ali-Boucetta, H.; Hong, B. H.; Min, D.-H.; Kostarelos, K. Prospects and Challenges of Graphene in Biomedical Applications. *Adv. Mater.* **2013**, *25* (16), 2258–2268. https://doi.org/10.1002/adma.201203700.

(74) Jakus, A. E.; Secor, E. B.; Rutz, A. L.; Jordan, S. W.; Hersam, M. C.; Shah, R. N. Three-Dimensional Printing of High-Content Graphene Scaffolds for Electronic and Biomedical Applications. *ACS Nano* **2015**, *9* (4), 4636–4648. https://doi.org/10.1021/acsnano.5b01179.

(75) He, Fupo, et al. "Improving bone repair of femoral and radial defects in rabbit by incorporating PRP into PLGA/CPC composite scaffold with unidirectional pore structure." *Journal of Biomedical Materials Research Part A* 103.4 **2015**: 1312-1324.
(76) Xu, Hockin HK, et al. "Synergistic reinforcement of in situ hardening calcium phosphate composite scaffold for bone tissue engineering." *Biomaterials* 25.6 **2004**: 1029-1037.
(77) Shao, Y.; Wang, J.; Wu, H.; Liu, J.; Aksay, I. A.; Lin, Y. Graphene Based Electrochemical Sensors and Biosensors: A Review. *Electroanalysis* **2010**, *22* (10), 1027–1036. https://doi.org/10.1002/elan.200900571.
(78) Wujcik, E. K.; Monty, C. N. Nanotechnology for Implantable Sensors: Carbon Nanotubes and Graphene in Medicine. *WIREs Nanomedicine Nanobiotechnology* **2013**, *5* (3), 233–249. https://doi.org/10.1002/wnan.1213.
(79) Oh, M. J.; Yoo, P. J. Graphene-Based 3D Lightweight Cellular Structures: Synthesis and Applications. *Korean J. Chem. Eng.* **2020**, *37* (2), 189–208. https://doi.org/10.1007/s11814-019-0437-1.
(80) Zhang, D.; Chi, B.; Li, B.; Gao, Z.; Du, Y.; Guo, J.; Wei, J. Fabrication of Highly Conductive Graphene Flexible Circuits by 3D Printing. *Synth. Met.* **2016**, *217*, 79–86. https://doi.org/10.1016/j.synthmet.2016.03.014.
(81) Fu, K.; Yao, Y.; Dai, J.; Hu, L. Progress in 3D Printing of Carbon Materials for Energy-Related Applications. *Adv. Mater.* **2017**, *29* (9), 1603486. https://doi.org/10.1002/adma.201603486.
(82) Jiang, Y.; Xu, Z.; Huang, T.; Liu, Y.; Guo, F.; Xi, J.; Gao, W.; Gao, C. Direct 3D Printing of Ultralight Graphene Oxide Aerogel Microlattices. *Adv. Funct. Mater.* **2018**, *28* (16), 1707024. https://doi.org/10.1002/adfm.201707024.
(83) An, B. W.; Kim, K.; Kim, M.; Kim, S.-Y.; Hur, S.-H.; Park, J.-U. Direct Printing of Reduced Graphene Oxide on Planar or Highly Curved Surfaces with High Resolutions Using Electrohydrodynamics. *Small* **2015**, *11* (19), 2263–2268. https://doi.org/10.1002/smll.201403131.
(84) Wang, Y.; Zhang, Y.; Wang, G.; Shi, X.; Qiao, Y.; Liu, J.; Liu, H.; Ganesh, A.; Li, L. Direct Graphene-Carbon Nanotube Composite Ink Writing All-Solid-State Flexible Microsupercapacitors with High Areal Energy Density. *Adv. Funct. Mater.* **2020**, 1907284. https://doi.org/10.1002/adfm.201907284.
(85) García-Tuñon, E.; Barg, S.; Franco, J.; Bell, R.; Eslava, S.; D'Elia, E.; Maher, R. C.; Guitian, F.; Saiz, E. Printing in Three Dimensions with Graphene. *Adv. Mater.* **2015**, *27* (10), 1688–1693. https://doi.org/10.1002/adma.201405046.
(86) Bonaccorso, F.; Sun, Z.; Hasan, T.; Ferrari, A. C. Graphene Photonics and Optoelectronics. *Nat. Photonics* **2010**, *4* (9), 611–622. https://doi.org/10.1038/nphoton.2010.186.
(87) Howe, Richard CT, et al. "Functional inks of graphene, metal dichalcogenides and black phosphorus for photonics and (opto) electronics." *Low-Dimensional Materials and Devices*. Vol. 9553. International Society for Optics and Photonics, **2015**.
(88) Kang, M. S.; Kim, K. T.; Lee, J. U.; Jo, W. H. Direct Exfoliation of Graphite Using a Non-Ionic Polymer Surfactant for Fabrication of Transparent and Conductive Graphene Films. *J. Mater. Chem. C* **2013**, *1* (9), 1870–1875. https://doi.org/10.1039/C2TC00586G.
(89) Kim, K. S.; Zhao, Y.; Jang, H.; Lee, S. Y.; Kim, J. M.; Kim, K. S.; Ahn, J.-H.; Kim, P.; Choi, J.-Y.; Hong, B. H. Large-Scale Pattern Growth of Graphene Films for Stretchable Transparent Electrodes. *Nature* **2009**, *457* (7230), 706–710. https://doi.org/10.1038/nature07719.

(90) De, S.; King, P. J.; Lotya, M.; O'Neill, A.; Doherty, E. M.; Hernandez, Y.; Duesberg, G. S.; Coleman, J. N. Flexible, Transparent, Conducting Films of Randomly Stacked Graphene from Surfactant-Stabilized, Oxide-Free Graphene Dispersions. *Small* **2010**, *6* (3), 458–464. https://doi.org/10.1002/smll.200901162.

(91) Bonaccorso, F.; Lombardo, A.; Hasan, T.; Sun, Z.; Colombo, L.; Ferrari, A. C. Production and Processing of Graphene and 2d Crystals. *Mater. Today* **2012**, *15* (12), 564–589. https://doi.org/10.1016/S1369-7021(13)70014-2.

(92) Granqvist, C. G. Transparent Conductors as Solar Energy Materials: A Panoramic Review. *Sol. Energy Mater. Sol. Cells* **2007**, *91* (17), 1529–1598. https://doi.org/10.1016/j.solmat.2007.04.031.

(93) Ginley, D. S.; Perkins, J. D. Transparent Conductors. In *Handbook of Transparent Conductors*; Ginley, D. S., Ed.; Springer US: Boston, MA, **2011**; pp 1–25. https://doi.org/10.1007/978-1-4419-1638-9_1.

(94) Cote, Laura J., Franklin Kim, and Jiaxing Huang. "Langmuir− Blodgett assembly of graphite oxide single layers." *Journal of the American Chemical Society* 131.3 **2009**: 1043-1049.

(95) Eda, G.; Fanchini, G.; Chhowalla, M. Large-Area Ultrathin Films of Reduced Graphene Oxide as a Transparent and Flexible Electronic Material. *Nat. Nanotechnol.* **2008**, *3* (5), 270–274. https://doi.org/10.1038/nnano.2008.83.

(96) Green, A. A.; Hersam, M. C. Solution Phase Production of Graphene with Controlled Thickness via Density Differentiation. *Nano Lett.* **2009**, *9* (12), 4031–4036. https://doi.org/10.1021/nl902200b.

(97) Bae, S.; Kim, H.; Lee, Y.; Xu, X.; Park, J.-S.; Zheng, Y.; Balakrishnan, J.; Lei, T.; Ri Kim, H.; Song, Y. I.; Kim, Y.-J.; Kim, K. S.; Özyilmaz, B.; Ahn, J.-H.; Hong, B. H.; Iijima, S. Roll-to-Roll Production of 30-Inch Graphene Films for Transparent Electrodes. *Nat. Nanotechnol.* **2010**, *5* (8), 574–578. https://doi.org/10.1038/nnano.2010.132.

(98) Secor, E. B.; Gao, T. Z.; Islam, A. E.; Rao, R.; Wallace, S. G.; Zhu, J.; Putz, K. W.; Maruyama, B.; Hersam, M. C. Enhanced Conductivity, Adhesion, and Environmental Stability of Printed Graphene Inks with Nitrocellulose. *Chem. Mater.* **2017**, *29* (5), 2332–2340. https://doi.org/10.1021/acs.chemmater.7b00029.

(99) Hyun, W. J.; Secor, E. B.; Hersam, M. C.; Frisbie, C. D.; Francis, L. F. High-Resolution Patterning of Graphene by Screen Printing with a Silicon Stencil for Highly Flexible Printed Electronics. *Adv. Mater.* **2015**, *27* (1), 109–115. https://doi.org/10.1002/adma.201404133.

(101) Arapov, K.; Bex, G.; Hendriks, R.; Rubingh, E.; Abbel, R.; With, G. de; Friedrich, H. Conductivity Enhancement of Binder-Based Graphene Inks by Photonic Annealing and Subsequent Compression Rolling. *Adv. Eng. Mater.* **2016**, *18* (7), 1234–1239. https://doi.org/10.1002/adem.201500646.

(102) Gerlach, C.; Krumm, D.; Illing, M.; Lange, J.; Kanoun, O.; Odenwald, S.; Hübler, A. Printed MWCNT-PDMS-Composite Pressure Sensor System for Plantar Pressure Monitoring in Ulcer Prevention. *IEEE Sens. J.* **2015**, *15* (7), 3647–3656. https://doi.org/10.1109/JSEN.2015.2392084.

(103) Yu, G.; Hu, J.; Tan, J.; Gao, Y.; Lu, Y.; Xuan, F. A Wearable Pressure Sensor Based on Ultra-Violet/Ozone Microstructured Carbon Nanotube/Polydimethylsiloxane Arrays for Electronic Skins. *Nanotechnology* **2018**, *29* (11), 115502. https://doi.org/10.1088/1361-6528/aaa855.

(104) Vuorinen, T.; Niittynen, J.; Kankkunen, T.; Kraft, T. M.; Mäntysalo, M. Inkjet-Printed Graphene/PEDOT:PSS Temperature Sensors on a Skin-Conformable Polyurethane Substrate. *Sci. Rep.* **2016**, *6* (1), 1–8. https://doi.org/10.1038/srep35289.

(105) De, S.; King, P. J.; Lotya, M.; O'Neill, A.; Doherty, E. M.; Hernandez, Y.; Duesberg, G. S.; Coleman, J. N. Flexible, Transparent, Conducting Films of Randomly Stacked Graphene from Surfactant-Stabilized, Oxide-Free Graphene Dispersions. *Small* **2010**, *6* (3), 458–464. https://doi.org/10.1002/smll.200901162.

(106) Bonaccorso, F.; Lombardo, A.; Hasan, T.; Sun, Z.; Colombo, L.; Ferrari, A. C. Production and Processing of Graphene and 2d Crystals. *Mater. Today* **2012**, *15* (12), 564–589. https://doi.org/10.1016/S1369-7021(13)70014-2.

(107) Granqvist, C. G. Transparent Conductors as Solar Energy Materials: A Panoramic Review. *Sol. Energy Mater. Sol. Cells* **2007**, *91* (17), 1529–1598. https://doi.org/10.1016/j.solmat.2007.04.031.

(108) Ginley, D. S.; Perkins, J. D. Transparent Conductors. In *Handbook of Transparent Conductors*; Ginley, D. S., Ed.; Springer US: Boston, MA, **2011**; pp 1–25. https://doi.org/10.1007/978-1-4419-1638-9_1.

(109) Cote, Laura J., Franklin Kim, and Jiaxing Huang. "Langmuir− Blodgett assembly of graphite oxide single layers." *Journal of the American Chemical Society* 131.3 **2009**: 1043-1049.

(110) Eda, G.; Fanchini, G.; Chhowalla, M. Large-Area Ultrathin Films of Reduced Graphene Oxide as a Transparent and Flexible Electronic Material. *Nat. Nanotechnol.* **2008**, *3* (5), 270–274. https://doi.org/10.1038/nnano.2008.83.

(111) Green, A. A.; Hersam, M. C. Solution Phase Production of Graphene with Controlled Thickness via Density Differentiation. *Nano Lett.* **2009**, *9* (12), 4031–4036. https://doi.org/10.1021/nl902200b.

(112) Bae, S.; Kim, H.; Lee, Y.; Xu, X.; Park, J.-S.; Zheng, Y.; Balakrishnan, J.; Lei, T.; Ri Kim, H.; Song, Y. I.; Kim, Y.-J.; Kim, K. S.; Özyilmaz, B.; Ahn, J.-H.; Hong, B. H.; Iijima, S. Roll-to-Roll Production of 30-Inch Graphene Films for Transparent Electrodes. *Nat. Nanotechnol.* **2010**, *5* (8), 574–578. https://doi.org/10.1038/nnano.2010.132.

(113) Secor, E. B.; Gao, T. Z.; Islam, A. E.; Rao, R.; Wallace, S. G.; Zhu, J.; Putz, K. W.; Maruyama, B.; Hersam, M. C. Enhanced Conductivity, Adhesion, and Environmental Stability of Printed Graphene Inks with Nitrocellulose. *Chem. Mater.* **2017**, *29* (5), 2332–2340. https://doi.org/10.1021/acs.chemmater.7b00029.

(114) Arapov, K.; Bex, G.; Hendriks, R.; Rubingh, E.; Abbel, R.; With, G. de; Friedrich, H. Conductivity Enhancement of Binder-Based Graphene Inks by Photonic Annealing and Subsequent Compression Rolling. *Adv. Eng. Mater.* **2016**, *18* (7), 1234–1239. https://doi.org/10.1002/adem.201500646.

(115) Gerlach, C.; Krumm, D.; Illing, M.; Lange, J.; Kanoun, O.; Odenwald, S.; Hübler, A. Printed MWCNT-PDMS-Composite Pressure Sensor System for Plantar Pressure Monitoring in Ulcer Prevention. *IEEE Sens. J.* **2015**, *15* (7), 3647–3656. https://doi.org/10.1109/JSEN.2015.2392084.

(116) Yu, G.; Hu, J.; Tan, J.; Gao, Y.; Lu, Y.; Xuan, F. A Wearable Pressure Sensor Based on Ultra-Violet/Ozone Microstructured Carbon Nanotube/Polydimethylsiloxane Arrays for Electronic Skins. *Nanotechnology* **2018**, *29* (11), 115502. https://doi.org/10.1088/1361-6528/aaa855.

(117) Vuorinen, T.; Niittynen, J.; Kankkunen, T.; Kraft, T. M.; Mäntysalo, M. Inkjet-Printed Graphene/PEDOT:PSS Temperature Sensors on a Skin-Conformable Polyurethane Substrate. *Sci. Rep.* **2016**, *6* (1), 1–8. https://doi.org/10.1038/srep35289.

3. Polyhydroxybutyrate/reduced graphene oxide composites

In this work, the effects of three reducing agents (sodium borohydride, hydrazine, and L-A.A (ascorbic acid)) have been systematically investigated, and the electrical and mechanical properties of composites formed with rGO prepared using each of these agents have been compared. This work suggests that when forming rGO-biopolymer composites from solution, an in-situ reduction process is advantageous for achieving good properties. The electrical properties of the L-AA in situ-reduced rGO/PHB composites achieved in our work are comparable to the best values known in the biopolymer composite field, including graphene gelatin composites (conductivity of 10 S/m for 10 vol% rGO loading) and rGO/poly(lactic acid) composites prepared using glucose as a reducing agent (conductivity ~2.2 S/m for 1.25 vol % loading). An additional advantage of the L-AA over N_2H_4 and $NaBH_4$ is the low toxicity of this material, which makes it much suitable for some bio-related applications. Furthermore, despite the intrinsic brittleness of PHB, these strips were bent over the radii of curvature of up to 0.5 cm. As composites are solution-processible, printing techniques could be potentially used to pattern the composites for applications including wearable sensors, biocompatible actuators, and biodegradable circuits.

A version of this chapter was published in *Journal of Physical Chemistry C*, under the title "Solution-Processed Conductive Biocomposites Based on Polyhydroxybutyrate and Reduced Graphene Oxide". The contents are reproduced with edits here in accordance with the author's rights and copyright policies of the publisher, American Chemistry Society.

Solution-Processed Conductive Biocomposites Based on Polyhydroxybutyrate and Reduced Graphene Oxide

Li Dan, Michael Pope, Anastasia Elias

Department of Chemical and Materials Engineering, University of Alberta, Edmonton, AB T6G 2V4 Canada

Department of Chemical Engineering, University of Waterloo, Waterloo, ON N2L 3G1, Canada

3.1 Abstract

Graphenic material/biopolymer nanocomposites have attracted attention for use in next generation flexible and degradable electronics. However, achieving high electrical conductivity (above 10 S/m) and favorable mechanical properties in such materials remains a challenge. In this work, reduced graphene oxide (rGO)/polyhydroxybutyrate (PHB) films were both prepared from solution. Three reducing agents were investigated: sodium borohydride, hydrazine, and L-ascorbic acid. While for the first two reducing agents (sodium borohydride and hydrazine), GO was first reduced and then added to dissolved PHB, for the third reducing agent (L-ascorbic acid) an in-situ reduction was performed. We systematically investigated the impacts of the three reducing agents, by comparing their reduction efficiency, the residual functional groups presented on the GO, and the properties of the resulting composites of all the composites, reduction by L-ascorbic acid gives the lowest electrical percolation threshold (~1 wt%) and the highest electrical conductivity (30 S/m on 8 wt% loading). This conductivity value is on par with reported values for rGO/biopolymer composites. The mechanical properties of the composites were characterized, and the Young's

modulus of all composites was found to be higher than pure PHB, reaching 5000 MPa for the maximum. A strain sensor was demonstrated using these composites.

3.2 Introduction

Biopolymers, derived from biological sources rather than oil – are increasingly attractive alternatives for conventional polymers. In addition to being "green", they exhibit excellent biocompatibility. Like all polymers, the properties of biopolymers may be modified through the addition of a filler. Conductive biopolymer nanocomposites – comprised of conductive nanofillers embedded within an insulating biopolymer matrix – have tremendous potential in applications such as sensors, nano-actuators, conductive adhesives, etc. [1]. Such materials have also been proposed for biomedical applications including wound-healing and tissue engineering [2]. In conductive polymer composites (CPCs), the concentration of the nanofiller impacts many properties of the network, including conductivity, with a minimum loading required to form a continuous network, causing the material to transition from insulating to conductive (i.e., the electrical percolation threshold). However, increasing the filler concentration may result in undesirable effects such as particle agglomeration, impaired mechanical properties and increased cost. [3] Thus, obtaining a relatively low percolation threshold for CPCs is highly desirable, and can be strategically achieved by a good dispersion of nanofillers with intrinsically high electrical conductivity. Among the material candidates for nanofillers, reduced graphene oxide (rGO) – a type of graphenic material synthesized by chemical or thermal reduction of exfoliated graphene oxide – has been widely used in biopolymer composites due to its excellent electrical and mechanical properties [4–7]. Among the methods that can be used for the preparation of rGO, solvent reduction is a versatile method, and many studies have focused on optimizing reducing agents and processes, as well as investigating the properties of the resulting rGO [8]. Sodium borohydride

($NaBH_4$) is a commonly used reducing agent, which can trigger a hydride transfer reaction and remove the oxygen functional groups on the GO. $NaBH_4$ is considered relatively safe to handle but with low reduction efficiency (i.e., a low ratio of C:O atoms in the final product) [9]. Hydrazine (N_2H_4) is another commonly used reducing agent for GO. Hydrazine has been shown to result in a high reduction efficiency [10], however it is toxic to humans and the environment. Ascorbic acid (L-A.A) is a natural "green" reducing agent [11], which has been previously used to make gelatin/graphene composites with a relatively low percolation threshold (0.033 vol%); however, the conductivity of these composites is also relatively low (10 S/m with 10 vol.% rGO loading) [12]. An additional advantage of L-A.A as a reducing agent is that it does not need to be removed after the GO reduction; residual L-A.A can, in fact, act as stabilizer for the rGO dispersion [11,13].

Polyhydroxybutyrate (PHB) is a biopolymer produced by bacteria that can be degraded by microorganisms in a natural environment [14]. Traditional uses of PHB include medical implants, surgical sutures, and food packaging due to its stability, non-toxicity, non-immunogenicity, and water-proof properties [15–17]. Most importantly, the biocompatibility of PHB makes it a promising material for biosensors. However, one of its drawbacks is its narrow processing window. The onset of thermal degradation begins at around (220 ºC), which is relatively close to its melting temperature (175 ºC) [18,19]. An alternative processing method is solvent casting, which involves dissolving polymer in a suitable solvent and then evaporating the solvent to obtain films with tunable properties. Recently, our group has shown that solution processing of PHB in boiling acetic acid can result in free-standing films with good mechanical properties [20]. In order to optimize the mechanical, electrical, and thermal properties of PHB, nanoparticles can be blended into PHB. Such materials have potential as the next generation green composites in many fields [21].

Nanofillers from the carbon family [22,23] are of particular interest due to their extraordinary electrical and thermal properties and low cost. It has been reported that adding graphenic materials to PHB not only improves the mechanical properties (e.g. Young's modulus, toughness, etc.), but also yields composites with good electrical properties (~1 S/m resistivity on 2.5 vol% graphene loading) [22,24].

In our work, the effects of different reducing agents (sodium borohydride, hydrazine, and L-A.A (ascorbic acid) have been systematically investigated, and the electrical and mechanical properties of composites formed with rGO prepared using each of these agents have been compared. The reduction efficiency of the reducing agents was measured using X-ray photoelectron spectroscopy, and the defects on the surface of rGO in pure form and within the composite were characterized by Raman spectroscopy. The morphology of the rGO and the filler dispersion were evaluated by SEM and optical microscopy, respectively. XRD was utilized to further probe the dispersion of the filler, and its effect on the crystallinity of the polymer. This characterization work was utilized to understand the differences in the electrical and mechanical properties of composites formed with each of the reducing agents. Finally, a proof-of-concept strain sensor was demonstrated using a PHB-rGO composite.

3.3 Experimental methods

Materials

Large flake graphite was obtained from Alfa Aesar. Sulfuric acid (98%), phosphoric acid (98%), hydrogen peroxide (30%), hydrochloric acid (37%) and potassium permanganate were purchased from Fisher Scientific. PHB biopellets were provided by Bulk Reef Supply, USA. Glacial acetic

acid (99 %), hydrazine monohydrate (N_2H_4 64-65 %), Sodium borohydride powder ($NaBH_4$), and L-ascorbic acid (L-A.A) were obtained from Sigma-Aldrich, Canada and used as received.

Preparation of GO slurry

The large flake graphite was oxidized using Tour's improved Hummer's method. [143] Briefly, 3g of graphite was added to a sulfuric acid (360 mL)/phosphoric acid (40 mL) mixture. The oxidizer, 18 g of potassium permanganate was then added slowly under stirring and the temperature raised to and maintained at 45 °C for 16 h**.** The mixture was then allowed to cool to room temperature before pouring the dispersion over 400 g of ice to quench the reaction. Hydrogen peroxide was slowly added to the reaction (~5 mL) causing effervescence until the dispersion turned a whitish yellow color. This dispersion/slurry was separated from the acids by centrifugation and the pellet re-suspended in water. This washing procedure was repeated twice using hydrochloric acid followed by three washes with ethanol. The resulting GO was kept in ethanol as a stock which we find useful for keeping the graphene oxide sheets exfoliated and solvated. XRD and AFM images of graphene oxide single layers prepared from a diluted stock dispersion in ethanol are shown in Figure 3.2 and 3.3. With the exception of some overlapping sheets, the exfoliated material all range in thickness from 0.7 to 1 nm which is thickness attributed to graphene oxide single layers.

Preparation of rGO/PHB thin films

Three different reducing agents were used, employing one of two methods: (1) a solvent exchange process (using either $NaBH_4$ or N_2H_4 as the reducing agent) (2) a simple in-situ reduction process (using L-A.A as the reducing agent), as shown in Figure 3.1. To reduce the GO using $NaBH_4$, the method described in Samulski's group[26] was adopted. The GO slurry described in the preceeding section was centrifuged at 20,000 for 20 min, and the supernatant was removed. The resulting

concentrated solution was then resuspended in water. This process was repeated twice, and the quantity of water added was selected to achieve a final concentration of 1 mg/mL. This GO solution was then heated to 100 °C on a hotplate under continuous stirring at 200 rpm. A chilled $NaBH_4$ (50 mM) solution was prepared and was immediately added drop-wise into the GO solution. The resulting solution was covered and heated to 80 °C under continuous stirring for 2 hrs. To prevent the hydrolysis of $NaBH_4$, sodium bicarbonate solution ($NaHCO_3$) was used to buffer the pH of the solution to 9. At the end of the two hours, the solution appeared to be totally black with no visible precipitation. This solution was cooled and then purified using dialysis. Approximately 50 mL of sample solution was added to a dialysis tube. The tube was then submersed in Millipore water, where the volume of the ultra-purified water was at least 40 times the volume of the sample. This water (which was kept at room temperature) was refreshed every 24 hrs for 3 days. After the dialysis, the solution (rGO in water) was kept in a beaker until use.

To reduce the GO using hydrazine, the method described in Ruoff's work [27] was adopted. Briefly, the GO was transferred from ethanol to water by two cycles of centrifuging (20,000 g, 10 min) and re-dispersion; with the volume of water the second time selected to achieve a concentration of 1 mg/mL. The solution was then heated to 100 ºC, and 98 % hydrazine solution (weight ratio of GO and hydrazine: 7:1) was added with continuous stirring at 100 ºC for 24 hrs under reflux. The solution turned from light brown to black immediately upon mixing. After cooling, 50 mL of sample solution was added to a dialysis tube where the tube was submersed in 0.5% ammonia solution refreshed every 24 hrs at room temperature for 3 days. After the reaction, the rGO solution was kept in a covered beaker until use. The rGO was dried in 80 °C oven overnight to get the rGO powder.

To form composites with rGO reduced by $NaBH_4$ and by N_2H_4, a solvent exchange procedure was first performed to transfer the rGO to acetic acid. The prepared rGO solutions were centrifuged (20,000 g, 10 min) to remove water and impurities and re-suspended in acetic acid (twice), to produce a slurry with a concentration of 0.75 mg/mL. The resulting rGO slurry was added to a prepared PHB dispersion (0.05 g/mL PHB in acetic acid) with vigorous stirring at acetic acid boiling temperature (118 ℃) for 4 hrs with refluxing acetic acid to obtain a homogeneous rGO/PHB dispersion. The rGO was dried overnight at 80 °C in an oven, yielding an rGO powder.

To reduce the GO by L-ascorbic acid, the method described by Guo's group [28] was adopted. Firstly, the slurry was centrifuged and resuspended in acetic acid two times, ultimately forming a solution with a concentration of 1 mg/ml. GO/acetic acid solution and was prepared and preheated to 118 ℃ (where the hot plate was set as 160 ℃). A small amount of PHB was added to act as a stabilizer (~0.04 g PHB) (note that this step was omitted for preparing samples for analysis by XPS, as in this case the PHB would contribute additional functional groups). L-A.A was added to the GO solution (2:1 wt, L-A.A: GO) under vigorous stirring and continuous heating at 118 °C for 2 hrs. No purification step was needed to remove the L-A.A residue, as it has been shown that the L-A.A can act as a stabilizer for rGO in an aqueous solution [13]. Subsequently, the prepared rGO solution (1 mg/ml) was further mixed with PHB (0.05 g/ml） by dissolved in acetic acid to form a homogeneous mixture at 118 ℃.

For rGO-PHB mixtures prepared using each type of reducing agent, thin films were prepared by solvent casting. Approximately 5 ml of solution at 140 ℃ was dispensed onto a glass substrate at 140 °C. Heating of the substrate continued until all of the solvent evaporated (as observed by eye), which usually took around 3 minutes.

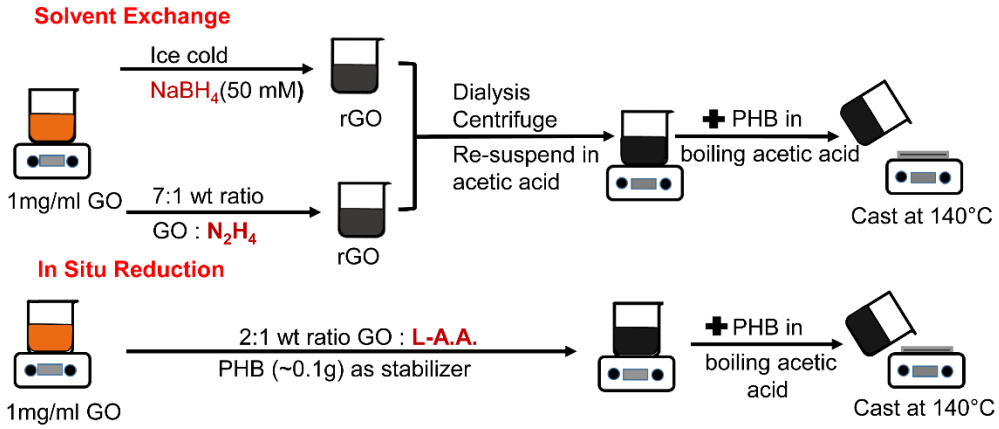

Figure 3.1. Schematic illustration of experimental process.

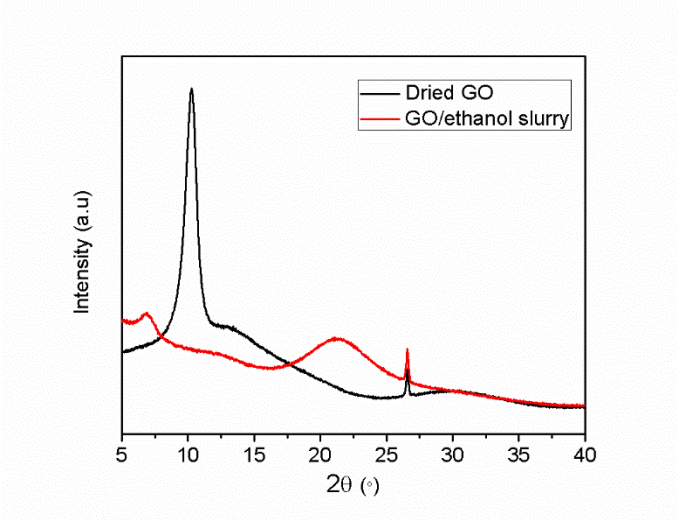

Figure 3.2 XRD patterns of GO/ethanol slurry before and after drying. Graphite was intentionally added as a reference to normalize the peak positions – see d_{002} peak near $2\theta = 27°$.

3.4 Characterization

X-ray photoelectron spectroscopy (XPS)

X-ray photoelectron spectroscopy (XPS) analysis was conducted at room temperature using a Kratos AXIS 165 spectrometer with a monochromatic (Al) X-ray source. XPS was performed over

binding energy values ranging from 0 eV to 10^3 eV at a scan rate and energy step of 2 eV/s and 400 meV, respectively. The chemical composition of the rGO sample was estimated by integrating the peaks at the known binding energies using CasaXPS software. To prepare the samples for XPS measurements, the GO slurry and the three types of rGO solutions were dried in the oven overnight at 60 ℃, and the resulting powders were then sandwiched between two glass slides and compressed by hand to form films.

X-ray diffraction

The crystallinity of GO, rGO, and of the composites was examined using a Rigaku XRD Ultimate IV (Cu-source) in the range of 2θ = 5° to 40° at a rate of 2°/min at 44 kV. GO and rGO powder samples were examined by sandwiching material between two glass slides to keep the surfaces flat. The composite film samples were cut into 2×2 cm^2 and kept flat for testing of thin films.

The degree of crystallinity was calculated using the equation: $X = \frac{I_c}{I_c + I_A} \times 100\%$, where Ic and I_A are the intensity of crystalline and the amorphous phases, respectively. A peak fitting procedure was implemented to determine these values; the sharp peaks were assumed to be crystalline and the rest of the area was considered to correspond to amorphous regions.

Raman spectroscopy

Raman spectra were recorded using a Thermo Nicolet Almega XR Raman Microscope at an excitation wavelength of 532 nm.

Surface Morphology and Dispersion

The surface morphologies of composites, the degree of dispersion within the matrix, and the thickness of composites were examined using both scanning electron microscopy (SEM, Zeiss Sigma FESEM w/EDX EBSD) and optical microscopy (Celestron 400x Laboratory Biological Microscope). SEM images were collected from powder rGO samples. To prepare these samples, rGO suspensions were dried in beakers in the oven at 60 ℃ overnight. To prepare samples for SEM, GO and rGO were mounted on carbon tape and sputter-coated with 10 nm of gold; samples were then imaged with 5 kV of accelerating voltage. To prepare composite films optical microscopy, 200 μm thin slices were cut using a microtome (allowing the cross-sectional area to be imaged).

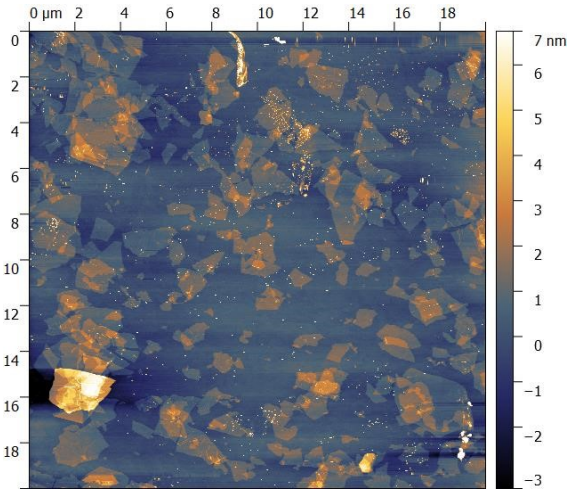

Figure 3.3 AFM topographic image of GO/ethanol stock suspension.

Electrical Characterization

The volume resistivity of high resistance samples (resitivity > 10^4 Ω-cm) was measured through the thickness of the sample with a ring electrode (model 8007) and Keithley 6517A electrometer.

The surface resistivity of samples with lower resistance was determined using a four point probe (Kelvin sensing) station with 1 mm probe spacing and a Keithley 2400 electrometer. The powder samples were compressed into thick films by a compressor with a loading of 2000 kg before resistance measurement. The resistance of the samples during bending was measured using a Keithley 2400 while the samples were deformed around cylinders with radii of curvature ranging from 1 cm to 2 cm.

Mechanical Characterization

Mechanical testing for the composites was carried out in tensile mode using an Instron 5943 (Instron, Norwood, MA, U.S.A.) with a 1 kN load cell at a strain rate of 10 mm/min. Samples were cut into rectangular strips by a razor blade, and five specimens of each type were measured. The error bar shown in the results represents the standard deviation of the five measurements.

Thermal Gravimetric Analysis

The thermal stability and actual content of filler of the blends was studied by using a thermogravimetric analyzer (TGA Model 1, Mettler Toledo, Columbus, OH, USA) equipped with the ultra-micro balance cell. Samples of 10 mg were prepared for characterization, from 25 to 400 ℃ at a heating rate of 10 ℃/min.

3.5 Results and discussion

X-Ray Photoelectron Spectroscopy

The effectiveness of the reducing agents (in terms of their ability to remove O groups) was measured by XPS analysis, and the results are shown in Figure 3.4 and 3.5 The spectra for GO and

rGO are shown in Figure 3.5(a): C and O are the dominant peaks. The atomic ratio of carbon and oxygen was obtained by taking the ratio of C 1s to O 1s peak area in XPS spectra. The initial C/O ratio of the GO sample was found to be 2.3, which matches the published value (~2) [29]. The high resolution spectrum of the GO sample (Figure 3.5(b)) shows that the main groups present are C=C, C-OH, C-N, and C=O groups. For the rGO prepared using the three different reducing agents, the C/O ratio of the GO increased from 2.3 to 3.8, 7.5, 10.2 after reduction using $NaBH_4$, L-A.A, and N_2H_4, respectively. Higher ratios indicate more effective removal of oxygen functional groups and are expected to result in higher conductivity. [30]

The high resolution N1s spectrum is shown in Figure 3.4, and shows a single peak at a binding energy of 400 eV – corresponding to pyrrolic N. This confirms the N doping of the rGO. Figure 3.5 (b) shows the deconvoluted high resolution spectra for rGO reduced by L-A.A. The residual oxygen-containing functional groups include C-OH/C-O-C (286 eV), C=O (287 eV), and O=C-O (289 eV), although with lower peak intensities than those observed for the GO. This confirms that most functional groups were removed during the reduction process, creating a larger amount of sp^2 hybridization with the sheets.

The C/O ratio achieved using $NaBH_4$ as the reducing agent was 3.8, which is only moderately higher than that of GO (2.3). The high resolution curve indicates that carbonyl group is reduced effectively, while the carboxyl group is reduced to a lesser degree, which agrees with results from the literature [126].

The highest C/O ratio (10.2) for the GO was achieved using N_2H_4, which agrees well with previous results from the literature (10.2). [31] The high resolution curve in Fig. 3.5 (b) shows that a number of functional groups – including, C-OH (binding energy = 286 eV), and C=O groups (binding

energy = 287 eV) – were mostly removed, but that the nitrogen group (binding energy = 401 eV) is present after the N_2H_4 reduction process (Figure 3.5a), N chemical dopants are introduced on

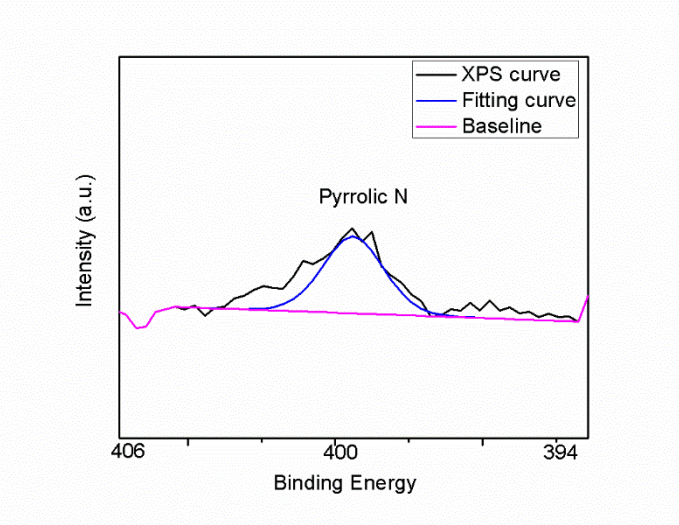

the surface of the resulting rGO.

Figure 3.4 High resolution XPS spectrum of N1s peak.

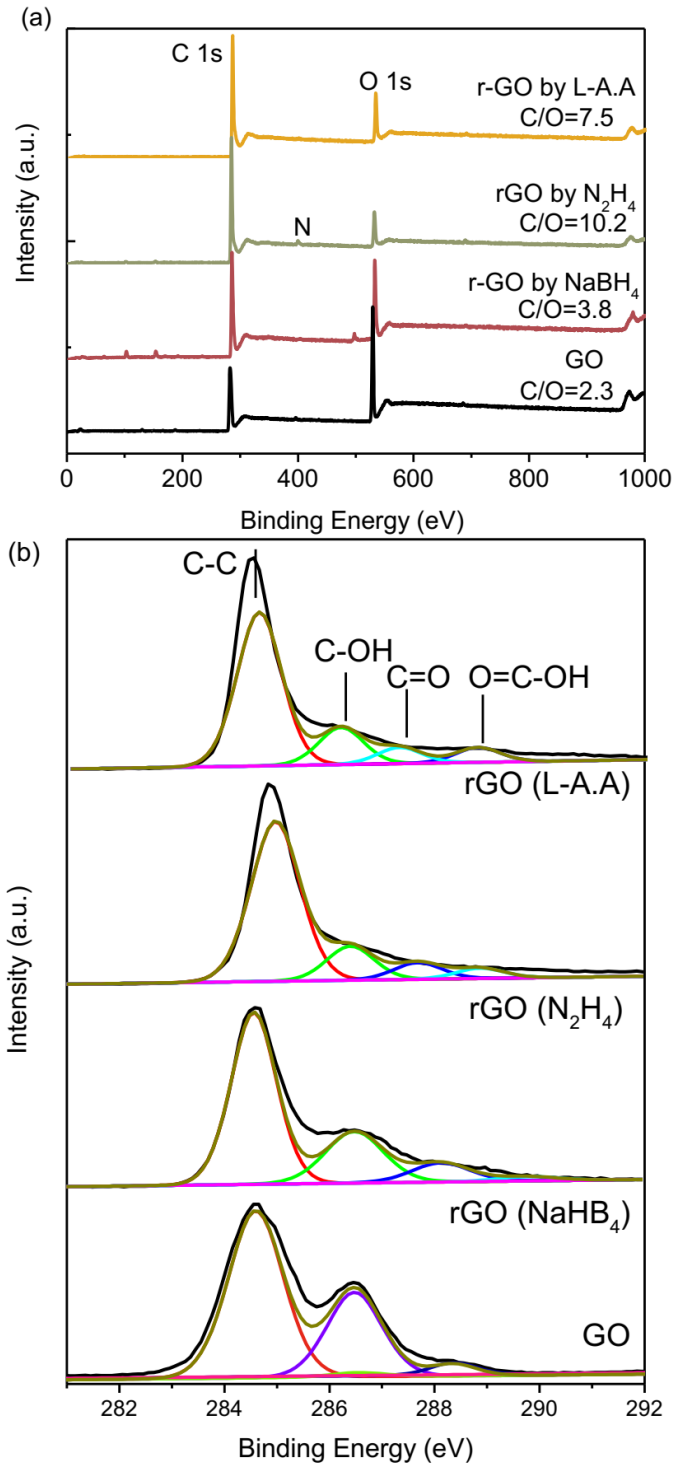

Figure 3.5 XPS spectra. (a) and (b) show the general XPS spectra and C 1s spectra of GO and rGO produced using the reducing agents L-A.A, N_2H_4, and $NaBH_4$.

Raman Spectroscopy

In order to confirm the existence of rGO-PHB complexes, the structure of both the rGO and the rGO-PHB composites was examined by Raman spectroscopy. The spectra of the GO and rGO reduced formed by the varying reducing agents and for GO are shown in Figure 3.6. Two distinct peaks and two broad peaks can be seen on the wavenumber regions of 1350, 1580, 2700, and 2900 cm^{-1}, corresponding to the D, G, 2D, and D' bands, respectively. These four peaks correspond to the main vibrations for sp^2-hybridized carbonaceous materials. The D band corresponds to the vibrations of aromatic domains but can only be observed in the presence of defects. The G band is attributed to the E^{2g} phonon of sp^2 carbon pairs. [27] The peak intensity ratio of D to G bands (I_D/I_G) is typically used to evaluate the properties of rGO, where the ratio is calculated based on the height of peaks. For carbons with small aromatic domains, the I_D/I_G ratio is expected to increase with domain size (up to ~2 nm). [32] This ratio then decreases as the domain size grows and defects are removed. The I_D/I_G ratio of each material (1.24, 1.28, and 1.32, for rGO reduced by $NaBH_4$, N_2H_4, and L-A.A, respectively) is higher than for GO (0.97), with the highest value corresponding to L-A.A (1.32). These increased values of I_D/I_G suggest the growth of sp^2 clusters since the defect density is expected to be high and the domain size is likely < 2 nm for such rGO. [33]

The Raman spectra of the composites formed using 4 wt% rGO (reduced by each of the three methods) are shown Figure 3.6. The I_D/I_G ratio of composites formed using different reducing agents follows the same trend as for the rGO itself ($I_D/I_{G\ L\text{-}A.A} > I_D/I_{G\ N2H4} > I_D/I_{G\ NaBH4}$). Overall, the values for the composites (1.11-1.18) are slightly lower than for the corresponding materials compared with rGO and GO values (1.24-1.32), indicating the covalent or non-covalent bonding of the polymer to basal and edge planes of the rGO in the composites. The I_D/I_G ratio were also

calculated based on the area of the two peaks, shown on Supplementary information Table 3.1. Results show the same trend and offer the same discussion as before.

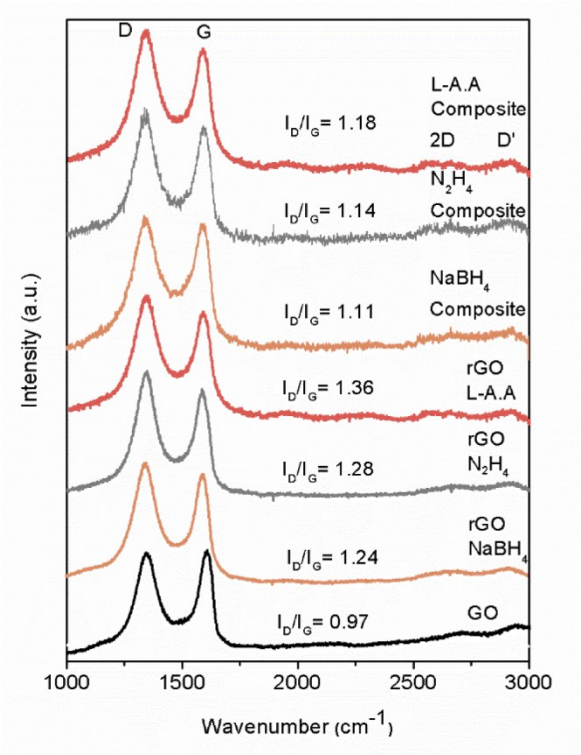

Figure 3.6 Raman spectra of GO, rGO (reduced from $NaBH_4$, N_2H_4, L-A.A from up to bottom), and rGO composites.

Table 3.1 Raman I_D/I_G Values calculated by integrated peak areas.

Material	GO	rGO ($NaBH_4$)	rGO (N_2H_4)	rGO (L-A.A)	Composites ($NaBH_4$)	Composites (N_2H_4)	Composites (L-A.A)
I_D/I_G	0.92	1.26	1.36	1.44	1.15	1.11	1.21

Electrical Characterization

The resistivity of rGO prepared using each reducing agent was measured, and the results are shown in Table 3.2. To calculate these values the film thickness was required; typical film thicknesses were around 80 μm. The resistivity of the material reduced using $NaBH_4$ (5.6 Ω-cm) was found to be the highest, which may be attributed to the comparatively low C/O ratio. The resistivity of rGO from L-A.A (4.65×10^{-11} Ω-cm) and N_2H_4 (4.53×10^{-11} Ω-cm) were found to be quite similar, despite their differences in C/O ratio.

Thermogravimetric analysis (TGA) was carried out to examine the real content in composites, and the results shown on Figure 3.7 and 3.8, showing that the real content of rGO (i.e. the mass remaining after the sample had been heated to 400 °C) matched the proportion added during the experiment, indicating GO has been almost fully converted to rGO during reduction process Figure 3.9 illustrates the electrical characteristics of the three kinds of composites, and all show decreasing resistance with increasing wt% of rGO. Pure PHB (0 wt% filler) was found to be an insulator, with a resistivity of 1×10^{15} Ω-cm. As expected, samples with a higher wt% of nanofiller were conductive than samples with lower wt% of nanofiller. Among three types of composites, those prepared from $NaBH_4$ were the most resistive (i.e., the poorest conductors) for all concentrations, with a resistivity of 5×10^5 Ω-cm at 2 wt% loading, 2×10^4 Ω-cm at 3 wt % loading, and 150 Ω-cm at 8 wt % loading (corresponding to a conductivity of 0.6 S/m). Those prepared from L-A.A. were least resistive, with a resistivity of 480 Ω-cm (corresponding to a conductivity 0.1 S/m) at 2 wt% rGO loading, and 80 Ω-cm (1 S/m) at around 3 wt% loading, and a resistivity of ~3 Ω-cm at 8 wt% loading (conductivity = 30 S/m). In contrast, the composites from N_2H_4 were found to have a resistivity of 8×10^4 Ω-cm (conductivity of 1×10^{-3} S/m) at 2wt % and 1000 Ω-cm (0.1 S/m) at 3

wt% loading, and the ultimate resistivity of 18 Ω-cm (conductivity of 5.3 S/m) on 8 wt% loading. The electrical percolation threshold – the critical filler content at which the conductivity increases greatly – was determined to be around 1.5, 2, 1 wt% for $NaBH_4$, N_2H_4, L-A.A. composites, respectively, by estimating between collected data points. The actual, measured values are comparable to the nominal values, so we can exclude these differences when explaining the properties of the resulting composites.

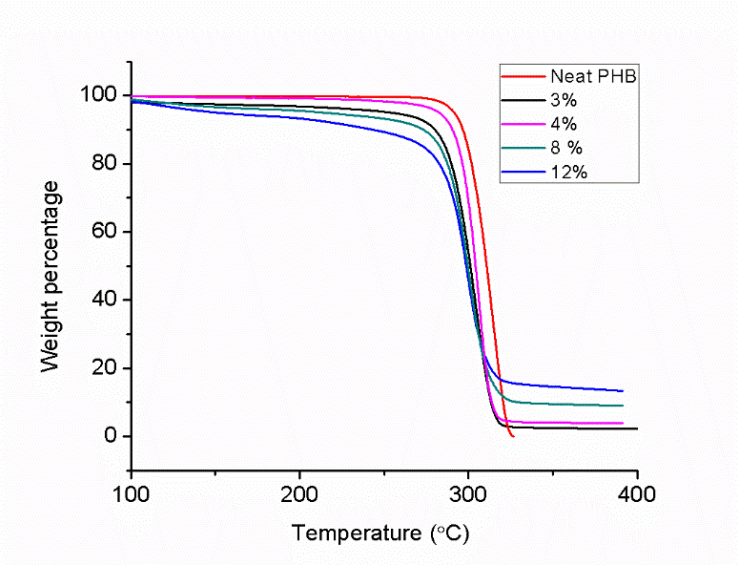

Figure 3.7 TGA data of L-A.A reduced GO composites.

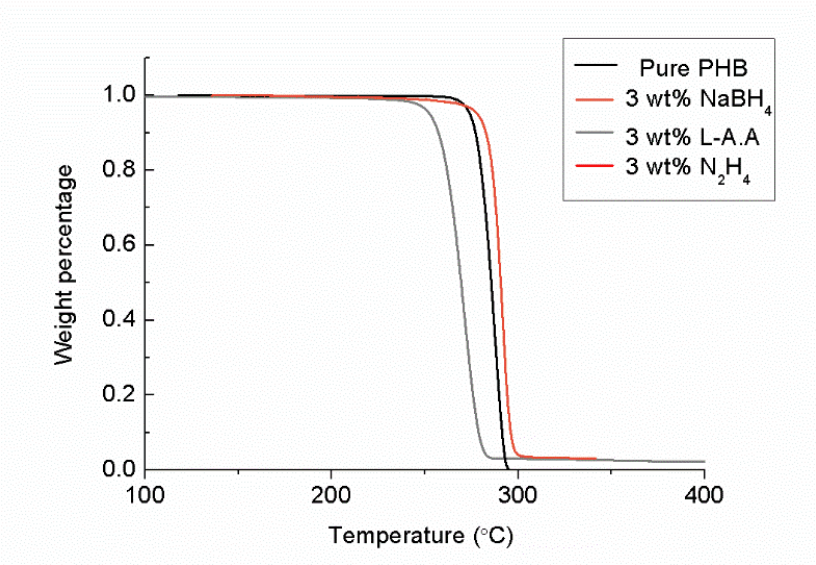

Figure 3.8 TGA data of pure PHB and 3 wt% composites reduced by $NaBH_4$, N_2H_4, and L-A.A reducing agents.

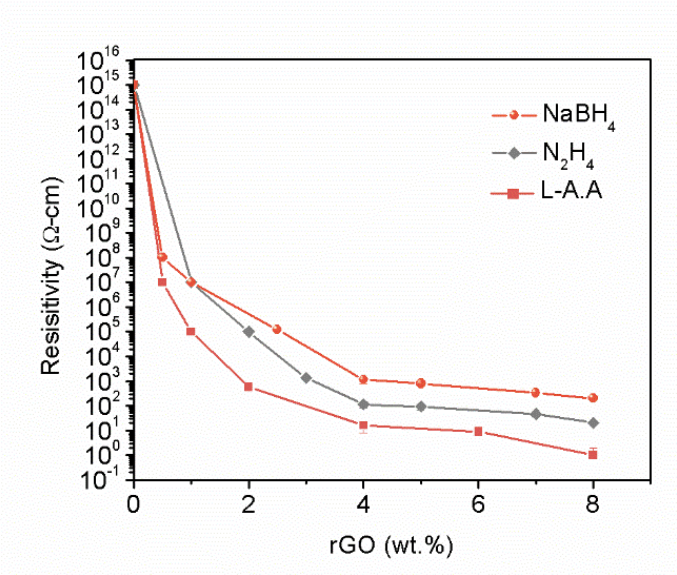

Figure 3.9 Electrical resistivity of three kinds of composites, plotted in terms of wt% loading of rGO.

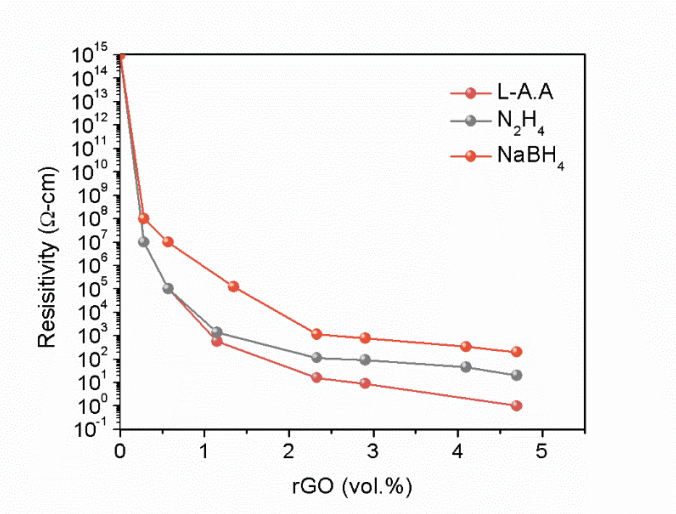

Figure 3.10 Electrical resistivity of three kinds of composites, plotted in terms of vol.% rGO loading.

Reducing agents	resistivity (Ω-cm)	C/O ratio	Doping	Conditions
$NaBH_4$	5.6	3.8	None	80~90°C, 4hrs
N_2H_4	0.0454	7.5	N-doped	100°C, 4hrs
L-A.A	0.0465	10.2	None	160°C, 2hrs
Untreated GO	$\sim 10^{12}$	1.8	None	None

Table 3.2 Resistivities of compressed GO and rGO powder films.

X-Ray Diffraction (XRD)

The crystal structures of the GO powder and rGO produced using each reducing agent (as both powders and composites) were studied by XRD, as shown in Figure 3.11. The specific crystalline

peaks were used to determine if we successfully reduced GO from rGO characterization peaks and to indicate the extent of rGO exfoliation by comparing the position of composite peaks. Figure 3.11 (a) shows the XRD patterns of GO and rGO prepared using $NaBH_4$, N_2H_4, and L-A.A. The GO exhibits a strong peak around 10°, characteristic of the (002) plane, while the reduced materials exhibit broader peaks at larger angles (~15°-20°) centered at ~20°. These broad peak suggests that the rGO sheets may exist as monolayers or as stacks consisting of only a few layers, thereby resulting in only limited diffractions over a variety of angles. The d-spacing of the sheets can be calculated from the value of the peak using Bragg's law. For the GO, the d-spacing was determined to be around 7.50 Å; as expected this is larger than the value known for natural graphite (3.34 Å) [34], indicating that an increase in interlayer spacing occurred due to the introduction of oxygen groups between the layers. The broad peaks of the reduced materials correspond to an interlayer distance of ~4Å (as calculated by Bragg's law). The d-spacing of the rGO (4 Å) falls between the d-spacing of GO (7.50 Å) and natural graphite (3.34 Å) , suggesting that the reduced material maintains a stacked structure.

Figure 3.11 (b) depicts the XRD patterns of the composites and also of pure PHB. The XRD pattern of pure PHB includes peaks at 2θ values of 13.1°, 16.7°, 19.5°, 21.2°, 22.4°, 25.4°, which can be attributed to the (020), (110), (021), (111), and (121) crystal planes of the polymer, respectively. The patterns of the composites are all quite similar to each other and to the pattern of the pure PHB. Each type of rGO powder exhibits a broad diffraction speak spanning from around 10° to 30°, suggesting that the material is amorphous. This broad peak is absent in the composite materials, indicating good exfoliation of rGO in the polymer matrix regardless of the type of reducing agent. The analysis of XRD different peaks revealed that the overall crystallinity of each of the composites (~60%) was lower than that of the pure PHB (73.8 %). In addition, the inclusion of

rGO also results in a change in the relative intensity of the peaks corresponding to the (020) and (110) planes of the polymer (both the peak intensity values and the integrated area for the (020) and (110) peaks are shown in the Table 3.3. For the pure polymer, the intensities of these peaks are approximately equal, and the ratio of integrated area for the (020):(110) peak is 0.83. For each composite, the integrated area of the (110) peak is less than the integrated area of the (020) peak; the ratio of these values is around 1.21. A similar change in the ratio of intensities of these peaks has been observed previously by Arza *et al.*, who observed an increasing ratio between the intensity of the (020):(110) peaks of PHB with graphene oxide (GO) filler. [35] In their work, this ratio increased with increasing wt% loading of GO. They attributed these differences to preferential orientation effects within the polymer.

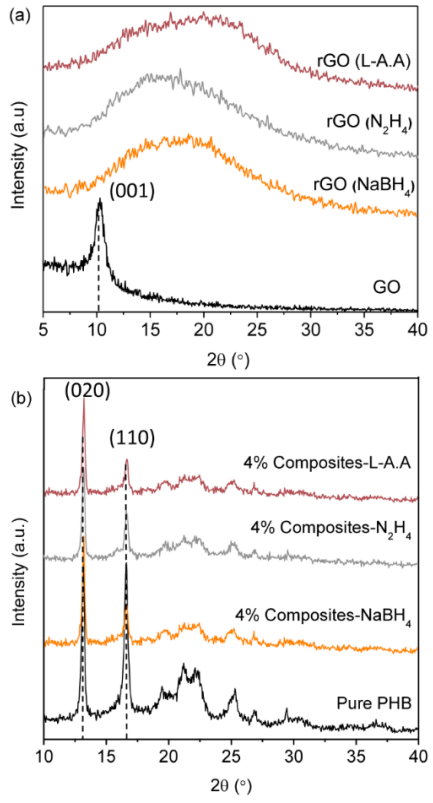

Figure 3.11 XRD pattern of GO, rGO, PHB (a), and 4wt% composites (b).

Table 3.3 XRD intensity ratios of pure PHB and composites.

Polymer	Total Crystallinity (%)	Intensity Height (020)	Intensity Height (110)	Area (020)	Area (110)	Ratio of (020):(110) (by area)
Pure PHB	73.78	453	422	3185	3839	0.83
4 wt% rGO/PHB (L-A.A)	62.45	302	208	1944	1613	1.21
4 wt% rGO /PHB (N_2H_4)	61.68	247	159	1569	1302	1.21
4 wt% rGO /PHB ($NaBH_4$)	59.61	237	139	1470	1211	1.21

Scanning Electron Microscopy (SEM)

To investigate the morphologies of GO and rGO from the different reducing reagents, scanning electron microscopy (SEM) was employed, and the results are shown in Figure 3.12. The size of the sheets of each type of material can be qualitatively observed from Figure 3.12; the sheets of the GO in its initial (unreduced state) were the largest in lateral size while the sheets of the rGO reduced by $NaHB_4$ were the smallest. Fragments of smaller particles were observed in all the rGO images (diameter of 5~10 μm), which is attributed to the inevitable fracture of the sheets during mechanical stirring.

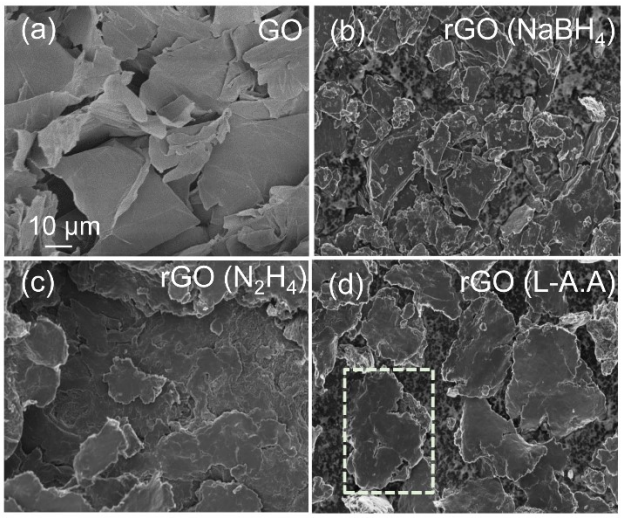

Figure 3.12 SEM images of GO (a), rGO-$NaBH_4$ (b), rGO-N_2H_4 (c), rGO-L-AA (d).

Optical Microscopy

To explore the rGO distribution in the polymer matrix, thin slices (200 µm) of composites prepared by each reducing agent (1 wt% rGO in PHB) were cut using a microtome and imaged using optical microscopy (Figure 3.13). Figure 3.13a and d depict low and high magnification images of composites prepared using $NaBH_4$. Agglomeration of the rGO can clearly be observed (particularly at high magnification). The films prepared using rGO reduced from N_2H_4 are shown in Figures 3.13 b and 3.13 e; this rGO tended to agglomerate more than other two types, with the largest clusters of material observed in the low magnification images. The films prepared using rGO reduced by L-A.A are shown in Figures 3.13 c and 3.13 f, and of the three types of composites, the best dispersion is seen in L-A.A reduced samples.

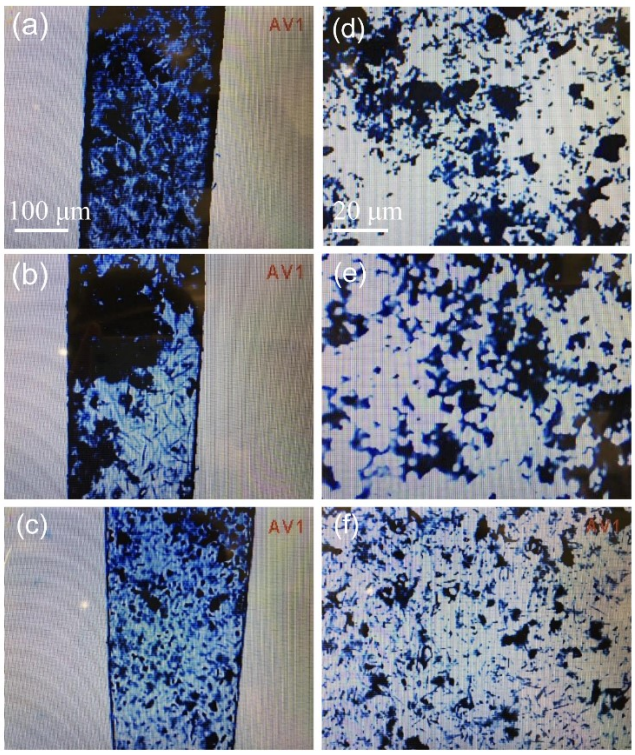

Figure 3. 13 Optical images of 1wt % rGO composites reduced from $NaBH_4$(a), N_2H_4(b), L-A.A. (c) and higher magnification images (d), (e), (f), respectively.

Mechanical Testing

The mechanical properties of the composites with the best electrical properties (those formed using L-A.A as the reducing agent) were characterized using a tensile tester (Figure 3.14). Figure 3.14 (a) shows typical strain-stress curves for pure PHB and reduced rGO-PHB composite (4 wt%), and Young's Modulus changes were given in Figure 3.14 (b). Table 3.4 shows the Young's modulus, ultimate tensile strength values, and strain at break of 4 wt% rGO samples. All 4 wt% loading composites show increases in the Young's modulus and ultimate strength. The differences may be related to the structure of rGO. For example, the Young's modulus of the pure PHB (~1000 MPa) increased to 5000 MPa (total increase in modulus: 400 %) in L-A.A samples but $NaBH_4$ reduced

samples show similar Young's modulus as pure PHB. However, the main drawback is that the addition of rGO reduces the elongation at break, meaning that the composites are more brittle than the pure material. Samples with higher loading rGO were fragile and difficult to characterize, results for these materials are therefore not shown.

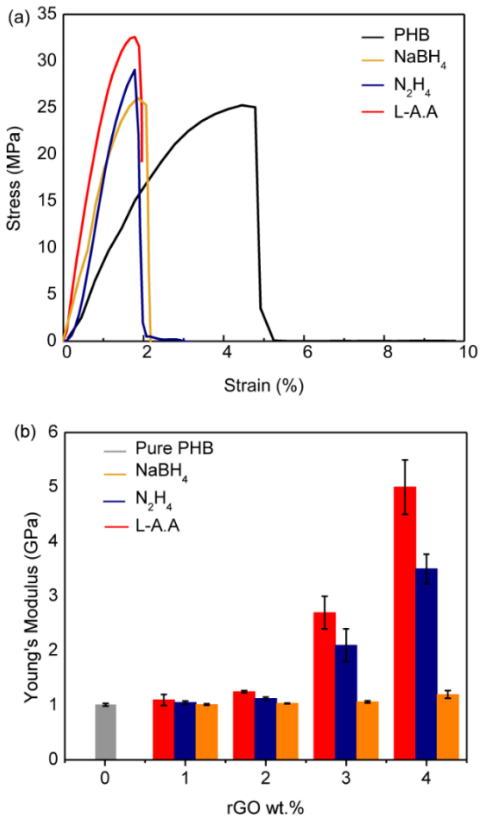

Figure 3. 14 Typical strain-stress curves of PHB and 4 wt% rGO composites (a), Young's Modulus change as a function of wt% loading (b).

Samples	Ultimate tensile strength (MPa)	Young's modulus (MPa)	Strain at break (%)
Pure PHB	22.10 ± 2.16	994.68 ± 329.21	4.64 ± 0.68
$NaBH_4$	24.66 ± 0.58	1145.40 ± 91.84	2.34 ± 0.35
N_2H_4	31.87 ± 1.07	3409.20 ± 953.53	2.29 ± 0.33
L-A.A	32.00 ± 1.43	4061.60 ± 1141.20	2.16 ± 0.52

Table 3.4 Mechanical properties of 4 wt% rGO samples and PHB.

Development of a strain sensor

Based on its relatively good mechanical and electrical properties, the 4 wt% composite of L-A.A-reduced rGO/PHB was further investigated as a strain sensor. The electrical properties of this material were measured as a strip of the composite was bent through decreasing radii of curvature. Figure 3.15 (a) shows the variation in resistivity as a function of the strain applied to the top surface of the sample during bending. As the radius of curvature decreases, the strain on the top edge of the sample increases, leading to a corresponding increase in resistance of up to 35% for a strain of 0.7%. The curve follows an approximately linear trend, and the results shown were measured on a single sample over 3 repeated cycles and averaged. These results suggest that these rGO/biopolymer composites could form the basis for the fabrication of biosensors. To further demonstrate the utility of the materials, Figure 3.15 (b) shows a 4 wt% composite used as the conductor to transfer current from a 3V battery to illuminate an LED.

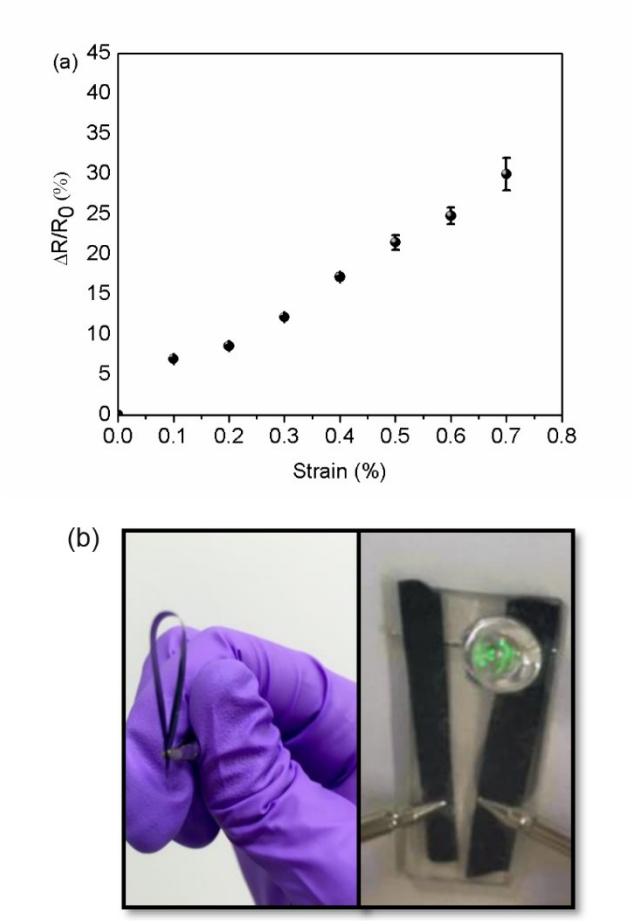

Figure 3.15 (a) Resistance change as a function of strain. (b) Images of 4wt% composite strips as a conductive and flexible circuits, and bulb was lit up under 3V.

3.6 Discussion

Chemical and physical analysis of the rGO prepared using three different reducing agents revealed a variety of differences. XPS revealed that hydrazine (N_2H_4) is the most effective reducing agent, with a C/O ratio of 10.2. Raman spectroscopy further showed the rGO produced from N_2H_4 had fewer oxygen functional groups on the basal and edge planes of carbon atoms, resulting in larger aromatic domains and thus less structural disorder. However, from the SEM images, it could also be seen that the reduction process resulted in relatively smaller sheets when N_2H_4 was used. Composites of this material and PHB were formed by first reducing the GO, and then blending the

resulting rGO with PHB dissolved in acetic acid. The dispersion of the resulting material was relatively poor, and larger clusters were visible in the 1 wt% samples by optical microscopy, indicating poor compatability between the nanosheets and polymer matrix. A similar effect was seen in the solution prior to casting: some small agglomerates were observed by eye. Despite the fact that N_2H_4 was the most effective reducing agent, the conductivity of the composites at each wt% loading was intermediate with respect to the other two reducing agents. The introduction of N groups (seen from XPS) may affect subsequent properties such as conductivity. While N is known to dope more pristine graphene which improves conductivity, the rGO is expected to be much more defective and the N may act as additional defect sites to the residual oxygen present which likely reduces the electronic mobility even further.

Composites formed with $NaBH_4$-reduced rGO exhibited the poorest electrical properties, due to a variety of reasons. $NaBH_4$ was the least effective reducing agent (C/O ratio of 3.8), with the most oxygen functional groups visible on the high resolution spectra (Fig 3.5 b). This result is further supported by the fact that no visible agglomeration was observed in the resulting rGO solution, indicating that this solution contained large quantities of unreduced GO (which is hydrophilic and therefore easily dispersed). The rGO itself is hydrophobic, and will naturally agglomerate in the solvent without surfactant or stabilizers. Similarly, characterization by Raman spectroscopy revealed that this material has the highest level of structural disorder. As for the N_2H_4, the reducing process led to a decrease in the size of the sheets from the GO (as seem by SEM), and these sheets maintained a fairly layered structure (as seen by XRD). All of these properties (surface defects, small sheet sizes) contributed to the relatively poor electrical conductivity of the rGO itself, which was an order of magnitude higher than for the rGO reduced by the other two reducing agents. The

rGO in the composites was poorly dispersed, and overall the electrical properties of these composites were the poorest.

The L-A.A- reduced rGO was found to be the best candidate as nanofiller to fabricate rGO/PHB composites, which has the smallest electrical threshold (1 wt%) and highest conductivity (30 S/m, 8 wt% loading). This value is on par with the highest demonstrated rGO biopolymer composites, including graphene gelatin composites (conductivity of 10 S/m for 10 vol.% rGO loading) and rGO/polylactic acid (PLA) composites prepared using glucose as a reducing agent (conductivity ~ 2.2 S/ for 1.25 vol.% loading) [12,36]. Several important factors could explain this result. First, the high intrinsic conductivity of L-A.A-reduced rGO (2150 S/m) is a prerequisite of forming highly conductive nanocomposites. The high I_D/I_G of the rGO itself suggests low defects in the structure of the material, which likely contributes to this high conductivity. Second, of the materials studied here, L-A.A-reduced rGO has the largest lateral size (as seen by SEM), which is beneficial for transporting electrons across the surface of the material. It has been reported that rGO sheets which are larger in size can result in composites with higher conductivity due to the increased contact area between conductive particles [37–39]. Of the rGO, the material reduced from L-A.A has the largest lateral size, followed by N_2H_4, which helps to explain why composites formed from rGO reduced by L-A.A and N_2H_4 showed higher conductivity than composites from $NaBH_4$. Characterization of the composites by Raman spectroscopy showed that the highest I_D/I_G value (1.18) was for the rGO (L-A.A)/PHB composite, indicating synergistic effects of covalent and non-covalent interactions between fillers and polymer chains. These strong interactions can positively impact both the electronic and mechanical properties of the composites. One reason for the strong interactions between the matrix and nanofiller is that the composites formed from L-

A.A-reduced rGO and PHB could be formed in-situ reduction process. In this process, a small amount of PHB was added to the solution during the reduction process to act as stabilizer to disperse the rGO. In L-A.A reduction and composite fabrication, no solvent change process is needed compared with using the other two reducing agents. Furthermore, L-A.A can also play a role of stabilizer, leading to a well-dispersed rGO (L-A.A) in the polymer matrix. Good dispersion was observed by optical microscopy of the 1 wt% samples, with the fewest and smallest clusters. An even distribution of nanofiller is vital for the good properties of composites as large agglomeration can deteriorate the mechanical properties (e.g. brittleness) or form weak electron movement path.

Based on the favorable electrical properties of the L-A.A-reduced rGO/PHB composites, this material was further characterized to investigate its potential for use as a material in biocompatible actuators and sensors. Mechanical characterization showed the strain to failure increased from 25 MPa for pure PHB samples to 34 MPa for 4 wt% composite samples, and that the modulus of all composite samples increased as a function of rGO loading. However, with increasing loading of rGO the ductility of the samples (elongation at break) dropped. Nevertheless, the composite samples were found to be flexible in bending. A proof-of-concept bending sensor was fabricated, and the resistivity of the sensor was found to increase reversibly by 35% as the sample was bent to a radius of curvature of 0.5 cm (corresponding to a strain of 0.8%). This suggests that the composites can be potentially used as flexible piezo-resistive type sensors for applications such as tracking the movement of the human body.

3.7 Conclusions

In this work, we systematically examined three types of rGO/PHB bio-inspired composites employing two methods: rGO blending (of $NaBH_4$ and N_2H_4-reduced rGO) and in-situ reduction of GO by L-A.A. L-A.A.-reduced rGO/PHB composites showed the best electronic properties, due to both the good dispersion of the nanofiller in the matrix, and the large sheet size and high intrinsic conductivity of the rGO itself. This work suggests that when forming rGO-biopolymer composites from solution, an in situ reduction process is advantageous for achieving good properties. The electrical properties of the L-A.A in-situ reduced rGO/PHB composites achieved in our work are comparable to the best values known in the biopolymer composite field. An additional advantage of the L-A.A. over N_2H_4 and $NaBH_4$ is the low toxicity of this material, which makes it much suitable for some bio-related applications.

One potential area of application for conductive rGO-PHB composites is in sensing mechanical deformations and pressures. As a proof-of-concept, a simple strain sensor was demonstrated simply by cutting the PHB into strips and measuring the resistivity of the material as it was deformed in bending mode. Despite the intrinsic brittleness of PHB, these strips were bent over radii of curvatures of up to 0.5 cm. As the materials are solution-processible, printing techniques could potentially be used to pattern the composites for applications including wearable sensors, biocompatible actuators, and biodegradable circuits.

3.8 References

(1) Zhang, R.; Agar, J. C.; Wong, C. P. Conductive Polymer Composites. In *Encyclopedia of Polymer Science and Technology*; John Wiley & Sons, Inc., **2002**. https://doi.org/10.1002/0471440264.pst430.pub2.

(2) Silva, C.; Caridade, S. G.; Cunha, E.; Sousa, M. P.; Rocha, H.; Mano, J. F.; Paiva, M. C.; Alves, N. M. Nanostructured Biopolymer/Few-Layer Graphene Freestanding Films with Enhanced Mechanical and Electrical Properties. *Macromol. Mater. Eng.***2017**. https://doi.org/10.1002/mame.201700316.

(3) Wan, Y.-J.; Tang, L.-C.; Yan, D.; Zhao, L.; Li, Y.-B.; Wu, L.-B.; Jiang, J.-X.; Lai, G.-Q. Improved Dispersion and Interface in the Graphene/Epoxy Composites via a Facile Surfactant-Assisted Process. *Compos. Sci. Technol.* **2013**, *82* (Supplement C), 60–68. https://doi.org/10.1016/j.compscitech.2013.04.009.

(4) Yun, S.; Kim, J. Mechanical, Electrical, Piezoelectric and Electro-Active Behavior of Aligned Multi-Walled Carbon Nanotube/Cellulose Composites. *Carbon* **2011**, *49* (2), 518–527. https://doi.org/10.1016/j.carbon.2010.09.051.

(5) Boffa, V.; Etmimi, H.; Mallon, P. E.; Tao, H. Z.; Magnacca, G.; Yue, Y. Z. Carbon-Based Building Blocks for Alcohol Dehydration Membranes with Disorder-Enhanced Water Permeability. *Carbon* **2017**, *118*, 458–466. https://doi.org/10.1016/j.carbon.2017.03.077.

(6) Wan, Y.-J.; Yang, W.-H.; Yu, S.-H.; Sun, R.; Wong, C.-P.; Liao, W.-H. Covalent Polymer Functionalization of Graphene for Improved Dielectric Properties and Thermal Stability of Epoxy Composites. *Compos. Sci. Technol.* **2016**, *122*, 27–35. https://doi.org/10.1016/j.compscitech.2015.11.005.

(7) Majidian, M.; Grimaldi, C.; Pisoni, A.; Forró, L.; Magrez, A. Electrical Conduction of Photo-Patternable SU8–Graphene Composites. *Carbon* **2014**, *80*, 364–372. https://doi.org/10.1016/j.carbon.2014.08.075.

(8) De Silva, K. K. H.; Huang, H.-H.; Joshi, R. K.; Yoshimura, M. Chemical Reduction of Graphene Oxide Using Green Reductants. *Carbon* **2017**, *119*, 190–199. https://doi.org/10.1016/j.carbon.2017.04.025.

(9) Shin, H.-J.; Kim, K. K.; Benayad, A.; Yoon, S.-M.; Park, H. K.; Jung, I.-S.; Jin, M. H.; Jeong, H.-K.; Kim, J. M.; Choi, J.-Y.; Lee, Y. H. Efficient Reduction of Graphite Oxide by Sodium Borohydride and Its Effect on Electrical Conductance. *Adv. Funct. Mater.* **2009**, *19* (12), 1987–1992. https://doi.org/10.1002/adfm.200900167.

(10) Park, S.; An, J.; Potts, J. R.; Velamakanni, A.; Murali, S.; Ruoff, R. S. Hydrazine-Reduction of Graphite- and Graphene Oxide. *Carbon* **2011**, *49* (9), 3019–3023. https://doi.org/10.1016/j.carbon.2011.02.071.

(11) Fernández-Merino, M. J.; Guardia, L.; Paredes, J. I.; Villar-Rodil, S.; Solís-Fernández, P.; Martínez-Alonso, A.; Tascón, J. M. D. Vitamin C Is an Ideal Substitute for Hydrazine in the Reduction of Graphene Oxide Suspensions. *J. Phys. Chem. C* **2010**, *114* (14), 6426–6432. https://doi.org/10.1021/jp100603h.

(12) Nassira, H.; Sánchez-Ferrer, A.; Adamcik, J.; Handschin, S.; Mahdavi, H.; Taheri Qazvini, N.; Mezzenga, R. Gelatin–Graphene Nanocomposites with Ultralow Electrical Percolation Threshold. *Adv. Mater.* **2016**, *28* (32), 6914–6920. https://doi.org/10.1002/adma.201601115.

(13) Zhang, J.; Shen, G.; Wang, W.; Zhou, X.; Guo, S. Individual Nanocomposite Sheets of Chemically Reduced Graphene Oxide and Poly(N-Vinyl Pyrrolidone): Preparation and

Humidity Sensing Characteristics. *J. Mater. Chem.* **2010**, *20* (48), 10824–10828. https://doi.org/10.1039/C0JM02440F.
(14) Kumagai, Y.; Kanesawa, Y.; Doi, Y. Enzymatic Degradation of Microbial Poly(3-Hydroxybutyrate) Films. *Makromol. Chem.* **1992**, *193* (1), 53–57. https://doi.org/10.1002/macp.1992.021930105.
(15) Ghaffar, Ahmed Mohamed El-Hadi Abdel. Development of a biodegradable material based on Poly (3-hydroxybutyrate) PHB.**2002**.
(16) Kuswandi, B. Environmental Friendly Food Nano-Packaging. *Environ. Chem. Lett.* **2017**, *15* (2), 205–221. https://doi.org/10.1007/s10311-017-0613-7.
(17) Bucci, D. Z.; Tavares, L. B. B.; Sell, I. PHB Packaging for the Storage of Food Products. *Polym. Test.* **2005**, *24* (5), 564–571. https://doi.org/10.1016/j.polymertesting.2005.02.008.
(18) Gogolewski, S.; Jovanovic, M.; Perren, S. M.; Dillon, J. G.; Hughes, M. K. The Effect of Melt-Processing on the Degradation of Selected Polyhydroxyacids: Polylactides, Polyhydroxybutyrate, and Polyhydroxybutyrate-Co-Valerates. *Polym. Degrad. Stab.* **1993**, *40* (3), 313–322. https://doi.org/10.1016/0141-3910(93)90137-8.
(19) Grassie, N.; Murray, E. J.; Holmes, P. A. The Thermal Degradation of Poly(-(d)-β-Hydroxybutyric Acid): Part 1—Identification and Quantitative Analysis of Products. *Polym. Degrad. Stab.* **1984**, *6* (1), 47–61. https://doi.org/10.1016/0141-3910(84)90016-8.
(20) Anbukarasu, P.; Sauvageau, D.; Elias, A. Tuning the Properties of Polyhydroxybutyrate Films Using Acetic Acid via Solvent Casting. *Sci. Rep.* **2015**, *5*. https://doi.org/10.1038/srep17884.
(21) Prakalathan, K.; Mohanty, S.; Nayak, S. K. Reinforcing Effect and Isothermal Crystallization Kinetics of Poly(3-Hydroxybutyrate) Nanocomposites Blended with Organically Modified Montmorillonite. *Polym. Compos.* **2014**, *35* (5), 999–1012. https://doi.org/10.1002/pc.22746.
(22) Abdala, A.; Barrett, J.; Srienc, F. Synthesis of Poly-(R)-3 Hydroxyoctanoate (PHO) and Its Graphene Nanocomposites. In *Green Polymer Chemistry: Biocatalysis and Materials II*; ACS Symposium Series; American Chemical Society, **2013**; Vol. 1144, pp 199–209. https://doi.org/10.1021/bk-2013-1144.ch014.
(23) Pramanik, N.; De, J.; Kumar Basu, R.; Rath, T.; Paban Kundu, P. Fabrication of Magnetite Nanoparticle Doped Reduced Graphene Oxide Grafted Polyhydroxyalkanoate Nanocomposites for Tissue Engineering Application. *RSC Adv.* **2016**, *6* (52), 46116–46133. https://doi.org/10.1039/C6RA03233H.
(24) Sridhar, V.; Lee, I.; Chun, H. H.; Park, H. Graphene Reinforced Biodegradable Poly (3-Hydroxybutyrate-Co-4-Hydroxybutyrate) Nano-Composites. *Express Polym. Lett.* **2013**, *7* (4), 320–328.
(25) Marcano, D. C.; Kosynkin, D. V.; Berlin, J. M.; Sinitskii, A.; Sun, Z.; Slesarev, A.; Alemany, L. B.; Lu, W.; Tour, J. M. Improved Synthesis of Graphene Oxide. *ACS Nano* **2010**, *4* (8), 4806–4814. https://doi.org/10.1021/nn1006368.
(26) Si, Y.; Samulski, E. T. Synthesis of Water Soluble Graphene. *Nano Lett.* **2008**, *8* (6), 1679–1682. https://doi.org/10.1021/nl080604h.
(27) Stankovich, S.; Dikin, D. A.; Piner, R. D.; Kohlhaas, K. A.; Kleinhammes, A.; Jia, Y.; Wu, Y.; Nguyen, S. T.; Ruoff, R. S. Synthesis of Graphene-Based Nanosheets via Chemical Reduction of Exfoliated Graphite Oxide. *Carbon* **2007**, *45* (7), 1558–1565. https://doi.org/10.1016/j.carbon.2007.02.034.

(28) Zhang, J.; Yang, H.; Shen, G.; Cheng, P.; Zhang, J.; Guo, S. Reduction of Graphene Oxide ViaL-Ascorbic Acid. *Chem. Commun.* **2010**, *46* (7), 1112–1114. https://doi.org/10.1039/B917705A.
(29) Chen, J.; Yao, B.; Li, C.; Shi, G. An Improved Hummers Method for Eco-Friendly Synthesis of Graphene Oxide. *Carbon* **2013**, *64*, 225–229. https://doi.org/10.1016/j.carbon.2013.07.055.
(30) Wang, H.; Wang, Y.; Cao, X.; Feng, M.; Lan, G. Vibrational Properties of Graphene and Graphene Layers. *J. Raman Spectrosc.* **2009**, *40* (12), 1791–1796. https://doi.org/10.1002/jrs.2321.
(31) Kiang Chua, C.; Pumera, M. Chemical Reduction of Graphene Oxide: A Synthetic Chemistry Viewpoint. *Chem. Soc. Rev.* **2014**, *43* (1), 291–312. https://doi.org/10.1039/C3CS60303B.
(32) Ferrari, A. C.; Robertson, J. Interpretation of Raman Spectra of Disordered and Amorphous Carbon. *Phys. Rev. B* **2000**, *61* (20), 14095–14107. https://doi.org/10.1103/PhysRevB.61.14095.
(33) Pope, M. A.; Aksay, I. A. Four-Fold Increase in the Intrinsic Capacitance of Graphene through Functionalization and Lattice Disorder. *J. Phys. Chem. C* **2015**, *119* (35), 20369–20378. https://doi.org/10.1021/acs.jpcc.5b07521.
(34) Pan, D.; Zhang, J.; Li, Z.; Wu, M. Hydrothermal Route for Cutting Graphene Sheets into Blue-Luminescent Graphene Quantum Dots. *Adv. Mater.* **2010**, *22* (6), 734–738. https://doi.org/10.1002/adma.200902825.
(35) Arza, C. R.; Jannasch, P.; Maurer, F. H. J. Network Formation of Graphene Oxide in Poly(3-Hydroxybutyrate) Nanocomposites. *Eur. Polym. J.* **2014**, *59*, 262–269. https://doi.org/10.1016/j.eurpolymj.2014.07.035.
(36) Shen, Y.; Jing, T.; Ren, W.; Zhang, J.; Jiang, Z.-G.; Yu, Z.-Z.; Dasari, A. Chemical and Thermal Reduction of Graphene Oxide and Its Electrically Conductive Polylactic Acid Nanocomposites. *Compos. Sci. Technol.* **2012**, *72* (12), 1430–1435. https://doi.org/10.1016/j.compscitech.2012.05.018.
(37) Aboutalebi, S. H.; Gudarzi, M. M.; Zheng, Q. B.; Kim, J.-K. Spontaneous Formation of Liquid Crystals in Ultralarge Graphene Oxide Dispersions. *Adv. Funct. Mater.* **2011**, *21* (15), 2978–2988. https://doi.org/10.1002/adfm.201100448.
(38) Lin, X.; Shen, X.; Zheng, Q.; Yousefi, N.; Ye, L.; Mai, Y.-W.; Kim, J.-K. Fabrication of Highly-Aligned, Conductive, and Strong Graphene Papers Using Ultralarge Graphene Oxide Sheets. *ACS Nano* **2012**, *6* (12), 10708–10719. https://doi.org/10.1021/nn303904z.
(39) Su, C.-Y.; Xu, Y.; Zhang, W.; Zhao, J.; Tang, X.; Tsai, C.-H.; Li, L.-J. Electrical and Spectroscopic Characterizations of Ultra-Large Reduced Graphene Oxide Monolayers. *Chem. Mater.* **2009**, *21* (23), 5674–5680. https://doi.org/10.1021/cm902182y.

4. A Flexible Temperature Sensor Based on Biopolymer-Reduced Graphene Oxide Composite

Sensors were fabricated by drop-coating PHB-rGO composites onto printed silver electrodes, and the devices were characterized. Both neat samples of pressed rGO and composites were found to be negative temperature coefficient materials. Thermal mapping was demonstrated using 6 x 7 and 12 x 12 array of sensing elements (over a total area of 10 cm x 10 cm). The sensors were found to have good selectivity to temperature with respect to pressure and moisture.

A version of this chapter has been published in *Advanced Healthcare Materials* entitled, "Flexible and Stretchable Temperature Sensors Fabricated Using Solution-Processable Conductive Polymer Composites". The contents are reproduced here in accordance with the author's rights and copyright policies of the publisher, Wiley.

Flexible and Stretchable Temperature Sensors Fabricated Using Solution-Processable Conductive Polymer Composites

Li Dan, Anastasia Elias

Department of Chemical and Materials Engineering, University of Alberta,` Edmonton, AB T6G 1H9 Canada

4.1 Abstract

Accurate monitoring of physiological temperatures is important for the diagnosis and tracking of various medical conditions. This work presents the design, fabrication and characterization of simple and low-cost temperature sensors using conductive polymer composites (CPCs). These composites were formed using a high melting point biopolymer polyhydroxybutyrate (PHB) as the

matrix and the graphenic nanomaterial reduced graphene oxide (rGO) as the nanofiller (from 3 to 12 wt%), resuting in a material that exhibits a temperature-dependent resistivity. At room temperature the composites exhibited electrical percolation behavior; samples with 3 wt% (1.74 vol%) rGO exhibited the largest resistivity (80 Ω cm). Around the percolation threshold, both the carrier concentration and mobility were found to increase sharply. Sensors were fabricated by coating PHB-rGO composites onto printed silver electrodes, and the devices were characterized. The temperature coefficient of resistance was determined to be 0.018 /°C for pressed rGO powders and 0.008 /°C for the 3 wt% samples (which exhibited the highest responsivity of all compoisites). All samples underwent fast responses of less than 70 ms. The composites were found to have good selectivity to temperature with respect to pressure and moisture. Thermal mapping was demonstrated using up to 12 x 12 array of sensing elements.

Keywords: flexible temperature sensor, conductive polymer composites, reduced graphene oxide, mobility, direct ink writing, polyhydroxybutyrate (PHB)

4.2 Introduction

Temperature, a fundamental physical parameter, varies spatially and temporally.[1–3] Accurate measurement of localized temperature on biological tissues – even while undergoing deformation or dynamic movement – would be useful in disease diagnosis and monitoring.[4] Distinguishing signals from the surface of skin without impeding the users' movement or measuring temperature on a curved surface such as a forehead is unachievable in traditional, rigid contact sensing devices.[5–9] While infrared (IR) devices and thermal imaging cameras can provide fast results, a line of sight with the object must be maintained, and knowledge of the emissive properties of the surface are required. To monitor dynamic and spatial variations in temperature, many approaches have been reported on the development of flexible and stretchable sensors. One approach is to pattern

temperature responsive materials on sheet-like flexible substrates.[10–14] Responsive elements are comprised of metals (e.g. platinum, nickel, gold, copper, etc.) that exhibit a linear increase in resistance as a function of temperature.[15–18] This change in resistance results from the fact that as temperature increases, so to do the number of collisions/scattering events between electrons and phonons. This behaviour can be described numerically by the *temperature coefficient of resistance* (TCR), which is defined as the relative change in resistance per degree Celsius change in temperature. Typical TCR values for metals fall in the range of 0.003 to 0.006 /°C, where higher values correspond to higher sensitivity. Substrate properties are also important; in addition to providing mechanical stability and flexibility, the total thermal mass of the device must be small to avoid interfering with measurements. Thin polymer sheets or films are therefore often used, including polyimide, elastomers, polyethylene terephthalate (PET), fabrics, etc.[12,19–22] For example, Rogers and coworkers designed platinum (Pt) patterns on the surface of Kapton^{TN} (polyimide) tape with a measurable range of 20 to 100 °C.[23] This Pt sensor is flexible, highly accurate, and resistant to oxidation; though Pt is quite expensive and difficult to process. An alternative metal is nickel (Ni), which has the highest known TCR amongst metals (0.006 /°C), and – like Pt – is processed using the standard microfabrication techniques of sputtering and lithography. [18]

Recently, electrically conductive polymer composites (CPCs) have been implemented as stimuli-response materials that undergo a measurable change in electrical properties (e.g. resistance, capacitance etc.) upon exposure to the stimulus of interest.[24–28] In these composites systems, conducting nanoparticles (e.g. carbon-based materials or metal particles) impart electrical conductivity to the composite, while the polymer matrix (which is typically insulating) provides mechanical stability.[29–31] At low concentration the composite may be non-conductive, however when the loading of nanomaterials is increased beyond a certain threshold the resistance may drop

abruptly. The particular filler content at which this change occurs is called the electrical percolation threshold. One advantageous property of CPCs is that they are compatible with printing techniques including direct ink writing (DIW), 3D printing, and screen printing, and may therefore be patterned without the use of photolithography. [32–35]

In a CPC, either the polymer or nanofiller (or a combination thereof) may act as the sensing element that responds to changes in temperature. For example, the polymer may expand upon heating, increasing the separation between the conductive particles, leading to an increase in resistance (indicating that the material has a positive temperature coefficient, PTC).[36] If the material composition is initially near the percolation threshold, the resistance can increase by several orders of magnitude upon heating.[37] Thus PTC-type temperature sensors have been intensively used in overheat protection and self-controlled heating.[38] The responsivity of a CPC may also result from the temperature-dependent properties of the nanofiller, some of which undergo a decrease in resistivity as a function of temperature (corresponding to a negative temperature coefficient, NTC). However, even if the filler undergoes a decrease in resistivity as temperature increases, the composite itself may have a PTC overall due to the thermal expansion of the polymer.[29,39] These competing effects can result in low or non-linear temperature-dependent electrical behaviour. To address these problems, one approach is to add large-aspect ratio fillers, which could create more electrical contacts, minimizing the effect brought from volume expansion under heating. For instance, Chu et al. compared the sensing performance of low and high aspect ratio carbon nanotube(CNT) /polydimethylsiloxane (PDMS) composites and found that composites formed with high aspect ratio CNTs underwent larger drops in resistance upon heating than composites formed with low aspect ratio CNTs; the authors hypothesized that the longer (higher aspect ratio) CNTs were able to maintain a more connected network upon thermal

expansion of the PDMS than the shorter (lower aspect ratio) CNTs.[40] In 2018, an NTC material was engineered by forming a foam of a CPC (carbon black/chlorinated poly(propylene carbonate)).[41] When this porous material was heated, the expansion of the gas trapped in the pores resulted in the compression of the walls, causing a reversible increase in conductivity (as measured from 20 °C to 70 °C). However, the behaviour of the material under mechanical deformation was not studied. Overall, very few polymer NTC materials with favorable sensing performance near body temperature have been illustrated.

Reduced graphene oxide (rGO) – a graphenic material synthesized by thermal or chemical reduction of exfoliated graphene oxide (GO) – has been used in composites due to its large surface area and favourable electrical properties (relatively good electrical conductivity, high charge carrier mobility, and large carrier density). Pressed powders of rGO have a NTC, as the number of charge carriers increases with temperature, resulting in a reduction in resistance.[42] However, these sheets tend to be very brittle and delicate, and therefore are not desirable for use in deformable sensors.[43] Furthermore, a variety of chemical sensors have been implemented that leverage the change in conductivity that occurs when a gaseous analyte (such as water vapor) interacts with the surface of rGO [44,45] suggesting that rGO-based sensors may not have good selectivity for temperature. The mechanical properties of rGO can be improved through the formation of a composite; likewise, embedding rGO in a polymer with limited permeability could reduce interference from undesired analytes such as water vapor. For example, Lee et al. reported a gated rGO/polyurethane composite temperature sensor fabricated using standard lithographic techniques. Their sensor array showed up to 0.001/ sensitivity, and can be mounted on skin to monitor human temperature.[46] However the sensor is sensitive to mechanical deformation, costly due to the complexity of lithographic fabrication, and exhibits relatively low sensitivity.

To engineer a highly responsive CPC based on rGO, the properties of the matrix must be carefully selected. A small thermal expansion coefficient is key to ensuring that the response of the material is dominated by the temperature-dependent properties of the rGO rather than by the thermal expansion of the polymer. In this work, we engineer rGO polymer composites for use in wearable temperature sensors utilizing a polymer matrix with low thermal expansion, high thermal stability, and good resistance to moisture: polyhydroxybutyrate (PHB). PHB is a biopolymer produced by bacteria that is biocompatible.[47,48] The thermal expansion coefficient of PHB (40 μm/mK) is relatively low compared to polyester (125 μm/mK), polyethylene (PE) (200 μm/mK), and polyethylene terephthalate (PET) (59.4 μm/mK).[49] PHB has a high melting temeprature (175 °C), which should enable stability over a wide range of temperatures.[50] PHB is also highly hydrophobic, which should make PHB-based devices and composites resistant to water. [48] Finally, PHB is soluble in chloroform and boiling acetic acid, enabling solutions to be formed that can be patterned using various printing techniques. In our previous work we compared the chemical and physical properties of PHB/rGO composites prepared using three different reducing agents, and found that – at room temperature – composites prepared using L-ascorbic acid by an in situ reduction method demonstrated very low percolation thresholds (0.1 vol%) and with relatively high conductivity at 8 % loading. The excellent dispersion of these materials was shown using x-ray diffraction (XRD). [48]

In this work, we investigate the suitability of a solution-processible polymer-reduced graphene oxide composite as a temperature-sensing material, and then manufacture and characterize printed devices incorporating this material. The responsive composite is formed from PHB matrix and sheet-like nanofiller (reduced graphene oxide (rGO)) with large lateral dimensions (40 to 50 μm). These composites are non-toxic and solution-processable. We first examine the temperature-

dependent electrical properties of the CPCs, for comparison against neat rGO. The physical, electrical and mechanical properties of composites with rGO loadings of 3 wt% to 12 wt% are systematically investigated. To explore the percolation behavior of the materials, in addition to the typical characterization of conductivity, both the mobility and charge carrier density of the samples at various filler loading are measured. To demonstrate the manufacturability of the materials, temperature sensing devices are fabricate by drop-casting rGO-PHB solutions on the surface of inkjet printed silver electrodes, and the temperature response, durability, stability, and water-resistance of the devices are characterized. An array of devices (6 x 7, 12 x 12) are printed on a flexible substrate, and used to map the temperature profile of an object. To demosntrate that the PHB/rGO composites can be used in mechanically flexible temperature sensors, both thin, stretchable elastomeric substrates and functional meandering composite lines are printed by DIW. High adhesion is achieved between the active layer and the substrate, and the resulting devices can withstand strain while undergoing only a small change in resistance. As a proof-of-concept, the printed devices are then used to monitor temperature on the surface of skin.

4.3 Materials

PHB biopellets were purchased from Bulk Reef Supply, USA. The molecular weight was determined by Gel Permeation Chromatography (GPC) to be Mw: 190 kDa. The GPC method is described in our previous work.[51] Large scale graphite flakes were purchased from Alfa Aesar Inc. Sulfuric acid (98%), hydrogen peroxide (30%), phosphoric acid (98%), hydrochloric acid (37%) and potassium permanganate particles were purchased from Fisher Scientific, Canada and used as received. Glacial acetic acid (99 %), L-ascorbic acid (L-A.A) were provided from Sigma-Aldrich, Canada and used as received. Silver ink was purchased from AgIC Inc, Japan and poured directly into the cartridge for inkjet printing. Polyethylene terephthalate (PET) film (Melinex 516, 3 mil) and silver paste (Pelco silver paste (Ted Pella, Inc.)) were used as received. Polydimethylsiloxane

(Sylgard 184, Dow Corning) was purchased from Sigma-Aldrich and was mixed in the standard 10:1 ratio of elastomer: crosslinker prior to use.

4.4 Experimental

Preparation of GO slurry

To synthesize graphene oxide (GO), graphite sheets with large lateral size were oxidized using the improved Hummer's method.[52] In detail, sulfuric acid (360 ml)/phosphoric acid (40 ml) was mixed with 3 g of graphite. 18 g of potassium permanganate, an oxidizer, was then added drop-wise into the above mixture under continuous stirring with constant maintaining temperature of 45 ℃ for 16 h. The mixture was then allowed to cool to the room temperature before pouring the dispersion over 400 g of ice to quench the reaction. Hydrogen peroxide was slowly added drop-wise to the chilled solution until the dispersion turned a whitish yellow color. The slurry was separated from the acid by centrifugation and then re-suspended in water. The resulting GO was washed twice by hydrochloric acid and followed by three washes with ethanol and then kept in beaker for use.

Preparation of rGO/PHB composite ink

The composite rGO/PHB ink was prepared using an in situ reduction method described in our previous work, as illustrated in Figure 4.1.[48] Figure 4. 1 The entire setup for direct ink writing. In detail, a solvent exchange was performed to transfer aqueous GO slurry to acetic acid by centrifuging the slurry at 20,000 rpm for 10 min and then replacing the solution with acetic acid (twice), ultimately forming a solution with a concentration of 1 mg/ml. The mixture was brought to a boil, and roughly 0.04 g of PHB pellets was added to act as a stabilizer; L-A.A was then added to the suspension (2:1 weight ratio, L-A.A:GO) under vigorous stirring and continuous heating at 118 ℃ for 2 hrs. No purification step was needed to remove the L-A.A. The desired proportion of

PHB was dissolved in A.A solution to form a homogeneous mixture at 118 ℃. The resulted black suspension was cooled to room temperature and kept in beaker for further use with no visible agglomeration. To fabricate temperature sensors, the composite ink was shaken well and a drop was dispensed onto the printed electrodes on a 140 ℃ hotplate. Substrate heating continued until all the solvent was evaporated (when the ink formed a visibly shiny and smooth surface, typically around 1 min).

To convert the weight fraction to volume fraction, both density of rGO and PHB were used, with a value of 2.2 g/cm^3 and 1.25 g/cm^3, respectively. These values were input into the following equation: $vol\ \% = \frac{\mathrm{A}/2.2\ (g/cm^3)}{\frac{\mathrm{A}}{2.2(g/cm^3)}+\frac{B}{1.25(g/cm^3)}} \times 100\ \%$, where A is the mass (g) of nanofiller, B is the mass (g) of the PHB matrix (0.5 g). For example, 3 wt % rGO loading equals to 1.74 vol% loading.

Preparation of rGO compressed powder

GO was reduced by L-ascorbic acid using the same method as for the composite preperation except that PHB was not added to the acetic acid solution. In detail, the centrifudged GO (20,000 rpm, 10 min) was dipensed in A.A solution with a concentration of 1mg/ml. The mixture was stirred continuously (200 rpm/min) on hot plate at the boiling point of A.A. Then, the L-A.A was added to the mixture with the weight ratio of 2:1 to GO, and the reduction process proceeded for 2 hrs under boiling. The resulting black suspension was washed by water three times and then dried in oven (80 ℃) overnight. The dried powder was compressed into films on hot compressor at a pressure of 25 GPa without adding heat. The entire setup for direct ink writing, shown in Figure 4.2.

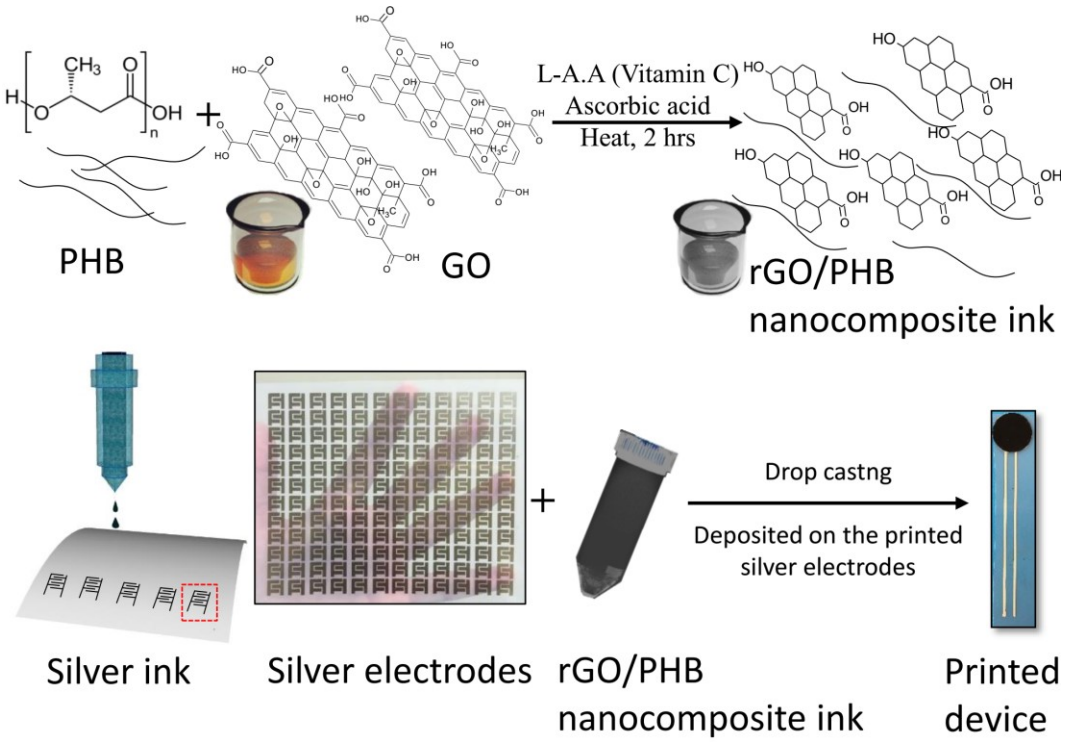

Figure 4.1 PHB and reduced graphene oxide (rGO) composites sythesis method and sensor fabrication through direct ink printing (μm thickness).

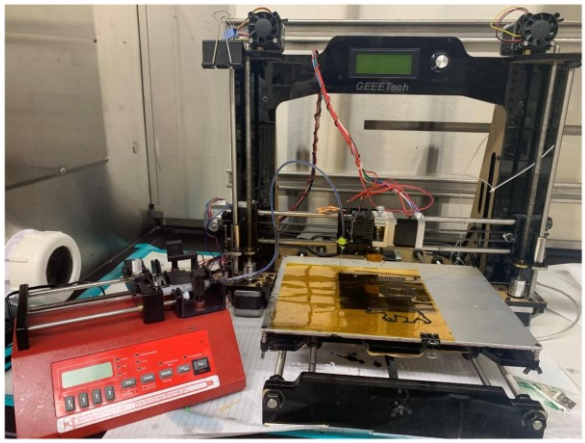

Figure 4.2 The entire setup for direct ink writing.

Preparation of silver electrodes

The branched electrodes were designed with the software SketchUp and printed using an office printer (Epson 2700) on glossy polyethylene terehthalate (PET) paper. No heat treatment was needed for the silver electrodes.

4.5 Characterization

Morphology

A Zeiss Sigma 300 VP field emission scanning electron microscope (FE-SEM, Cambridge, UK) was used to observe the cross-sectional images of samples. A thin layer of gold (10 nm) was deposited onto the sample by using Denton sputter (DVISJ/24LL, Denton Vacuum, USA) to avoid surface charging during SEM observation. The images were collected using the secondary electron (SE) mode with a voltage of 3 kV. Cross-sectional images were obtained by fracture frozen samples under liquid nitrogen for SEM imaging. To prepare samples for optical microscope, composites were microtomed to slices 200 µm thick and mounted on glass slides. A Celestron 400x optical microscope (Laboratory Biological Microscope Inc., Canada) was used to investigate the micromtomed surfaces. Figure 4. 3 Optical images of microtomed cross-sectional composite samples with varying wt % loading of rGO.

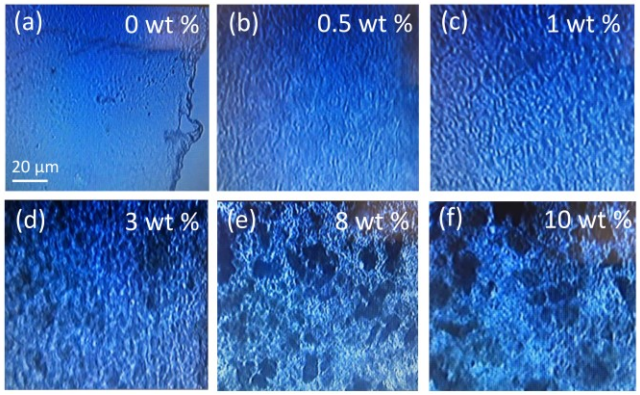

Figure 4.3 Optical images of microtomed cross-sectional composite samples with varying wt % loading of rGO.

Resistance measurement

The resistance of patterned sensors was was measured as a function of temperature using a homemade setup. A Peltier thermoelectric stage (Adcol, China) with voltage supply source was used as a heating source. The temperature was varied from -10 to 100 ℃, at heating rate of roughly 1 ℃/min. Samples were mounted on the centre area of the Peltier stage and looesely covered by cotton pads to avoid heat loss. The samples were connected by Al wires to a source meter (Keithley 2401, USA), which supplied a voltage of 1 V; the resistance of each individual sensor was recorded serially as the temperature was varied.

Conductivity and mobility measurement

The in-plane conductivity, mobility, charge carrier density, and Hall voltage of both pressed rGO powder and composite films were determined by ACCENT HL5500 Hall System at room temperature using the van der Pauw method. Films were prepared with a thickness of 80 µm and cut into 7 mm × 7 mm squares. Contacts were defined at each of the four corners of the sample

using a layer of silver paste followed by aluminum electrodes to which wires were connected. Photographs of the setup and sample configuration are shown in Fig. 4.4. During measurement, a magnetic field (0.325 T) was applied perpendicular to the plane of the film, and current (0.1 μA for highly resistive materials to 0.1 mA for less resistive materials) was applied between two of the electrodes at opposite corners while the voltage was measured between the remaining two electrodes.

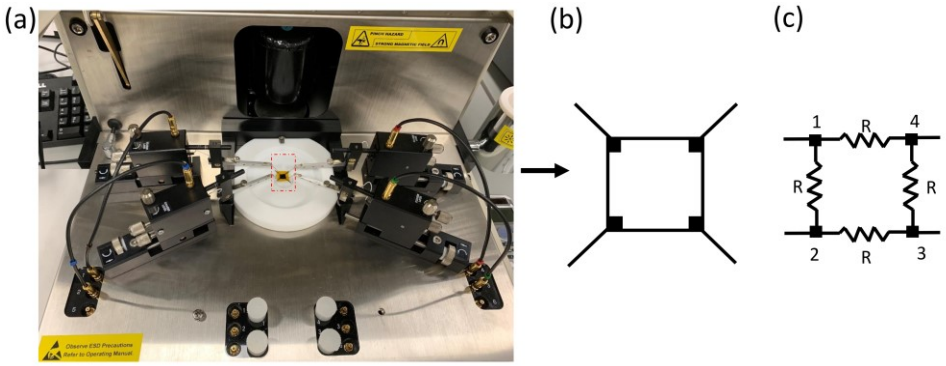

Figure 4.4 Hall effect measurement setup: (a) sample characterization with four electrodes underneath (b), schematic depicting the location of the four electrodes on the square sample and the measurement principle.

Mechanical properties

An Instron 5943 tensile tester (Instron, Norwood, MA, USA) equiped with a 1 kN load cell was used to investigate the mechanical properties. Compressions tests were performed on all devices to test the cyclability. Samples were fixed on the center of compression flaten, and rod with a flat, circular end (diameter 10 mm) was clamped with the top set of clamps to apply a load. A constant load of 40 kPa was applied at a rate of 0.5 mm/min. Bending tests were performed by fixing one end of a sample to a stationary holder while using a linear motor to displace the other end. During

compression and bending tests, electrodes were connected to the Keithley 2401 so that resistance data could be recorded.

Statistical Analysis

The sensitivity value were displayed as the mean stand ± standard deviation (SD). Sample number were for $n \geq 3$ per group. Statistical calculations were utilized by one-way analysis of variance (ANOVA), followed by student's t-test was utilized to determine the statistical significance of resistivity data for each type composites. The statistical significance was determined as $P < 0.05$. (Figure 4.5)

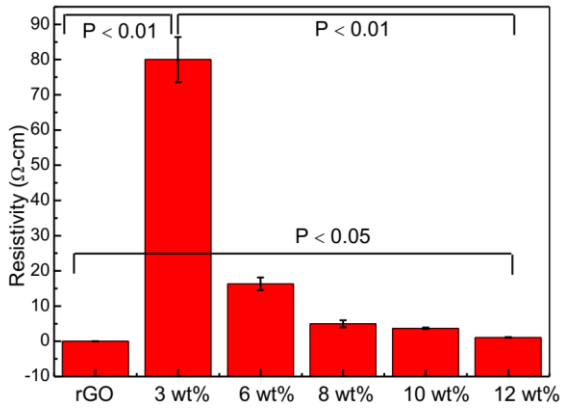

Figure 4.5 Significance values of resistivity data for rGO and each composite.

4.6 Results and Discussion

Morphoplogy of rGO/PHB composites

To investigate the cross-sectional morphologies of plain PHB and composites, samples were imaged using both scanning electron microscopy and transmission electron microscopy, and the results were shown in Figure 4.6. For neat PHB and samples with lower concentrations of rGO (1 wt% and 2 wt%), relatively homogeneous fracture surfaces were observed by SEM. However, at

these low concentration values, rGO was difficult to observe in the SEM images. At higher concentrations of rGO (3 wt% and above) the fractured surface appeared increasingly brittle, and the rGO flakes (indicated by dashed squares) were visible and appeared randomly distributed in the matrix. The observed change in the brittleness of the fractured surface suggests that the presence of the rGO impedes the deformation of the polymer under elongation. The optical images of microtomed surfaces of the composites are shown in Figure 4.3, and these images indicated a similar trend as the SEM images, where rGO sheets were randomly distributed through the PHB matrix with no visible large agglomerations of filler. These results confirmed that the rGO was well-distributed in the polymer matrix.

To better observe the dispersion of rGO inside PHB matrix, TEM was used to image a 1 wt% composite sample that was microtomed to 200 nm in thickness. In Figure 46 (d), fairly uniformly distributed wrinkles (dark grey in color) are visible in the polymer matrix (light grey). At higher magnification (Figure 4.6 (h) the wrinkles appear to be rGO sheets. Overall, a relatively good rGO dispersion was achieved in the composite material, although some rGO agglomeration can be seen.

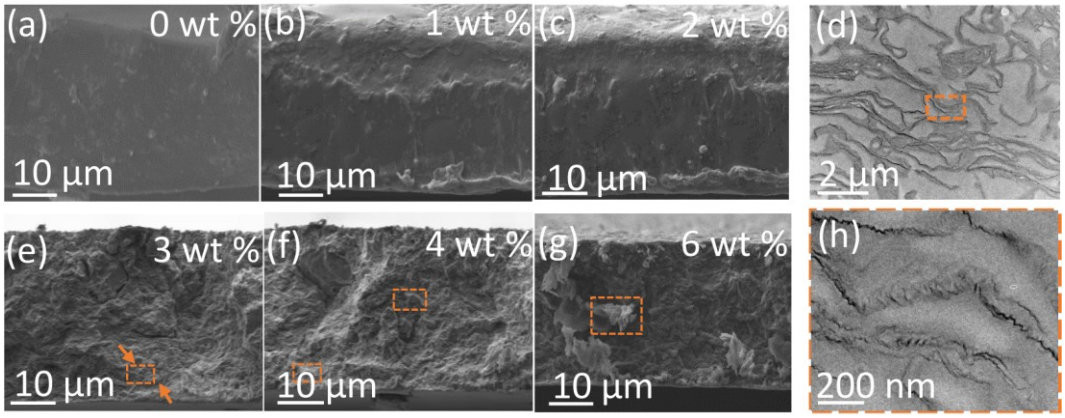

Figure 4. 6 Side view SEM micrographs of cleaved samples of plain PHB (a), and 1 wt%, 2 wt%, 3 wt%, 4 wt%, 6 wt% composites are in (b), (c), (e), (f), (g), respectively. Boxes identify rGO flakes. TEM images of 1 wt% 200 nm thick sample in (d) and (h).

Electrical Testing

The resistivity of a neat, hard-pressed film of rGO powder was investigated as the sample was heated from 20 °C to 70 °C (Figure 4.7). As shown in Figure 4.8, the normalized resistance $(R_0-R)/R_0$ underwent a decrease as a function of temperature, indicating that the material has a NTC. A non-linear relationship was observed, which is consistent with previous measurements in the literature, which have been shown to follow an Arrhenius-like dependence on temperature, consistent with a model in which the bandgap of the rGO dominates the temperature-dependent charge transport behavior. [53,53,54] The TCR over the range of measurement was calculated to be –0.0184 /°C from 20 to 60 °C , the absolute value of which is much higher than for Nickel (0.006 /°C), indicating that the material is quite sensitive to temperature. These results suggested that rGO material is capable of making good temperature sensor.

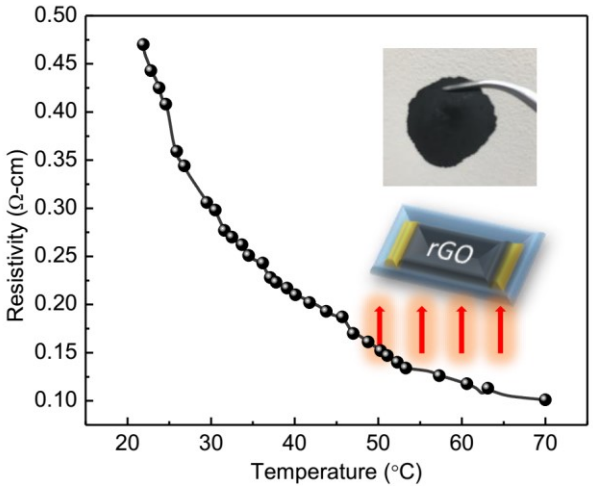

Figure 4.7 The resistivity vs. temperature curve of compressed rGO powder.

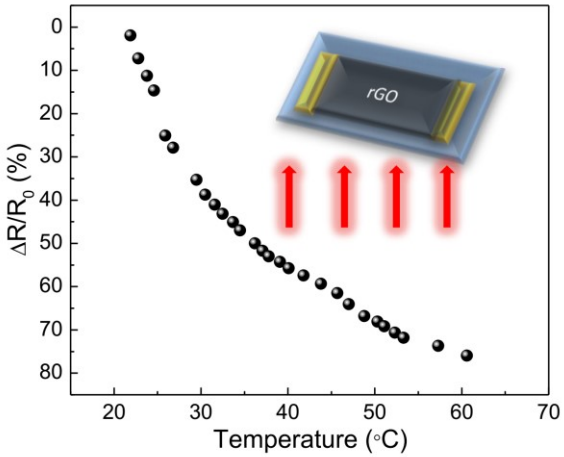

Figure 4.8 Normalized resistance change upon varying temperature on the pure compressed rGO sample (as measured in the direction parallel to the plane).

To investigte the mechanism of charge transfer in the materials, the temperature-dependent I-V characteristics of both neat, pressed rGO powder and 3 wt% composite were characterized from 20 ℃ to 70 ℃ (Figure 4.9). Figure 4.10 Relative resistance change of composites and the rGO. As the voltage was swept from -5 to +5 V, a linear and symmetric response was observed for both types of samples. This linear relationship indicates that both pressed rGO pattern and rGO-PHB

composites exhibited ohmic behavior at a given temperature. In addition, the higher current seen at a given voltage for a higher temperature indicated that the resistance of the sample decreased as the temeprature increased, due either to a change in the number of charge carriers or a change in carrier mobility, or due to a synergistic combination of the two. No obvious lag or hysterious was observed in any of the measurements, showing that fast response of composites to the external temperature change.

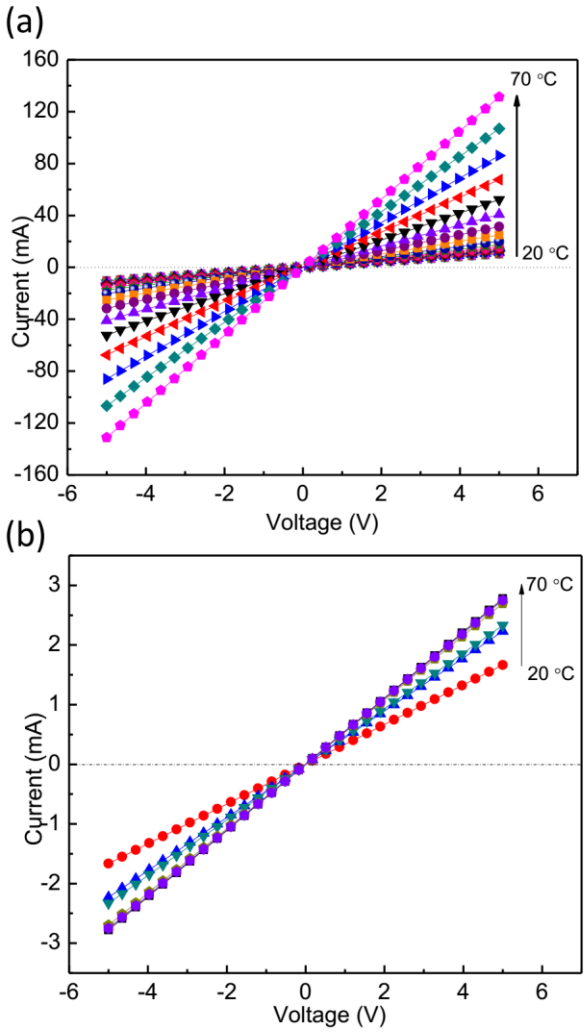

Figure 4.9 I-V curves (-5 to 5 V) of rGO compressed sample (a) and 3 wt% (1.73 vol%) composite (b) with varying temperature (20 to 70 °C).

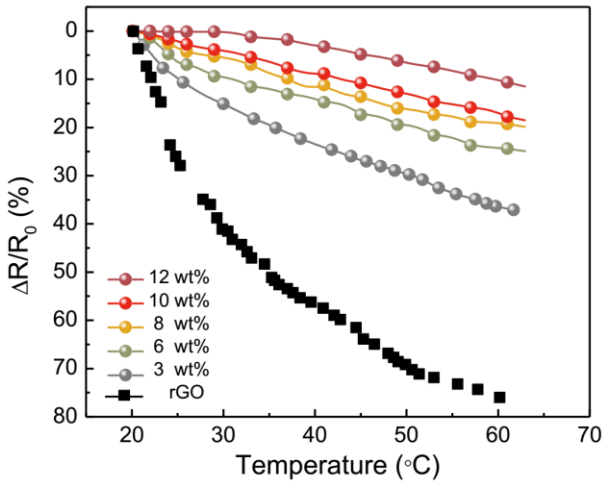

Figure 4.10 Normalized relative resistance change of composites and the rGO.

The electrical conductivity of nanocomposites with different rGO concentration was measured by electrometer model 6517A (resistivity > 10^4 Ω cm), and four point probe method (Kelvin sensing), and the results are shown in Figure 4.11 a. The conductivity of plain PHB was measured to be 10^{-15} S/cm (indicating that it is highly insulating); composites with very low loading of rGO also exhibited very low conductivity. As the loading of rGO increased past 0.56 vol% (around 1 wt%), the conductivity rose sharply to 10^{-5} S/cm. This increase of 10 orders of magnitude can be explained using percolation theory, where a fully conductive network forms when a threshold volume fraction is reached. This effect can be described by the electrical percolation theory equation, $\sigma_c = \sigma_f[(\emptyset - \emptyset_c)/(1 - \emptyset_c)]^t$; where σ_f is the intrinsic conductivity of nanofiller (here, rGO), $\emptyset$ is the volume concentraion of filler, $\emptyset_c$ is the concentration of nanofiller at the percolation threshold, and t is the critical exponent (calculated by fitting the curve). To report conductivity measurements, the mass fraction of each rGO concentraion was converted to volume fraction based on the densities of PHB and rGO (as described in the Experimental Section). In our system, the measured percolation threshold was determined to be 0.56 vol% (around 1 wt%), which is a very low value reported in rGO-based nanocomposites. This is due to the large aspect

ratio of the rGO achieved using our in situ reduction process of rGO, which resulted in a relatively high intrinsic conductivity (10^2 S/cm). A rapid increase in the plane electrical conductivity was observed as increasing the concentration of rGO filler (Figure 4.11 a). The critical exponent *t* was derived from linear fitting of the log σ_c vs. $(\emptyset - \emptyset_c)/(1 - \emptyset_c)$ data (shown inset in Figure 4.11 a, and was found to be 3.39 ± 0.38. For three dimensional networks, *t* has been predicted to be between 1.65 and 2,[202] while for 2D networks *t* is expected to be 1.33. [56] A larger *t* suggests larger size of the clusters inside the polymer matrix. [57–59] Values larger than 2 have been determined experimentally for conductive composites formed from materials such as multiwalled carbon nanotubes in poly(methyl methacrylate) ($t = 2.34 \pm 0.19$ [55]); solvothermally reduced graphene oxide polyvinylidene fluoride ($t = 2.64$ [60]) and emulsion mixing of graphene and polycarbonate ($t = 4.18$ [61]). These different values of the critical exponent *t* are dependent not only on the dimensionality of the filler but on the physical characteristics – including size and orientation of the conductive filler.

The Hall mobility and charge carrier density of the composites were measured using the Van der Pauw method, and the results are shown in Figure 4.11b and c. As expected, the charge carriers were determined to be electrons based on the polarity of the measured voltage. These data showed that both mobility and number of carriers increased with increasing the rGO filler content, and significant changes in each of these properties occured near the same vol% loading as for the changes in conductivity (~0.56 vol%). The Hall effect measurements of the composites suggested that mobility and the number of carriers are highly influenced by the addition of the nanofiller. Both of these properties increased significantly above the percolation threshold (0.56 vol%) and increased steadily with the relative high loading of rGO filler in the polymer. The rGO mobility determined here (2100 ± 566 cm^2/Vs) is one order of magnitude higher than reported for other

rGO.[43] This increase can be attributed to the effectiveness of our in-situ solution-based processing route. We found the charge carrier density can be broadly fit in the threshold equation: $n_c = n_f[(\emptyset - \emptyset_c)/(1 - \emptyset_c)]^t$, where n_c is the composite charge carrier density, n_f is the carrier density of nanofiller (here is the rGO, 10^{16} cm^{-2}), where the rest of the parameters are the same as electrical threshold.

Below the electrical percolation threshold, both mobility (< 10^{-3} cm^2/Vs) and charge carrier density (< 10^6 cm^{-2}) were very low, thus resulting in high electrical resistivity (> MΩ cm). Once the filler content was close to the electrical threshold (e.g. 3 wt% or .056 vol % rGO), although the carrier density was still low, the mobility increased around 4 orders of magnitude to 1 cm^2/Vs; thereby increasing the overall conductivity.

As was seen in Figure 4.11, inreasing the temperature either a pressed rGO powder or a 3wt% rGO-polymer composites results in an increase in conductivity. As we were unable to perform Van der Pauw measurements at elevated temperatures, we were unable to directly determine whether this effect was due to an increase in the number of charge carriers or an increase in carrier mobility. However, in general, the mobility of the charge carriers is expected to decline as a funciton of temperature due to an increase in phonon scattering. [62] This suggested that there must be an increase in the number of carriers as the temperature increases.

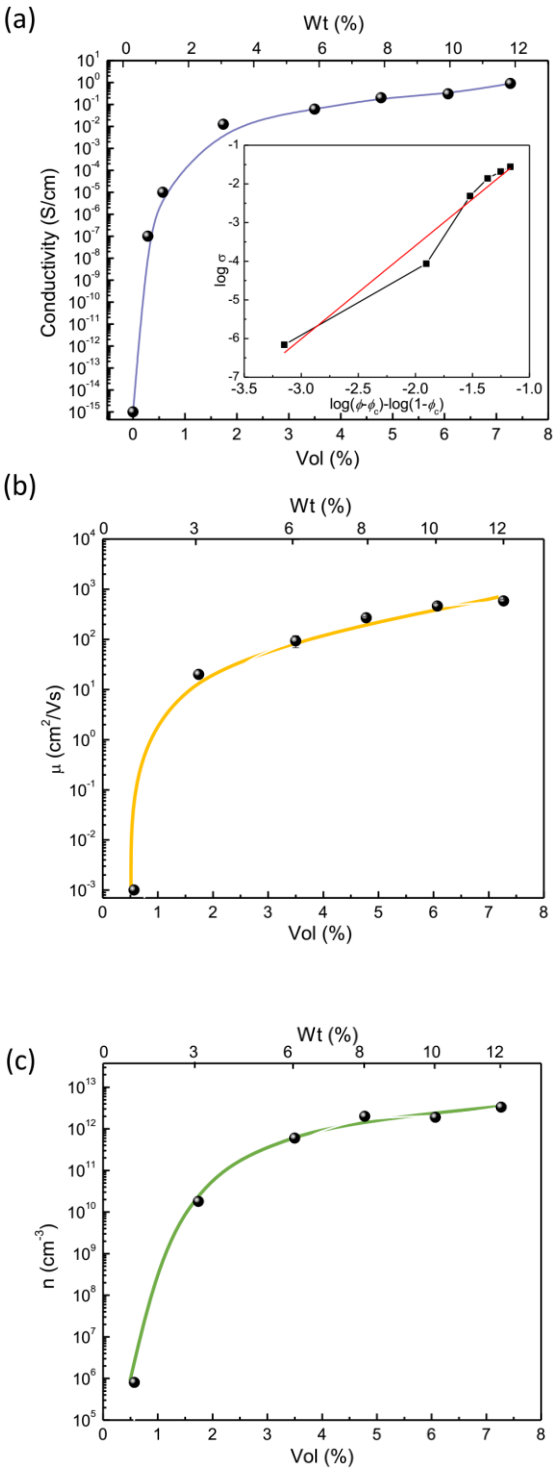

Figure 4.11 (a) Conductivity vs. volume fraction of the composites at room temperature, and the inside graph is the fitting curve for calculating the critical exponent (t). (b) and (c) are mobility and charge carrier density change as a function of rGO volume fraction, respectively.

The change in relative resistance as a function of temperature was explored for devices consisting of rGO-PHB composites of varying composition drop-coated on printed silver electrodes. Relative resistance was measured from room temperature to 70 °C, and the results are shown in Fig 4.12. Like the pure rGO sample, the resistance of all devices decreases with temperature, exhibting a NTC effect. Among these devices, those fabricated wtih the 3 wt% composite uderwent the largest change in relative resistance upon heating (-0.008 /°C), with TCR values of -0.006 /°C, -0.005 /°C, -0.004 /°C, -0.003 /°C for devices made using 6, 8, 10, and 12 wt% composites, respectively. The resistivity and calculated TCR values were summarized in Table 4.1.

The device made using the 3 wt% composite, exhibited the highest absolute TCR value. The 3 wt% composite is the closest to the percolation threshold, which should make it the most sensitive to variations in rGO loading: our results show that this sample is also the most sensitive to changes in temperature. Samples which are further below the threshold – such as 1 wt% and 2 wt% rGO-PHB composites – show high resistivity at room temperature, and this value changes little as temperature increases (data not shown). Similarly, samples with rGO content well above the percolation threshold (e.g. 10 wt% and 12 wt%) have relatively low resistivity at room temperature, and the resistivity of these composites varies little with temperature, despite the fact that the number of charge carriers in the rGO itself increases with temperature (as discussed above). This suggests there the mobility of the composite as a whole is more restricted at elevated temperatures at higher wt% rGO loadings than for lower wt % rGO loadings.

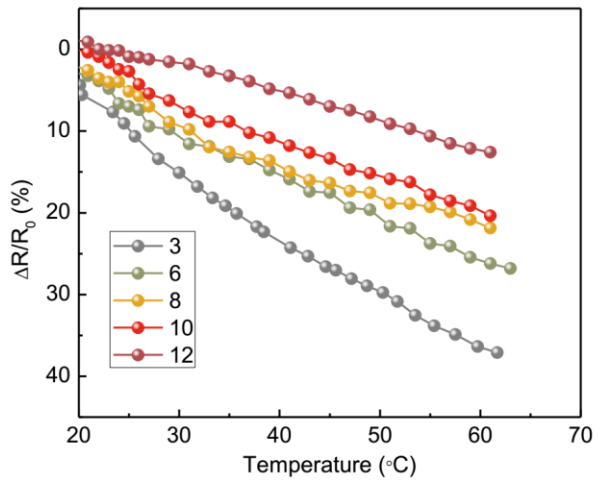

Figure 4.12 Relative resistance change (20 to 65 °C) under temperature scan for different composite samples (i.e. 3 wt%, 6 wt%, 8 wt%, 10 wt%, 12 wt%).

Table 4.1 TCR and resistivity values for compressed rGO and different concentration composites.

Material	TCR value (/°C)	Resistivity (Ω-cm)
rGO	- 0.018	$(1.1 \pm 0.2) \times 10^{-2}$
3 wt% Composites	- 0.008	80 ± 6.4
6 wt% Composites	- 0.006	16.3 ± 1.8
8 wt% Composites	- 0.005	5 ± 1.0
10 wt% Composites	- 0.005	3.7 ± 0.2
12 wt% Composites	- 0.003	1.1 ± 0.1

Drop-coated devices incorporating both neat rGO (without PHB) and composites films were also subjected to cyclic changes in temperature as their resistance was monitored and the results are shown in Fig 4.13. The devices were heated from room temperature to a peak temperature of 30 °C, kept at the peak temperature for 5 min, and then cooled to the room temperature; similar heating cycles were subsequently applied to peak temperatures of 40 °C and 50 °C. During each heating

cycle the absolute relative resistance of each device increased; upon cooling the resistance of each device returned to its initial value. As in the previous characterization the devices constructed with pure rGO exhibited the highest response (largest change in relative resistance), followed by devices fabricated using 3 wt%, 6 wt%, 8 wt%, 10 wt%, 12 wt% composites. For example, the sensitivity of rGO sample at 30 °C was almost double than the 8 wt% sample. The 3 wt%, critical filler content near threshold, had the highest $(R_0\text{-}R)/R_0$ among composites in each temperature step. Although 12 wt% had the lowest $(R_0\text{-}R)/R_0$ values, the overall resistance measured from instrument was quite stable with no obvious fluctuations (very narrow error bars). This is an important point considering for real applications.

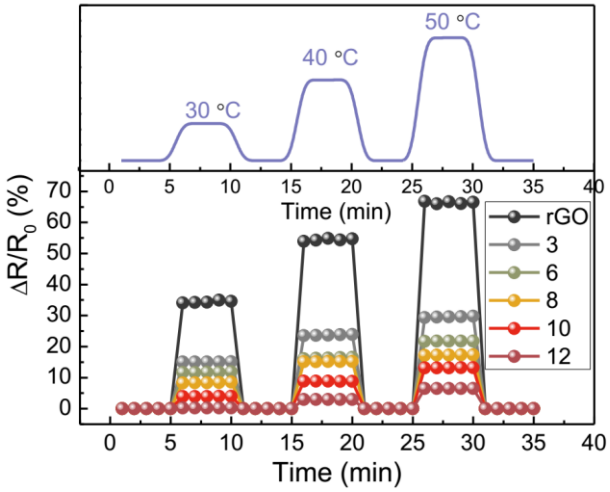

Figure 4.13 Temperature step measurement (30, 40, 50 °C) on rGO and rGO-PHB composite devices. The heating profile is shown in the top portion of the figure, while the relative change in resistance of the various samples is plotted below.

Selectivity is an important characteristic of a sensor. To determine whether the materials are responsive to pressure and humidity, the resistivity of a set of rGO-PHB composite devices were characterized during cyclic compression, bending, and upon exposure to water. Figure 4.14 A

typical 8 wt% composite (a) on Kapton substrate, (b) under bending (tensile strain) and (c) under bending (compressive strain). (d) A pressed rGO sample after bending. To fabricate functional devices, a responsive composite with high sensitivity (i.e. high TCR) and low resistivity (to achieve a more stable signal and to minimize ohmic heating during measurement) was desired. To balance these characteristics, the 6 wt% and 8 wt% composites were therefore selected for device fabrication and selectivity testing; as was summarized in Table 4.1, these material showed intermediate TCR values comparable to those of bulk nickel (-0.006 /°C and -0.005 /°C, for the 6 wt% and 8 wt% materials, respectively. Nickel: 0.006 /°C), and also exhibited relatively low resistivity at room temperature (16. 3 ± 1.0 Ω-cm and 5 ± 1.0 Ω-cm for the 6 wt% and 8 wt % materials, respectively).

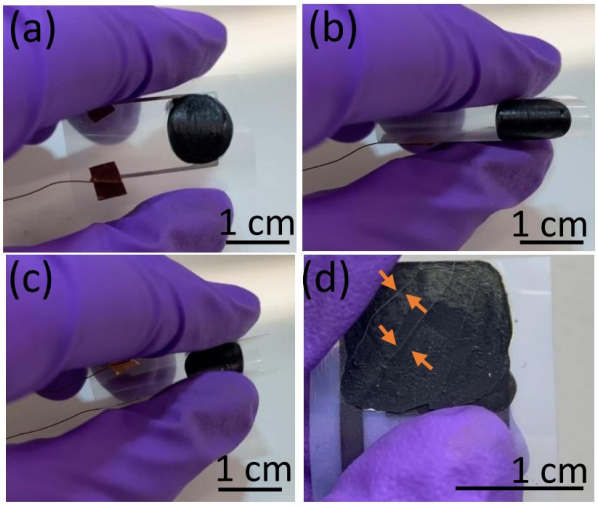

Figure 4.14 A typical 8 wt% composite (a) on Kapton substrate, (b) under bending (tensile strain) and (c) under bending (compressive strain). (d) A pressed rGO sample after bending.

The resistance of pressed rGO , 6 wt% and 8 wt% rGO-PHB devices were characterized upon exposure to water vapor (Figures 4.15). While the relative resistance of the composite remained

fairly constant, the resistanceof the pressed rGO increased by over 100% as the relative humidity was varied from 20 % to 90 %. The relative resistance of the composite film was further tested during immersion in water as the temperature was cycled to 80 °C (Figures 4.15 (b) and 4.15 (c)). The results were highly repeatable, showing the stability of the measurements even upon immersion in water. Overall, these results suggest that the drop-cast film devices are almost inert to the external pressure, moisture and gave stable response over cyclic measurement, but are sensitive to the mechanical deformation (bending). This indicates that care should therefore be taken to calibrate and operate devices at a relatively fixed radius of curvature. Stretching was not investigated for any of these devices as the PET substrate is not itself able to undergo a significant elongation before break.

The response of the 8 wt% composite to compression and bending are shown in Figure 4.16. The relative resistance change over 1600 cycles of cyclic compression (loading and unloading test) (20 kPa), are shown in Figure 4.16 (a), and the set-up for the compression test is shown in Figure 4.16(b). Only a small change in relative resistance is observed, indicationg that the device is relatively stable in compression. When the samples undergo bending, the relative resistance changes by up to 25 % over an applied tensile strain of 3 % (Figure 4.16 (c) and (d)). Similar results were observed for the 6 wt% samples, undergoing a change in relative resistance of up to 23% over an applied tensile strain of 3 % (results not shown).

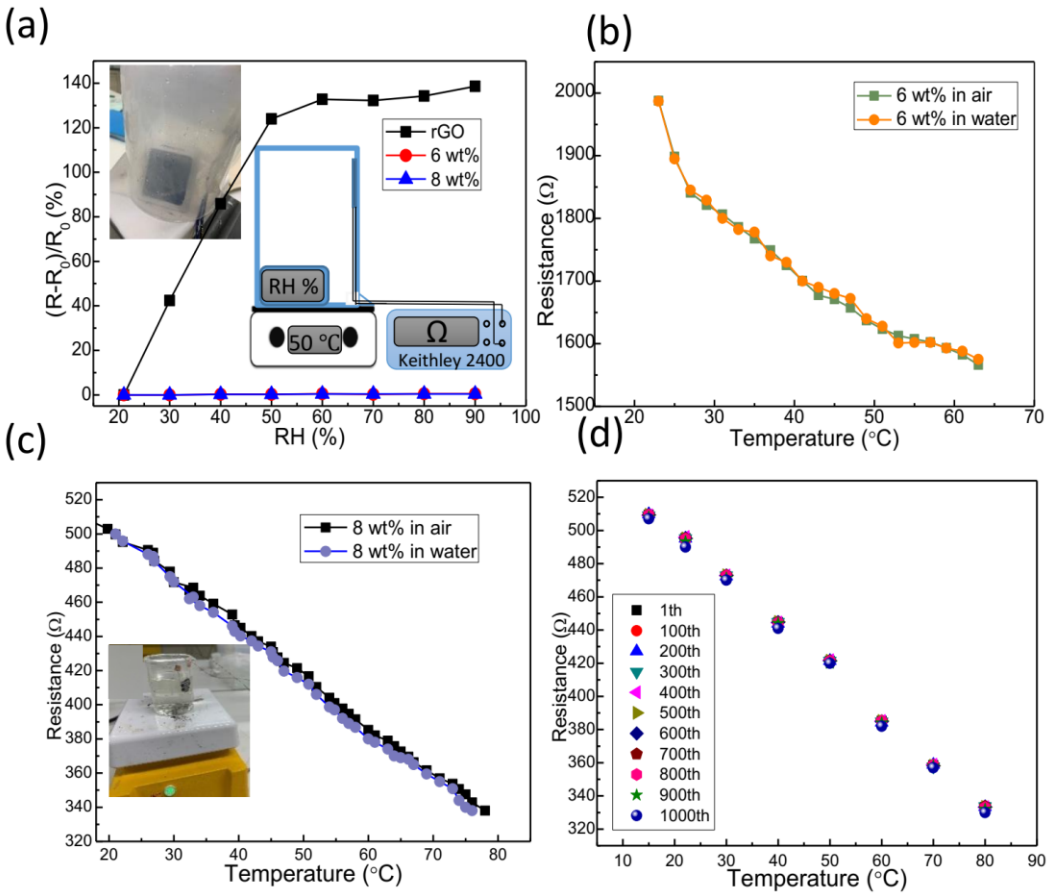

Figure 4.15 (a) Humidty tests: Relative resistance change of rGO and 6 wt% and 8 wt% drop-casting device upon varying the relative humidity. The top inset picture shows the setup of the humidity measurement, where sample was fixed on top side of the big container and the humidity reader (ThermoPro TP-60) was placed inside the beaker. The bottom picture gave the setup and data aquisition illustration. (b) and (c) are resistance of the device while immersed in water as the temperature was increased to 80 °C and then reduced to 20 °C in 6 wt% and 8 wt% drop-casting devices. (d) 1000 cyclic repetitions of the water immersion test for 8 wt% drop-casting device.

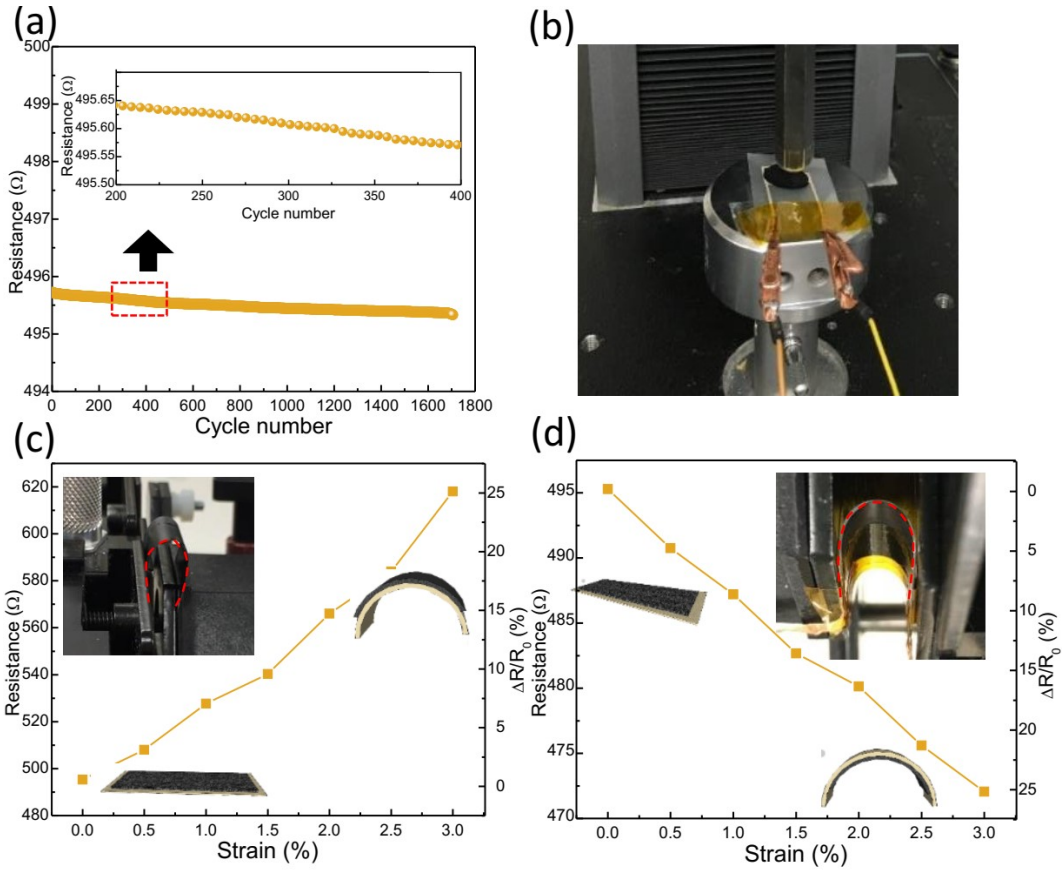

Figure 4.16 Selectivity testing on 8 wt% device. (a) Results of a cyclic compression test (20 kPa) (b) compression test setup using an Instron mechanical testing system in compression mode, (c) resistance change under bending (tensile strain), (d) resistance change under bending test (compressive strain).

For measuring spatial temperatures, a 6 x 7 array of devices using was printed on a PET substrate (Figure 4.17). The 8 wt% composites were selected for this application due to its low resistivity and acceptable TCR value. Each device consisted of a set of silver electrodes (Figure 4.17 b) onto which the desired composite was deposited. To demonstrate spatial mapping, a piece of alloy metal in the shape of a bear was heated to roughly 30 °C, and was placed on a table; the printed array of

sensors was placed over the bear with the contacts facing upward so the resistance at each point could be measured individually and sequentially using the source meter. The experiment setup was under IR camera, and the resulting image is shown in Figure 4.17c. The resistance of each pixel of the array was recorded, and a calibration curve was used to convert the measured resistance to a temperature (Figure 4.17d). The results indicate that the sensor array is able to map the temperature of the 2D dimensional objectIn all of our experiments, the surrounding temperature ranged from 22 °C to 24 °C; is expected that excessively hot or cold surroundings may have an effect on the measurements. In significantly cooler or warmer environments, devices should be re-calibrated to obtain accurate results.

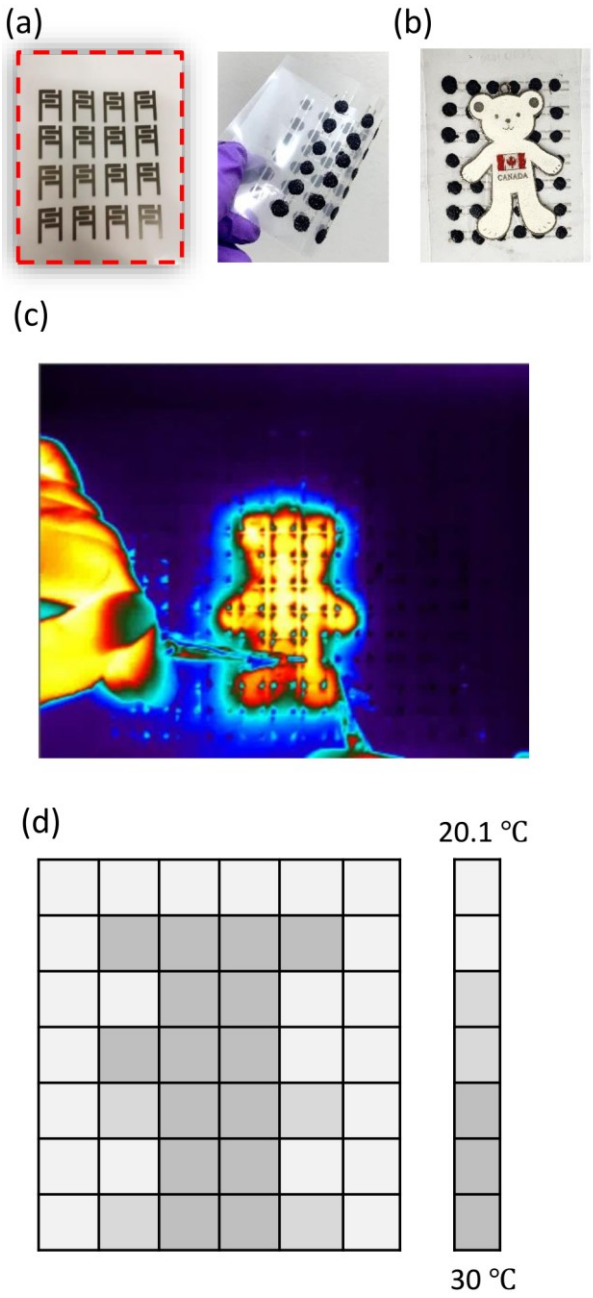

Figure 4.17 Enlarged silver electrodes and ink-jet printed patterned silver electrodes on PET substrate (left) (right) (a), composite ink was direct ink printed on each of the silver electrodes and the sensor array was covered by an alloy bear (b), heated bear and sensor array was under the device, and each element was individually measured (c), temperature mapping (6 × 7 pixels) on 8 wt % sample.

To engineer stretchable devices, meandering or serpentine shapes were fabricated by DIW (Figure 4.18). The 6 wt% composite ink was chosen for this application instead of the 8 wt% ink as it exhibits similar properties but results in less clogging of the nozzle during printing. The conductive and responsive 6 wt% composite ink was deposited on top of the Kapton film (Figure 9a), achieving good adhesion between the two layers. Figure 4.18 b shows temperature dependent I-V performance of meandering temperature sensor using 6 wt% composite ink here from 20 ℃ to 70 ℃. As the voltage was swept from -5 to +5 V, a linear and symmetric response was observed for both types of samples. This linear relationship indicates that DIW-printed meandering sample, pressed rGO pattern and rGO-PHB composites (Figure 4.18) exhibited ohmic behaviour at a given temperature. The results in Figure 9c demonstrated that the device was nearly unresponsive when exposed to bending of up to 3 % strain; the meandering devices are much less vulnerable to bending deformation than the drop-cast film devices. Figure 9d shows the printed meandering temperature sensor can be stretched and twisted without delamination of the functional layer. . Figure 4.18e shows the images of the meandering temperature sensor at relaxed (0 % strain) and stretched (10 % strain) states; the measured TCR values are all around 0.005/℃. This value is slightly lower than the drop-coated film 6 wt % device (0.006/℃) mainly because of the difference in geometry. The DIW printed lines are around 10 μm in thickness, which is much less thicker than the drop-casted films (80 μm). We also tested the real-time performance of the device on human temperature monitoring, listed in Figure 4.18f. The meandering device was initially measuring the temperature of the room, and was then applied rapidly to the surface of the forehead, held for about 2 seconds, and then removed. It can be seen that the response of this device exhibits no obvious time delay upon contact or removing from the heated object.

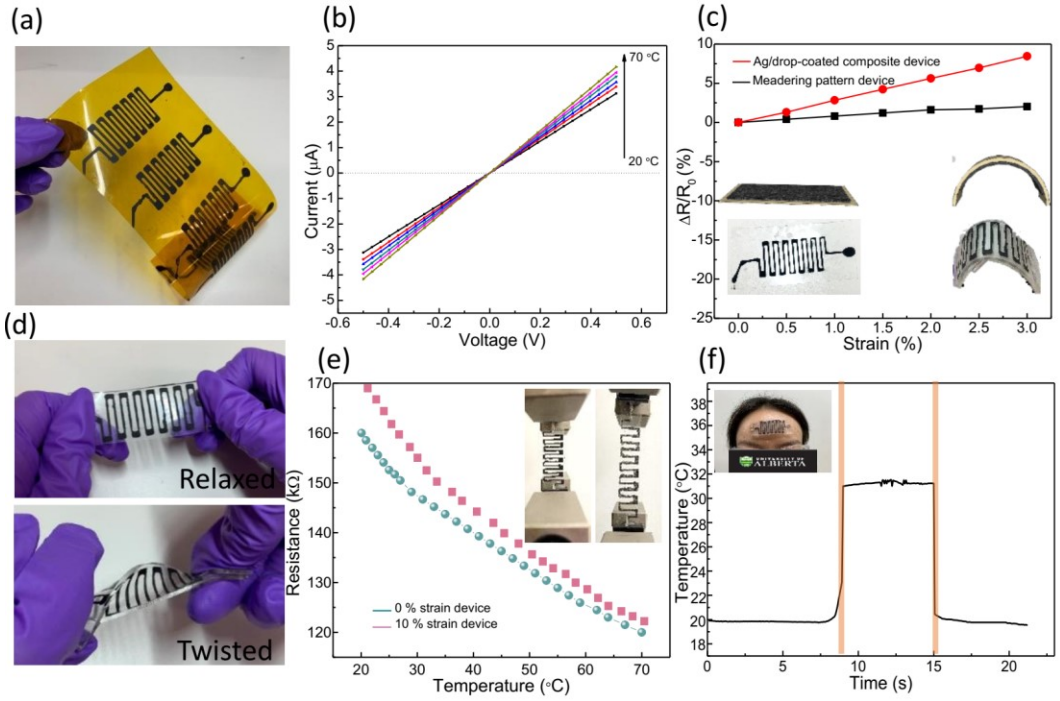

Figure 4.18 a) Meandering structures of conductive rGO/PHB ink patterned on a flexible Kapton substrate by DIW. b) I-V curves of the temperature at 0% strain in the temperature range of 20 to 70 °C. c) Strain sensitivity of the 6 wt% meandering temperature sensor (red curve is 10 % strain device, black curve is 0 % strain device). Inset pictures depict the device in the flat state and during bending (tensile strain). d) Meandering temperature sensor (6 wt% rGO/PHB) patterned on a PDMS substrate that was also printed by DIW, depicted in the relaxed and twisted states. e) Strain sensitivity of the 6 wt% meandering temperature sensor; inset images showing the device at 0 % and 10 % strain. f) Real-time temperature measurement of forehead skin (adult female) with the 6 wt% meandering temperature sensor. The vertical lines indicate a fast response upon loading and removing the device from heated object.

With the help of DIW, different shapes of sensors can be easily and quickly manufactured, with potential for scale-up. We designed a temperature sensing patch in the shape of a flower comprised of a meandering pattern fabricated between two thin layers of PDMS, as shown in Figure 4.19a. The measured TCR value is 0.0046/°C using 6 wt% conductive ink, in Figure 4.19b. Figure 10c shows that device is capable of detecting small human temperature difference with stable output data during human movement. Here, the patch was mounted on the hand surface and wrist area, and temperatures were recorded.

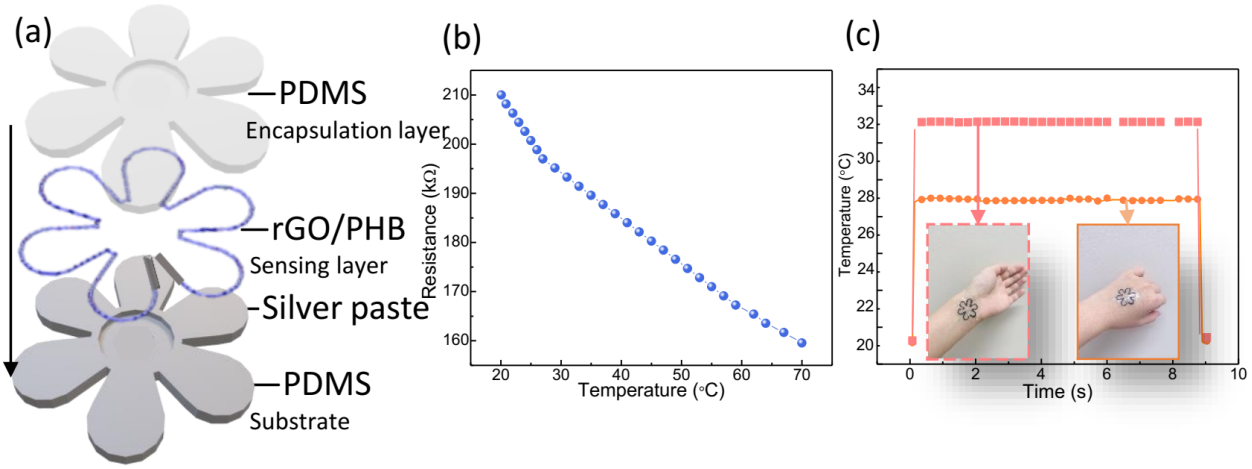

Figure 4.19 a) Schematic diagram of DIW flower shape temperature sensor structure using 6wt % composite ink. b) Resistance variation with temperature in a range of 20 to 70 °C. c) Real-time temperature measurement of the hand surface and wrist (adult female).

4.7 Conclusions

In this study, rGO was introduced as a nanofiller (at concetrations from 3 wt% to 12 wt%) for PHB polymer to fabricate temperature-responsive materials with negative TCR using a solution processing method. Both the room temperature resistivity and the variation in resistance as a function of temperature depends strongly on the wt% loading of the nanofiller. At room

temperature, the samples showed classic percolation behavior in terms of both conductivity, charge carrier mobility, and carrier concentration. In terms of heating, below the percolation threshold, the composites are generally insulating and show little change in resistnace as a function of temperature. Near the percolation threshold (3 wt% in this work), composites exhhibited intermediate resistivities which varied strongly as a function of temperature. Above the percolation threshold, samples were reasonably conductive and underwent smaller but stable and repeatable reductions in resistance upon heating.

The 8 wt% devices were found to be quite stable in response to pressure but responsive to bending. Care should therefore be taken to operate these particular devices at a constant radius of curvature. Due to the hydrophobicity of the polymer matrix, they were additionally found to be insensitve to both exposure to moisture and to immersion in water.

Our work offered a strategy to fabricate arrays of temperature-responsive devices from conductive composites using solution-based methods including printing and drop-casting. These devices are made using inexpensive materials on polymer substrates, and the devices themselves can be re-used. These arrays could be useful for monitoring temperature profiles in wet environments, including in the body or underwater.

4.9 References

(1) Yokota, T.; Inoue, Y.; Terakawa, Y.; Reeder, J.; Kaltenbrunner, M.; Ware, T.; Yang, K.; Mabuchi, K.; Murakawa, T.; Sekino, M.; Voit, W.; Sekitani, T.; Someya, T. Ultraflexible, Large-Area, Physiological Temperature Sensors for Multipoint Measurements. *Proc. Natl. Acad. Sci.* **2015**, *112* (47), 14533–14538. https://doi.org/10.1073/pnas.1515650112.

(2) Li, Q.; Zhang, L.-N.; Tao, X.-M.; Ding, X. Review of Flexible Temperature Sensing Networks for Wearable Physiological Monitoring. *Adv. Healthc. Mater. 6* **2016** (12), 1601371. https://doi.org/10.1002/adhm.201601371.

(3) Hammock, M. L.; Chortos, A.; Tee, B. C.-K.; Tok, J. B.-H.; Bao, Z. 25th Anniversary Article: The Evolution of Electronic Skin (E-Skin): A Brief History, Design Considerations, and Recent Progress. *Adv. Mater.* **2013**, *25* (42), 5997–6038. https://doi.org/10.1002/adma.201302240.

(4) Ghassemi, P.; Pfefer, T. J.; Casamento, J. P.; Simpson, R.; Wang, Q. Best Practices for Standardized Performance Testing of Infrared Thermographs Intended for Fever Screening. *PLOS ONE* **2018**, *13* (9), e0203302. https://doi.org/10.1371/journal.pone.0203302.

(5) Madhvapathy, S. R.; Ma, Y.; Patel, M.; Krishnan, S.; Wei, C.; Li, Y.; Xu, S.; Feng, X.; Huang, Y.; Rogers, J. A. Epidermal Electronic Systems for Measuring the Thermal Properties of Human Skin at Depths of up to Several Millimeters. *Adv. Funct. Mater.* **2018**, *28* (34), 1802083. https://doi.org/10.1002/adfm.201802083.

(6) Jeong, J.-W.; Kim, M. K.; Cheng, H.; Yeo, W.-H.; Huang, X.; Liu, Y.; Zhang, Y.; Huang, Y.; Rogers, J. A. Epidermal Electronics: Capacitive Epidermal Electronics for Electrically Safe, Long-Term Electrophysiological Measurements (Adv. Healthcare Mater. 5/2014). *Adv. Healthc. Mater.* **2014**, *3* (5), 621–621. https://doi.org/10.1002/adhm.201470022.

(7) Lee, C.-Y.; Weng, F.-B.; Cheng, C.-H.; Shiu, H.-R.; Jung, S.-P.; Chang, W.-C.; Chan, P.-C.; Chen, W.-T.; Lee, C.-J. Use of Flexible Micro-Temperature Sensor to Determine Temperature in Situ and to Simulate a Proton Exchange Membrane Fuel Cell. *J. Power Sources* **2011**, *196* (1), 228–234. https://doi.org/10.1016/j.jpowsour.2010.06.051.

(8) Huynh, T.-P.; Haick, H. Autonomous Flexible Sensors for Health Monitoring. *Adv. Mater.* **2018**, *30* (50), 1802337. https://doi.org/10.1002/adma.201802337.

(9) M. Perfecto, T.; A. Zito, C.; Mazon, T.; P. Volanti, D. Flexible Room-Temperature Volatile Organic Compound Sensors Based on Reduced Graphene Oxide–WO 3 ·0.33H 2 O Nano-Needles. *J. Mater. Chem. C* **2018**, *6* (11), 2822–2829. https://doi.org/10.1039/C8TC00324F.

(10) Xiao, S.; Che, L.; Li, X.; Wang, Y. A Cost-Effective Flexible MEMS Technique for Temperature Sensing. *Microelectron. J.* **2007**, *38* (3), 360–364. https://doi.org/10.1016/j.mejo.2007.01.022.

(11) Yang, Y.-J.; Cheng, M.-Y.; Chang, W.-Y.; Tsao, L.-C.; Yang, S.-A.; Shih, W.-P.; Chang, F.-Y.; Chang, S.-H.; Fan, K.-C. An Integrated Flexible Temperature and Tactile Sensing Array Using PI-Copper Films. *Sens. Actuators Phys.* **2008**, *143* (1), 143–153. https://doi.org/10.1016/j.sna.2007.10.077.

(12) Dankoco, M. D.; Tesfay, G. Y.; Benevent, E.; Bendahan, M. Temperature Sensor Realized by Inkjet Printing Process on Flexible Substrate. *Mater. Sci. Eng. B* **2016**, *205*, 1–5. https://doi.org/10.1016/j.mseb.2015.11.003.

(13) Aliane, A.; Fischer, V.; Galliari, M.; Tournon, L.; Gwoziecki, R.; Serbutoviez, C.; Chartier, I.; Coppard, R. Enhanced Printed Temperature Sensors on Flexible Substrate. *Microelectron. J.* **2014**, *45* (12), 1621–1626. https://doi.org/10.1016/j.mejo.2014.08.011.

(14) Liu, Qingxia, et al. A High-Performances Flexible Temperature Sensor Composed of Polyethyleneimine/Reduced Graphene Oxide Bilayer for Real-Time Monitoring. *Advanced Materials Technologies* 4.3 **2019**: 1800594.
(15) Lichtenwalner, D. J.; Hydrick, A. E.; Kingon, A. I. Flexible Thin Film Temperature and Strain Sensor Array Utilizing a Novel Sensing Concept. *Sens. Actuators Phys.* **2007**, *135* (2), 593–597. https://doi.org/10.1016/j.sna.2006.07.019.
(16) Xiao, S. Y.; Che, L. F.; Li, X. X.; Wang, Y. L. A Novel Fabrication Process of MEMS Devices on Polyimide Flexible Substrates. *Microelectron. Eng.* **2008**, *85* (2), 452–457. https://doi.org/10.1016/j.mee.2007.08.004.
(17) Lee, C.-Y.; Lee, S.-J.; Tang, M.-S.; Chen, P.-C.; Lee, C.-Y.; Lee, S.-J.; Tang, M.-S.; Chen, P.-C. In Situ Monitoring of Temperature inside Lithium-Ion Batteries by Flexible Micro Temperature Sensors. *Sensors* **2011**, *11* (10), 9942–9950. https://doi.org/10.3390/s111009942.
(18) Husain, M.; Kennon, R.; Husain, M. D.; Kennon, R. Preliminary Investigations into the Development of Textile Based Temperature Sensor for Healthcare Applications. *Fibers* **2013**, *1* (1), 2–10. https://doi.org/10.3390/fib1010002.
(19) Liu, P.; Zhu, R.; Que, R.; Liu, P.; Zhu, R.; Que, R. A Flexible Flow Sensor System and Its Characteristics for Fluid Mechanics Measurements. *Sensors* **2009**, *9* (12), 9533–9543. https://doi.org/10.3390/s91209533.
(20) Kim, D.-H.; Liu, Z.; Kim, Y.-S.; Wu, J.; Song, J.; Kim, H.-S.; Huang, Y.; Hwang, K.; Zhang, Y.; Rogers, J. A. Optimized Structural Designs for Stretchable Silicon Integrated Circuits. *Small* **2009**, *5* (24), 2841–2847. https://doi.org/10.1002/smll.200900853.
(21) Gray, D. S.; Tien, J.; Chen, C. S. High-Conductivity Elastomeric Electronics. *Adv. Mater.* **2004**, *16* (5), 393–397. https://doi.org/10.1002/adma.200306107.
(22) Cottet, D.; Grzyb, J.; Kirstein, T.; Troster, G. Electrical Characterization of Textile Transmission Lines. *IEEE Trans. Adv. Packag.* **2003**, *26* (2), 182–190. https://doi.org/10.1109/TADVP.2003.817329.
(23) Kim, D.-H.; Lu, N.; Ghaffari, R.; Kim, Y.-S.; Lee, S. P.; Xu, L.; Wu, J.; Kim, R.-H.; Song, J.; Liu, Z.; Viventi, J.; de Graff, B.; Elolampi, B.; Mansour, M.; Slepian, M. J.; Hwang, S.; Moss, J. D.; Won, S.-M.; Huang, Y.; Litt, B.; Rogers, J. A. Materials for Multifunctional Balloon Catheters with Capabilities in Cardiac Electrophysiological Mapping and Ablation Therapy. *Nat. Mater.* **2011**, *10* (4), 316–323. https://doi.org/10.1038/nmat2971.
(24) Song, W.; Lee, J.-K.; Gong, M. S.; Heo, K.; Chung, W.-J.; Lee, B. Y. Cellulose Nanocrystal-Based Colored Thin Films for Colorimetric Detection of Aldehyde Gases. *ACS Appl. Mater. Interfaces* **2018**, *10* (12), 10353–10361. https://doi.org/10.1021/acsami.7b19738.
(25) Doshi, S. M.; Thostenson, E. T. Thin and Flexible Carbon Nanotube-Based Pressure Sensors with Ultrawide Sensing Range. *ACS Sens.* **2018**, *3* (7), 1276–1282. https://doi.org/10.1021/acssensors.8b00378.
(26) Sadasivuni, K. K.; Kafy, A.; Kim, H.-C.; Ko, H.-U.; Mun, S.; Kim, J. Reduced Graphene Oxide Filled Cellulose Films for Flexible Temperature Sensor Application. *Synth. Met.* **2015**, *206*, 154–161. https://doi.org/10.1016/j.synthmet.2015.05.018.
(27) Lee, H.; Choi, T. K.; Lee, Y. B.; Cho, H. R.; Ghaffari, R.; Wang, L.; Choi, H. J.; Chung, T. D.; Lu, N.; Hyeon, T.; Choi, S. H.; Kim, D.-H. A Graphene-Based Electrochemical Device with Thermoresponsive Microneedles for Diabetes Monitoring and Therapy. *Nat. Nanotechnol.* **2016**, *11* (6), 566–572. https://doi.org/10.1038/nnano.2016.38.

(28) Dan, Li, et al. Porous Polydimethylsiloxane–Silver Nanowire Devices for Wearable Pressure Sensors. *ACS Applied Nano Materials* 2.8 **2019**: 4869-4878.
(29) Shih, W.-P.; Tsao, L.-C.; Lee, C.-W.; Cheng, M.-Y.; Chang, C.; Yang, Y.-J.; Fan, K.-C.; Flexible Temperature Sensor Array Based on a Graphite-Polydimethylsiloxane Composite. *Sensors* **2010**, *10* (4), 3597–3610. https://doi.org/10.3390/s100403597.
(30) Di, J.; Zhang, X.; Yong, Z.; Zhang, Y.; Li, D.; Li, R.; Li, Q. Carbon-Nanotube Fibers for Wearable Devices and Smart Textiles. *Adv. Mater.* **2016**, *28* (47), 10529–10538. https://doi.org/10.1002/adma.201601186.
(31) Hong, S. Y.; Lee, Y. H.; Park, H.; Jin, S. W.; Jeong, Y. R.; Yun, J.; You, I.; Zi, G.; Ha, J. S. Stretchable Active Matrix Temperature Sensor Array of Polyaniline Nanofibers for Electronic Skin. *Adv. Mater.* **2016**, *28* (5), 930–935. https://doi.org/10.1002/adma.201504659.
(32) Lopera-Valle, A.; Elias, A. Low-Resistance Silver Microparticle-HEMA-PEGDA Composites for Humidity Sensing. *Smart Mater. Struct.* **2018**, *27* (10), 105030. https://doi.org/10.1088/1361-665X/aad355.
(33) García-Tuñon, E.; Barg, S.; Franco, J.; Bell, R.; Eslava, S.; D'Elia, E.; Maher, R. C.; Guitian, F.; Saiz, E. Printing in Three Dimensions with Graphene. *Adv. Mater.* **2015**, *27* (10), 1688–1693. https://doi.org/10.1002/adma.201405046.
(34) Wei, X.; Li, D.; Jiang, W.; Gu, Z.; Wang, X.; Zhang, Z.; Sun, Z. 3D Printable Graphene Composite. *Sci. Rep.* **2015**, *5*, 11181. https://doi.org/10.1038/srep11181.
(35) Gnanasekaran, K.; Heijmans, T.; van Bennekom, S.; Woldhuis, H.; Wijnia, S.; de With, G.; Friedrich, H. 3D Printing of CNT- and Graphene-Based Conductive Polymer Nanocomposites by Fused Deposition Modeling. *Appl. Mater. Today* **2017**, *9*, 21–28. https://doi.org/10.1016/j.apmt.2017.04.003.
(36) Jeevananda, T.; Siddaramaiah; Hee Lee, J. Fabrication of Carbon Black/HDPE/Polyaniline Functionalized Multi-Walled Carbon Nanotube Composites for Enhancing PTC Characteristics. *Mater. Today Proc.* **2018**, *5* (10, Part 1), 20890–20898. https://doi.org/10.1016/j.matpr.2018.06.476.
(37) Gao, J.; Wang, H.; Huang, X.; Hu, M.; Xue, H.; Li, R. K. Y. Electrically Conductive Polymer Nanofiber Composite with an Ultralow Percolation Threshold for Chemical Vapour Sensing. *Compos. Sci. Technol.* **2018**, *161*, 135–142. https://doi.org/10.1016/j.compscitech.2018.04.014.
(38) Huang, Y.; Zeng, X.; Wang, W.; Guo, X.; Hao, C.; Pan, W.; Liu, P.; Liu, C.; Ma, Y.; Zhang, Y.; Yang, X. High-Resolution Flexible Temperature Sensor Based Graphite-Filled Polyethylene Oxide and Polyvinylidene Fluoride Composites for Body Temperature Monitoring. *Sens. Actuators Phys.* **2018**, *278*, 1–10. https://doi.org/10.1016/j.sna.2018.05.024.
(39) He, Y.; Yang, S.; Liu, H.; Shao, Q.; Chen, Q.; Lu, C.; Jiang, Y.; Liu, C.; Guo, Z. Reinforced Carbon Fiber Laminates with Oriented Carbon Nanotube Epoxy Nanocomposites: Magnetic Field Assisted Alignment and Cryogenic Temperature Mechanical Properties. *J. Colloid Interface Sci.* **2018**, *517*, 40–51. https://doi.org/10.1016/j.jcis.2018.01.087.
(40) Chu, K.; Park, S.-H. Electrical Heating Behavior of Flexible Carbon Nanotube Composites with Different Aspect Ratios. *J. Ind. Eng. Chem.* **2016**, *35*, 195–198. https://doi.org/10.1016/j.jiec.2015.12.033.
(41) Cui, X.; Chen, J.; Zhu, Y.; Jiang, W. Lightweight and Conductive Carbon Black/Chlorinated Poly(Propylene Carbonate) Foams with a Remarkable Negative Temperature Coefficient

Effect of Resistance for Temperature Sensor Applications. *J. Mater. Chem. C* **2018**. https://doi.org/10.1039/C8TC02123F.

(42) Neella, N.; Gaddam, V.; Rajanna, K.; Nayak, M. M. Negative Temperature Coefficient Behavior of Graphene-Silver Nanocomposite Films for Temperature Sensor Applications. In **2016** *IEEE 11th Annual International Conference on Nano/Micro Engineered and Molecular Systems (NEMS)*; 2016; pp 329–332. https://doi.org/10.1109/NEMS.2016.7758260.

(43) Zhao, S.; Lou, D.; Zhan, P.; Li, G.; Dai, K.; Guo, J.; Zheng, G.; Liu, C.; Shen, C.; Guo, Z. Heating-Induced Negative Temperature Coefficient Effect in Conductive Graphene/Polymer Ternary Nanocomposites with a Segregated and Double-Percolated Structure. *J. Mater. Chem. C* **2017**, *5* (32), 8233–8242. https://doi.org/10.1039/C7TC02472J.

(44) Gao, R.; Lu, D.; Cheng, J.; Jiang, Y.; Jiang, L.; Qi, Z. Humidity Sensor Based on Power Leakage at Resonance Wavelengths of a Hollow Core Fiber Coated with Reduced Graphene Oxide. *Sens. Actuators B Chem.* **2016**, *222*, 618–624. https://doi.org/10.1016/j.snb.2015.08.108.

(45) Lipatov, A.; Varezhnikov, A.; Wilson, P.; Sysoev, V.; Kolmakov, A.; Sinitskii, A. Highly Selective Gas Sensor Arrays Based on Thermally Reduced Graphene Oxide. *Nanoscale* **2013**, *5* (12), 5426–5434. https://doi.org/10.1039/C3NR00747B.

(46) Trung, T. Q.; Ramasundaram, S.; Hwang, B.-U.; Lee, N.-E. An All-Elastomeric Transparent and Stretchable Temperature Sensor for Body-Attachable Wearable Electronics. *Adv. Mater.* **2016**, *28* (3), 502–509. https://doi.org/10.1002/adma.201504441.

(47) Martínez-Tobón, D. I.; Gul, M.; Elias, A. L.; Sauvageau, D. Polyhydroxybutyrate (PHB) Biodegradation Using Bacterial Strains with Demonstrated and Predicted PHB Depolymerase Activity. *Appl. Microbiol. Biotechnol.* **2018**, *102* (18), 8049–8067. https://doi.org/10.1007/s00253-018-9153-8.

(48) Dan, L.; Pope, M. A.; Elias, A. L. Solution-Processed Conductive Biocomposites Based on Polyhydroxybutyrate and Reduced Graphene Oxide. *J. Phys. Chem. C* **2018**, *122* (30), 17490–17500. https://doi.org/10.1021/acs.jpcc.8b02515.

(49) Scalioni, L. V.; Gutiérrez, M. C.; Felisberti, M. I. Green Composites of Poly(3-Hydroxybutyrate) and Curaua Fibers: Morphology and Physical, Thermal, and Mechanical Properties. *J. Appl. Polym. Sci.* **2017**, *134* (14). https://doi.org/10.1002/app.44676.

(50) Tuning the properties of polyhydroxybutyrate films using acetic acid via solvent casting | Scientific Reports https://www.nature.com/articles/srep17884 (accessed Apr 1, 2020).

(51) Lopera-Valle, A.; Caputo, J. V.; Leão, R.; Sauvageau, D.; Luz, S. M.; Elias, A. Influence of Epoxidized Canola Oil (ECO) and Cellulose Nanocrystals (CNCs) on the Mechanical and Thermal Properties of Polyhydroxybutyrate (PHB)—Poly(Lactic Acid) (PLA) Blends. *Polymers* **2019**, *11* (6), 933. https://doi.org/10.3390/polym11060933.

(52) Chen, J.; Yao, B.; Li, C.; Shi, G. An Improved Hummers Method for Eco-Friendly Synthesis of Graphene Oxide. *Carbon* **2013**, *64*, 225–229. https://doi.org/10.1016/j.carbon.2013.07.055.

(53) Haque, A.; Mamun, M. A.-A.; Taufique, M. F. N.; Karnati, P.; Ghosh, K. Temperature Dependent Electrical Transport Properties of High Carrier Mobility Reduced Graphene Oxide Thin Film Devices. *IEEE Trans. Semicond. Manuf.* **2018**, *31* (4), 535–544. https://doi.org/10.1109/TSM.2018.2873202.

(54) McIntosh, R.; Mamo, M. A.; Jamieson, B.; Roy, S.; Bhattacharyya, S. Improved Electronic and Magnetic Properties of Reduced Graphene Oxide Films. *EPL Europhys. Lett.* **2012**, *97* (3), 38001. https://doi.org/10.1209/0295-5075/97/38001.
(55) Coelho, P. H. da S. L.; Marchesin, M. S.; Morales, A. R.; Bartoli, J. R. Electrical Percolation, Morphological and Dispersion Properties of MWCNT/PMMA Nanocomposites. *Mater. Res.* **2014**, *17*, 127–132. https://doi.org/10.1590/S1516-14392014005000059.
(56) Marsden, A. J.; Papageorgiou, D. G.; Vallés, C.; Liscio, A.; Palermo, V.; Bissett, M. A.; Young, R. J.; Kinloch, I. A. Electrical Percolation in Graphene–Polymer Composites. *2D Mater.* **2018**, *5* (3), 032003. https://doi.org/10.1088/2053-1583/aac055.
(57) Vo, N. H.; Dao, T. D.; Jeong, H. M. Electrically Conductive Graphene/Poly(Methyl Methacrylate) Composites with Ultra-Low Percolation Threshold by Electrostatic Self-Assembly in Aqueous Medium. *Macromol. Chem. Phys.* **2015**, *216* (7), 770–782. https://doi.org/10.1002/macp.201400560.
(58) Tang, Z.; Kang, H.; Shen, Z.; Guo, B.; Zhang, L.; Jia, D. Grafting of Polyester onto Graphene for Electrically and Thermally Conductive Composites. *Macromolecules* **2012**, *45* (8), 3444–3451. https://doi.org/10.1021/ma300450t.
(59) Stauffer, D.; Aharony, A.; Aharony, A. *Introduction To Percolation Theory : Second Edition*; Taylor & Francis, **2018**. https://doi.org/10.1201/9781315274386.
(60) He, L.; Tjong, S. C. Low Percolation Threshold of Graphene/Polymer Composites Prepared by Solvothermal Reduction of Graphene Oxide in the Polymer Solution. *Nanoscale Res. Lett.* **2013**, *8* (1), 132. https://doi.org/10.1186/1556-276X-8-132.
(61) Yoonessi, M.; Gaier, J. R. Highly Conductive Multifunctional Graphene Polycarbonate Nanocomposites. *ACS Nano* **2010**, *4* (12), 7211–7220. https://doi.org/10.1021/nn1019626.
(62) Kumar Srivastava, P.; Ghosh, S. Defect Engineering as a Versatile Route to Estimate Various Scattering Mechanisms in Monolayer Graphene on Solid Substrates. *Nanoscale* **2015**, *7* (38), 16079–16086. https://doi.org/10.1039/C5NR04293C.
(63) Justin, R.; Chen, B. Strong and Conductive Chitosan–Reduced Graphene Oxide Nanocomposites for Transdermal Drug Delivery. *J. Mater. Chem. B* **2014**, *2* (24), 3759–3770. https://doi.org/10.1039/C4TB00390J.

5. 3D printing polyhydroxybutyrate/carbon nanotubes composites

3D Printed and Biocompatible Conductive Composites Comprised of Polyhydroxybutyrate and Multi-Walled Carbon Nanotubes

Li Dan, Qiuli Cheng, Ravin Narain, Beate Krause, Petra Pötschke, Anastasia Elias

Department of Chemical and Materials Engineering, University of Alberta, Edmonton, AB T6G 1H9 Canada

Leibniz Institute of Polymer Research Dresden, Hohe Straße 6, Dresden D-01069, Germany

5.1. Abstract

As the field of 3D printing continues to enable the fabrication of biomedical materials and devices, there is increasing demand for the development of biocompatible functional materials with tailorable properties. Here, we utilized a desktop 3D printer to fabricate porous structures of electrically conductive polymer composites comprised of multiwalled carbon nanotubes (MWCNTs) in a matrix of polyhydroxybutyrate (PHB). PHB is a biocompatible, biodegradable, and piezoelectric polymer. The MWCNTs were melt-mixed in amounts from 0.25 to 5 wt % in PHB from two different suppliers with slightly different physical properties. The nanomaterial dispersion, morphology, electrical, thermal, and mechanical properties, and the crystallization behavior of both types of composites were investigated. A good dispersion at the macro- and microscale was observed in both types of composites. Electrical percolation threshold ranges of 0.25–0.5 wt % and 0.5–0.75 wt % were found for composites made with the two different types of PHB. The addition of MWCNTs resulted in an increase of Young's modulus and decrease of strain at break for both composites. The processability of the materials was demonstrated by 3D printing both stretchable meandering conductive traces and well-defined pore structure scaffolds. Biocompatibility tests were performed with MRC-5 cells and showed that the materials lack cytotoxicity. These results show the potential of these electrically conductive materials for use in biomedical electronic devices or as electro-active scaffolds for tissue regeneration applications, which require biocompatible, porous materials with microscaled architectures.

5.2 Introduction

Fused deposition modelling (FDM) is increasingly being utilized in the production of biomedical devices due to its ability to rapidly manufacture structures of arbitrary size and shape.[1–3] In this technique, a plastic filament is fed by a motor into a heated extruding print head. By moving the position of the print head with respect to the stage, three-dimensional structures are produced with

a controllable layer thickness. [4–7] As this field of manufacturing has expanded, a few materials have been widely adopted, including polylactic acid (PLA) (which is easy to pattern due to its low melting point) and acrylonitrile butadiene styrene (ABS) (which produces tough and durable 3D printed pieces). When designing materials for chronic use in the body, several parameters must be considered, including stability, biocompatibility, and mechanical strength. In addition, materials with added functionality such as conductivity are in demand for applications such as wearable electronics, energy harvesting, and tissue scaffolds.[8–10] Materials with diverse properties are therefore desired.

Polyhydroxybutyrate (PHB) is a versatile thermoplastic material with potential for use in FDM. Derived from natural sources, PHB is both biodegradable and biocompatible.[11] Although it can be enzymatically degraded in the environment, PHB is not degradable under most conditions inside the body; therefore, PHB can be a good candidate for bioelectronics and implants as the designed products are expected to be stable and to elicit a low foreign body response.[11,12] Its monomer, hydroxybutyryl-CoA, produced bacterially through a fermentation process utilizing agricultural waste as the source, is found in all living cells.[13] In addition, PHB is mildly piezoelectric, producing small electric potentials upon mechanical stimulation.[14] Bone tissue is known to be piezoelectric, and this characteristic has been shown to play a role in osteoblast proliferation.[15] This suggests that piezoelectric PHB scaffolds could provide additional function in scaffolds beyond merely providing a physical structure for cell growth. These properties present advantages over PLA, the most used biopolymer for in vivo structural applications such as 3D printed scaffolds.[12]

Polymers that are normally electrically insulating can be made conductive through the addition of conducting fillers such as carbon nanomaterials.[16,17] Carbon nanotubes (CNTs) in particular have received much attention in composite research owing to both their exceptional electrical properties (conductivity of 10^7 to 10^8 S/m) and mechanical properties (Young's modulus of 1 TPa and yield strength of 100 GPa).[18,19] Because of their high surface area, the addition of even a small fraction of CNTs can lead to a substantial change in characteristics (i.e. the materials exhibit a low electrical percolation threshold, at which concentration the filler forms a connected, conductive network).[20] CNTs can be either single-walled (SWCNTs) or multi-walled (MWCNTs). MWCNTs, which are comprised of several concentric SWCNTs connected by Van der Waals forces, are less expensive than single-walled CNTs. Like other carbon-based nanomaterials, CNTs have a long shelf life and good stability under heated or moist environments, and can be combined with polymers to form conductive materials.[21–23].

Recently, a number of electrically-conductive scaffolds have been demonstrated in the literature, for applications including cardiac and neuronal engineering, as reviewed in a recent article.[24] Conductive scaffolds have been made using MWCNTs and gelatin, which showed improved cell organization and maturation.[25] In this study, presence of nanofillers added the micro roughness to the scaffolds, thereby improving the cell attachment. In addition, the presence of the conductive fillers in the scaffolds enhanced the synchronous beating of the cardiomyocytes seeded upon them. Similarly, another gelatin and CNTs scaffold presented good mechanical integrity while also exhibiting electrophysiological functions.[26] As a soft hydrogel, gelatin is particularly useful for mimicking tissue for a limited period of time, but less useful for mimicking stiffer materials such as cartilage and bone. Such scaffold materials must be biocompatible, mechanically stable,

and exhibit organized pore distribution and reasonable porosity, requiring materials with higher modulus and stability. Three-dimensional printing of suitable materials – such as the biopolymer PHB – could potentially be used to address these challenges. A few demonstrations of PHB/CNT composites can be found in the literature,[27,28] for instance, PHB/CNT composites were processed in solution and used as hole collector in a solar cell, with an electrical percolation threshold of 0.2 wt%.[29] A triboelectric generator and pressure sensor has also been made by blending CNTs with PHB.[30] While PHB is inherently brittle with a low strain at break (typically ~ 5%), the brittleness of PHB can be reduced through adding plasticizers. Three-dimensional printing of biopolymer polyhydroxybutyrate (PHB) and conductive PHB/CNT composites has not yet been demonstrated.

In this study, we evaluate the suitability of PHB/CNT composites for use in 3D printing of conductive and porous materials, for applications such as circuits and scaffolds. Firstly, we prepared composite filaments by extrusion of PHB composites with varying concentrations of MWCNTs (0.25 wt% to 5 wt%), and for use as multifunctionality 3D printing (Figure 1). This range was selected as it is expected to capture the electrical percolation threshold, allowing a low electrical resistivity to be achieved at minimal loading of filler. As PHB is generally a brittle material, it was desirable to investigate a commercial formulation that includes additives. Two base biopolymers (PHB) were therefore compared: Biomer P209 (PHB with nucleating agent and plasticizers) and BRS Biopellets (PHB with 1 wt% Si impurity, without plasticizers). As dispersion is an important determinant of the properties of a composite, filler dispersions and morphologies were observed using scanning electron microscopy (SEM) and transmission electron microscopy (TEM). The mechanical properties of both pristine PHB and composites were evaluated using a tensile tester. To demonstrate the manufacturability of the materials, 2D and 3D designs were

produced, including conductive meandering traces, solid 3D designs, and scaffold structures. To determine how printing affects the properties of the composites, the mechanical and electrical properties of the resulting structures were evaluated and compared to those of the filaments. To evaluate their suitability as cell-scaffolds and implant materials, the mechanical, electrical properties, and cytotoxicity of the resulting structures were characterized.

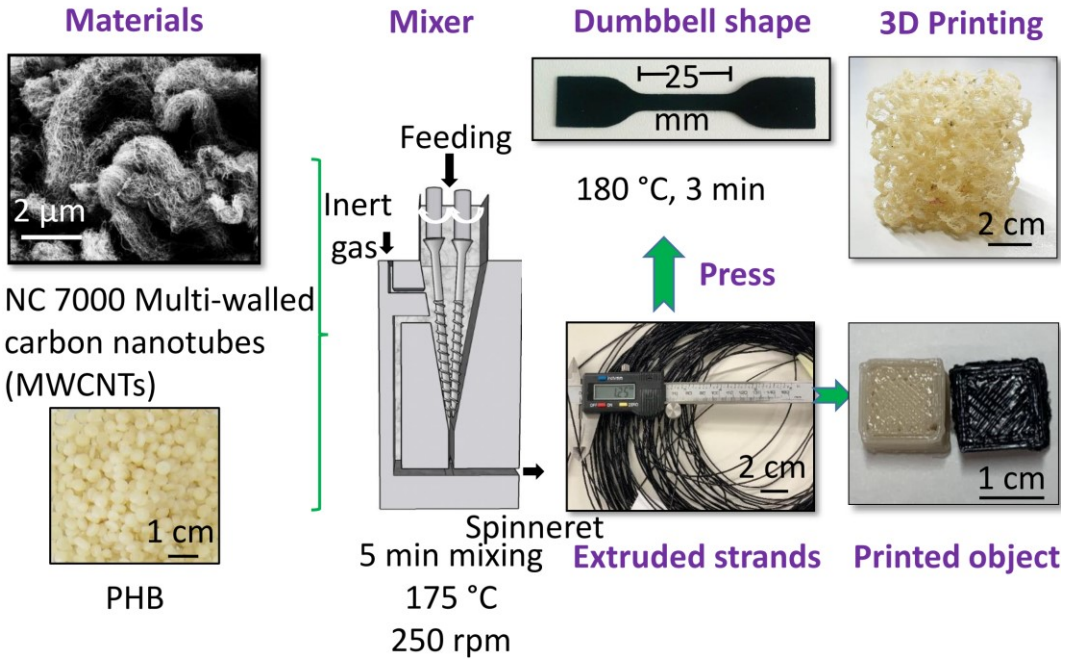

Figure 5.1 MWCNT powder and PHB pellets were fed into the mixer, and then extruded into the strands Filaments, remolded from strands, were then hot compressed to the desired shape using alloy mold or 3D printed into designs.

5.3 Materials

NC 7000 MWCNTs were obtained from Nanocyl S.A. (Nanocryl^{TM}, Sambreville, Belgium), with an average diameter of 9.5 nm, a length of 1.5 µm, carbon purity of 90 %, density of 2.6 g/cm^3, and surface area of roughly 300 m^2/g. Two types of biopolymers were used in this work, BRS Biopellets (BRS Bulk pellets, Bulk Reef Supply, Golden Valley, USA) and Biomer 209 (Biomer

Ltd. Krailing, Germany), with a molecular weight (as determined by Gel Permeation Chromatography (GPC)) and density of 190 kDa and 560 kDa, 1.25 g/cm^3, and 1.29 g/cm^3, respectively. Each of these PHB polymers were received as pellets produced by melt mixing pelletization. The BRS pellets had less than 1 wt% impurity of Si, while Biomer P209 contained both a nucleating agent (boron nitride) and plasticizers.

5.4 Methods

Hot compression molded samples

The overall experimental process is shown in Figure 5.1. The melt-mixing of the samples with calculated concentrations of 0, 0.1, 0.25, 0.5, 0.75, 1 and 5 wt% MWCNTs with the polymer matrices was carried out using a small-scale twin-screw compounder (DSM Xplore Instruments BV, Sittard, The Netherland, 15 cm^3 volume) at a temperature of 175 ℃ and extrusion speed of 250 rpm with a mixing time of 5 min. Subsequently, the extruded filaments were compression molded using a hot press (No. 4386, Carver Inc, Wabash, IN, U.S.A.). To produce 70 cm × 80 cm × 0.2 cm square sheets, a three part AISI 1008 steel mold was used with two flat top and bottom mold sheets, while the middle part was a 2 mm thick steel with a rectangular 70 cm × 80 cm cut-out. Approximately 5 g of extruded filaments were placed over the cut-out of the mold and heated for 5min, at 175 ℃. A gentle pressure was then pressed onto the whole mold to allow the melt materials to spread throughout the cut-out area. Then a pressure of 2.1 MPa was applied for 1 min, and the mold was removed after cooling down to ambient temperature. The resulted sheets were cut into dumbbell shapes using blade cutter.

FDM 3D-printed samples

Neat PHB and composite filaments (1.75 mm thickness) were made from strands using a FilaFab PRO 350 extruder (FD3D Innovations Limited, U.K.) at 170 ℃ at 20 rpm. A MACHINA MK3 X24 desktop 3D printer was used to produce structures of programmable shapes and sizes. The metal print head could be heated up to 500 ℃, and included a nozzle with a diameter of 0.40 mm. The printing parameters for the PHB/MWCNTs and PHB filaments were set in the printer software (Slic3r) and are listed below in Table 1. Elmer's adhesive spray was used on the printing substrate to improve the adhesion of the printed pieces to the metal bed during processing.

Table 5.1 Printing parameters for FDM processing for 3D designs

	Value
Nozzle Temperature (℃)	195
Printed Bed Temperature (℃)	70
Layer thickness (mm)	0.27
Print Speed (mm/s)	80
Infill Pattern (degrees)	Rectilinear (90 °)
Fill Density (%)	100

5.5 Characterization

Morphology

The morphology of the microtomed Biomer PHB/MWCNTs and BRS PHB/MWCNTs samples (1 µm thickness) containing 1 wt% nanofiller were observed using optical microscopy (microscope

BX53M combined with a camera DP 71 (both Olympus Deutschland GMbH, Hamburg, Germany)) and transmission electron microscopy (TEM) (JEOL, Ltd, Japan) at a voltage of 120 kV. The fracture surface morphology of composites with 1 wt% MWCNTs was observed using a field emission scanning electron microscope (FE-SEM) (Zeiss Sigma 300, Zeiss, Cambridge, UK) using secondary electron (SE) mode at a voltage of 3 kV. To prepare SEM samples, all samples were mounted on carbon tape and sputter-coated with a 10 nm gold layer.

Mechanical Analysis

An Instron 5943 tensile tester (Instron, Norwood, MA, U.S.A.) with a 1 kN load cell was used to measure the mechanical properties. Measurements were carried out based on the ASTM Standard D638: a strain rate of 2 mm/min was applied to dumbbell shape specimens (25 mm length between the shoulders, 2 mm in thickness). Five samples of each type were characterised. Strain and stress data were collected, and Young's modulus was calculated from the slope of the linear region of the strain-stress curve.

A PerkinElmer dynamic mechanical analyzer (DMA 8000) was used to characterize the compressive modulus of 3D printed scaffolds at room temperature under a range of frequencies (0.01 to 100 Hz). Measurements were performed in compression mode using a cubic scaffold sample (1 cm^3) with a standard displacement of 0.05 mm.

Thermal Characterization

Differential Scanning Calorimetry (DSC) was used to obtain the melting temperature (*Tm*) and crystallinity was estimated by integrating the area of the melting endotherm peaks. This thermal test was carried out for each specimen (approximately 5 mg) in a sealed aluminium crucible. The

temperature was scanned from - 20 to 195 ℃, held at 195 ℃ for 5 min, and then cooled to -20 ℃, all at a heating/cooling rate of 5 ℃/min. The degree of crystallinity of all samples was calculated by integrating the area of specific melting enthalpy over the melting heat related to the neat crystalline material and the proportion of PHB within the composite.

X-ray Diffraction

The crystallinity of neat biopolymers and composites was investigated using a Rigaku XRD Ultimate IV (Cu-source) in the scan range of 2θ = 5- 40° at rate of 2 ℃/min at 44 kV. The composite samples (sheets) were kept flat for testing.

Differential Scanning Calorimetry

To calculate the percent crystallinity of each sample, a peak fitting procedure was implemented, where the sharp peaks were assumed to be crystalline, and the rest of the area was considered to correspond to amorphous regions. The degree of crystallinity (X_C) of the BRS, Biomer, and was calculated using the following equation: $X_C = \frac{\Delta H_m}{\Delta H_{m100} \times w}$, where ΔH_m is the integrated area of the melting peak and ΔH_{m100} is the enthalpy of neat 100 % PHB crystalline (146.6 J mol^{-1}).

Electrical Characterization

Electrical characterization was performed on compression molded samples with a thickness of 400 to 500 μm. The volume resistivity of high resistance samples (resistivity > 10^9 Ω cm) was measured through the thickness of the sample with a ring-opening electrode (Model 8009) and a Keithley 6517A electrometer. The in-plane resistivity of lower resistivity samples (high concentration of MWCNTs) was determined using a Four Point probe (Kelvin sensing) station with a 1 mm probe spacing and powered by a Keithley 6517A electrometer.

Dielectric Properties

The dielectric properties of materials were measured for three replicates using a Model 894 Bench LCR meter in the frequency range of 20 to 500,000 Hz. The capacitance was directly measured from the instrument, where the samples were sandwiched by a round copper electrode with a diameter of 10 mm. The capacitance of a parallel capacitor is defined as $C = \frac{\varepsilon A}{d}$, where C is capacitance, ε is real permittivity, A is surface area, and d is the thickness of the capacitor. Once C, A, d, are measured, the real permittivity of the samples can be calculated.

Porosity measurement

The porosity P of the PHB and composite scaffolds was estimated by taking into account the weight and volume of scaffolds as well as the density of the two types of PHB and MWCNTs, $P = \frac{\rho V - M}{\rho V} \times 100\ \%$. In this equation, P (%) is defined as porosity, ρ (g/cm^3)is the density of the material, V (cm^3) is the volume of the scaffold, and M (g) is the measured weight of the scaffold.

Cell proliferation

The biocompatibility of the materials was evaluated with Medical Research Council cell strain-5 (MRC-5) fibroblast cells using a cell proliferation kit. Briefly, PHB films (1 cm^2) were sterilized with ultraviolet light and immersed in 1 ml Dulbecco's Modified Eagle Medium (DMEM) culture medium for 24 h and the extracted liquid was collected. MRC-5 fibroblast cells were seeded onto a 96-well plate at a density of 6,000 cells per well with 100 µL of DMEM medium. The cells were incubated at 37 ℃ in a balanced air humidified incubator with an atmosphere of 5 % CO_2. After incubation of the cells for 24 h, the culture media were removed and replaced by 100 µL of fresh DMEM media. The cells were allowed to be further incubated for 24 h. 20 µL (3-(4,5-

Dimethylthiazol-2-yl)-2, 5-diphenyltetrazolium bromide (MTT) solution (5 mg/ml) was then added per well, and then incubated for 4 h. The culture media were then carefully removed, and 100 µL of lysis buffer (dimethyl sulfoxide (DMSO)/isopropanol = 1:1 volume ratio) solution was used to dissolve the crystal formation. An optical absorption spectrometer was used to measure the absorbance at 570 nm, and cell viability was calculated by comparing optical density 570 nm values of cells treated with/without the extracted liquid.

Scaffold and Cell Morphology Examination

Top-view and side-view scaffolds, and cell morphology were observed by optical microscopy. Before evaluating the cell proliferation, all the tested samples (neat PHB, composite, and printed scaffolds) underwent 72 h incubation.

5.6 Results and Discussions

Nanocomposite Morphological Characterization

Figure 2 (a) and (b) show the optical images of microtomed thin sections (1 µm) of Biomer PHB/MWCNT and BRS PHB/MWCNT composites (compression molded) exemplarily shown at 1 wt% nanofiller. This loading of nanofiller was selected as it was expected to be high enough to allow numerous agglomerations to be observed in a single view, while low enough that individual agglomerations could be discerned. The dark spots appeared on both images are remaining large agglomerates of NC7000 MWCNTs. A relatively good dispersion was observed at the macroscopic scale with some visible nanofiller agglomerates. Overall, the maximum size of remaining agglomerates (dark spots) in the Biomer composite system (Figure 2 (b)) was greater than that in BRS PHB (Figure 2(a)). Figure 2 (c) and (d) show the the TEM micrographs of the

composites. Rectangular annotations on the images are used to highlight the agglomerates of CNTs. Both TEM graphs showed reasonable MWCNT distribution at the nanoscale, wherein individually dispersed MWCNT threads can be observed as well as some larger clusters (around 1 μm in size). Similar structures have been observed in previous work, e.g. for polycarbonate-CNT composites.[32] In the Biomer PHB-MWCNT composites these agglomerates tend to be comprised of a more dense cluster of MWCNTs, whereas in the BRS PHB-MWNCT composites the agglomerates have a more fluffy structure, made up of fewer MWCNTs. This confirms better dispersion at the nanoscale for BRS PHB/MWCNT composites.

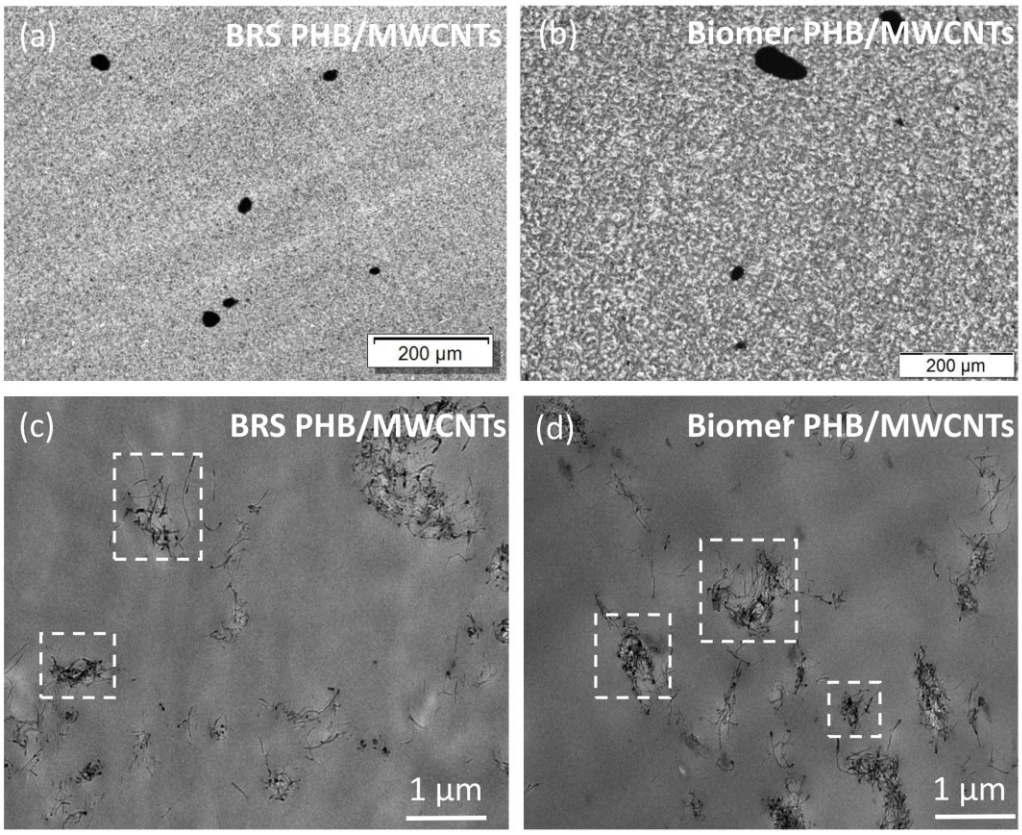

Figure 5.2 Optical images of microtomed BRS PHB/MWCNTs (1 wt%) composite (a) and Biomer PHB/MWCNTs (1 wt%) (b). TEM images of BRS PHB/MWCNTs (1 wt%) composite (c) and Biomer PHB/MWCNTs (1 wt%) (d).

SEM images were collected to analyze the fracture surface of 1 wt% samples, shown in Figure 5.3 (a) and (b). The cryofractured surfaces of both samples showed the presence of wrinkle-like structures with no visible cracks, indicating that MWCNTs were well mixed with the polymer matrix, and also well-adhered to the matrix. The Biomer composite (Figure 5.3 (b)) includes larger visible agglomerates of MWCNTs than the BRS sample (Figure 5.3 (a)); this is in agreement with the TEM and optical results. This may influence the mechanical and electrical properties of the resulting composites. The more pronounced visibility of the MWCNTs in the Biomer PHB composite may result from a less perfect infiltration of the PHB chains into the primary MWCNTs bundles, leading to easier separation of the nanotubes during the cryofracturing.

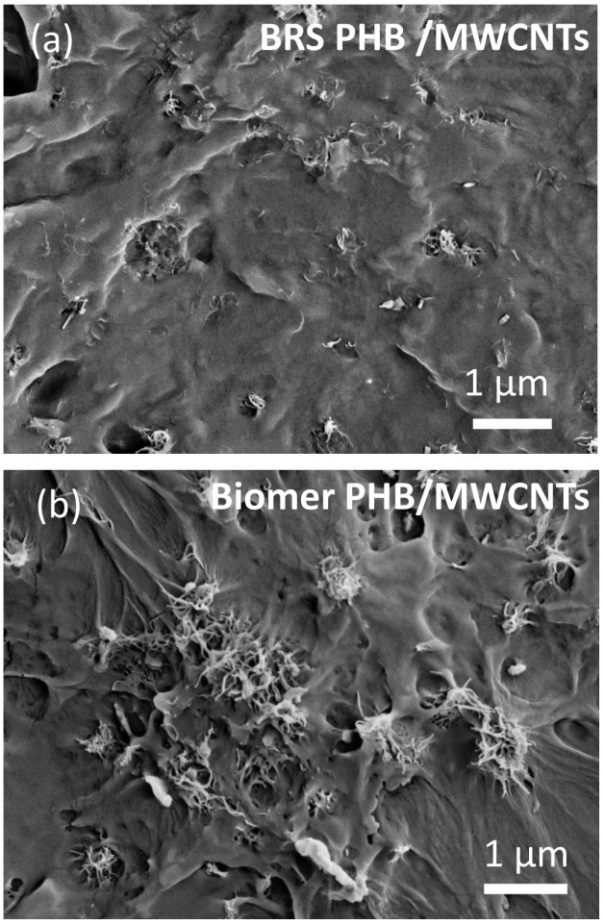

Figure 5.3 SEM images of cryofractured surfaces of composites with 1 wt% MWCNTs in BRS PHB (a) and in Biomer PHB (b).

Mechanical Properties

Representative stress-strain curves of the neat biopolymer (i.e. BRS and Biomer), 1 wt%, and 5 wt% composites are plotted in Figure 5.4 (a) and (b). The value of Young's modulus (E) and strain at break (ε) are plotted in the bar charts in Figure 5.4 (c) and (d). The characteristics of neat BRS PHB align with those reported in our previous work, [28,29] and reflect the brittleness of this material, particularly exhibiting a low strain at break. As can be seen in Figs. 4 (a) and (b), the neat Biomer PHB is less brittle than the BRS PHB, with higher strain at break and lower Young's modulus. These differences in mechanical properties occur because the Biomer PHB contains a plasticizers to lubricant the polymer chains, which makes it less brittle.

For very low MWCNTs content (0.1 wt%, 0.25 wt%) no obvious change in modulus occurred in either type of composite. At high loading (5 wt%), both types of composites undergo a large increase in Young's modulus with respect to the Neat polymer (without MWCNTs). For example, the Young's modulus of Biomer PHB increased from 1390 ± 50 MPa for the neat polymer to 1730 ± 100 MPa for the 5 wt% composite, while the strain at break decreased from 6.4 % to 5.0%. This corresponds to an approximately 25 % increase in Young' s modulus and 21 % decrease in strain at break. The Young's modulus of the BRS PHB increased from 1844 ± 108 MPa for the neat polymer to 2263 ± 23 MPa for the 5 wt% composite, which is almost a 23 % rise in Young' s modulus and a 24 % decrease in strain at break. These trends (decreasing strain in break and increasing Young's modulus) as frequently observed in CNTs-polymer composites [30]

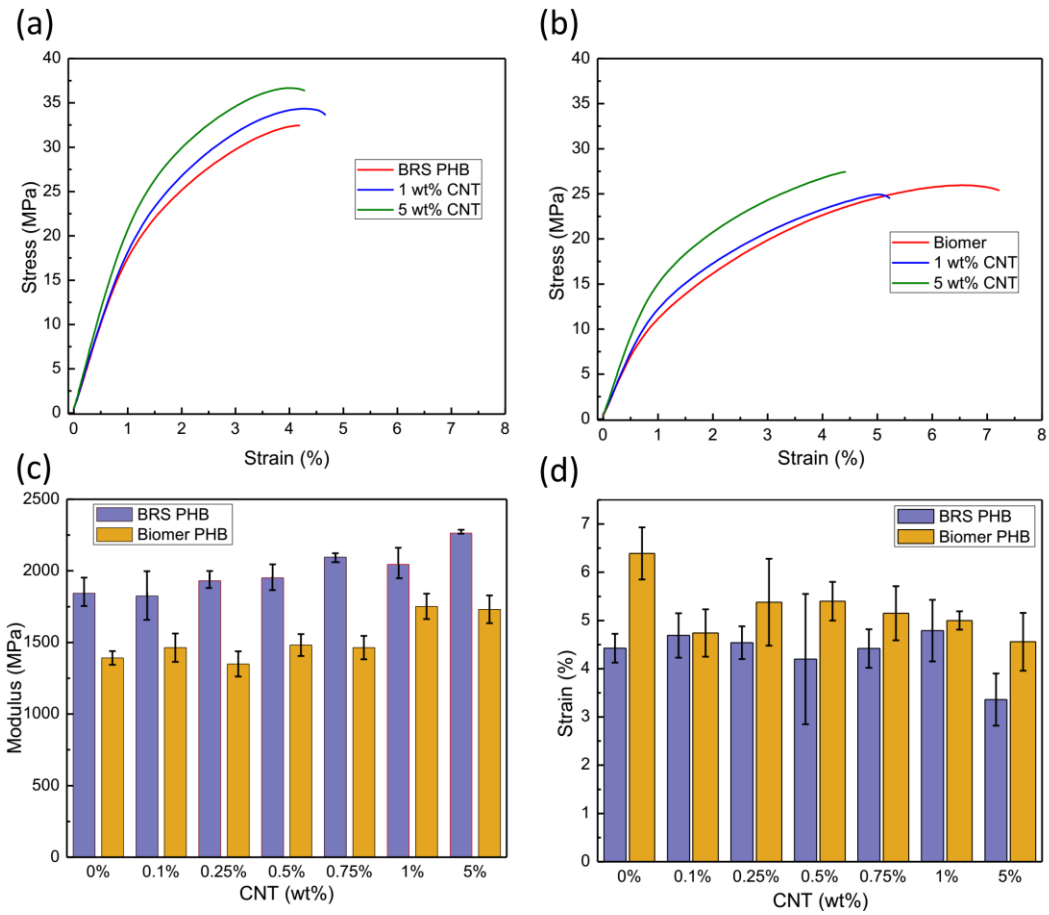

Figure 5.4 Representative strain-stress curves of neat and 1 wt% BRS PHB/MWCNTs composite (a) and Biomer PHB/MWCNTs (b). The bar chart of Youngs' modulus (c) and strain at break (d) of composites with different MWCNTs concentration, representing the average and standard deviation of 5 samples each.

Crystallinity and Thermal Behavior

The crystallinity and thermal properties of Biomer PHB, BRS PHB and PHB/MWCNTs composites were evaluated using DSC. Figure 5.5 shows the representative DSC second run heating curves for each material, where neat BRS and Biomer PHB presented a double melting peak at T_{m1} (158 ℃), T_{m2} (170 ℃), and T_{m1} (164 ℃), T_{m2} (170 ℃), respectively. The double

melting peak of PHB type biopolymer is often observed, and is generally attributed to the presence of metastable crystals that melt at a lower temperature than stable ones.[31]

The degree of crystallinity (X_C) of the BRS, Biomer, and composites with MWCNTs is summarized in Table 2. X_C was calculated using the following equation: $X_C = \frac{\Delta H_m}{\Delta H_{m100} \times w}$, where ΔH_m is the integrated area of the melting peak, ΔH_{m100} is the enthalpy of neat 100 % PHB crystalline (146.6 J mol^{-1}), *w* is the fraction of PHB.[32] Initial crystallinity values for the BRS PHB agree with our previous work,[230] and, as expected, the Biomer formulation exhibited a lower value due to the inclusion of plasticizers. The crystallinity for both types of PHB decreased with increasing the content of MWCNTs. The crystallinity of neat BRS and Biomer were 29.1 % and 32.3 %, respectively, and at 5 wt% loading of MWCNs these values dropped substantially to 16.6 % and 19.2 %, respectively. The composites showed decreasing crystallinity with increasing the % loading of MWCNTs, indicating that MWCNTs suppress crystallization by pinning the polymer chains.[33 34]. While each neat PHB (0 wt % MWCNTs) exhibits two peaks, for the composites formed with Biomer PHB as the wt% of the MWCNTs increases, the distinction between these two peaks lessens. This may be due to the fact that the position of these peaks is relatively close together, causing them to overlap as the intensity of the peak at the higher Tm decreases.

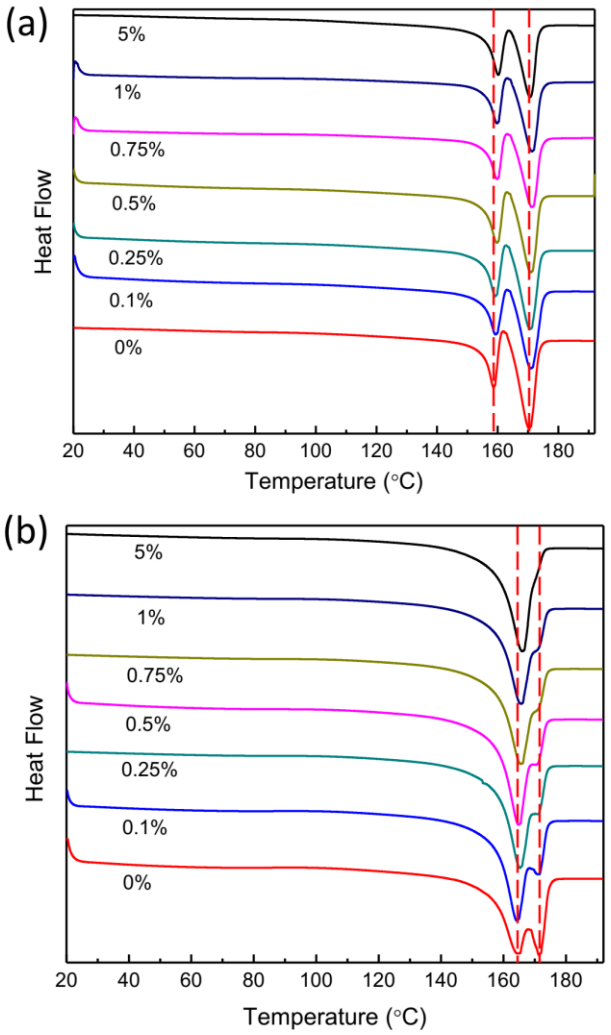

Figure 5.5 DSC heating endotherms of composites of BRS PHB c (a) and Biomer PHB (b) containing different concentration of MWCNTs.

Table 5.2 Crystallinity of biopolymer (BRS and Biomer) and MWCNTs composites as obtained by DSC.

CNTs loading (wt %)	Crystallinity (%) BRS Composites	Crystallinity (%) Biomer Composites
0	29.1	32.3
0.1	24.9	28.4
0.25	21.3	27.0
0.5	19.3	26.1
0.75	17.4	22.5
1	16.6	19.2
5	14.1	17.4

XRD

Figure 5.6 depicts the XRD patterns of the composites and also of neat BRS PHB and Biomer PHB. The XRD pattern of neat BRS and Biomer show similar appearance, including peaks at 2θ values that can be attributed to the (020), (110), (021), (111), and (121) crystal planes of the polymer. The MWCNTs XRD pattern has a typical sharp peak at 25°, and this peak is absent in the composite materials, suggesting that the MWCNTs were well mixed with the polymer matrix. In the composites, the peaks appeared very similar to each other and to the neat biopolymer, suggesting a minimal effect of MWCNTs on the type of crystals formed in the polymer. However, an overall decrease in peak area with increasing filler concentration was observed in Figure 5.6 (a), indicating that the overall crystallinity of the composites decreased with increasing MWCNT

content. This suggests that the presence of MWCNTs may limit the movement of polymer (BRS) chains into crystalline lamellaes to form the crystals. The ratio of the integrated area for the (020):(110) peaks was 0.87:1 and 0.8:1 in BRS PHB and Biomer PHB polymers (without filler), respectively. For each composite, the integrated area of (020) is larger than the area of (110) in both PHB types; the ratio of these values are around 1.14:1, 1.21:1 for BRS PHB and Biomer PHB, respectively. A similar change in the ratio of intensities has been observed in previous rGO/PHB work and by Arza et al. [28,35] In these works, the ratio of the integrated area for the (020):(110) peaks increased with increasing wt% amount of rGO. This change was attributed to preferential orientation effects within the polymer. [28,36]At further increase in the MWCNTs content (> 0.1 wt%) such as 0.25 wt%, the peak intensities were increased.

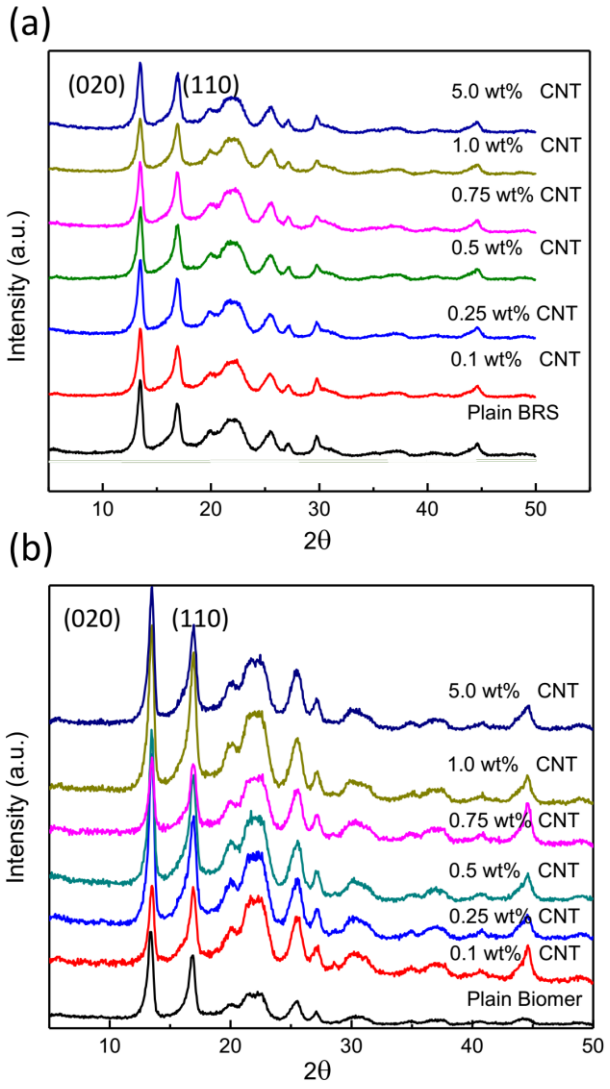

Figure 5.6 XRD patterns of BRS PHB/MWCNTs composites (a) and Biomer PHB/MWCNT composites (b) containing different concentration of MWCNTs.

Electrical properties

Figure 5.7 illustrates the electrical volume resistivity of the two kinds of composites; as expected, both types of composites exhibit decreasing resistivity with increasing wt% of MWCNTs. Neat BRS PHB and Biomer PHB (0 wt% filler) were found to be insulating, with resistivity values of 10^{16} Ω cm and 10^{14} Ω cm, respectively. The resistivity of the BRS PHB was two orders of

magnitude higher than that of the Biomer, likely due to small differences is impurities and additives in these PHB materials. Above 0.5 wt% loading, the resistivity decreased in each type of composite. The BRS composites have a lower electrical percolation threshold (0.5 wt%) compared to Biomer composites (0.8 wt%), suggesting the formation of a more connected network. This observation is in agreement with the morphological characterization, which showed better dispersion of the CNTs in the Biomer composites. At each wt% loading above 5 wt%, the BRS composites were less resistive than Biomer samples. Overall, both PHB/MWCNTs composites showed quite low resistivity above the electrical percolation threshold. At 5 wt % loading, the resistivity of the BRS PHB-MWCNT composite and the Biomer PHB/MWCNT composite were 2.2 ± 0.4 Ω cm, 5.8 ± 0.6 Ω cm, respectively. Each PHB/MWCNT (1 wt%) composite showed lower resistivity values than currently reported poly(lactic acid)/polystyrene/MWCNT, polypropylene/MWCNT and polyamide-4/MWCNT composites.[37–39]

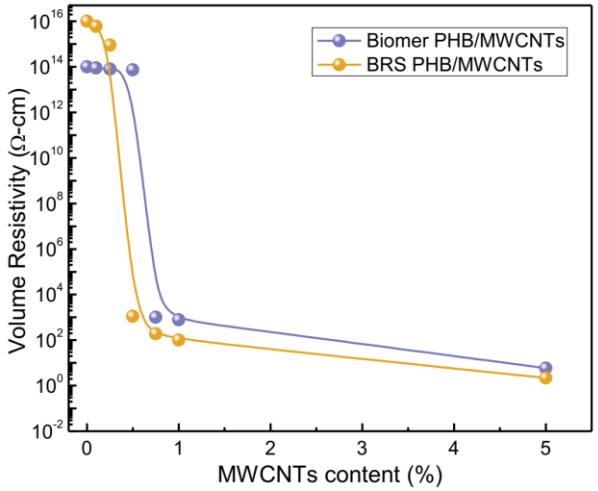

Figure 5.7 Electrical resistivity of the composites of two types of biopolymer (BRS PHB and Biomer PHB) with different MWCNTs content.

Dielectric properties

Flexible electronics with a high dielectric constant are important for many biomedical applications (e.g. physiological signals monitoring).[26] While polymers usually exhibit a low dielectric constant (< 10), flexible dielectrics with a high dielectric constant can be achieved by the addition of conductive particles to a polymer matrix. The capacitance of a parallel capacitor is defined as $C = \frac{\varepsilon A}{d}$, where C is capacitance, is real permittivity, A is surface area, and d is the thickness of the capacitor. By knowing the C, A, d, the real permittivity of the samples can be calculated. Figure 5.8 (a) and (b) show the real permittivity and Figure 5.8 (c) and (d) depicts the imaginary permittivity of the two types of composites, BRS PHB/MWCNTs and Biomer PHB/MWCNTs, respectively. As expected, both neat biopolymers have very low real permittivity (< 10). All samples showed a decrease in both real and imaginary permittivity as the frequency was increased from 20 to 500 kHz. As the MWCNT contents was increased in each type of composite, the real permittivity increased, and a permittivity value of greater than 10^4 is reached at 5 wt% loading for each type of composite. The real permittivity originates from the inner polarization of charge carriers, and a rise in real permittivity occurs with increasing the MWCNTs content as more conductive nanofillers results in more charge carriers. The high dielectric constant suggests more surface charges on the composite scaffold, indicating a better electroactive response formed between scaffold and tissue interfaces. [40] These values are comparable to the current reported high dielectric polymer/CNTs composites.[41,42] Likewise, the imaginary permittivity rises with MWCNTs content, reaching a fairly low overall value between 11 and 14 for the 5 wt% composites. The imaginary permittivity, referred to as the Ohmic loss, comes from the dissipation of electrical energy through a dielectric material. A low imaginary permittivity is critical for antennas and other radio frequency related applications.

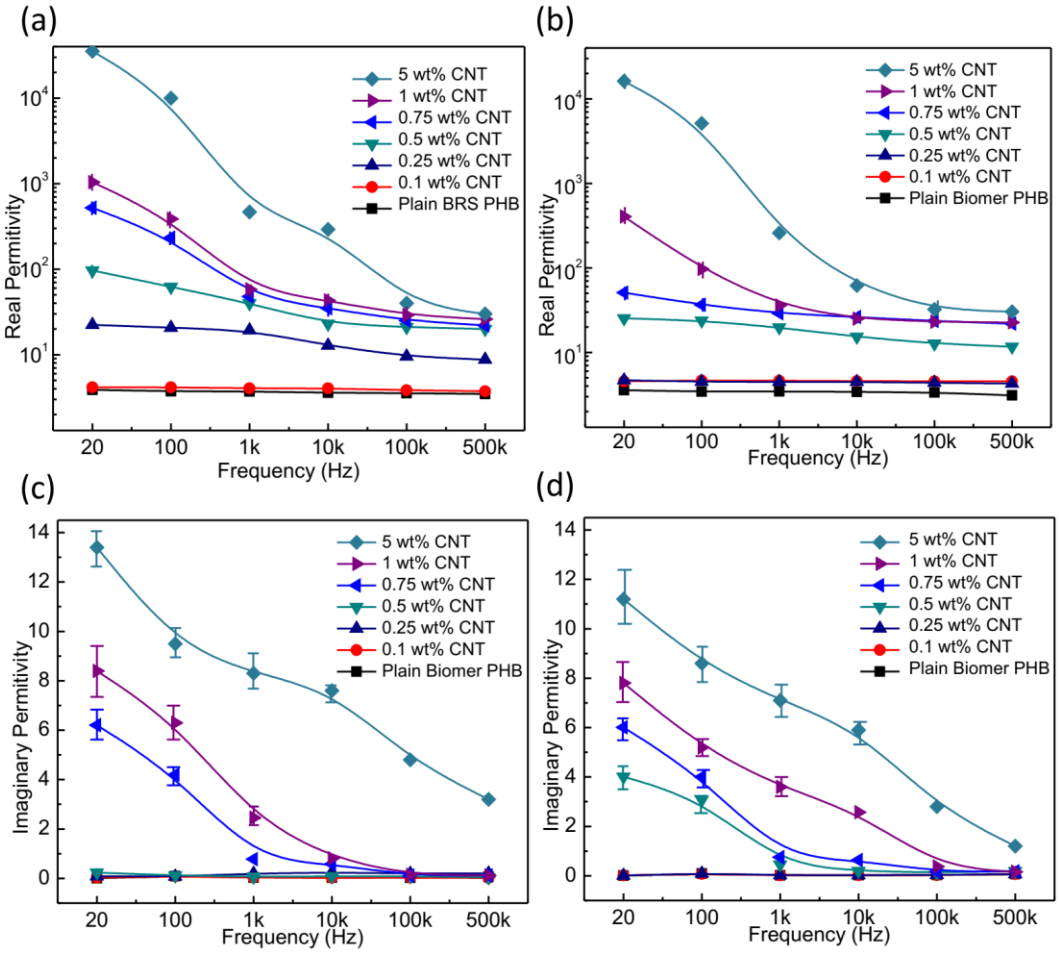

Figure 5.8 Real permittivity of BRS PHB/MWCNT composites (a) and Biomer PHB/MWCNTs composites (b), and imaginary permittivity of BRS PHB/MWCNTs composites (c) Biomer PHB/MWCNTs composites (d).

Planar and 3D Printed Structures

Having characterized the morphology, electrical, and dielectrical properties of composites and biopolymer, the extruded filaments were used to print – by FDM – dumbbell shapes for tensile testing, 2D circuits and 3D designs. Composites with 1 wt% loading of MWCNTs in Biomer PHB were selected for printing because they exhibited the best combination of low resistivity and

acceptable flexbility. Figure 5.9 (a) shows tensile tests conducted on 3D printed dumbbells; in general the 3D printed dumbbells exhibited lower Young's modulus than the compression molded materials but similar elongation at break. This reduction in modulus likely results from the fact that the 3D printed structures are not perfectly compact, rather they incorporate some air space introduced as a part of the printing process. [29] Figure 5.9 (b) compares the average conductivity of the extruded filaments (Biomer: 1200 Ω cm, BRS: 5000 Ω cm at 1 wt %), compression molded samples (Biomer: 780 Ω cm, BRS: 100 Ω cm at 1 wt %), and printed 3D object (Biomer: 900 Ω cm, BRS: 240 Ω cm at 1 wt %). Overall, the compression molded samples had slightly lower resistivity compared to the printed materials, suggesting the voids and air bubbles increased the resistivity of composites. Figure 5.9 (c) compares the resistivity change of 1 wt% Biomer filament under bending test with the strain up to 2 %. The result suggested that resistivity of filaments is slightly influenced by mechanical deformation (bending). Figure 5.9 (d) and (e) showed the 2D circuits that can light up the led lights from 3V. Figure 5. 9 (f) showed that the filaments were capable of being used in the printing of complicated 2D designs.

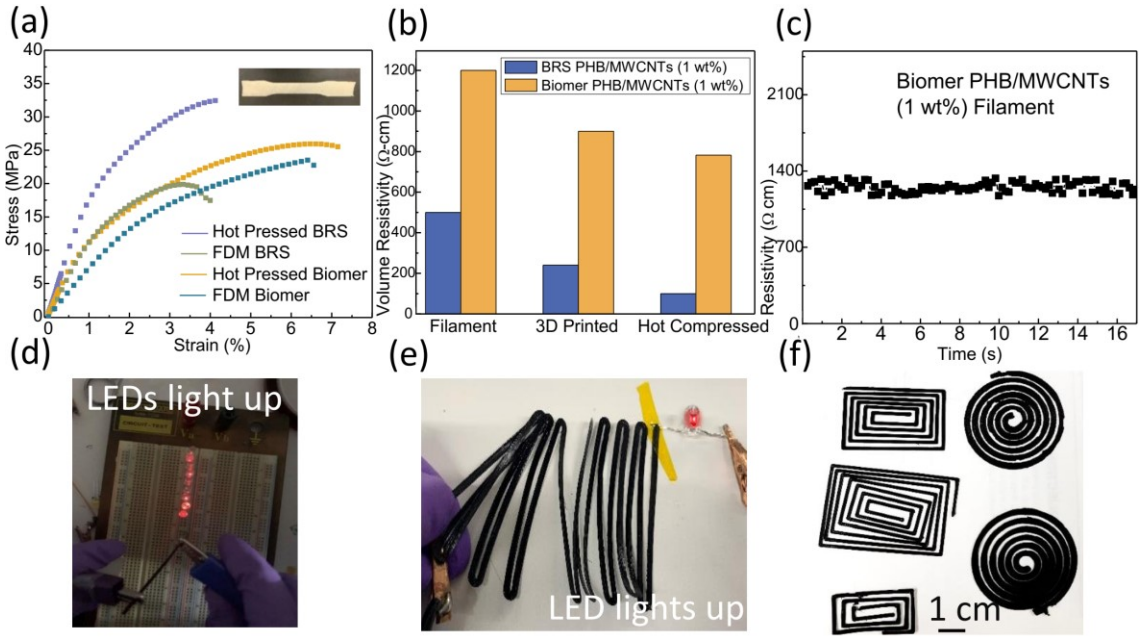

Figure 5.9 (a) Stress-strain curves of 3D printed and compression molded dumbbell shape biopolymers. (b) Average volume resistivity comparison among compressed PHB/CNTs samples, extruded composite filaments, and printed 3D objects using filaments. (c) Resistivity change of 1 wt% Biomer/CNTs filament under bending deformation (strain up to 2 %). (d) A series of LED light up under 3 V using 1 wt % Biomer/CNTs filament as wire. (e) and (f) Printed meandering, zigzag, and spiral-shaped conductive leads.

3D Printed Scaffolds

Porous scaffold structures with dimensions of 1 cm^3 cube were printed using each type of PHB with a range of filler content. To characterize the structure of 3D printed scaffolds, optical microscopy was used. Figures 5.10 (a) and (d) are optical images of the pores on the scaffold, and inset pictures depict top view of scaffolds. Both PHB biopolymer and PHB/MWCNTs composite scaffolds have a spongy appearance, with square-like organized pores ranging from 50 to 100 µm in size. Figure 5.10 (b) and (e) show the structure of the side view of scaffolds, where the printed

layers are uniform and around 150 μm in thickness. The porosity P of the PHB and composite scaffolds was estimated by taking into account the weight and volume of scaffolds as well as the density of the two types of PHB and MWCNTs, $P = \frac{\rho V - M}{\rho V} \times 100\ \%$. The P (%) is defined as porosity, ρ (g/cm^3)is the density of the material, V (cm^3) is the volume of the scaffold, and M (g) is the measured weight of the scaffold. The porosity results are shown in Figure 5.10 (c). Each of these structures was found to have a high porosity (over 40 %), in line with the porosity of trabecular bones in human body (30% to 90%).[43,44] Figure 5.10 (f) presents the compressive modulus of BRS and Biomer scaffolds as well as Biomer PHB/MWCNTs (1 wt%) composite scaffolds under standard DMA frequency sweeping (0.01 Hz to 100 Hz). All of three of the scaffolds had a compressive modulus on the order of 10^2 MPa, where the 1 wt% composite scaffold showed slightly higher compressive modulus than the other two. This range of compressive modulus is comparable to the modulus of bone (70 to 400 MPa). [44,45]

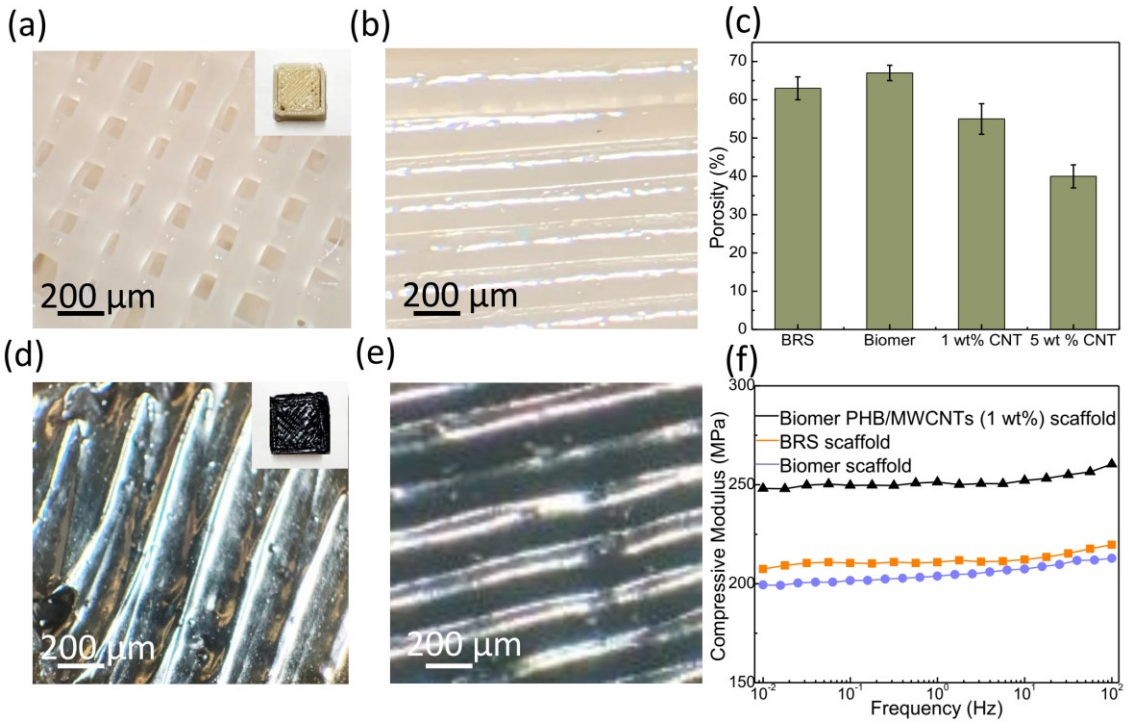

Figure 5.10 (a) and (d) are the optical images of Biomer PHB and Biomer PHB/MWCNTs composite scaffolds, and the inside pictures are top view pictures of each scaffold (1 cm^3). (b) and (e) are the optical images of the side view of Biomer PHB and Biomer PHB/MWCNTs scaffolds. (c) is the porosity comparison among biopolymer and composite scaffolds. (f) is the compressive modulus of BRS, Biomer, and 1 wt % composite Biomer PHB/MWCNTs scaffolds under DMA frequency sweeping.

Cell Cytotoxicity

Biocompatibility is an important requirement for composite materials used in biomedical applications. The cytotoxicity of PHB/MWCNTs composites is not known though the PHB biopolymer itself is biocompatible and free MWCNTs may be toxic. The MRC-5 (Medical Research Council cell strain 5) fibroblast cells were incubated with our printed scaffolds (with CNTs content of up to 5 wt%), and cell viabilities were analyzed by standard cell proliferation test

(MTT) assay, listed in Figure 5.11. After 24 h of incubation, cell viabilities of 94.6% and 97.9% were obtained from Medical Research Council cell strain-5 (MRC-5) fibroblast cells, in neat BRS and Biomer neat polymer samples. Overall, cell viabilities gradually decreased in composites by increasing the MWCNTs content, with 80.7% and 81.3%, respectively in 5 wt % composites. In spite of this small difference of cell viabilities among neat polymer and 5 wt% MWCNTs composites, this result suggests that adding MWCNTs into the PHB polymer may be very low cytotoxic to cell lines. Overall excellent biocompatibility may be ascribed to the fact that fixed MWCNTs that was mixed into the polymer matrix is not toxic at a cellular level. The morphology of cell attachment on the scaffolds is listed in Figure 5.12 observed using optical microscopy, showing good cell proliferation and no obvious cell shape deformation on printed scaffolds.

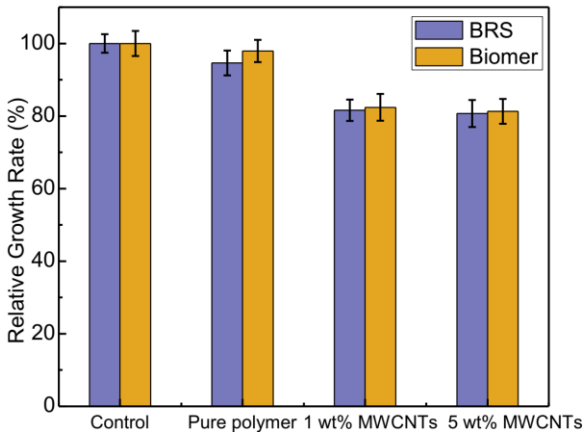

Figure 5.11 Cell viability of MRC-5 normal cells after 24 h incubation with biopolymer and MWCNTs composites.

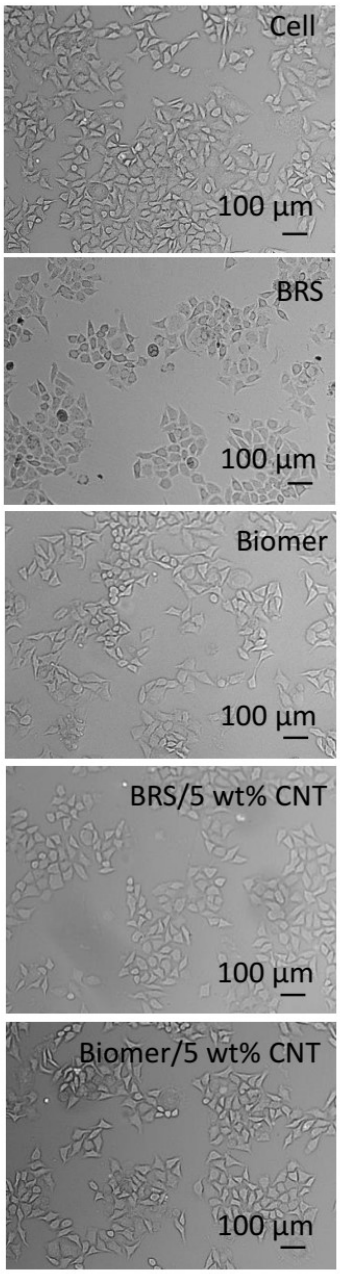

Figure 5.12 Optical images of cell morphologies attached on different samples.

5.7 Discussion

In recent years, PHB has become increasingly utilized in medical applications due to its good biological performance, thermal stability, and thermoplastic properties. Although it has been shown that PHB can be enzymatically degraded in the environment by various types of bacteria,[51,52] it has also been shown to be relatively stable in the body, undergoing a mass loss of

only 0 to 1.6 wt% during 6 months implantation (depending on its chemical formulation).[53] For some applications, electrical conductivity would be a benefit. PHB can be made conductive through the addition of conductive nanofillers. Two types of PHB – BRS (neat PHB) and Biomer P209 (containing plasticizers and nucleating agents) – were examined in this work. As observed by both SEM and TEM of 1 wt% samples, the BRS PHB/MWCNT composites had slightly better dispersion at microscale compared to the Biomer composites. In a previous study from one of the coauthors, it was shown that for polycarbonate (PC)-CNT composites prepared under conditions where the melt viscosity was kept constant for the different samples, composites made from lower molecular weight PC exhibited smaller undispersed primary agglomerates compared to composites formed using higher molecular weight PC.[53] Although in our study temperature, rather than melt viscosity, was kept constant during processing, differences in the molecular weight (MW) of the two types of polymers are expected to contribute to differences in dispersion. Our observation of better dispersion being achieved in the lower MW polymer is consistent with the previous results from the PC-CNT study.

The mechanical properties of the composites were strongly related to the mechanical properties of the polymers. Structures 3D-printed from the Biomer polymer exhibited a lower Young's modulus and larger strain to break compared to BRS biopolymer. At each wt% loading of MWCNTs (from 0 wt% to 5 wt%), the Biomer PHB/MWCNT composites – which had higher MW but also included additives such as plasticizers) – were more ductile than the BRS PHB/MWCNT composites (exhibiting a smaller Young's modulus and larger strain at break at each wt% loading).

As expected, the addition of MWCNTs led to a gradual increase in Young's modulus as a function of wt% loading in each type of polymer. While the use of a commercially-formulated PHB

containing plasticizers can enhance the flexibility of polymer, the addition of a stiff nanofiller like MWCNTs will inevitably increase the stiffness of materials.

Incorporating MWCNTs into the polymer matrix also resulted in a reduction in strain at break (as a function of wt% loading) for each type of polymer. Interestingly, the strain at break of the Biomer PHB MWCNT composite decreased noticeably upon the addition of even the lowest wt% MWCNTs; this may result from the formation of agglomerations that acted as weak points during mechanical testing. In comparison, the decline in strain at break of the BRS PHB-MWCNT composite was more gradual, decreasing from an already low value of 4.4 % at 0 wt% loading to 3.4 % at 5 wt% loading of MWCNTs.

The composites prepared using the lower molecular weight BRS PHB (containing no plasticizers) showed slightly better electrical and dielectric properties than composites incorporating the Biomer (higher conductivity and real permittivity at the same wt% loading). The sharp changes in properties achieved at relatively low loading results both from the high intrinsic conductivity of the MWCNTs, and the good dispersion achieved in each material. Importantly, this dispersion was maintained through multiple processing steps, from mixing the composites in a twin screw extruder, forming filaments, and 3D printing.

FDM, the 3D printing technique utilized in our work, can be used to construct complex 3D designs with well-defined details. While the biopolymer PLA has been utilized extensively as a 3D printing filament, to our knowledge, thermoplastic PHB and PHB/CNTs composite filaments have not been demonstrated previously by FDM. Optimal printing parameters have been established in this work, and structure characterization of printed subjects has been investigated. Printed samples showed lower mechanical properties (smaller Young's modulus and strain at break) compared with

polymer samples manufactured through molding. 3D printing enables us to print complex 2D or 3D designs, such as conductive circuits, scaffolds.

The 3D printed scaffolds demonstrated here are good candidates for use in bone tissue engineering applications. The compressive modulus of fabricated scaffolds is comparable to that of bone tissue, suggesting that these structures can mimic the mechanical environment in which bone cells can develop. The conductivity of the materials is also of interest for tissue engineering applications, as it has been shown that conductive scaffolds can be used to stimulate function in cells.[14,25] Our work has shown that the composites utilized in these scaffolds show low cytotoxicity to fibroblasts. Through variation of the printing parameters, the size of the pores can be tuned using the 3D printing process. As has been shown previously, both porosity and pore size will influence cell infiltration, and higher infiltration is expected in high porosity samples with large pores.[54,55] The next step in these studies will be to seed the scaffolds with osteoblasts and study their viability, morphology, and growth over time.

5.8 Conclusions

In this work, we demonstrate that functional PHB composites can be printed by FDM to form porous scaffolds and other 3D structures. Filaments were prepared from extruded composites, and patterned in a desktop 3D printer. To address the inherent brittleness of PHB, a commercial polymer (Biomer) containing plasticizers and nucleating agents was utilized and the properties of this material were compared to a more homogeneous PHB. Conductive composites could be prepared from each type of material, however when MWCNTs were introduced into the PHBs the stiffening effect of the nanofiller outweighed the plasticizing effect of the additives in the Biomer material. PHB and PHB/MWCNT composite scaffolds with hierarchically pore structure have

been made through 3D printing. 3D cubic scaffolds have relatively uniform inner pores, with a high porosity, high compressive modulus, and no obvious toxicity. This work presents opportunities for the development of biopolymers that can be functionalized for use in electronic devices such as sensors and bone regeneration applications.

5.9 References

(1) Lawson, S.; Snarzyk, M.; Hanify, D.; Rownaghi, A. A.; Rezaei, F. Development of 3D-Printed Polymer-MOF Monoliths for CO2 Adsorption. *Ind. Eng. Chem. Res.* **2020**, *59 (15), 7151–7160.*

(2) Uz, M.; Donta, M.; Mededovic, M.; Sakaguchi, D. S.; Mallapragada, S. K. Development of Gelatin and Graphene-Based Nerve Regeneration Conduits Using Three-Dimensional (3D) Printing Strategies for Electrical Transdifferentiation of Mesenchymal Stem Cells. *Ind. Eng. Chem. Res.* **2019**, *58 (18), 7421–7427.*

(3) Yang, L.; Chen, Y.; Wang, M.; Shi, S.; Jing, J. Fused Deposition Modeling 3D Printing of Novel Poly(Vinyl Alcohol)/Graphene Nanocomposite with Enhanced Mechanical and Electromagnetic Interference Shielding Properties. *Ind. Eng. Chem. Res.* **2020**, *59 (16), 8066–8077.*

(4) Bitounis, D.; Ali-Boucetta, H.; Hong, B. H.; Min, D.-H.; Kostarelos, K. Prospects and Challenges of Graphene in Biomedical Applications. *Adv. Mater.* **2013**, *25 (16), 2258–2268*.

(5) Jakus, A. E.; Secor, E. B.; Rutz, A. L.; Jordan, S. W.; Hersam, M. C.; Shah, R. N. Three-Dimensional Printing of High-Content Graphene Scaffolds for Electronic and Biomedical Applications. *ACS Nano* **2015**, *9 (4), 4636–4648.*

(6) Shao, Y.; Wang, J.; Wu, H.; Liu, J.; Aksay, I. A.; Lin, Y. Graphene Based Electrochemical Sensors and Biosensors: A Review. *Electroanalysis* **2010**, *22 (10), 1027–1036.*

(7) Wujcik, E. K.; Monty, C. N. Nanotechnology for Implantable Sensors: Carbon Nanotubes and Graphene in Medicine. *WIREs Nanomedicine Nanobiotechnology* **2013**, *5 (3), 233–249.*

(8) Dan, L.; Shi, S.; Chung, H.-J.; Elias, A. Porous Polydimethylsiloxane–Silver Nanowire Devices for Wearable Pressure Sensors. *ACS Appl. Nano Mater.* **2019**, *2 (8), 4869–4878.*

(9) Martinelli, V.; Cellot, G.; Toma, F. M.; Long, C. S.; Caldwell, J. H.; Zentilin, L.; Giacca, M.; Turco, A.; Prato, M.; Ballerini, L.; Mestroni, L. Carbon Nanotubes Promote Growth and Spontaneous Electrical Activity in Cultured Cardiac Myocytes. *Nano Lett.* **2012**, *12 (4), 1831–1838.*

(10) Köse, G. T.; Korkusuz, F.; Korkusuz, P.; Hasirci, V. In Vivo Tissue Engineering of Bone Using Poly(3-Hydroxybutyric Acid-Co-3-Hydroxyvaleric Acid) and Collagen Scaffolds. *Tissue Eng.* **2004**, *10 (7–8), 1234–1250.*

(11) Zhao, K.; Deng, Y.; Chun Chen, J.; Chen, G.-Q. Polyhydroxyalkanoate (PHA) Scaffolds with Good Mechanical Properties and Biocompatibility. *Biomaterials* **2003**, *24 (6), 1041–1045.*

(12) Amaro, L.; Correia, D. M.; Marques-Almeida, T.; Martins, P. M.; Pérez, L.; Vilas, J. L.; Botelho, G.; Lanceros-Mendez, S.; Ribeiro, C. Tailored Biodegradable and Electroactive Poly(Hydroxybutyrate-Co-Hydroxyvalerate) Based Morphologies for Tissue Engineering Applications. *Int. J. Mol. Sci.* **2018**, *19 (8), 2149.*

(13) Nguyen, T. H.; Ishizuna, F.; Sato, Y.; Arai, H.; Ishii, M. Physiological Characterization of Poly-β-Hydroxybutyrate Accumulation in the Moderately Thermophilic Hydrogen-Oxidizing Bacterium Hydrogenophilus Thermoluteolus TH-1. *J. Biosci. Bioeng.* **2019**, *127 (6), 686–689.*

(14) Knowles, J. C.; Mahmud, F. A.; Hastings, G. W. Piezoelectric Characteristics of a Polyhydroxybutyrate-Based Composite. *Clin. Mater.* **1991**, *8 (1), 155–158.*

(15) Jiang, S.; Wang, M.; He, J. A Review of Biomimetic Scaffolds for Bone Regeneration: Towards a Cell-Free Strategy. *Bioeng. Transl. Med.* **2020**, *e10206.*

(16) Alamusi; Hu, N.; Fukunaga, H.; Atobe, S.; Liu, Y.; Li, J. Piezoresistive Strain Sensors Made from Carbon Nanotubes Based Polymer Nanocomposites. *Sensors* **2011**, 1*1 (11), 10691–10723.*
(17) Bonaccorso, F.; Bartolotta, A.; Coleman, J. N.; Backes, C. 2D-Crystal-Based Functional Inks. *Adv. Mater.* **2016**, *28 (29), 6136–6166.*
(18) Eatemadi, A.; Daraee, H.; Karimkhanloo, H.; Kouhi, M.; Zarghami, N.; Akbarzadeh, A.; Abasi, M.; Hanifehpour, Y.; Joo, S. W. Carbon Nanotubes: Properties, Synthesis, Purification, and Medical Applications. *Nanoscale Res. Lett.* **2014**, *9 (1), 393.*
(19) Coleman, J. N.; Khan, U.; Blau, W. J.; Gun'ko, Y. K. Small but Strong: A Review of the Mechanical Properties of Carbon Nanotube–Polymer Composites. *Carbon* **2006**, *44 (9), 1624–1652.*
(20) Mora, A.; Verma, P.; Kumar, S. Electrical Conductivity of CNT/Polymer Composites: 3D Printing, Measurements and Modeling. *Compos. Part B Eng.* **2020**, *183, 107600.*
(21) Herzberger, J.; Sirrine, J. M.; Williams, C. B.; Long, T. E. Polymer Design for 3D Printing Elastomers: Recent Advances in Structure, Properties, and Printing. *Prog. Polym. Sci.* **2019**, *97, 101144.*
(22) Kwok, S. W.; Goh, K. H. H.; Tan, Z. D.; Tan, S. T. M.; Tjiu, W. W.; Soh, J. Y.; Ng, Z. J. G.; Chan, Y. Z.; Hui, H. K.; Goh, K. E. J. Electrically Conductive Filament for 3D-Printed Circuits and Sensors. *Appl. Mater. Today* **2017**, *9, 167–175.*
(23) Gnanasekaran, K.; Heijmans, T.; van Bennekom, S.; Woldhuis, H.; Wijnia, S.; de With, G.; Friedrich, H. 3D Printing of CNT- and Graphene-Based Conductive Polymer Nanocomposites by Fused Deposition Modeling. *Appl. Mater. Today* **2017***, 9, 21–28.*
(24) Burnstine-Townley, Alex, Yoni Eshel, and Nadav Amdursky. "Conductive Scaffolds for Cardiac and Neuronal Tissue Engineering: Governing Factors and Mechanisms." *Advanced Functional Materials 30.18* **2020***: 1901369.*
(25) Kharaziha, M.; Shin, S. R.; Nikkhah, M.; Topkaya, S. N.; Masoumi, N.; Annabi, N.; Dokmeci, M. R.; Khademhosseini, A. Tough and Flexible CNT–Polymeric Hybrid Scaffolds for Engineering Cardiac Constructs. *Biomaterials* **2014**, *35 (26), 7346–7354.*
(26) Shin, S. R.; Jung, S. M.; Zalabany, M.; Kim, K.; Zorlutuna, P.; Kim, S. bok; Nikkhah, M.; Khabiry, M.; Azize, M.; Kong, J.; Wan, K.; Palacios, T.; Dokmeci, M. R.; Bae, H.; Tang, X. (Shirley); Khademhosseini, A. Carbon-Nanotube-Embedded Hydrogel Sheets for Engineering Cardiac Constructs and Bioactuators. *ACS Nano* **2013**, *7 (3), 2369–2380.*
(27) Yun, S. I.; Gadd, G. E.; Latella, B. A.; Lo, V.; Russell, R. A.; Holden, P. J. Mechanical Properties of Biodegradable Polyhydroxyalkanoates/Single Wall Carbon Nanotube Nanocomposite Films. *Polym. Bull*. **2008**, *61 (2), 267–275.*
(28) Lai, M.; Li, J.; Yang, J.; Liu, J.; Tong, X.; Cheng, H. The Morphology and Thermal Properties of Multi-Walled Carbon Nanotube and Poly(Hydroxybutyrate-Co-Hydroxyvalerate) Composite. *Polym. Int*. **2004**, *53 (10), 1479–1484.*
(29) Valentini, L.; Fabbri, P.; Messori, M.; Esposti, M. D.; Bon, S. B. Multilayer Films Composed of Conductive Poly(3-Hydroxybutyrate)/Carbon Nanotubes Bionanocomposites and a Photoresponsive Conducting Polymer. J. Polym. *Sci. Part B Polym. Phys*. **2014**, *52 (8), 596–602.*
(30) Valentini, L.; Cardinali, M.; Kenny, J. Flexible Triboelectric Generator and Pressure Sensor Based on Poly[(R)-3-Hydroxybutyric Acid] Biopolymer. *J. Polym. Sci. Part B Polym. Phys.* **2014**, *52 (13), 859–863.*

(31) Anbukarasu, P.; Sauvageau, D.; Elias, A. Tuning the Properties of Polyhydroxybutyrate Films Using Acetic Acid via Solvent Casting. *Sci. Rep.* **2015**, *5.*
(32) Pegel, S.; Pötschke, P.; Villmow, T.; Stoyan, D.; Heinrich, G. Spatial Statistics of Carbon Nanotube Polymer Composites. *Polymer* **2009**, *50 (9), 2123–2132.*
(33) Dan, L.; Pope, M. A.; Elias, A. L. Solution-Processed Conductive Biocomposites Based on Polyhydroxybutyrate and Reduced Graphene Oxide. *J. Phys. Chem. C* **2018**, *122 (30), 17490–17500.*
(34) Lopera-Valle, A.; Caputo, J. V.; Leão, R.; Sauvageau, D.; Luz, S. M.; Elias, A. Influence of Epoxidized Canola Oil (ECO) and Cellulose Nanocrystals (CNCs) on the Mechanical and Thermal Properties of Polyhydroxybutyrate (PHB)—Poly(Lactic Acid) (PLA) Blends. *Polymers* **2019**, *11 (6), 933.*
(35) Li, Y.; Huang, X.; Zeng, L.; Li, R.; Tian, H.; Fu, X.; Wang, Y.; Zhong, W.-H. A Review of the Electrical and Mechanical Properties of Carbon Nanofiller-Reinforced Polymer Composites. *J. Mater. Sci.* **2019**, *54 (2), 1036–1076.*
(36) Lopes, A. C.; Costa, C. M.; Tavares, C. J.; Neves, I. C.; Lanceros-Mendez, S. Nucleation of the Electroactive γ Phase and Enhancement of the Optical Transparency in Low Filler Content Poly(Vinylidene)/Clay Nanocomposites. *J. Phys. Chem. C* **2011**, *115 (37), 18076–18082.*
(37) Sencadas, V.; Martins, P.; Pitães, A.; Benelmekki, M.; Gómez Ribelles, J. L.; Lanceros-Mendez, S. Influence of Ferrite Nanoparticle Type and Content on the Crystallization Kinetics and Electroactive Phase Nucleation of Poly(Vinylidene Fluoride). *Langmuir* **2011**, *27 (11), 7241–7249.*
(38) Arza, C. R.; Jannasch, P.; Maurer, F. H. J. Network Formation of Graphene Oxide in Poly(3-Hydroxybutyrate) Nanocomposites. *Eur. Polym. J.* **2014**, *59, 262–269.*
(39) Ferrari, A. C.; Robertson, J. Interpretation of Raman Spectra of Disordered and Amorphous Carbon. *Phys. Rev. B* **2000**, *61 (20), 14095–14107.*
(40) Socher, R.; Krause, B.; Müller, M. T.; Boldt, R.; Pötschke, P. The Influence of Matrix Viscosity on MWCNT Dispersion and Electrical Properties in Different Thermoplastic Nanocomposites. *Polymer* **2012**, *53 (2), 495–504.*
(41) Krause, B.; Rzeczkowski, P.; Pötschke, P. Thermal Conductivity and Electrical Resistivity of Melt-Mixed Polypropylene Composites Containing Mixtures of Carbon-Based Fillers. *Polymers* **2019**, *11 (6), 1073.*
(42) Li, Y.; Pionteck, J.; Pötschke, P.; Voit, B. Thermal Annealing to Influence the Vapor Sensing Behavior of Co-Continuous Poly(Lactic Acid)/Polystyrene/Multiwalled Carbon Nanotube Composites. *Mater. Des*. **2020**, *187, 108383.*
(43) Otaegi, I.; Aranburu, N.; Iturrondobeitia, M.; Ibarretxe, J.; Guerrica-Echevarría, G. The Effect of the Preparation Method and the Dispersion and Aspect Ratio of CNTs on the Mechanical and Electrical Properties of Bio-Based Polyamide-4,10/CNT Nanocomposites. *Polymers* **2019**, *11 (12), 2059.*
(44) Ribeiro, C.; Costa, C. M.; Correia, D. M.; Nunes-Pereira, J.; Oliveira, J.; Martins, P.; Gonçalves, R.; Cardoso, V. F.; Lanceros-Méndez, S. Electroactive Poly(Vinylidene Fluoride)-Based Structures for Advanced Applications. *Nat. Protoc.* **2018**, *13 (4), 681–704.*
(45) Ren, L., Zha, J. W., Li, R. K., Shi, C. Y., & Dang, Z. M.. Co-continuous structural polystyrene/poly (vinylidene fluoride) nanocomposites with high dielectric constant and magnetic properties. *Composites Communications*, **2017**, *4, 24-32.*

(46) Sabet, Maziyar, and Hassan Soleimani. "Mechanical and electrical properties of low density polyethylene filled with carbon nanotubes." *IOP Conference Series: Materials Science and Engineering. Vol. 64*. **2014**.
(47) Cabral, C. S., Miguel, S. P., de Melo-Diogo, D., Louro, R. O., & Correia, I. J.. Green reduced graphene oxide functionalized 3D printed scaffolds for bone tissue regeneration. *Carbon*, **2019**,*146, 513-523*.
(48) Zhao, S., Zhu, M., Zhang, J., Zhang, Y., Liu, Z., Zhu, Y., & Zhang, C.. Three dimensionally printed mesoporous bioactive glass and poly (3-hydroxybutyrate-co-3-hydroxyhexanoate) composite scaffolds for bone regeneration. *Journal of Materials Chemistry B*, **2014**, *2(36), 6106-6118.*
(49) Xi, J., Zhang, L., Zheng, Z. A., Chen, G., Gong, Y., Zhao, N., & Zhang, X.. Preparation and evaluation of porous poly (3-hydroxybutyrate-co-3-hydroxyhexanoate)—hydroxyapatite composite scaffolds. *Journal of biomaterials applications*, **2008**, *22(4), 293-307.*
(50) Wei, Y.-H.; Chen, W.-C.; Wu, H.-S.; Janarthanan, O.-M. Biodegradable and Biocompatible Biomaterial, Polyhydroxybutyrate, Produced by an Indigenous Vibrio Sp. BM-1 Isolated from Marine Environment. *Mar. Drugs* **2011**, *9 (4), 615–624.*
(51) Martínez-Tobón, D. I.; Gul, M.; Elias, A. L.; Sauvageau, D. Polyhydroxybutyrate (PHB) Biodegradation Using Bacterial Strains with Demonstrated and Predicted PHB Depolymerase Activity. *Appl. Microbiol. Biotechnol.* **2018**, *102 (18), 8049–8067*.
(52) Martínez-Tobón, D. I.; Waters, B.; Elias, A. L.; Sauvageau, D. Streamlined Production, Purification, and Characterization of Recombinant Extracellular Polyhydroxybutyrate Depolymerases. *Microbiology Open* **2020**, *9 (4), e1001*.
(53) Kasaliwal, G. R., Göldel, A., Pötschke, P., & Heinrich, G.. Influences of polymer matrix melt viscosity and molecular weight on MWCNT agglomerate dispersion. *Polymer,* **2011**, *52(4), 1027-1036.*
(54) Wu, J.; Hong, Y. Enhancing Cell Infiltration of Electrospun Fibrous Scaffolds in Tissue Regeneration. *Bioact. Mater*. **2016**, *1 (1), 56–64*.
(55) Rasoulianboroujeni, M.; Kiaie, N.; Tabatabaei, F. S.; Yadegari, A.; Fahimipour, F.; Khoshroo, K.; Tayebi, L. Dual Porosity Protein-Based Scaffolds with Enhanced Cell Infiltration and Proliferation. *Sci. Rep.* **2018**, *8 (1), 14889*.

6. Summary and Conclusions

The work described in this thesis demonstrates that conductive biopolymer composites comprised of reduced graphene oxide (rGO) in a polyhydroxybutyrate (PHB) matrix can be achieved by using in-situ reduction with the presence of acetic acid and suitable processing parameters. Conductive rGO/PHB composites show temperature-dependent resistance; thus temperature sensors have been fabricated using the composite as sensing layers. Printing techniques have been used in this work to pattern composite inks, in some cases on elastomeric substrates that were also printed. Together, printed, intrinsically elastic substrates and responsive layers shaped in a meandering pattern form sensors that are both stretchable and highly flexible, and which do not undergo a noticeable sensitivity change (in response to temperature) under deformation. These sensors are capable of monitoring human body temperature on curved surfaces such as the forehead or wrist. It was also shown that highly conductive PHB-carbon nanotube (CNT) composites could be fabricated using melt mixing, which does not require the use of organic solvent. The desired portion of CNTs was blended with PHB pellets in a twin-screw extruder, and then shaped in a filament extruder to form conductive filaments for use in 3D printing. These filaments could be printed out by standard 3D printer with controllable porosity and architecture. More detailed conclusion of the studies presented in each chapter follow.

Three different reducing agents (e.g. hydrazine (N_2H_4), sodium borohydride ($NaBH_4$), L-ascorbic acid (L-A.A)) were utilized to reduce rGO to form conductive rGO/PHB composite in the presence of ascorbic acid. The Chapter 3 was entitled: “Solution-processed conductive biocomposites based on polyhydroxybutyrate and reduced graphene oxide”. The work systematically compared the effects of three reducing agents by comparing reduction efficiency, carbon and oxygen atom ratio presented on the resulted rGO, and the conductivity, morphologies of the formed composites. L-

ascorbic acid shows the lowest electrical percolation threshold (1 wt%) and the highest known values for rGO/PHB composites. The mechanical properties were characterized, and a strain sensor was demonstrated using these composites. This work provides insight into the fundamental properties of biopolymer-graphenic nanomaterial composites, and shows how highly conductive composites can be prepared from solution.

A simple and low-cost temperature sensor was proposed in Chapter 4 entitled "Flexible and stretchable temperature sensors fabricated using solution-processable conductive polymer composites". The responsive element of the temperature sensor is a conductive rGO/PHB composite deposited on both flexible and stretchable polymer substrates through both drop coating and direct ink writing (DIW). A high melting point biopolymer PHB was used as the matrix and the graphenic material rGO as the nanofiller, resulting in a material that exhibits a temperature-dependent resistivity. One important property of sensors is selectivity to the desired stimulus. To compensate for the mechanical stress that occurs during bending, a meandering pattern was deposited. This pattern showed no obvious resistivity change under bending. This chapter adds to the current literature about composite printing and offers exciting future directions on designing and patterning flexible composite electronics.

Chapter 5 is entitled "3D Printed and Biocompatible Conductive Composites Comprised of Polyhydroxybutyrate and Multi-Walled Carbon Nanotubes ". Multi-walled nanotubes (MWCNTs) and PHB were blend in amount from 0.25 to 5 wt% and then 3D printed using a commercially available desktop 3D printer. It was shown that MWCNTs/PHB composites could be printed out smoothly into neat scaffolds structure with tunable porosity and architecture, and low cytotoxicity. These materials may be potentially used in bone regeneration applications. The results of this

research may help to advance work on 3D printing of composites involving other thermal plastics and fillers such as cellulose, graphenic materials.

The findings in this thesis, in addition to forming an integral part of conductive biopolymer composites (CPCs) development, could have applications in biomedical fields for healthcare monitoring. For example, the in-situ reduction method (Chapter 3) to reduce graphene oxide (GO) in the presence of PHB and acetic acid using ascorbic acid can be utilized to prepare other rGO related CPCs for better rGO compatibility and distribution. The temperature sensor comprised of rGO/PHB responsive patterns and flexible polymer substrates (Chapter 4) has potential use for the next generation stretchable electronics. The 3D printed CNTs/PHB composite scaffolds presented in Chapter 5 provides an insight into the composite applications in biomedical field, indicating that PHB can be used for bone regeneration as the modulus of scaffolds are comparable to the trabecular bones.

One aspect of my work focused on patterning composites using direct ink writing (DIW), a technique that is compatible with a wide range of viscosity of inks and different materials. DIW is an extrusion-based system with a size-tunable nozzle, which can therefore be used to print inks with a wider range of viscosities than printing. DIW is particularly useful in working with soft materials (solution-based inks, hydrogels, composites), and is more versatile comparted to fused deposition modelling (FDM), which can only be used with thermoplastic materials. Recent advances in DIW have focused heavily on printing hydrogels laden with cells, creating organ-like structures that let living cells multiply. These printed “mini organs” and vascularized tissues are under development for fundamental research related to drug screening, disease modeling, and tissue repair and regeneration.[1,2] However, my work has focused on another direction: patterning

of solution-processible conductive and responsive composites. The ability to print new functional materials, including conductive composites, will open up many new possibilities for the fabrication of both stretchable and conductive electrodes and responsive materials. This will allow the development of real-time, low-cost electronics and sensors on flexible substrates. Challenge of this technique that must be addressed moving forward are in printing smaller scale (μm) with fine details, and printing structures with sufficient mechanical strength for specific applications.

Overall, the work described in this thesis led to improved knowledge on conductive polymer composites which can be used in a variety of fields and applications, from biomedical fields to PHB-based sensors and devices. It established clear comparisons of different reducing agents in reducing GO with the presence of acetic acid and PHB-such studies are scarce in the available literature.[3,4,5] In the course of the work, printing technique was developed that can pattern the composite ink to desired designs. This offered a platform for the rapid development of printing electronics – demonstrated with printed meandering designs using composite inks. This system may be used to print other types of composite inks that contain filler particles, which has rarely reported before. This is a big step for widening the use of conductive composites, with the aim of large-scale fabrication in making printable and low-cost electronics.[6–8] Finally, conductive PHB composites have been fabricated through compression molding without the deployment of organic solvent, and the molded filaments can be 3D printed into different designs. These materials may have applications as conductive scaffolds that are capable of communicating with intercellular cells. Conductive scaffolds made from polymer composites are an emerging topic in current research. [9-11] Overall, my contributions add new knowledge on the 3D printing unconventional composite materials.

6.1 Future Work

Several projects can expand from the findings presented in this PhD work. Some of them could include:

An exciting avenue to investigate is designing new functional composite inks. Conductive composite inks that can be printed in a cost-effective manner could have industrial applications. Both graphenic nanofillers and metallic nanoparticles are highly conductive, but tend to have poor solubility in most common solvents. In addition, these materials tend to form agglomerates when blended with polymers. Proper ink formulation requires choosing compatible solvents and forming stable dispersions. By designing new compositions of composite inks, both conductivity and function of inks could be modified and improved. This can be achieved by using different dimensions and properties of nanofiller and polymers. Various 2D materials composite inks have been established with different functionalities, and environmentally friendly, sustainable, low cost, and highly conductive inks still need further investigation. [250]

Further development of printing techniques will be beneficial to realize more applications for conductive composite flexible electronics. The compatibility of inkjet printing is limited to inks with suitable viscosities, though good resolution print designs produced. Direct ink writing can be further investigated by improving the extrusion system to improve the print quality. Thermoplastic conductive composites can be compression molded into different dimensions including filaments that can be printed using 3D printer. Better control of filament feed system and nozzle designs can expand the use of low melting temperature polymer composites for bio printing,[9] including scaffolds demonstrated in this thesis.

Finally, aging and degradation studies could be performed on the composites demonstrated in this work so as to determine their suitability for use in various applications. They should also be subjected to *in vitro* and *in vivo* testing to determine their stability under biological conditions.

6.2 References

(1) Chortos, A., Hajiesmaili, E., Morales, J., Clarke, D. R., & Lewis, J. A.. 3D Printing of Interdigitated Dielectric Elastomer Actuators. *Advanced Functional Materials*, **2020**, *30*(1), 1907375.

(2) Skylar-Scott, M. A., Uzel, S. G., Nam, L. L., Ahrens, J. H., Truby, R. L., Damaraju, S., & Lewis, J. A.. Biomanufacturing of organ-specific tissues with high cellular density and embedded vascular channels. *Science advances*, **2019**, *5*(9), eaaw2459.

(3) Manikandan, N. A.; Pakshirajan, K.; Pugazhenthi, G. Preparation and Characterization of Environmentally Safe and Highly Biodegradable Microbial Polyhydroxybutyrate (PHB) Based Graphene Nanocomposites for Potential Food Packaging Applications. *Int. J. Biol. Macromol.* **2020**, *154*, 866–877. https://doi.org/10.1016/j.ijbiomac.2020.03.084.

(4) Daisy, E. R. A. C.; Rajendran, N. K.; Houreld, N. N.; Marraiki, N.; Elgorban, A. M.; Rajan, M. Curcumin and Gymnema Sylvestre Extract Loaded Graphene Oxide-Polyhydroxybutyrate-sodium Alginate Composite for Diabetic Wound Regeneration. *React. Funct. Polym.* **2020**, *154*, 104671. https://doi.org/10.1016/j.reactfunctpolym.2020.104671.

(5) More, N.; Srivastava, A.; Kapusetti, G. Graphene Oxide Reinforcement Enhances the Piezoelectric and Mechanical Properties of Poly(3-Hydroxybutyrate-Co-3-Hydroxy Valerate)-Based Nanofibrous Scaffolds for Improved Proliferation of Chondrocytes and ECM Production. *ACS Appl. Bio Mater.* **2020**. https://doi.org/10.1021/acsabm.0c00765.

(6) Zhang, M.; Yeow, J. T. W. A Flexible, Scalable, and Self-Powered Mid-Infrared Detector Based on Transparent PEDOT: PSS/Graphene Composite. *Carbon* **2020**, *156*, 339–345. https://doi.org/10.1016/j.carbon.2019.09.062.

(7) Soni, M.; Bhattacharjee, M.; Ntagios, M.; Dahiya, R. Printed Temperature Sensor Based on PEDOT: PSS-Graphene Oxide Composite. *IEEE Sens. J.* **2020**, *20* (14), 7525–7531. https://doi.org/10.1109/JSEN.2020.2969667.

(8) Liu, Q.; Tai, H.; Yuan, Z.; Zhou, Y.; Su, Y.; Jiang, Y. A High-Performances Flexible Temperature Sensor Composed of Polyethyleneimine/Reduced Graphene Oxide Bilayer for Real-Time Monitoring. *Adv. Mater. Technol.* **2019**, *4* (3), 1800594. https://doi.org/10.1002/admt.201800594.

(9) Codreanu, A.; Balta, C.; Herman, H.; Cotoraci, C.; Mihali, C. V.; Zurbau, N.; Zaharia, C.; Rapa, M.; Stanescu, P.; Radu, I.-C.; Vasile, E.; Lupu, G.; Galateanu, B.; Hermenean, A. Bacterial Cellulose-Modified Polyhydroxyalkanoates Scaffolds Promotes Bone Formation in Critical Size Calvarial Defects in Mice. *Materials* **2020**, *13* (6), 1433. https://doi.org/10.3390/ma13061433.

(10) Pan, K.; Fan, Y.; Leng, T.; Li, J.; Xin, Z.; Zhang, J.; Hao, L.; Gallop, J.; Novoselov, K. S.; Hu, Z. Sustainable Production of Highly Conductive Multilayer Graphene Ink for Wireless Connectivity and IoT Applications. *Nat. Commun.* **2018**, *9* (1), 5197. https://doi.org/10.1038/s41467-018-07632-w.

(11) Tran, T. S.; Dutta, N. K.; Choudhury, N. R. Graphene Inks for Printed Flexible Electronics: Graphene Dispersions, Ink Formulations, Printing Techniques and Applications. *Adv. Colloid Interface Sci.* **2018**, *261*, 41–61. https://doi.org/10.1016/j.cis.2018.09.003.

Bibliography

A bibliography of all the works cited in the thesis is listed below. The references are sorted in alphabetical order by the author's last name.

Abd El-Rehim, H. A.; Hegazy, E.-S. A.; Ali, A. M.; Rabie, A. M. Synergistic Effect of Combining UV-Sunlight–Soil Burial Treatment on the Biodegradation Rate of LDPE/Starch Blends. J. Photochem. Photobiol. Chem. 2004, 163 (3), 547–556. https://doi.org/10.1016/j.jphotochem.2004.02.003.

Abdala, A.; Barrett, J.; Srienc, F. Synthesis of Poly-(R)-3 Hydroxyoctanoate (PHO) and Its Graphene Nanocomposites. In Green Polymer Chemistry: Biocatalysis and Materials II; ACS Symposium Series; American Chemical Society, 2013; Vol. 1144, pp 199–209. https://doi.org/10.1021/bk-2013-1144.ch014.

Aboutalebi, S. H.; Gudarzi, M. M.; Zheng, Q. B.; Kim, J.-K. Spontaneous Formation of Liquid Crystals in Ultralarge Graphene Oxide Dispersions. Adv. Funct. Mater. 2011, 21 (15), 2978–2988. https://doi.org/10.1002/adfm.201100448.

Ajayan, P. M.; Stephan, O.; Colliex, C.; Trauth, D. Aligned Carbon Nanotube Arrays Formed by Cutting a Polymer Resin—Nanotube Composite. Science 1994, 265 (5176), 1212–1214. https://doi.org/10.1126/science.265.5176.1212.

Alamusi; Hu, N.; Fukunaga, H.; Atobe, S.; Liu, Y.; Li, J. Piezoresistive Strain Sensors Made from Carbon Nanotubes Based Polymer Nanocomposites. Sensors 2011, 11 (11), 10691–10723.

Aliane, A.; Fischer, V.; Galliari, M.; Tournon, L.; Gwoziecki, R.; Serbutoviez, C.; Chartier, I.; Coppard, R. Enhanced Printed Temperature Sensors on Flexible Substrate. Microelectron. J. 2014, 45 (12), 1621–1626. https://doi.org/10.1016/j.mejo.2014.08.011.

Amaro, L.; Correia, D. M.; Marques-Almeida, T.; Martins, P. M.; Pérez, L.; Vilas, J. L.; Botelho, G.; Lanceros-Mendez, S.; Ribeiro, C. Tailored Biodegradable and Electroactive Poly(Hydroxybutyrate-Co-Hydroxyvalerate) Based Morphologies for Tissue Engineering Applications. Int. J. Mol. Sci. 2018, 19 (8), 2149.

An, B. W.; Kim, K.; Kim, M.; Kim, S.-Y.; Hur, S.-H.; Park, J.-U. Direct Printing of Reduced Graphene Oxide on Planar or Highly Curved Surfaces with High Resolutions Using Electrohydrodynamics. Small 2015, 11 (19), 2263–2268. https://doi.org/10.1002/smll.201403131.

Anbukarasu, P., Sauvageau, D., & Elias, A. Tuning the properties of polyhydroxybutyrate films using acetic acid via solvent casting. Scientific reports, 2015, 5, 17884.

Anbukarasu, P.; Sauvageau, D.; Elias, A. Tuning the Properties of Polyhydroxybutyrate Films Using Acetic Acid via Solvent Casting. Sci. Rep. 2015, 5.

Anbukarasu, P.; Sauvageau, D.; Elias, A. Tuning the Properties of Polyhydroxybutyrate Films Using Acetic Acid via Solvent Casting. Sci. Rep. 2015, 5. https://doi.org/10.1038/srep17884.

Anbukarasu, Preetam, Dominic Sauvageau, and Anastasia Elias. "Tuning the properties of polyhydroxybutyrate films using acetic acid via solvent casting." Scientific reports 5 2015: 17884.

Arapov, K.; Bex, G.; Hendriks, R.; Rubingh, E.; Abbel, R.; With, G. de; Friedrich, H. Conductivity Enhancement of Binder-Based Graphene Inks by Photonic Annealing and Subsequent

Compression Rolling. Adv. Eng. Mater. 2016, 18 (7), 1234–1239. https://doi.org/10.1002/adem.201500646.

Arapov, K.; Bex, G.; Hendriks, R.; Rubingh, E.; Abbel, R.; With, G. de; Friedrich, H. Conductivity Enhancement of Binder-Based Graphene Inks by Photonic Annealing and Subsequent Compression Rolling. Adv. Eng. Mater. 2016, 18 (7), 1234–1239. https://doi.org/10.1002/adem.201500646.

Arza, C. R.; Jannasch, P.; Maurer, F. H. J. Network Formation of Graphene Oxide in Poly(3-Hydroxybutyrate) Nanocomposites. Eur. Polym. J. 2014, 59, 262–269.

Arza, C. R.; Jannasch, P.; Maurer, F. H. J. Network Formation of Graphene Oxide in Poly(3-Hydroxybutyrate) Nanocomposites. Eur. Polym. J. 2014, 59, 262–269. https://doi.org/10.1016/j.eurpolymj.2014.07.035.

Auras, R.; Harte, B.; Selke, S. An Overview of Polylactides as Packaging Materials. Macromol. Biosci. 2004, 4 (9), 835–864. https://doi.org/10.1002/mabi.200400043.

Bae, S.; Kim, H.; Lee, Y.; Xu, X.; Park, J.-S.; Zheng, Y.; Balakrishnan, J.; Lei, T.; Ri Kim, H.; Song, Y. I.; Kim, Y.-J.; Kim, K. S.; Özyilmaz, B.; Ahn, J.-H.; Hong, B. H.; Iijima, S. Roll-to-Roll Production of 30-Inch Graphene Films for Transparent Electrodes. Nat. Nanotechnol. 2010, 5 (8), 574–578. https://doi.org/10.1038/nnano.2010.132.

Bae, S.; Kim, H.; Lee, Y.; Xu, X.; Park, J.-S.; Zheng, Y.; Balakrishnan, J.; Lei, T.; Ri Kim, H.; Song, Y. I.; Kim, Y.-J.; Kim, K. S.; Özyilmaz, B.; Ahn, J.-H.; Hong, B. H.; Iijima, S. Roll-to-Roll

Production of 30-Inch Graphene Films for Transparent Electrodes. Nat. Nanotechnol. 2010, 5 (8), 574–578. https://doi.org/10.1038/nnano.2010.132.

Barletta, M.; Trovalusci, F.; Puopolo, M.; Tagliaferri, V.; Vesco, S. Engineering and Processing of Poly(HydroxyButyrate) (PHB) Modified by Nano-Sized Graphene Nanoplatelets (GNP) and Amino-Functionalized Silica (A-FnSiO2). J. Polym. Environ. 2016, 24 (1), 1–11. https://doi.org/10.1007/s10924-016-0753-z.

Basirun, W. J.; Sookhakian, M.; Baradaran, S.; Mahmoudian, M. R.; Ebadi, M. Solid-Phase Electrochemical Reduction of Graphene Oxide Films in Alkaline Solution. Nanoscale Res. Lett. 2013, 8 (1), 397. https://doi.org/10.1186/1556-276X-8-397.

Bitounis, D.; Ali-Boucetta, H.; Hong, B. H.; Min, D.-H.; Kostarelos, K. Prospects and Challenges of Graphene in Biomedical Applications. Adv. Mater. 2013, 25 (16), 2258–2268.

Bitounis, D.; Ali-Boucetta, H.; Hong, B. H.; Min, D.-H.; Kostarelos, K. Prospects and Challenges of Graphene in Biomedical Applications. Adv. Mater. 2013, 25 (16), 2258–2268. https://doi.org/10.1002/adma.201203700.

Boffa, V.; Etmimi, H.; Mallon, P. E.; Tao, H. Z.; Magnacca, G.; Yue, Y. Z. Carbon-Based Building Blocks for Alcohol Dehydration Membranes with Disorder-Enhanced Water Permeability. Carbon 2017, 118, 458–466. https://doi.org/10.1016/j.carbon.2017.03.077.

Bonaccorso, F.; Bartolotta, A.; Coleman, J. N.; Backes, C. 2D-Crystal-Based Functional Inks. Adv. Mater. 2016, 28 (29), 6136–6166.

Bonaccorso, F.; Lombardo, A.; Hasan, T.; Sun, Z.; Colombo, L.; Ferrari, A. C. Production and Processing of Graphene and 2d Crystals. Mater. Today 2012, 15 (12), 564–589. https://doi.org/10.1016/S1369-7021(13)70014-2.

Bonaccorso, F.; Lombardo, A.; Hasan, T.; Sun, Z.; Colombo, L.; Ferrari, A. C. Production and Processing of Graphene and 2d Crystals. Mater. Today 2012, 15 (12), 564–589. https://doi.org/10.1016/S1369-7021(13)70014-2.

Bonaccorso, F.; Sun, Z.; Hasan, T.; Ferrari, A. C. Graphene Photonics and Optoelectronics. Nat. Photonics 2010, 4 (9), 611–622. https://doi.org/10.1038/nphoton.2010.186.

Brodie, B. C. XIII. On the Atomic Weight of Graphite. Philos. Trans. R. Soc. Lond. 1859, 149, 249–259. https://doi.org/10.1098/rstl.1859.0013.

Brody, T. P. The Birth and Early Childhood of Active Matrix — A Personal Memoir. J. Soc. Inf. Disp. 1996, 4 (3), 113–127. https://doi.org/10.1889/1.1985000.

Bucci, D. Z.; Tavares, L. B. B.; Sell, I. PHB Packaging for the Storage of Food Products. Polym. Test. 2005, 24 (5), 564–571. https://doi.org/10.1016/j.polymertesting.2005.02.008.

Burnstine-Townley, Alex, Yoni Eshel, and Nadav Amdursky. "Conductive Scaffolds for Cardiac and Neuronal Tissue Engineering: Governing Factors and Mechanisms." Advanced Functional Materials 30.18 2020: 1901369.

Cabral, C. S., Miguel, S. P., de Melo-Diogo, D., Louro, R. O., & Correia, I. J.. Green reduced graphene oxide functionalized 3D printed scaffolds for bone tissue regeneration. Carbon, 2019,146, 513-523.

Castro-Aguirre, E.; Iñiguez-Franco, F.; Samsudin, H.; Fang, X.; Auras, R. Poly(Lactic Acid)—Mass Production, Processing, Industrial Applications, and End of Life. Adv. Drug Deliv. Rev. 2016, 107, 333–366. https://doi.org/10.1016/j.addr.2016.03.010.

Chakravarty, D.; Late, D. J. Exfoliation of Bulk Inorganic Layered Materials into Nanosheets by the Rapid Quenching Method and Their Electrochemical Performance. Eur. J. Inorg. Chem. 2015, 2015 (11), 1973–1980. https://doi.org/10.1002/ejic.201500039.

Chan, R. T. H.; Russell, R. A.; Marçal, H.; Lee, T. H.; Holden, P. J.; Foster, L. J. R. BioPEGylation of Polyhydroxybutyrate Promotes Nerve Cell Health and Migration. Biomacromolecules 2014, 15 (1), 339–349. https://doi.org/10.1021/bm401572a.

Chen, C.; Yang, Q.-H.; Yang, Y.; Lv, W.; Wen, Y.; Hou, P.-X.; Wang, M.; Cheng, H.-M. Self-Assembled Free-Standing Graphite Oxide Membrane. Adv. Mater. 2009, 21 (29), 3007–3011. https://doi.org/10.1002/adma.200803726.

Chen, G.-Q. A Microbial Polyhydroxyalkanoates (PHA) Based Bio- and Materials Industry. Chem. Soc. Rev. 2009, 38 (8), 2434–2446. https://doi.org/10.1039/B812677C.

Chen, J.; Tee, C. K.; Shtein, M.; Martin, D. C.; Anthony, J. Controlled Solution Deposition and Systematic Study of Charge-Transport Anisotropy in Single Crystal and Single-Crystal Textured TIPS Pentacene Thin Films. Org. Electron. 2009, 10 (4), 696–703. https://doi.org/10.1016/j.orgel.2009.03.007.

Chen, J.; Yao, B.; Li, C.; Shi, G. An Improved Hummers Method for Eco-Friendly Synthesis of Graphene Oxide. Carbon 2013, 64, 225–229. https://doi.org/10.1016/j.carbon.2013.07.055.

Chen, J.; Yao, B.; Li, C.; Shi, G. An Improved Hummers Method for Eco-Friendly Synthesis of Graphene Oxide. Carbon 2013, 64, 225–229. https://doi.org/10.1016/j.carbon.2013.07.055.

Cheng, Yehong, et al. "Enhanced mechanical, thermal, and electric properties of graphene aerogels via supercritical ethanol drying and high-temperature thermal reduction." Scientific reports 7.1 2017: 1-11.

Chiellini, E.; Corti, A.; D'Antone, S.; Solaro, R. Biodegradation of Poly (Vinyl Alcohol) Based Materials. Prog. Polym. Sci. 2003, 28 (6), 963–1014. https://doi.org/10.1016/S0079-6700(02)00149-1.

Chu, K.; Park, S.-H. Electrical Heating Behavior of Flexible Carbon Nanotube Composites with Different Aspect Ratios. J. Ind. Eng. Chem. 2016, 35, 195–198. https://doi.org/10.1016/j.jiec.2015.12.033.

Codreanu, A.; Balta, C.; Herman, H.; Cotoraci, C.; Mihali, C. V.; Zurbau, N.; Zaharia, C.; Rapa, M.; Stanescu, P.; Radu, I.-C.; Vasile, E.; Lupu, G.; Galateanu, B.; Hermenean, A. Bacterial Cellulose-Modified Polyhydroxyalkanoates Scaffolds Promotes Bone Formation in Critical Size Calvarial Defects in Mice. Materials 2020, 13 (6), 1433. https://doi.org/10.3390/ma13061433.

Coelho, P. H. da S. L.; Marchesin, M. S.; Morales, A. R.; Bartoli, J. R. Electrical Percolation, Morphological and Dispersion Properties of MWCNT/PMMA Nanocomposites. Mater. Res. 2014, 17, 127–132. https://doi.org/10.1590/S1516-14392014005000059.

Cole, M.; Lindeque, P.; Halsband, C.; Galloway, T. S. Microplastics as Contaminants in the Marine Environment: A Review. Mar. Pollut. Bull. 2011, 62 (12), 2588–2597. https://doi.org/10.1016/j.marpolbul.2011.09.025.

Coleman, J. N.; Khan, U.; Blau, W. J.; Gun'ko, Y. K. Small but Strong: A Review of the Mechanical Properties of Carbon Nanotube–Polymer Composites. Carbon 2006, 44 (9), 1624–1652.

Coleman, J. N.; Khan, U.; Blau, W. J.; Gun'ko, Y. K. Small but Strong: A Review of the Mechanical Properties of Carbon Nanotube–Polymer Composites. Carbon 2006, 44 (9), 1624–1652. https://doi.org/10.1016/j.carbon.2006.02.038.

Compton, O. C.; Nguyen, S. T. Graphene Oxide, Highly Reduced Graphene Oxide, and Graphene: Versatile Building Blocks for Carbon-Based Materials. Small 2010, 6 (6), 711–723. https://doi.org/10.1002/smll.200901934.

Cote, Laura J., Franklin Kim, and Jiaxing Huang. "Langmuir− Blodgett assembly of graphite oxide single layers." Journal of the American Chemical Society 131.3 2009: 1043-1049.

Cote, Laura J., Franklin Kim, and Jiaxing Huang. "Langmuir− Blodgett assembly of graphite oxide single layers." Journal of the American Chemical Society 131.3 2009: 1043-1049.

Cottet, D.; Grzyb, J.; Kirstein, T.; Troster, G. Electrical Characterization of Textile Transmission Lines. IEEE Trans. Adv. Packag. 2003, 26 (2), 182–190. https://doi.org/10.1109/TADVP.2003.817329.

Cui, X.; Chen, J.; Zhu, Y.; Jiang, W. Lightweight and Conductive Carbon Black/Chlorinated Poly(Propylene Carbonate) Foams with a Remarkable Negative Temperature Coefficient Effect of Resistance for Temperature Sensor Applications. J. Mater. Chem. C 2018. https://doi.org/10.1039/C8TC02123F.

Daisy, E. R. A. C.; Rajendran, N. K.; Houreld, N. N.; Marraiki, N.; Elgorban, A. M.; Rajan, M. Curcumin and Gymnema Sylvestre Extract Loaded Graphene Oxide-Polyhydroxybutyrate-sodium Alginate Composite for Diabetic Wound Regeneration. React. Funct. Polym. 2020, 154, 104671. https://doi.org/10.1016/j.reactfunctpolym.2020.104671.

Dan, L.; Pope, M. A.; Elias, A. L. Solution-Processed Conductive Biocomposites Based on Polyhydroxybutyrate and Reduced Graphene Oxide. J. Phys. Chem. C 2018, 122 (30), 17490–17500.

Dan, L.; Pope, M. A.; Elias, A. L. Solution-Processed Conductive Biocomposites Based on Polyhydroxybutyrate and Reduced Graphene Oxide. J. Phys. Chem. C 2018, 122 (30), 17490–17500. https://doi.org/10.1021/acs.jpcc.8b02515.

Dan, L.; Shi, S.; Chung, H.-J.; Elias, A. Porous Polydimethylsiloxane–Silver Nanowire Devices for Wearable Pressure Sensors. ACS Appl. Nano Mater. 2019, 2 (8), 4869–4878.

Dan, Li, et al. Porous Polydimethylsiloxane–Silver Nanowire Devices for Wearable Pressure Sensors. ACS Applied Nano Materials 2.8 2019: 4869-4878.

Dankoco, M. D.; Tesfay, G. Y.; Benevent, E.; Bendahan, M. Temperature Sensor Realized by Inkjet Printing Process on Flexible Substrate. Mater. Sci. Eng. B 2016, 205, 1–5. https://doi.org/10.1016/j.mseb.2015.11.003.

Das, A.; Pisana, S.; Chakraborty, B.; Piscanec, S.; Saha, S. K.; Waghmare, U. V.; Novoselov, K. S.; Krishnamurthy, H. R.; Geim, A. K.; Ferrari, A. C.; Sood, A. K. Monitoring Dopants by Raman Scattering in an Electrochemically Top-Gated Graphene Transistor. Nat. Nanotechnol. 2008, 3 (4), 210–215. https://doi.org/10.1038/nnano.2008.67.

De Silva, K. K. H.; Huang, H.-H.; Joshi, R. K.; Yoshimura, M. Chemical Reduction of Graphene Oxide Using Green Reductants. Carbon 2017, 119, 190–199. https://doi.org/10.1016/j.carbon.2017.04.025.

De, S.; King, P. J.; Lotya, M.; O'Neill, A.; Doherty, E. M.; Hernandez, Y.; Duesberg, G. S.; Coleman, J. N. Flexible, Transparent, Conducting Films of Randomly Stacked Graphene from Surfactant-Stabilized, Oxide-Free Graphene Dispersions. Small 2010, 6 (3), 458–464. https://doi.org/10.1002/smll.200901162.

De, S.; King, P. J.; Lotya, M.; O'Neill, A.; Doherty, E. M.; Hernandez, Y.; Duesberg, G. S.; Coleman, J. N. Flexible, Transparent, Conducting Films of Randomly Stacked Graphene from Surfactant-Stabilized, Oxide-Free Graphene Dispersions. Small 2010, 6 (3), 458–464. https://doi.org/10.1002/smll.200901162.

Derraik, J. G. B. The Pollution of the Marine Environment by Plastic Debris: A Review. Mar. Pollut. Bull. 2002, 44 (9), 842–852. https://doi.org/10.1016/S0025-326X(02)00220-5.

Di, J.; Zhang, X.; Yong, Z.; Zhang, Y.; Li, D.; Li, R.; Li, Q. Carbon-Nanotube Fibers for Wearable Devices and Smart Textiles. Adv. Mater. 2016, 28 (47), 10529–10538. https://doi.org/10.1002/adma.201601186.

Dorgan, J. R.; Braun, B.; Wegner, J. R.; Knauss, D. M. Poly(Lactic Acids): A Brief Review. In Degradable Polymers and Materials; ACS Symposium Series; American Chemical Society, 2006; Vol. 939, pp 102–125. https://doi.org/10.1021/bk-2006-0939.ch007.

Doshi, S. M.; Thostenson, E. T. Thin and Flexible Carbon Nanotube-Based Pressure Sensors with Ultrawide Sensing Range. ACS Sens. 2018, 3 (7), 1276–1282. https://doi.org/10.1021/acssensors.8b00378.

Drumright, R. E.; Gruber, P. R.; Henton, D. E. Polylactic Acid Technology. Adv. Mater. 2000, 12 (23), 1841–1846. https://doi.org/10.1002/1521-4095(200012)12:23<1841::AID-ADMA1841>3.0.CO;2-E.

Eatemadi, A.; Daraee, H.; Karimkhanloo, H.; Kouhi, M.; Zarghami, N.; Akbarzadeh, A.; Abasi, M.; Hanifehpour, Y.; Joo, S. W. Carbon Nanotubes: Properties, Synthesis, Purification, and Medical Applications. Nanoscale Res. Lett. 2014, 9 (1), 393.

Eatemadi, A.; Daraee, H.; Karimkhanloo, H.; Kouhi, M.; Zarghami, N.; Akbarzadeh, A.; Abasi, M.; Hanifehpour, Y.; Joo, S. W. Carbon Nanotubes: Properties, Synthesis, Purification, and Medical Applications. Nanoscale Res. Lett. 2014, 9 (1), 393. https://doi.org/10.1186/1556-276X-9-393.

Eda, G.; Fanchini, G.; Chhowalla, M. Large-Area Ultrathin Films of Reduced Graphene Oxide as a Transparent and Flexible Electronic Material. Nat. Nanotechnol. 2008, 3 (5), 270–274. https://doi.org/10.1038/nnano.2008.83.

Eda, G.; Fanchini, G.; Chhowalla, M. Large-Area Ultrathin Films of Reduced Graphene Oxide as a Transparent and Flexible Electronic Material. Nat. Nanotechnol. 2008, 3 (5), 270–274. https://doi.org/10.1038/nnano.2008.83.

Eom, T. H.; Han, J. I. The Effect of the Nickel and Chromium Concentration Ratio on the Temperature Coefficient of the Resistance of a Ni–Cr Thin Film-Based Temperature Sensor. Sens. Actuators Phys. 2017, 260, 198–205. https://doi.org/10.1016/j.sna.2017.04.024.

Fernández-Merino, M. J.; Guardia, L.; Paredes, J. I.; Villar-Rodil, S.; Solís-Fernández, P.; Martínez-Alonso, A.; Tascón, J. M. D. Vitamin C Is an Ideal Substitute for Hydrazine in the Reduction of Graphene Oxide Suspensions. J. Phys. Chem. C 2010, 114 (14), 6426–6432. https://doi.org/10.1021/jp100603h.

Ferrari, A. C.; Robertson, J. Interpretation of Raman Spectra of Disordered and Amorphous Carbon. Phys. Rev. B 2000, 61 (20), 14095–14107.

Ferrari, A. C.; Robertson, J. Interpretation of Raman Spectra of Disordered and Amorphous Carbon. Phys. Rev. B 2000, 61 (20), 14095–14107. https://doi.org/10.1103/PhysRevB.61.14095.

Fu, K.; Yao, Y.; Dai, J.; Hu, L. Progress in 3D Printing of Carbon Materials for Energy-Related Applications. Adv. Mater. 2017, 29 (9), 1603486. https://doi.org/10.1002/adma.201603486.

Gao, J.; Wang, H.; Huang, X.; Hu, M.; Xue, H.; Li, R. K. Y. Electrically Conductive Polymer Nanofiber Composite with an Ultralow Percolation Threshold for Chemical Vapour Sensing. Compos. Sci. Technol. 2018, 161, 135–142. https://doi.org/10.1016/j.compscitech.2018.04.014.

Gao, R.; Lu, D.; Cheng, J.; Jiang, Y.; Jiang, L.; Qi, Z. Humidity Sensor Based on Power Leakage at Resonance Wavelengths of a Hollow Core Fiber Coated with Reduced Graphene Oxide. Sens. Actuators B Chem. 2016, 222, 618–624. https://doi.org/10.1016/j.snb.2015.08.108.

García-Tuñon, E.; Barg, S.; Franco, J.; Bell, R.; Eslava, S.; D'Elia, E.; Maher, R. C.; Guitian, F.; Saiz, E. Printing in Three Dimensions with Graphene. Adv. Mater. 2015, 27 (10), 1688–1693. https://doi.org/10.1002/adma.201405046.

García-Tuñon, E.; Barg, S.; Franco, J.; Bell, R.; Eslava, S.; D'Elia, E.; Maher, R. C.; Guitian, F.; Saiz, E. Printing in Three Dimensions with Graphene. Adv. Mater. 2015, 27 (10), 1688–1693. https://doi.org/10.1002/adma.201405046.

Gerlach, C.; Krumm, D.; Illing, M.; Lange, J.; Kanoun, O.; Odenwald, S.; Hübler, A. Printed MWCNT-PDMS-Composite Pressure Sensor System for Plantar Pressure Monitoring in Ulcer Prevention. IEEE Sens. J. 2015, 15 (7), 3647–3656. https://doi.org/10.1109/JSEN.2015.2392084.

Gerlach, C.; Krumm, D.; Illing, M.; Lange, J.; Kanoun, O.; Odenwald, S.; Hübler, A. Printed MWCNT-PDMS-Composite Pressure Sensor System for Plantar Pressure Monitoring in Ulcer Prevention. IEEE Sens. J. 2015, 15 (7), 3647–3656. https://doi.org/10.1109/JSEN.2015.2392084.

Ghaffar, Ahmed Mohamed El-Hadi Abdel. Development of a biodegradable material based on Poly (3-hydroxybutyrate) PHB.2002.

Ghassemi, P.; Pfefer, T. J.; Casamento, J. P.; Simpson, R.; Wang, Q. Best Practices for Standardized Performance Testing of Infrared Thermographs Intended for Fever Screening. PLOS ONE 2018, 13 (9), e0203302. https://doi.org/10.1371/journal.pone.0203302.

Ginley, D. S.; Perkins, J. D. Transparent Conductors. In Handbook of Transparent Conductors; Ginley, D. S., Ed.; Springer US: Boston, MA, 2011; pp 1–25. https://doi.org/10.1007/978-1-4419-1638-9_1.

Ginley, D. S.; Perkins, J. D. Transparent Conductors. In Handbook of Transparent Conductors; Ginley, D. S., Ed.; Springer US: Boston, MA, 2011; pp 1–25. https://doi.org/10.1007/978-1-4419-1638-9_1.

Gnanasekaran, K.; Heijmans, T.; van Bennekom, S.; Woldhuis, H.; Wijnia, S.; de With, G.; Friedrich, H. 3D Printing of CNT- and Graphene-Based Conductive Polymer Nanocomposites by Fused Deposition Modeling. Appl. Mater. Today 2017, 9, 21–28.

Gnanasekaran, K.; Heijmans, T.; van Bennekom, S.; Woldhuis, H.; Wijnia, S.; de With, G.; Friedrich, H. 3D Printing of CNT- and Graphene-Based Conductive Polymer Nanocomposites by Fused Deposition Modeling. Appl. Mater. Today 2017, 9, 21–28. https://doi.org/10.1016/j.apmt.2017.04.003.

Gogolewski, S.; Jovanovic, M.; Perren, S. M.; Dillon, J. G.; Hughes, M. K. The Effect of Melt-Processing on the Degradation of Selected Polyhydroxyacids: Polylactides, Polyhydroxybutyrate, and Polyhydroxybutyrate-Co-Valerates. Polym. Degrad. Stab. 1993, 40 (3), 313–322. https://doi.org/10.1016/0141-3910(93)90137-8.

Granqvist, C. G. Transparent Conductors as Solar Energy Materials: A Panoramic Review. Sol. Energy Mater. Sol. Cells 2007, 91 (17), 1529–1598. https://doi.org/10.1016/j.solmat.2007.04.031.

Granqvist, C. G. Transparent Conductors as Solar Energy Materials: A Panoramic Review. Sol. Energy Mater. Sol. Cells 2007, 91 (17), 1529–1598. https://doi.org/10.1016/j.solmat.2007.04.031.

Grassie, N.; Murray, E. J.; Holmes, P. A. The Thermal Degradation of Poly(-(d)-β-Hydroxybutyric Acid): Part 1—Identification and Quantitative Analysis of Products. Polym. Degrad. Stab. 1984, 6 (1), 47–61. https://doi.org/10.1016/0141-3910(84)90016-8.

Gray, D. S.; Tien, J.; Chen, C. S. High-Conductivity Elastomeric Electronics. Adv. Mater. 2004, 16 (5), 393–397. https://doi.org/10.1002/adma.200306107.

Green, A. A.; Hersam, M. C. Solution Phase Production of Graphene with Controlled Thickness via Density Differentiation. Nano Lett. 2009, 9 (12), 4031–4036. https://doi.org/10.1021/nl902200b.

Green, A. A.; Hersam, M. C. Solution Phase Production of Graphene with Controlled Thickness via Density Differentiation. Nano Lett. 2009, 9 (12), 4031–4036. https://doi.org/10.1021/nl902200b.

Hammock, M. L.; Chortos, A.; Tee, B. C.-K.; Tok, J. B.-H.; Bao, Z. 25th Anniversary Article: The Evolution of Electronic Skin (E-Skin): A Brief History, Design Considerations, and Recent Progress. Adv. Mater. 2013, 25 (42), 5997–6038. https://doi.org/10.1002/adma.201302240.

Hankermeyer, C. R.; Tjeerdema, R. S. Polyhydroxybutyrate: Plastic Made and Degraded by Microorganisms. In Reviews of Environmental Contamination and Toxicology: Continuation of

Residue Reviews; Ware, G. W., Ed.; Reviews of Environmental Contamination and Toxicology; Springer: New York, NY, 1999; pp 1–24.

Haque, A.; Mamun, M. A.-A.; Taufique, M. F. N.; Karnati, P.; Ghosh, K. Temperature Dependent Electrical Transport Properties of High Carrier Mobility Reduced Graphene Oxide Thin Film Devices. IEEE Trans. Semicond. Manuf. 2018, 31 (4), 535–544. https://doi.org/10.1109/TSM.2018.2873202.

He, L.; Tjong, S. C. Low Percolation Threshold of Graphene/Polymer Composites Prepared by Solvothermal Reduction of Graphene Oxide in the Polymer Solution. Nanoscale Res. Lett. 2013, 8 (1), 132. https://doi.org/10.1186/1556-276X-8-132.

He, Y.; Yang, S.; Liu, H.; Shao, Q.; Chen, Q.; Lu, C.; Jiang, Y.; Liu, C.; Guo, Z. Reinforced Carbon Fiber Laminates with Oriented Carbon Nanotube Epoxy Nanocomposites: Magnetic Field Assisted Alignment and Cryogenic Temperature Mechanical Properties. J. Colloid Interface Sci. 2018, 517, 40–51. https://doi.org/10.1016/j.jcis.2018.01.087.

Herzberger, J.; Sirrine, J. M.; Williams, C. B.; Long, T. E. Polymer Design for 3D Printing Elastomers: Recent Advances in Structure, Properties, and Printing. Prog. Polym. Sci. 2019, 97, 101144.

Hidalgo-Ruz, V.; Gutow, L.; Thompson, R. C.; Thiel, M. Microplastics in the Marine Environment: A Review of the Methods Used for Identification and Quantification. Environ. Sci. Technol. 2012, 46 (6), 3060–3075. https://doi.org/10.1021/es2031505.

Hong, S. Y.; Lee, Y. H.; Park, H.; Jin, S. W.; Jeong, Y. R.; Yun, J.; You, I.; Zi, G.; Ha, J. S. Stretchable Active Matrix Temperature Sensor Array of Polyaniline Nanofibers for Electronic Skin. Adv. Mater. 2016, 28 (5), 930–935. https://doi.org/10.1002/adma.201504659.

Howe, Richard CT, et al. "Functional inks of graphene, metal dichalcogenides and black phosphorus for photonics and (opto) electronics." Low-Dimensional Materials and Devices. Vol. 9553. International Society for Optics and Photonics, 2015.

Huang, Y.; Zeng, X.; Wang, W.; Guo, X.; Hao, C.; Pan, W.; Liu, P.; Liu, C.; Ma, Y.; Zhang, Y.; Yang, X. High-Resolution Flexible Temperature Sensor Based Graphite-Filled Polyethylene Oxide and Polyvinylidene Fluoride Composites for Body Temperature Monitoring. Sens. Actuators Phys. 2018, 278, 1–10. https://doi.org/10.1016/j.sna.2018.05.024.

Husain, M.; Kennon, R.; Husain, M. D.; Kennon, R. Preliminary Investigations into the Development of Textile Based Temperature Sensor for Healthcare Applications. Fibers 2013, 1 (1), 2–10. https://doi.org/10.3390/fib1010002.

Huynh, T.-P.; Haick, H. Autonomous Flexible Sensors for Health Monitoring. Adv. Mater. 2018, 30 (50), 1802337. https://doi.org/10.1002/adma.201802337.

Hyun, W. J.; Secor, E. B.; Hersam, M. C.; Frisbie, C. D.; Francis, L. F. High-Resolution Patterning of Graphene by Screen Printing with a Silicon Stencil for Highly Flexible Printed Electronics. Adv. Mater. 2015, 27 (1), 109–115. https://doi.org/10.1002/adma.201404133.

Jakus, A. E.; Secor, E. B.; Rutz, A. L.; Jordan, S. W.; Hersam, M. C.; Shah, R. N. Three-Dimensional Printing of High-Content Graphene Scaffolds for Electronic and Biomedical Applications. ACS Nano 2015, 9 (4), 4636–4648.

Jakus, A. E.; Secor, E. B.; Rutz, A. L.; Jordan, S. W.; Hersam, M. C.; Shah, R. N. Three-Dimensional Printing of High-Content Graphene Scaffolds for Electronic and Biomedical Applications. ACS Nano 2015, 9 (4), 4636–4648. https://doi.org/10.1021/acsnano.5b01179.

Jayathilaka, Wanasinghe Arachchige Dumith Madushanka, et al. Significance of nanomaterials in wearables: a review on wearable actuators and sensors. Advanced Materials 31.7 2019, 1805921.

Jeevananda, T.; Siddaramaiah; Hee Lee, J. Fabrication of Carbon Black/HDPE/Polyaniline Functionalized Multi-Walled Carbon Nanotube Composites for Enhancing PTC Characteristics. Mater. Today Proc. 2018, 5 (10, Part 1), 20890–20898. https://doi.org/10.1016/j.matpr.2018.06.476.

Jeong, J.-W.; Kim, M. K.; Cheng, H.; Yeo, W.-H.; Huang, X.; Liu, Y.; Zhang, Y.; Huang, Y.; Rogers, J. A. Epidermal Electronics: Capacitive Epidermal Electronics for Electrically Safe, Long-Term Electrophysiological Measurements (Adv. Healthcare Mater. 5/2014). Adv. Healthc. Mater. 2014, 3 (5), 621–621. https://doi.org/10.1002/adhm.201470022.

Jiang, S.; Wang, M.; He, J. A Review of Biomimetic Scaffolds for Bone Regeneration: Towards a Cell-Free Strategy. Bioeng. Transl. Med. 2020, e10206.

Jiang, Y.; Xu, Z.; Huang, T.; Liu, Y.; Guo, F.; Xi, J.; Gao, W.; Gao, C. Direct 3D Printing of Ultralight Graphene Oxide Aerogel Microlattices. Adv. Funct. Mater. 2018, 28 (16), 1707024. https://doi.org/10.1002/adfm.201707024.

Jung, I. L.; Phyo, K. H.; Kim, K. C.; Park, H. K.; Kim, I. G. Spontaneous Liberation of Intracellular Polyhydroxybutyrate Granules in Escherichia Coli. Res. Microbiol. 2005, 156 (8), 865–873. https://doi.org/10.1016/j.resmic.2005.04.004.

Justin, R.; Chen, B. Strong and Conductive Chitosan–Reduced Graphene Oxide Nanocomposites for Transdermal Drug Delivery. J. Mater. Chem. B 2014, 2 (24), 3759–3770. https://doi.org/10.1039/C4TB00390J.

Kang, M. S.; Kim, K. T.; Lee, J. U.; Jo, W. H. Direct Exfoliation of Graphite Using a Non-Ionic Polymer Surfactant for Fabrication of Transparent and Conductive Graphene Films. J. Mater. Chem. C 2013, 1 (9), 1870–1875. https://doi.org/10.1039/C2TC00586G.

Karlsson, S.; Albertsson, A. Biodegradable Polymers and Environmental Interaction. Polym. Eng. Sci. 1998, 38 (8), 1251–1253. https://doi.org/10.1002/pen.10294.

Kasaliwal, G. R., Göldel, A., Pötschke, P., & Heinrich, G.. Influences of polymer matrix melt viscosity and molecular weight on MWCNT agglomerate dispersion. Polymer, 2011, 52(4), 1027-1036.

Kay, M. J.; McCabe, R. W.; Morton, L. H. G. Chemical and Physical Changes Occurring in Polyester Polyurethane during Biodegradation. Int. Biodeterior. Biodegrad. 1993, 31 (3), 209–225. https://doi.org/10.1016/0964-8305(93)90006-N.

Khanna, S.; Srivastava, A. K. Recent Advances in Microbial Polyhydroxyalkanoates. Process Biochem. 2005, 40 (2), 607–619. https://doi.org/10.1016/j.procbio.2004.01.053.

Kharaziha, M.; Shin, S. R.; Nikkhah, M.; Topkaya, S. N.; Masoumi, N.; Annabi, N.; Dokmeci, M. R.; Khademhosseini, A. Tough and Flexible CNT–Polymeric Hybrid Scaffolds for Engineering Cardiac Constructs. Biomaterials 2014, 35 (26), 7346–7354.

Kiang Chua, C.; Pumera, M. Chemical Reduction of Graphene Oxide: A Synthetic Chemistry Viewpoint. Chem. Soc. Rev. 2014, 43 (1), 291–312. https://doi.org/10.1039/C3CS60303B.

Kim, D.-H.; Liu, Z.; Kim, Y.-S.; Wu, J.; Song, J.; Kim, H.-S.; Huang, Y.; Hwang, K.; Zhang, Y.; Rogers, J. A. Optimized Structural Designs for Stretchable Silicon Integrated Circuits. Small 2009, 5 (24), 2841–2847. https://doi.org/10.1002/smll.200900853.

Kim, D.-H.; Lu, N.; Ghaffari, R.; Kim, Y.-S.; Lee, S. P.; Xu, L.; Wu, J.; Kim, R.-H.; Song, J.; Liu, Z.; Viventi, J.; de Graff, B.; Elolampi, B.; Mansour, M.; Slepian, M. J.; Hwang, S.; Moss, J. D.; Won, S.-M.; Huang, Y.; Litt, B.; Rogers, J. A. Materials for Multifunctional Balloon Catheters with Capabilities in Cardiac Electrophysiological Mapping and Ablation Therapy. Nat. Mater. 2011, 10 (4), 316–323. https://doi.org/10.1038/nmat2971.

Kim, Dae-Hyeong, et al. Materials for multifunctional balloon catheters with capabilities in cardiac electrophysiological mapping and ablation therapy. Nature materials 10.4, 2011, 316-323.

Kim, K. S.; Zhao, Y.; Jang, H.; Lee, S. Y.; Kim, J. M.; Kim, K. S.; Ahn, J.-H.; Kim, P.; Choi, J.-Y.; Hong, B. H. Large-Scale Pattern Growth of Graphene Films for Stretchable Transparent Electrodes. Nature 2009, 457 (7230), 706–710. https://doi.org/10.1038/nature07719.

Knowles, J. C.; Mahmud, F. A.; Hastings, G. W. Piezoelectric Characteristics of a Polyhydroxybutyrate-Based Composite. Clin. Mater. 1991, 8 (1), 155–158.

Köse, G. T.; Korkusuz, F.; Korkusuz, P.; Hasirci, V. In Vivo Tissue Engineering of Bone Using Poly(3-Hydroxybutyric Acid-Co-3-Hydroxyvaleric Acid) and Collagen Scaffolds. Tissue Eng. 2004, 10 (7–8), 1234–1250.

Krause, B.; Rzeczkowski, P.; Pötschke, P. Thermal Conductivity and Electrical Resistivity of Melt-Mixed Polypropylene Composites Containing Mixtures of Carbon-Based Fillers. Polymers 2019, 11 (6), 1073.

Krueger, M.; Berg, S.; Stone, D.; Strelcov, E.; Dikin, D. A.; Kim, J.; Cote, L. J.; Huang, J.; Kolmakov, A. Drop-Casted Self-Assembling Graphene Oxide Membranes for Scanning Electron Microscopy on Wet and Dense Gaseous Samples. ACS Nano 2011, 5 (12), 10047–10054. https://doi.org/10.1021/nn204287g.

Kumagai, Y.; Kanesawa, Y.; Doi, Y. Enzymatic Degradation of Microbial Poly(3-Hydroxybutyrate) Films. Makromol. Chem. 1992, 193 (1), 53–57. https://doi.org/10.1002/macp.1992.021930105.

Kumar Srivastava, P.; Ghosh, S. Defect Engineering as a Versatile Route to Estimate Various Scattering Mechanisms in Monolayer Graphene on Solid Substrates. Nanoscale 2015, 7 (38), 16079–16086. https://doi.org/10.1039/C5NR04293C.

Kuswandi, B. Environmental Friendly Food Nano-Packaging. Environ. Chem. Lett. 2017, 15 (2), 205–221. https://doi.org/10.1007/s10311-017-0613-7.

Kwok, S. W.; Goh, K. H. H.; Tan, Z. D.; Tan, S. T. M.; Tjiu, W. W.; Soh, J. Y.; Ng, Z. J. G.; Chan, Y. Z.; Hui, H. K.; Goh, K. E. J. Electrically Conductive Filament for 3D-Printed Circuits and Sensors. Appl. Mater. Today 2017, 9, 167–175.

Labet, M.; Thielemans, W. Synthesis of Polycaprolactone: A Review. Chem. Soc. Rev. 2009, 38 (12), 3484–3504. https://doi.org/10.1039/B820162P.

Lai, M.; Li, J.; Yang, J.; Liu, J.; Tong, X.; Cheng, H. The Morphology and Thermal Properties of Multi-Walled Carbon Nanotube and Poly(Hydroxybutyrate-Co-Hydroxyvalerate) Composite. Polym. Int. 2004, 53 (10), 1479–1484.

Lawson, S.; Snarzyk, M.; Hanify, D.; Rownaghi, A. A.; Rezaei, F. Development of 3D-Printed Polymer-MOF Monoliths for CO2 Adsorption. Ind. Eng. Chem. Res. 2020, 59 (15), 7151–7160.

Lee, C.-Y.; Lee, S.-J.; Tang, M.-S.; Chen, P.-C.; Lee, C.-Y.; Lee, S.-J.; Tang, M.-S.; Chen, P.-C. In Situ Monitoring of Temperature inside Lithium-Ion Batteries by Flexible Micro Temperature Sensors. Sensors 2011, 11 (10), 9942–9950. https://doi.org/10.3390/s111009942.

Lee, C.-Y.; Weng, F.-B.; Cheng, C.-H.; Shiu, H.-R.; Jung, S.-P.; Chang, W.-C.; Chan, P.-C.; Chen, W.-T.; Lee, C.-J. Use of Flexible Micro-Temperature Sensor to Determine Temperature in Situ and to Simulate a Proton Exchange Membrane Fuel Cell. J. Power Sources 2011, 196 (1), 228–234. https://doi.org/10.1016/j.jpowsour.2010.06.051.

Lee, H.; Choi, T. K.; Lee, Y. B.; Cho, H. R.; Ghaffari, R.; Wang, L.; Choi, H. J.; Chung, T. D.; Lu, N.; Hyeon, T.; Choi, S. H.; Kim, D.-H. A Graphene-Based Electrochemical Device with

Thermoresponsive Microneedles for Diabetes Monitoring and Therapy. Nat. Nanotechnol. 2016, 11 (6), 566–572. https://doi.org/10.1038/nnano.2016.38.

Lee, S. Y. Bacterial Polyhydroxyalkanoates. Biotechnol. Bioeng. 1996, 49 (1), 1–14. https://doi.org/10.1002/(SICI)1097-0290(19960105)49:1<1::AID-BIT1>3.0.CO;2-P.

Lee, S. Y. Plastic Bacteria? Progress and Prospects for Polyhydroxyalkanoate Production in Bacteria. Trends Biotechnol. 1996, 14 (11), 431–438. https://doi.org/10.1016/0167-7799(96)10061-5.

Lenz, R. W.; Marchessault, R. H. Bacterial Polyesters: Biosynthesis, Biodegradable Plastics and Biotechnology. Biomacromolecules 2005, 6 (1), 1–8. https://doi.org/10.1021/bm049700c.

Li, Q.; Zhang, L.-N.; Tao, X.-M.; Ding, X. Review of Flexible Temperature Sensing Networks for Wearable Physiological Monitoring. Adv. Healthc. Mater. 6 2016 (12), 1601371. https://doi.org/10.1002/adhm.201601371.

Li, Y.; Huang, X.; Zeng, L.; Li, R.; Tian, H.; Fu, X.; Wang, Y.; Zhong, W.-H. A Review of the Electrical and Mechanical Properties of Carbon Nanofiller-Reinforced Polymer Composites. J. Mater. Sci. 2019, 54 (2), 1036–1076.

Li, Y.; Pionteck, J.; Pötschke, P.; Voit, B. Thermal Annealing to Influence the Vapor Sensing Behavior of Co-Continuous Poly(Lactic Acid)/Polystyrene/Multiwalled Carbon Nanotube Composites. Mater. Des. 2020, 187, 108383.

Li, Z.; Ju, D.; Han, L.; Dong, L. Formation of More Efficient Thermally Conductive Pathways Due to the Synergistic Effect of Boron Nitride and Alumina in Poly(3-Hydroxylbutyrate). Thermochim. Acta 2017, 652, 9–16. https://doi.org/10.1016/j.tca.2017.03.006.

Lichtenwalner, D. J.; Hydrick, A. E.; Kingon, A. I. Flexible Thin Film Temperature and Strain Sensor Array Utilizing a Novel Sensing Concept. Sens. Actuators Phys. 2007, 135 (2), 593–597. https://doi.org/10.1016/j.sna.2006.07.019.

Lin, X.; Shen, X.; Zheng, Q.; Yousefi, N.; Ye, L.; Mai, Y.-W.; Kim, J.-K. Fabrication of Highly-Aligned, Conductive, and Strong Graphene Papers Using Ultralarge Graphene Oxide Sheets. ACS Nano 2012, 6 (12), 10708–10719. https://doi.org/10.1021/nn303904z.

Lipatov, A.; Varezhnikov, A.; Wilson, P.; Sysoev, V.; Kolmakov, A.; Sinitskii, A. Highly Selective Gas Sensor Arrays Based on Thermally Reduced Graphene Oxide. Nanoscale 2013, 5 (12), 5426–5434. https://doi.org/10.1039/C3NR00747B.

Liu, P.; Zhu, R.; Que, R.; Liu, P.; Zhu, R.; Que, R. A Flexible Flow Sensor System and Its Characteristics for Fluid Mechanics Measurements. Sensors 2009, 9 (12), 9533–9543. https://doi.org/10.3390/s91209533.

Liu, Q.; Tai, H.; Yuan, Z.; Zhou, Y.; Su, Y.; Jiang, Y. A High-Performances Flexible Temperature Sensor Composed of Polyethyleneimine/Reduced Graphene Oxide Bilayer for Real-Time Monitoring. Adv. Mater. Technol. 2019, 4 (3), 1800594. https://doi.org/10.1002/admt.201800594.

Liu, Qingxia, et al. A High-Performances Flexible Temperature Sensor Composed of Polyethyleneimine/Reduced Graphene Oxide Bilayer for Real-Time Monitoring. Advanced Materials Technologies 4.3 2019: 1800594.

Liu, X.; Gao, C.; Sangwan, P.; Yu, L.; Tong, Z. Accelerating the Degradation of Polyolefins through Additives and Blending. J. Appl. Polym. Sci. 2014, 131 (18). https://doi.org/10.1002/app.40750.

Lopera-Valle, A.; Caputo, J. V.; Leão, R.; Sauvageau, D.; Luz, S. M.; Elias, A. Influence of Epoxidized Canola Oil (ECO) and Cellulose Nanocrystals (CNCs) on the Mechanical and Thermal Properties of Polyhydroxybutyrate (PHB)—Poly(Lactic Acid) (PLA) Blends. Polymers 2019, 11 (6), 933. https://doi.org/10.3390/polym11060933.

Lopera-Valle, A.; Caputo, J. V.; Leão, R.; Sauvageau, D.; Luz, S. M.; Elias, A. Influence of Epoxidized Canola Oil (ECO) and Cellulose Nanocrystals (CNCs) on the Mechanical and Thermal Properties of Polyhydroxybutyrate (PHB)—Poly(Lactic Acid) (PLA) Blends. Polymers 2019, 11 (6), 933.

Lopera-Valle, A.; Elias, A. Low-Resistance Silver Microparticle-HEMA-PEGDA Composites for Humidity Sensing. Smart Mater. Struct. 2018, 27 (10), 105030. https://doi.org/10.1088/1361-665X/aad355.

Lopes, A. C.; Costa, C. M.; Tavares, C. J.; Neves, I. C.; Lanceros-Mendez, S. Nucleation of the Electroactive γ Phase and Enhancement of the Optical Transparency in Low Filler Content Poly(Vinylidene)/Clay Nanocomposites. J. Phys. Chem. C 2011, 115 (37), 18076–18082.

M. Perfecto, T.; A. Zito, C.; Mazon, T.; P. Volanti, D. Flexible Room-Temperature Volatile Organic Compound Sensors Based on Reduced Graphene Oxide–WO 3 ·0.33H 2 O Nano-Needles. J. Mater. Chem. C 2018, 6 (11), 2822–2829. https://doi.org/10.1039/C8TC00324F.

Madhvapathy, S. R.; Ma, Y.; Patel, M.; Krishnan, S.; Wei, C.; Li, Y.; Xu, S.; Feng, X.; Huang, Y.; Rogers, J. A. Epidermal Electronic Systems for Measuring the Thermal Properties of Human Skin at Depths of up to Several Millimeters. Adv. Funct. Mater. 2018, 28 (34), 1802083. https://doi.org/10.1002/adfm.201802083.

Madison, L. L.; Huisman, G. W. Metabolic Engineering of Poly(3-Hydroxyalkanoates): From DNA to Plastic. Microbiol. Mol. Biol. Rev. 1999, 63 (1), 21–53.

Mahmood, Javeed, et al. "Nitrogenated holey two-dimensional structures." Nature communications 6.1 2015: 1-7.

Majidian, M.; Grimaldi, C.; Pisoni, A.; Forró, L.; Magrez, A. Electrical Conduction of Photo-Patternable SU8–Graphene Composites. Carbon 2014, 80, 364–372. https://doi.org/10.1016/j.carbon.2014.08.075.

Manikandan, N. A.; Pakshirajan, K.; Pugazhenthi, G. Preparation and Characterization of Environmentally Safe and Highly Biodegradable Microbial Polyhydroxybutyrate (PHB) Based Graphene Nanocomposites for Potential Food Packaging Applications. Int. J. Biol. Macromol. 2020, 154, 866–877. https://doi.org/10.1016/j.ijbiomac.2020.03.084.

Marcano, D. C.; Kosynkin, D. V.; Berlin, J. M.; Sinitskii, A.; Sun, Z.; Slesarev, A.; Alemany, L. B.; Lu, W.; Tour, J. M. Improved Synthesis of Graphene Oxide. ACS Nano 2010, 4 (8), 4806–4814. https://doi.org/10.1021/nn1006368.

Marsden, A. J.; Papageorgiou, D. G.; Vallés, C.; Liscio, A.; Palermo, V.; Bissett, M. A.; Young, R. J.; Kinloch, I. A. Electrical Percolation in Graphene–Polymer Composites. 2D Mater. 2018, 5 (3), 032003. https://doi.org/10.1088/2053-1583/aac055.

Martinelli, V.; Cellot, G.; Toma, F. M.; Long, C. S.; Caldwell, J. H.; Zentilin, L.; Giacca, M.; Turco, A.; Prato, M.; Ballerini, L.; Mestroni, L. Carbon Nanotubes Promote Growth and Spontaneous Electrical Activity in Cultured Cardiac Myocytes. Nano Lett. 2012, 12 (4), 1831–1838.

Martínez-Tobón, D. I.; Gul, M.; Elias, A. L.; Sauvageau, D. Polyhydroxybutyrate (PHB) Biodegradation Using Bacterial Strains with Demonstrated and Predicted PHB Depolymerase Activity. Appl. Microbiol. Biotechnol. 2018, 102 (18), 8049–8067.

Martínez-Tobón, D. I.; Gul, M.; Elias, A. L.; Sauvageau, D. Polyhydroxybutyrate (PHB) Biodegradation Using Bacterial Strains with Demonstrated and Predicted PHB Depolymerase Activity. Appl. Microbiol. Biotechnol. 2018, 102 (18), 8049–8067. https://doi.org/10.1007/s00253-018-9153-8.

Martínez-Tobón, D. I.; Waters, B.; Elias, A. L.; Sauvageau, D. Streamlined Production, Purification, and Characterization of Recombinant Extracellular Polyhydroxybutyrate Depolymerases. Microbiology Open 2020, 9 (4), e1001.

McIntosh, R.; Mamo, M. A.; Jamieson, B.; Roy, S.; Bhattacharyya, S. Improved Electronic and Magnetic Properties of Reduced Graphene Oxide Films. EPL Europhys. Lett. 2012, 97 (3), 38001. https://doi.org/10.1209/0295-5075/97/38001.

Miloaga, Dana Gabriela. Nucleating effect of exfoliated graphite nanoplatelets on poly (hydroxybutyrate) and poly (lactic acid) and their nanocomposites properties. Thesis, 2008.

Mora, A.; Verma, P.; Kumar, S. Electrical Conductivity of CNT/Polymer Composites: 3D Printing, Measurements and Modeling. Compos. Part B Eng. 2020, 183, 107600.

More, N.; Srivastava, A.; Kapusetti, G. Graphene Oxide Reinforcement Enhances the Piezoelectric and Mechanical Properties of Poly(3-Hydroxybutyrate-Co-3-Hydroxy Valerate)-Based Nanofibrous Scaffolds for Improved Proliferation of Chondrocytes and ECM Production. ACS Appl. Bio Mater. 2020. https://doi.org/10.1021/acsabm.0c00765.

Nair, R. R.; Blake, P.; Grigorenko, A. N.; Novoselov, K. S.; Booth, T. J.; Stauber, T.; Peres, N. M. R.; Geim, A. K. Fine Structure Constant Defines Visual Transparency of Graphene. Science 2008, 320 (5881), 1308–1308. https://doi.org/10.1126/science.1156965.

Nassira, H.; Sánchez-Ferrer, A.; Adamcik, J.; Handschin, S.; Mahdavi, H.; Taheri Qazvini, N.; Mezzenga, R. Gelatin–Graphene Nanocomposites with Ultralow Electrical Percolation Threshold. Adv. Mater. 2016, 28 (32), 6914–6920. https://doi.org/10.1002/adma.201601115.

Neella, N.; Gaddam, V.; Rajanna, K.; Nayak, M. M. Negative Temperature Coefficient Behavior of Graphene-Silver Nanocomposite Films for Temperature Sensor Applications. In 2016 IEEE

11th Annual International Conference on Nano/Micro Engineered and Molecular Systems (NEMS); 2016; pp 329–332. https://doi.org/10.1109/NEMS.2016.7758260.

Nguyen, D. A.; Lee, Y. R.; Raghu, A. V.; Jeong, H. M.; Shin, C. M.; Kim, B. K. Morphological and Physical Properties of a Thermoplastic Polyurethane Reinforced with Functionalized Graphene Sheet. Polym. Int. 2009, 58 (4), 412–417. https://doi.org/10.1002/pi.2549.

Nguyen, T. H.; Ishizuna, F.; Sato, Y.; Arai, H.; Ishii, M. Physiological Characterization of Poly-β-Hydroxybutyrate Accumulation in the Moderately Thermophilic Hydrogen-Oxidizing Bacterium Hydrogenophilus Thermoluteolus TH-1. J. Biosci. Bioeng. 2019, 127 (6), 686–689.

Oh, M. J.; Yoo, P. J. Graphene-Based 3D Lightweight Cellular Structures: Synthesis and Applications. Korean J. Chem. Eng. 2020, 37 (2), 189–208. https://doi.org/10.1007/s11814-019-0437-1.

Orts, W. J.; Nobes, G. A. R.; Kawada, J.; Nguyen, S.; Yu, G.; Ravenelle, F. Poly(Hydroxyalkanoates): Biorefinery Polymers with a Whole Range of Applications. The Work of Robert H. Marchessault. Can. J. Chem. 2008, 86 (6), 628–640. https://doi.org/10.1139/v08-050.

Otaegi, I.; Aranburu, N.; Iturrondobeitia, M.; Ibarretxe, J.; Guerrica-Echevarría, G. The Effect of the Preparation Method and the Dispersion and Aspect Ratio of CNTs on the Mechanical and Electrical Properties of Bio-Based Polyamide-4,10/CNT Nanocomposites. Polymers 2019, 11 (12), 2059.

Paganelli, F. L.; de Macedo Lemos, E. G.; Alves, L. M. C. Polyhydroxybutyrate in Rhizobium and Bradyrhizobium: Quantification and PhbC Gene Expression. World J. Microbiol. Biotechnol. 2011, 27 (4), 773–778. https://doi.org/10.1007/s11274-010-0515-3.

Pan, D.; Zhang, J.; Li, Z.; Wu, M. Hydrothermal Route for Cutting Graphene Sheets into Blue-Luminescent Graphene Quantum Dots. Adv. Mater. 2010, 22 (6), 734–738. https://doi.org/10.1002/adma.200902825.

Pan, K.; Fan, Y.; Leng, T.; Li, J.; Xin, Z.; Zhang, J.; Hao, L.; Gallop, J.; Novoselov, K. S.; Hu, Z. Sustainable Production of Highly Conductive Multilayer Graphene Ink for Wireless Connectivity and IoT Applications. Nat. Commun. 2018, 9 (1), 5197. https://doi.org/10.1038/s41467-018-07632-w.

Park, S.; An, J.; Potts, J. R.; Velamakanni, A.; Murali, S.; Ruoff, R. S. Hydrazine-Reduction of Graphite- and Graphene Oxide. Carbon 2011, 49 (9), 3019–3023. https://doi.org/10.1016/j.carbon.2011.02.071.

Park, S.; An, J.; Potts, J. R.; Velamakanni, A.; Murali, S.; Ruoff, R. S. Hydrazine-Reduction of Graphite- and Graphene Oxide. Carbon 2011, 49 (9), 3019–3023. https://doi.org/10.1016/j.carbon.2011.02.071.

Pegel, S.; Pötschke, P.; Villmow, T.; Stoyan, D.; Heinrich, G. Spatial Statistics of Carbon Nanotube Polymer Composites. Polymer 2009, 50 (9), 2123–2132.

Pei, S.; Zhao, J.; Du, J.; Ren, W.; Cheng, H.-M. Direct Reduction of Graphene Oxide Films into Highly Conductive and Flexible Graphene Films by Hydrohalic Acids. Carbon 2010, 48 (15), 4466–4474. https://doi.org/10.1016/j.carbon.2010.08.006.

Plastic Pollution in the World's Oceans: More than 5 Trillion Plastic Pieces Weighing over 250,000 Tons Afloat at Sea (accessed Apr 14, 2020).

Pope, M. A.; Aksay, I. A. Four-Fold Increase in the Intrinsic Capacitance of Graphene through Functionalization and Lattice Disorder. J. Phys. Chem. C 2015, 119 (35), 20369–20378. https://doi.org/10.1021/acs.jpcc.5b07521.

Prakalathan, K.; Mohanty, S.; Nayak, S. K. Reinforcing Effect and Isothermal Crystallization Kinetics of Poly(3-Hydroxybutyrate) Nanocomposites Blended with Organically Modified Montmorillonite. Polym. Compos. 2014, 35 (5), 999–1012. https://doi.org/10.1002/pc.22746.

Pramanik, N.; De, J.; Kumar Basu, R.; Rath, T.; Paban Kundu, P. Fabrication of Magnetite Nanoparticle Doped Reduced Graphene Oxide Grafted Polyhydroxyalkanoate Nanocomposites for Tissue Engineering Application. RSC Adv. 2016, 6 (52), 46116–46133. https://doi.org/10.1039/C6RA03233H.

Publications : PlasticsEurope https://www.plasticseurope.org/en/resources/publications/3-plastics-facts-2016 (accessed Apr 14, 2020).

R. Dreyer, D.; Park, S.; W. Bielawski, C.; S. Ruoff, R. The Chemistry of Graphene Oxide. Chem. Soc. Rev. 2010, 39 (1), 228–240. https://doi.org/10.1039/B917103G.

Rasoulianboroujeni, M.; Kiaie, N.; Tabatabaei, F. S.; Yadegari, A.; Fahimipour, F.; Khoshroo, K.; Tayebi, L. Dual Porosity Protein-Based Scaffolds with Enhanced Cell Infiltration and Proliferation. Sci. Rep. 2018, 8 (1), 14889.

Ren, J. M.; McKenzie, T. G.; Fu, Q.; Wong, E. H. H.; Xu, J.; An, Z.; Shanmugam, S.; Davis, T. P.; Boyer, C.; Qiao, G. G. Star Polymers. Chem. Rev. 2016, 116 (12), 6743–6836. https://doi.org/10.1021/acs.chemrev.6b00008.

Ren, L., Zha, J. W., Li, R. K., Shi, C. Y., & Dang, Z. M.. Co-continuous structural polystyrene/poly (vinylidene fluoride) nanocomposites with high dielectric constant and magnetic properties. Composites Communications, 2017, 4, 24-32.

Ribeiro, C.; Costa, C. M.; Correia, D. M.; Nunes-Pereira, J.; Oliveira, J.; Martins, P.; Gonçalves, R.; Cardoso, V. F.; Lanceros-Méndez, S. Electroactive Poly(Vinylidene Fluoride)-Based Structures for Advanced Applications. Nat. Protoc. 2018, 13 (4), 681–704.

Sabet, Maziyar, and Hassan Soleimani. "Mechanical and electrical properties of low density polyethylene filled with carbon nanotubes." IOP Conference Series: Materials Science and Engineering. Vol. 64. 2014.

Sadasivuni, K. K.; Kafy, A.; Kim, H.-C.; Ko, H.-U.; Mun, S.; Kim, J. Reduced Graphene Oxide Filled Cellulose Films for Flexible Temperature Sensor Application. Synth. Met. 2015, 206, 154–161. https://doi.org/10.1016/j.synthmet.2015.05.018.

Scalioni, L. V.; Gutiérrez, M. C.; Felisberti, M. I. Green Composites of Poly(3-Hydroxybutyrate) and Curaua Fibers: Morphology and Physical, Thermal, and Mechanical Properties. J. Appl. Polym. Sci. 2017, 134 (14). https://doi.org/10.1002/app.44676.

Schubert, C.; Langeveld, M. C. van; Donoso, L. A. Innovations in 3D Printing: A 3D Overview from Optics to Organs. Br. J. Ophthalmol. 2014, 98 (2), 159–161. https://doi.org/10.1136/bjophthalmol-2013-304446.

Secor, E. B.; Gao, T. Z.; Islam, A. E.; Rao, R.; Wallace, S. G.; Zhu, J.; Putz, K. W.; Maruyama, B.; Hersam, M. C. Enhanced Conductivity, Adhesion, and Environmental Stability of Printed Graphene Inks with Nitrocellulose. Chem. Mater. 2017, 29 (5), 2332–2340. https://doi.org/10.1021/acs.chemmater.7b00029.

Secor, E. B.; Gao, T. Z.; Islam, A. E.; Rao, R.; Wallace, S. G.; Zhu, J.; Putz, K. W.; Maruyama, B.; Hersam, M. C. Enhanced Conductivity, Adhesion, and Environmental Stability of Printed Graphene Inks with Nitrocellulose. Chem. Mater. 2017, 29 (5), 2332–2340. https://doi.org/10.1021/acs.chemmater.7b00029.

Sencadas, V.; Martins, P.; Pitães, A.; Benelmekki, M.; Gómez Ribelles, J. L.; Lanceros-Mendez, S. Influence of Ferrite Nanoparticle Type and Content on the Crystallization Kinetics and Electroactive Phase Nucleation of Poly(Vinylidene Fluoride). Langmuir 2011, 27 (11), 7241–7249.

Shah, A. A.; Hasan, F.; Hameed, A.; Ahmed, S. Biological Degradation of Plastics: A Comprehensive Review. Biotechnol. Adv. 2008, 26 (3), 246–265. https://doi.org/10.1016/j.biotechadv.2007.12.005.

Shao, Y.; Wang, J.; Wu, H.; Liu, J.; Aksay, I. A.; Lin, Y. Graphene Based Electrochemical Sensors and Biosensors: A Review. Electroanalysis 2010, 22 (10), 1027–1036.

Shao, Y.; Wang, J.; Wu, H.; Liu, J.; Aksay, I. A.; Lin, Y. Graphene Based Electrochemical Sensors and Biosensors: A Review. Electroanalysis 2010, 22 (10), 1027–1036. https://doi.org/10.1002/elan.200900571.

Shen, Y.; Jing, T.; Ren, W.; Zhang, J.; Jiang, Z.-G.; Yu, Z.-Z.; Dasari, A. Chemical and Thermal Reduction of Graphene Oxide and Its Electrically Conductive Polylactic Acid Nanocomposites. Compos. Sci. Technol. 2012, 72 (12), 1430–1435. https://doi.org/10.1016/j.compscitech.2012.05.018.

Shih, W.-P.; Tsao, L.-C.; Lee, C.-W.; Cheng, M.-Y.; Chang, C.; Yang, Y.-J.; Fan, K.-C. Flexible Temperature Sensor Array Based on a Graphite-Polydimethylsiloxane Composite. Sensors 2010, 10 (4), 3597–3610. https://doi.org/10.3390/s100403597.

Shih, W.-P.; Tsao, L.-C.; Lee, C.-W.; Cheng, M.-Y.; Chang, C.; Yang, Y.-J.; Fan, K.-C.; Flexible Temperature Sensor Array Based on a Graphite-Polydimethylsiloxane Composite. Sensors 2010, 10 (4), 3597–3610. https://doi.org/10.3390/s100403597.

Shin, H.-J.; Kim, K. K.; Benayad, A.; Yoon, S.-M.; Park, H. K.; Jung, I.-S.; Jin, M. H.; Jeong, H.-K.; Kim, J. M.; Choi, J.-Y.; Lee, Y. H. Efficient Reduction of Graphite Oxide by Sodium Borohydride and Its Effect on Electrical Conductance. Adv. Funct. Mater. 2009, 19 (12), 1987–1992. https://doi.org/10.1002/adfm.200900167.

Shin, H.-J.; Kim, K. K.; Benayad, A.; Yoon, S.-M.; Park, H. K.; Jung, I.-S.; Jin, M. H.; Jeong, H.-K.; Kim, J. M.; Choi, J.-Y.; Lee, Y. H. Efficient Reduction of Graphite Oxide by Sodium Borohydride and Its Effect on Electrical Conductance. Adv. Funct. Mater. 2009, 19 (12), 1987–1992. https://doi.org/10.1002/adfm.200900167.

Shin, S. R.; Jung, S. M.; Zalabany, M.; Kim, K.; Zorlutuna, P.; Kim, S. bok; Nikkhah, M.; Khabiry, M.; Azize, M.; Kong, J.; Wan, K.; Palacios, T.; Dokmeci, M. R.; Bae, H.; Tang, X. (Shirley); Khademhosseini, A. Carbon-Nanotube-Embedded Hydrogel Sheets for Engineering Cardiac Constructs and Bioactuators. ACS Nano 2013, 7 (3), 2369–2380.

Si, Y.; Samulski, E. T. Synthesis of Water Soluble Graphene. Nano Lett. 2008, 8 (6), 1679–1682. https://doi.org/10.1021/nl080604h.

Silva, C.; Caridade, S. G.; Cunha, E.; Sousa, M. P.; Rocha, H.; Mano, J. F.; Paiva, M. C.; Alves, N. M. Nanostructured Biopolymer/Few-Layer Graphene Freestanding Films with Enhanced Mechanical and Electrical Properties. Macromol. Mater. Eng.2017. https://doi.org/10.1002/mame.201700316.

Socher, R.; Krause, B.; Müller, M. T.; Boldt, R.; Pötschke, P. The Influence of Matrix Viscosity on MWCNT Dispersion and Electrical Properties in Different Thermoplastic Nanocomposites. Polymer 2012, 53 (2), 495–504.

Song, W.; Lee, J.-K.; Gong, M. S.; Heo, K.; Chung, W.-J.; Lee, B. Y. Cellulose Nanocrystal-Based Colored Thin Films for Colorimetric Detection of Aldehyde Gases. ACS Appl. Mater. Interfaces 2018, 10 (12), 10353–10361. https://doi.org/10.1021/acsami.7b19738.

Soni, M.; Bhattacharjee, M.; Ntagios, M.; Dahiya, R. Printed Temperature Sensor Based on PEDOT: PSS-Graphene Oxide Composite. IEEE Sens. J. 2020, 20 (14), 7525–7531. https://doi.org/10.1109/JSEN.2020.2969667.

Sreedevi, S.; Unni, K. N.; Sajith, S.; Priji, P.; Josh, M. S.; Benjamin, S. Bioplastics: Advances in Polyhydroxybutyrate Research. 2014, 1–30. https://doi.org/10.1007/12_2014_297.

Sridhar, V.; Lee, I.; Chun, H. H.; Park, H. Graphene Reinforced Biodegradable Poly (3-Hydroxybutyrate-Co-4-Hydroxybutyrate) Nano-Composites. Express Polym. Lett. 2013, 7 (4), 320–328.

Stankovich, S.; Dikin, D. A.; Dommett, G. H. B.; Kohlhaas, K. M.; Zimney, E. J.; Stach, E. A.; Piner, R. D.; Nguyen, S. T.; Ruoff, R. S. Graphene-Based Composite Materials. Nature 2006, 442 (7100), 282–286. https://doi.org/10.1038/nature04969.

Stankovich, S.; Dikin, D. A.; Piner, R. D.; Kohlhaas, K. A.; Kleinhammes, A.; Jia, Y.; Wu, Y.; Nguyen, S. T.; Ruoff, R. S. Synthesis of Graphene-Based Nanosheets via Chemical Reduction of Exfoliated Graphite Oxide. Carbon 2007, 45 (7), 1558–1565. https://doi.org/10.1016/j.carbon.2007.02.034.

Stauffer, D.; Aharony, A. Introduction To Percolation Theory: Second Edition; CRC Press, 2018.

Stauffer, D.; Aharony, A.; Aharony, A. Introduction To Percolation Theory : Second Edition; Taylor & Francis, 2018. https://doi.org/10.1201/9781315274386.

Su, C.-Y.; Xu, Y.; Zhang, W.; Zhao, J.; Tang, X.; Tsai, C.-H.; Li, L.-J. Electrical and Spectroscopic Characterizations of Ultra-Large Reduced Graphene Oxide Monolayers. Chem. Mater. 2009, 21 (23), 5674–5680. https://doi.org/10.1021/cm902182y.

Sun, H.; Castillo, A. E. D. R.; Monaco, S.; Capasso, A.; Ansaldo, A.; Prato, M.; Dinh, D. A.; Pellegrini, V.; Scrosati, B.; Manna, L.; Bonaccorso, F. Binder-Free Graphene as an Advanced Anode for Lithium Batteries. J. Mater. Chem. A 2016, 4 (18), 6886–6895. https://doi.org/10.1039/C5TA08553E.

Sun, Z.; Hasan, T.; Torrisi, F.; Popa, D.; Privitera, G.; Wang, F.; Bonaccorso, F.; Basko, D. M.; Ferrari, A. C. Graphene Mode-Locked Ultrafast Laser. ACS Nano 2010, 4 (2), 803–810. https://doi.org/10.1021/nn901703e.

Tang, Z.; Kang, H.; Shen, Z.; Guo, B.; Zhang, L.; Jia, D. Grafting of Polyester onto Graphene for Electrically and Thermally Conductive Composites. Macromolecules 2012, 45 (8), 3444–3451. https://doi.org/10.1021/ma300450t.

Tawakkal, I. S. M. A.; Cran, M. J.; Miltz, J.; Bigger, S. W. A Review of Poly(Lactic Acid)-Based Materials for Antimicrobial Packaging. J. Food Sci. 2014, 79 (8), R1477–R1490. https://doi.org/10.1111/1750-3841.12534.

Tran, T. S.; Dutta, N. K.; Choudhury, N. R. Graphene Inks for Printed Flexible Electronics: Graphene Dispersions, Ink Formulations, Printing Techniques and Applications. Adv. Colloid Interface Sci. 2018, 261, 41–61. https://doi.org/10.1016/j.cis.2018.09.003.

Trung, T. Q.; Ramasundaram, S.; Hwang, B.-U.; Lee, N.-E. An All-Elastomeric Transparent and Stretchable Temperature Sensor for Body-Attachable Wearable Electronics. Adv. Mater. 2016, 28 (3), 502–509. https://doi.org/10.1002/adma.201504441.

Trusovas, R.; Ratautas, K.; Račiukaitis, G.; Barkauskas, J.; Stankevičienė, I.; Niaura, G.; Mažeikienė, R. Reduction of Graphite Oxide to Graphene with Laser Irradiation. Carbon 2013, 52, 574–582. https://doi.org/10.1016/j.carbon.2012.10.017.

Tuning the properties of polyhydroxybutyrate films using acetic acid via solvent casting | Scientific Reports https://www.nature.com/articles/srep17884 (accessed Apr 1, 2020).

Tyler, B.; Gullotti, D.; Mangraviti, A.; Utsuki, T.; Brem, H. Polylactic Acid (PLA) Controlled Delivery Carriers for Biomedical Applications. Adv. Drug Deliv. Rev. 2016, 107, 163–175. https://doi.org/10.1016/j.addr.2016.06.018.

Uz, M.; Donta, M.; Mededovic, M.; Sakaguchi, D. S.; Mallapragada, S. K. Development of Gelatin and Graphene-Based Nerve Regeneration Conduits Using Three-Dimensional (3D) Printing Strategies for Electrical Transdifferentiation of Mesenchymal Stem Cells. Ind. Eng. Chem. Res. 2019, 58 (18), 7421–7427.

Valentini, L.; Cardinali, M.; Fortunati, E.; Torre, L.; Kenny, J. M. A Novel Method to Prepare Conductive Nanocrystalline Cellulose/Graphene Oxide Composite Films. Mater. Lett. 2013, 105, 4–7. https://doi.org/10.1016/j.matlet.2013.04.034.

Valentini, L.; Cardinali, M.; Kenny, J. Flexible Triboelectric Generator and Pressure Sensor Based on Poly[(R)-3-Hydroxybutyric Acid] Biopolymer. J. Polym. Sci. Part B Polym. Phys. 2014, 52 (13), 859–863.

Valentini, L.; Fabbri, P.; Messori, M.; Esposti, M. D.; Bon, S. B. Multilayer Films Composed of Conductive Poly(3-Hydroxybutyrate)/Carbon Nanotubes Bionanocomposites and a Photoresponsive Conducting Polymer. J. Polym. Sci. Part B Polym. Phys. 2014, 52 (8), 596–602.

Verlinden, R. a. J.; Hill, D. J.; Kenward, M. A.; Williams, C. D.; Radecka, I. Bacterial Synthesis of Biodegradable Polyhydroxyalkanoates. J. Appl. Microbiol. 2007, 102 (6), 1437–1449. https://doi.org/10.1111/j.1365-2672.2007.03335.x.

Vert, M. Aliphatic Polyesters: Great Degradable Polymers That Cannot Do Everything. Biomacromolecules 2005, 6 (2), 538–546. https://doi.org/10.1021/bm0494702.

Vert, M.; Li, S. M.; Spenlehauer, G.; Guerin, P. Bioresorbability and Biocompatibility of Aliphatic Polyesters. J. Mater. Sci. Mater. Med. 1992, 3 (6), 432–446. https://doi.org/10.1007/BF00701240.

Vo, N. H.; Dao, T. D.; Jeong, H. M. Electrically Conductive Graphene/Poly(Methyl Methacrylate) Composites with Ultra-Low Percolation Threshold by Electrostatic Self-Assembly in Aqueous Medium. Macromol. Chem. Phys. 2015, 216 (7), 770–782. https://doi.org/10.1002/macp.201400560.

Vuorinen, T.; Niittynen, J.; Kankkunen, T.; Kraft, T. M.; Mäntysalo, M. Inkjet-Printed Graphene/PEDOT:PSS Temperature Sensors on a Skin-Conformable Polyurethane Substrate. Sci. Rep. 2016, 6 (1), 1–8. https://doi.org/10.1038/srep35289.

Vuorinen, T.; Niittynen, J.; Kankkunen, T.; Kraft, T. M.; Mäntysalo, M. Inkjet-Printed Graphene/PEDOT:PSS Temperature Sensors on a Skin-Conformable Polyurethane Substrate. Sci. Rep. 2016, 6 (1), 1–8. https://doi.org/10.1038/srep35289.

Wan, Y.-J.; Tang, L.-C.; Yan, D.; Zhao, L.; Li, Y.-B.; Wu, L.-B.; Jiang, J.-X.; Lai, G.-Q. Improved Dispersion and Interface in the Graphene/Epoxy Composites via a Facile Surfactant-Assisted Process. Compos. Sci. Technol. 2013, 82 (Supplement C), 60–68. https://doi.org/10.1016/j.compscitech.2013.04.009.

Wan, Y.-J.; Yang, W.-H.; Yu, S.-H.; Sun, R.; Wong, C.-P.; Liao, W.-H. Covalent Polymer Functionalization of Graphene for Improved Dielectric Properties and Thermal Stability of Epoxy Composites. Compos. Sci. Technol. 2016, 122, 27–35. https://doi.org/10.1016/j.compscitech.2015.11.005.

Wan, Yan-Jun, et al. Improved dispersion and interface in the graphene/epoxy composites via a facile surfactant-assisted process. Composites science and technology 82, 2013, 60-68.

Wang, H.; Wang, Y.; Cao, X.; Feng, M.; Lan, G. Vibrational Properties of Graphene and Graphene Layers. J. Raman Spectrosc. 2009, 40 (12), 1791–1796. https://doi.org/10.1002/jrs.2321.

Wang, Y.; Zhang, Y.; Wang, G.; Shi, X.; Qiao, Y.; Liu, J.; Liu, H.; Ganesh, A.; Li, L. Direct Graphene-Carbon Nanotube Composite Ink Writing All-Solid-State Flexible Microsupercapacitors with High Areal Energy Density. Adv. Funct. Mater. 2020, 1907284. https://doi.org/10.1002/adfm.201907284.

Wei, X.; Li, D.; Jiang, W.; Gu, Z.; Wang, X.; Zhang, Z.; Sun, Z. 3D Printable Graphene Composite. Sci. Rep. 2015, 5, 11181. https://doi.org/10.1038/srep11181.

Wei, Y.-H.; Chen, W.-C.; Wu, H.-S.; Janarthanan, O.-M. Biodegradable and Biocompatible Biomaterial, Polyhydroxybutyrate, Produced by an Indigenous Vibrio Sp. BM-1 Isolated from Marine Environment. Mar. Drugs 2011, 9 (4), 615–624.

Wick, P.; Manser, P.; Limbach, L. K.; Dettlaff-Weglikowska, U.; Krumeich, F.; Roth, S.; Stark, W. J.; Bruinink, A. The Degree and Kind of Agglomeration Affect Carbon Nanotube Cytotoxicity. Toxicol. Lett. 2007, 168 (2), 121–131. https://doi.org/10.1016/j.toxlet.2006.08.019.

Withers, F.; Yang, H.; Britnell, L.; Rooney, A. P.; Lewis, E.; Felten, A.; Woods, C. R.; Sanchez Romaguera, V.; Georgiou, T.; Eckmann, A.; Kim, Y. J.; Yeates, S. G.; Haigh, S. J.; Geim, A. K.; Novoselov, K. S.; Casiraghi, C. Heterostructures Produced from Nanosheet-Based Inks. Nano Lett. 2014, 14 (7), 3987–3992. https://doi.org/10.1021/nl501355j.

Wu, J.; Hong, Y. Enhancing Cell Infiltration of Electrospun Fibrous Scaffolds in Tissue Regeneration. Bioact. Mater. 2016, 1 (1), 56–64.

Wujcik, E. K.; Monty, C. N. Nanotechnology for Implantable Sensors: Carbon Nanotubes and Graphene in Medicine. WIREs Nanomedicine Nanobiotechnology 2013, 5 (3), 233–249.

Wujcik, E. K.; Monty, C. N. Nanotechnology for Implantable Sensors: Carbon Nanotubes and Graphene in Medicine. WIREs Nanomedicine Nanobiotechnology 2013, 5 (3), 233–249. https://doi.org/10.1002/wnan.1213.

Xi, J., Zhang, L., Zheng, Z. A., Chen, G., Gong, Y., Zhao, N., & Zhang, X.. Preparation and evaluation of porous poly (3-hydroxybutyrate-co-3-hydroxyhexanoate)—hydroxyapatite composite scaffolds. Journal of biomaterials applications, 2008, 22(4), 293-307.

Xiao, S. Y.; Che, L. F.; Li, X. X.; Wang, Y. L. A Novel Fabrication Process of MEMS Devices on Polyimide Flexible Substrates. Microelectron. Eng. 2008, 85 (2), 452–457. https://doi.org/10.1016/j.mee.2007.08.004.

Xiao, S.; Che, L.; Li, X.; Wang, Y. A Cost-Effective Flexible MEMS Technique for Temperature Sensing. Microelectron. J. 2007, 38 (3), 360–364. https://doi.org/10.1016/j.mejo.2007.01.022.

Xu, Baoxing, et al. An epidermal stimulation and sensing platform for sensorimotor prosthetic control, management of lower back exertion, and electrical muscle activation. Advanced Materials 28.22, 2016, 4462-4471.

Yang, L.; Chen, Y.; Wang, M.; Shi, S.; Jing, J. Fused Deposition Modeling 3D Printing of Novel Poly(Vinyl Alcohol)/Graphene Nanocomposite with Enhanced Mechanical and Electromagnetic Interference Shielding Properties. Ind. Eng. Chem. Res. 2020, 59 (16), 8066–8077.

Yang, Weixing, et al. Ultrathin flexible reduced graphene oxide/cellulose nanofiber composite films with strongly anisotropic thermal conductivity and efficient electromagnetic interference shielding. Journal of Materials Chemistry C 5.15, 2017, 3748-3756.

Yang, Y.-J.; Cheng, M.-Y.; Chang, W.-Y.; Tsao, L.-C.; Yang, S.-A.; Shih, W.-P.; Chang, F.-Y.; Chang, S.-H.; Fan, K.-C. An Integrated Flexible Temperature and Tactile Sensing Array Using PI-

Copper Films. Sens. Actuators Phys. 2008, 143 (1), 143–153. https://doi.org/10.1016/j.sna.2007.10.077.

Yoonessi, M.; Gaier, J. R. Highly Conductive Multifunctional Graphene Polycarbonate Nanocomposites. ACS Nano 2010, 4 (12), 7211–7220. https://doi.org/10.1021/nn1019626.

Yu, G.; Hu, J.; Tan, J.; Gao, Y.; Lu, Y.; Xuan, F. A Wearable Pressure Sensor Based on Ultra-Violet/Ozone Microstructured Carbon Nanotube/Polydimethylsiloxane Arrays for Electronic Skins. Nanotechnology 2018, 29 (11), 115502. https://doi.org/10.1088/1361-6528/aaa855.

Yu, G.; Hu, J.; Tan, J.; Gao, Y.; Lu, Y.; Xuan, F. A Wearable Pressure Sensor Based on Ultra-Violet/Ozone Microstructured Carbon Nanotube/Polydimethylsiloxane Arrays for Electronic Skins. Nanotechnology 2018, 29 (11), 115502. https://doi.org/10.1088/1361-6528/aaa855.

Yun, S. I.; Gadd, G. E.; Latella, B. A.; Lo, V.; Russell, R. A.; Holden, P. J. Mechanical Properties of Biodegradable Polyhydroxyalkanoates/Single Wall Carbon Nanotube Nanocomposite Films. Polym. Bull. 2008, 61 (2), 267–275.

Yun, S.; Kim, J. Mechanical, Electrical, Piezoelectric and Electro-Active Behavior of Aligned Multi-Walled Carbon Nanotube/Cellulose Composites. Carbon 2011, 49 (2), 518–527. https://doi.org/10.1016/j.carbon.2010.09.051.

Yun, Sungryul, and Jaehwan Kim. Mechanical, electrical, piezoelectric and electro-active behavior of aligned multi-walled carbon nanotube/cellulose composites. Carbon 49.2, 2011, 518-527.

Zhang, D.; Chi, B.; Li, B.; Gao, Z.; Du, Y.; Guo, J.; Wei, J. Fabrication of Highly Conductive Graphene Flexible Circuits by 3D Printing. Synth. Met. 2016, 217, 79–86. https://doi.org/10.1016/j.synthmet.2016.03.014.

Zhang, J.; Shen, G.; Wang, W.; Zhou, X.; Guo, S. Individual Nanocomposite Sheets of Chemically Reduced Graphene Oxide and Poly(N-Vinyl Pyrrolidone): Preparation and Humidity Sensing Characteristics. J. Mater. Chem. 2010, 20 (48), 10824–10828. https://doi.org/10.1039/C0JM02440F.

Zhang, J.; Yang, H.; Shen, G.; Cheng, P.; Zhang, J.; Guo, S. Reduction of Graphene Oxide ViaL-Ascorbic Acid. Chem. Commun. 2010, 46 (7), 1112–1114. https://doi.org/10.1039/B917705A.

Zhang, J.; Yang, H.; Shen, G.; Cheng, P.; Zhang, J.; Guo, S. Reduction of Graphene Oxide ViaL-Ascorbic Acid. Chem. Commun. 2010, 46 (7), 1112–1114. https://doi.org/10.1039/B917705A.

Zhang, M.; Yeow, J. T. W. A Flexible, Scalable, and Self-Powered Mid-Infrared Detector Based on Transparent PEDOT: PSS/Graphene Composite. Carbon 2020, 156, 339–345. https://doi.org/10.1016/j.carbon.2019.09.062.

Zhang, R.; Agar, J. C.; Wong, C. P. Conductive Polymer Composites. In Encyclopedia of Polymer Science and Technology; John Wiley & Sons, Inc., 2002. https://doi.org/10.1002/0471440264.pst430.pub2.

Zhao, C.; Xing, L.; Xiang, J.; Cui, L.; Jiao, J.; Sai, H.; Li, Z.; Li, F. Formation of Uniform Reduced Graphene Oxide Films on Modified PET Substrates Using Drop-Casting Method. Particuology 2014, 17, 66–73. https://doi.org/10.1016/j.partic.2014.02.005.

Zhao, K.; Deng, Y.; Chun Chen, J.; Chen, G.-Q. Polyhydroxyalkanoate (PHA) Scaffolds with Good Mechanical Properties and Biocompatibility. Biomaterials 2003, 24 (6), 1041–1045.

Zhao, S., Zhu, M., Zhang, J., Zhang, Y., Liu, Z., Zhu, Y., & Zhang, C.. Three dimensionally printed mesoporous bioactive glass and poly (3-hydroxybutyrate-co-3-hydroxyhexanoate) composite scaffolds for bone regeneration. Journal of Materials Chemistry B, 2014, 2(36), 6106-6118.

Zhao, S.; Lou, D.; Zhan, P.; Li, G.; Dai, K.; Guo, J.; Zheng, G.; Liu, C.; Shen, C.; Guo, Z. Heating-Induced Negative Temperature Coefficient Effect in Conductive Graphene/Polymer Ternary Nanocomposites with a Segregated and Double-Percolated Structure. J. Mater. Chem. C 2017, 5 (32), 8233–8242. https://doi.org/10.1039/C7TC02472J.

Zinn, M.; Witholt, B.; Egli, T. Occurrence, Synthesis and Medical Application of Bacterial Polyhydroxyalkanoate. Adv. Drug Deliv. Rev. 2001, 53 (1), 5–21. https://doi.org/10.1016/S0169-409X(01)00218-6.